



*sustainability*

# Radioactivity

## Sustainable Materials and Innovative Techniques

---

Edited by  
Hosam M. Saleh and Mohammad Mahmoud Dawoud  
Printed Edition of the Special Issue Published in *Sustainability*

# **Radioactivity: Sustainable Materials and Innovative Techniques**



# Radioactivity: Sustainable Materials and Innovative Techniques

Editors

**Hosam M. Saleh**

**Mohammad Mahmoud Dawoud**

MDPI • Basel • Beijing • Wuhan • Barcelona • Belgrade • Manchester • Tokyo • Cluj • Tianjin



*Editors*

Hosam M. Saleh  
Egyptian Atomic Energy  
Authority  
Egypt

Mohammad Mahmoud Dawoud  
Egyptian Atomic Energy  
Authority  
Egypt

*Editorial Office*

MDPI  
St. Alban-Anlage 66  
4052 Basel, Switzerland

This is a reprint of articles from the Special Issue published online in the open access journal *Sustainability* (ISSN 2071-1050) (available at: [https://www.mdpi.com/journal/sustainability/special\\_issues/Radioactive.Waste.Management](https://www.mdpi.com/journal/sustainability/special_issues/Radioactive.Waste.Management)).

For citation purposes, cite each article independently as indicated on the article page online and as indicated below:

LastName, A.A.; LastName, B.B.; LastName, C.C. Article Title. *Journal Name* **Year**, *Volume Number*, Page Range.

**ISBN 978-3-0365-7248-2 (Hbk)**

**ISBN 978-3-0365-7249-9 (PDF)**

© 2023 by the authors. Articles in this book are Open Access and distributed under the Creative Commons Attribution (CC BY) license, which allows users to download, copy and build upon published articles, as long as the author and publisher are properly credited, which ensures maximum dissemination and a wider impact of our publications.

The book as a whole is distributed by MDPI under the terms and conditions of the Creative Commons license CC BY-NC-ND.

# Contents

|                                                                                                                                                                                                                                                                                                                                                                                                          |     |
|----------------------------------------------------------------------------------------------------------------------------------------------------------------------------------------------------------------------------------------------------------------------------------------------------------------------------------------------------------------------------------------------------------|-----|
| <b>About the Editors</b> . . . . .                                                                                                                                                                                                                                                                                                                                                                       | vii |
| <b>Hosam M. Saleh and Amal I. Hassan</b><br>Radioactivity: Sustainable Materials and Innovative Techniques<br>Reprinted from: <i>Sustainability</i> <b>2023</b> , <i>15</i> , 5792, doi:10.3390/su15075792 . . . . .                                                                                                                                                                                     | 1   |
| <b>Young Jae Jang, Na Hye Kwon, Seong Hee Park, Yona Choi, Kum Bae Kim, Dong Wook Kim, et al.</b><br>Analysis of Activated Materials of Disposed Medical Linear Accelerators according to Clearance Level for Self-Disposal<br>Reprinted from: <i>Sustainability</i> <b>2023</b> , <i>15</i> , 4100, doi:10.3390/su15054100 . . . . .                                                                    | 7   |
| <b>Arwa A. Abdelhamid, Mogeda H. Badr, Ramadan A. Mohamed and Hosam M. Saleh</b><br>Using Agricultural Mixed Waste as a Sustainable Technique for Removing Stable Isotopes and Radioisotopes from the Aquatic Environment<br>Reprinted from: <i>Sustainability</i> <b>2023</b> , <i>15</i> , 1600, doi:10.3390/su15021600 . . . . .                                                                      | 19  |
| <b>Essam Sidiqie, Sedky H. A. Hassan and Mohammad Mahmoud Dawoud</b><br>Natural Radioactivity Measurements and Radiological Hazards Evaluation for Some Egyptian Granites and Ceramic Tiles<br>Reprinted from: <i>Sustainability</i> <b>2022</b> , <i>14</i> , 14611, doi:10.3390/su142114611 . . . . .                                                                                                  | 35  |
| <b>Mohamed Ehab, Elsayed Salama, Ahmed Ashour, Mohamed Attallah and Hosam M. Saleh</b><br>Optical Properties and Gamma Radiation Shielding Capability of Transparent Barium Borosilicate Glass Composite<br>Reprinted from: <i>Sustainability</i> <b>2022</b> , <i>14</i> , 13298, doi:10.3390/su142013298 . . . . .                                                                                     | 55  |
| <b>Prasoon Raj, Nemeer Padiyath, Natalia Semioshkina, Francois Foulon, Ahmed K. Alkaabi, Gabriele Voigt and Yacine Addad</b><br>Transfer of Natural Radionuclides from Soil to Abu Dhabi Date Palms<br>Reprinted from: <i>Sustainability</i> <b>2022</b> , <i>14</i> , 11327, doi:10.3390/su141811327 . . . . .                                                                                          | 73  |
| <b>Tarek E. Sayed and El-Sayed S. Ahmed</b><br>Elicitation Promoability with Gamma Irradiation, Chitosan and Yeast to Perform Sustainable and Inclusive Development for Marjoram under Organic Agriculture<br>Reprinted from: <i>Sustainability</i> <b>2022</b> , <i>14</i> , 9608, doi:10.3390/su14159608 . . . . .                                                                                     | 87  |
| <b>Elsayed Salama, Dalal A. Aloraini, Sara A. El-Khateeb and Mohamed Moustafa</b><br>Rhyolite as a Naturally Sustainable Thermoluminescence Material for Dose Assessment Applications<br>Reprinted from: <i>Sustainability</i> <b>2022</b> , <i>14</i> , 6918, doi:10.3390/su14116918 . . . . .                                                                                                          | 97  |
| <b>Mohammad Khairul Azhar Abdul Razab, Norazlina Mat Nawi, Fara Hana Mohd Hadzuan, Nor Hakim Abdullah, Maimanah Muhamad, Rosidah Sunaiwi, et al.</b><br>Fluorine-18 Fluorodeoxyglucose Isolation Using Graphene Oxide for Alternative Radiopharmaceutical Spillage Decontamination in PET Scan<br>Reprinted from: <i>Sustainability</i> <b>2022</b> , <i>14</i> , 4492, doi:10.3390/su14084492 . . . . . | 111 |
| <b>Hosam M. Saleh, Ibrahim I. Bondouk, Elsayed Salama, Hazem H. Mahmoud, Khalid Omar and Heba A. Esawii</b><br>Asphaltene or Polyvinylchloride Waste Blended with Cement to Produce a Sustainable Material Used in Nuclear Safety<br>Reprinted from: <i>Sustainability</i> <b>2022</b> , <i>14</i> , 3525, doi:10.3390/su14063525 . . . . .                                                              | 125 |

**Yue You, Junfeng Dou, Yu Xue, Naifu Jin and Kai Yang**

Chelating Agents in Assisting Phytoremediation of Uranium-Contaminated Soils: A Review

Reprinted from: *Sustainability* **2022**, *14*, 6379, doi:10.3390/su14106379 . . . . . **139**

## About the Editors

### **Hosam M. Saleh**

Hosam M. Saleh is a professor of radioactive waste management at the Radioisotope Department, Egyptian Atomic Energy Authority, Egypt. He was awarded MSc and Ph.D. degrees in Physical Chemistry from Cairo University. Saleh has more than 26 years of experience in hazardous waste management with an emphasis on treatment and developing new matrixes for the immobilization of these wastes. He is also interested in studying innovative economic and environmentally friendly techniques for the management of hazardous and radioactive wastes. He authored many peer-reviewed scientific papers and chapters and served as a Book Editor of several books related to international publishers. He has been named among the top 2% of scientists in the world according to the Stanford University report for 2020, 2021 and 2022. He is also a reviewer, an Editor in Chief or Associate Editor for different journals as well as a member of the Technical Program Committee for international conferences. He won the Scientific Encouragement Award from Atomic Energy Authority (2013) and the Encouragement Prize in Advanced Technical Sciences from the Academy of Scientific Research (2014).

### **Mohammad Mahmoud Dawoud**

Dr. Mohammad Mahmoud Dawoud is an environmental researcher at the Radioisotope Department, Egyptian Atomic Energy Authority, Egypt. He graduated from the Agricultural Engineering Department, Faculty of Agriculture, Ainshams University. BSc. Agricultural Engineering (Excellent with Rank of Honors); M.Sc. (Detoxification of Heavy metals From wastewater using Agriculture residues as absorbent material and Nuclear Technique); Ph.D. (Remediation of contaminated water using some physical and radiation techniques). He specializes in environmental chemistry and engineering redox and adsorption interactions, and he has more than ten years of experience in water treatment systems (reverse osmosis, sewage plants and filtration units for poultry farms, livestock and fish farms). He has designed and implemented more than 380 water treatment projects. He has participated in many research projects related to the environmental field and sustainability. Currently, he is considered one of the most important consultants in the field of water treatment in Egypt. He is also an environmental consultant for major international NGOs such as Rotary Egypt and the Alpha foundation for Environmental Technologies, and he has won many awards in this regard.





# Radioactivity: Sustainable Materials and Innovative Techniques

Hosam M. Saleh \* and Amal I. Hassan

Radioisotope Department, Nuclear Research Center, Egyptian Atomic Energy Authority, Cairo 11787, Egypt

\* Correspondence: hosamsaleh70@yahoo.com or hosam.saleh@eaea.org.eg

Radioisotopes, also known as radionuclides, are atoms with unstable nuclei that emit ionizing radiation. Radioisotopes have a wide range of applications in medicine, industry, and scientific research, including in cancer diagnosis and treatment, sterilization of medical equipment, and dating of geological and archaeological materials [1,2]. However, the use of radioisotopes also poses significant risks to human health and the environment due to their potential for radioactive contamination and exposure [3,4].

Radioactive waste management is a critical component of nuclear safety. It involves the safe and sustainable disposal of nuclear waste generated from various sources, including nuclear power plants, medical facilities, research facilities, and industrial processes [5]. With the advancement of technology and scientific research, innovative approaches to radioactive waste management have emerged, ensuring sustainable nuclear safety [6].

Waste management and nuclear safety are critical issues that need to be addressed with utmost seriousness. Proper waste management ensures that the environment and the public are not exposed to harmful materials, while nuclear safety measures are necessary to prevent accidents and incidents that could result in radiation leaks [7–9].

Waste treatment and disposal methods are crucial components of waste management. Several methods are used for waste treatment, including recycling, incineration, and landfilling. Recycling involves converting waste materials into new products or materials, while incineration involves burning waste materials to reduce their volume and weight [10]. Landfilling is the most common method of waste disposal, where waste is buried in a designated area [11].

Nuclear waste, which is generated from nuclear power plants, research facilities, and medical institutions, requires special treatment and disposal methods due to its radioactive nature. The most common method of nuclear waste treatment is reprocessing, which involves extracting useful materials from nuclear waste [12]. The remaining waste is then disposed of in specialized facilities designed for storage or final disposal [13].

Nuclear safety measures are critical to prevent accidents that could lead to radiation leaks. Nuclear power plants are designed with multiple layers of safety systems, including automated shutdown systems and emergency cooling systems. Regular inspections, maintenance, and training of personnel are also necessary to ensure nuclear safety [14].

Overall, waste management and nuclear safety are complex issues that require a comprehensive approach. Governments, industries, and individuals must work together to develop effective waste treatment and disposal methods while also implementing strict safety measures to prevent nuclear accidents [15].

Innovative approaches to radioactive waste management are critical for ensuring sustainable nuclear safety [16]. The use of natural materials, radiation techniques, and waste management methods can ensure the safe and sustainable disposal of radioactive waste generated by various sources, including nuclear power plants, medical facilities, research facilities, and industrial processes [17]. These innovative approaches ensure the protection of the environment and public health, while also promoting sustainable nuclear safety. Several sustainable materials have been used in nuclear applications such as cellulosic waste in treatment [18,19] or cement mixed with bitumen [20,21], cement waste [22,23], glass [24,25], and natural clay [26,27] for radioactive waste stabilization and radiation shielding.

**Citation:** Saleh, H.M.; Hassan, A.I. Radioactivity: Sustainable Materials and Innovative Techniques. *Sustainability* **2023**, *15*, 5792. <https://doi.org/10.3390/su15075792>

Received: 21 March 2023  
Accepted: 23 March 2023  
Published: 27 March 2023



**Copyright:** © 2023 by the authors. Licensee MDPI, Basel, Switzerland. This article is an open access article distributed under the terms and conditions of the Creative Commons Attribution (CC BY) license (<https://creativecommons.org/licenses/by/4.0/>).

In this Special Issue, Young Jae Jang, Hye Kwon, Seong Hee Park, Yona Choi, Kum Bae Kim, Dong Wook Kim, Suk Ho Bhang, and Sang Hyoun Choi discuss discarding parts of a medical linear accelerator (linac). The study emphasizes the importance of checking the activity of each part to determine the disposal time according to the clearance level for self-disposal. The clearance level for self-disposal for each radionuclide-activated part was applied by three manufacturers to confirm the timing of self-disposal and to predict when workers are not exposed to radiation during disassembly/disposal. In the interest of establishing the framework for unambiguous safety management standards for the disposal of decommissioned linacs, a qualitative and quantitative study of radionuclides was undertaken using high-purity Germanium (HPGe)-based gamma spectroscopy in addition to the Monte (contribution 1).

Natural mixed waste biomass is an innovative approach to the remediation of contaminated sites. The use of natural mixed waste biomass as a radioisotope biosorbent is a cost-effective approach to the remediation of contaminated sites. Natural mixed waste biomass is an excellent radioisotope biosorbent that can remove radioactive contaminants from soil and water. This approach ensures the safe and sustainable disposal of radioactive waste generated by nuclear facilities. Arwa Abdelhamid, Mogeda Badr, Ramadan Mohamed, and Hosam Saleh explain a sustainable treatment system that uses dry biomass from mixed trash to show synergistic benefits such as high efficiency and cost-effectiveness. The removal of stable and radioisotopes of cobalt and cesium from aqueous solutions was examined in this work using biosorption in dried mixed waste of olive waste and water hyacinth as a low-cost and naturally accessible sorbent. The findings indicate that the natural biomass of mixed garbage is a good biosorbent for the isotopes studied. According to the experimental and mathematical results in this study, a mixed dry waste of water hyacinth and olive waste might be proposed as a sustainable low-cost and effective natural adsorbent material for the efficient remediation of radio or stable cobalt and cesium ions from wastewater. In addition, this method is expected to successfully decontaminate toxic metals and radionuclides in an ecologically benign and sustainable way while significantly lowering wastewater treatment costs (contribution 2).

Natural radioactivity is present in many materials, including granite and ceramic tiles, which contain small amounts of naturally occurring radioactive elements such as  $^{232}\text{Th}$  and  $^{238}\text{U}$  [28]. These elements emit ionizing radiation in the form of alpha, beta, and gamma rays, which can potentially pose health risks to humans if they are exposed to them for prolonged periods. However, research has shown that the use of mainly granite and ceramic tiles in construction and decoration does not present significant risks to human health. To this effect, Essam Sidiq, Sedky Hassan, and Mohammad Mahmoud Dawoud evaluated twenty-three well-known brands of Egyptian commercial granites and ceramic tile samples radiologically using an HPGe detector, consisting of 107 samples of typical materials. The concentrations of radioisotopes were found to be greater in most granite samples compared to the ceramic samples. Additionally, the concentration values of terrestrial radionuclides showed considerable variations in granite and ceramic tile samples obtained from various manufacturers. This is important in distinguishing between the brands under consideration. The concentration of  $^{40}\text{K}$  was discovered to be the greatest contribution to the overall concentration for all samples, followed by  $^{232}\text{Th}$  and  $^{238}\text{U}$  (contribution 3).

A study by Mohamed Ehab, Elsayed Salama, Ahmed Ashour, Mohamed Attallah, and Hosam Saleh investigated the radiation shielding capabilities as well as the optical qualities of a prepared  $\text{SiO}_2\text{-ZnO-Na}_2\text{CO}_3\text{-H}_3\text{BO}_3\text{-BaCO}_3$  glass composite with varying amounts of barium carbonate (0–30 mol%). Therefore, fabricated glass is an innovative approach to transparent shielding. The use of fabricated glass for applications requiring transparent shielding can reduce the volume of radioactive waste generated by nuclear facilities. This approach ensures the safe and sustainable disposal of radioactive waste while also providing transparent shielding for various applications (contribution 4).

In a study by Prasoon Raj, Nemeer Padiyath, Natalia Semioshkina, Francois Foulon, Ahmed Alkaabi Gabriele Voigt, and Yacine Addad seven date palm plants in Abu Dhabi

were tested. Their root zone soils, fruits, and leaves were sampled and analyzed for gamma-emitting naturally occurring radioactive materials (NORM) radionuclide activity. The soil samples exhibit significant levels of  $^{40}\text{K}$ , while the levels of  $^{238}\text{U}$  and  $^{232}\text{Th}$  are substantially lower. The measured soil radioactivity is below the global average (contribution 5).

The goal of Tarek Sayed and El-Sayed Ahmed's research is to see if gamma irradiation, chitosan, and yeast may help promote the sustainable development of marjoram in the context of organic farming. The primary plot has an abiotic elicitor (15 Gy gamma irradiation), two biotic elicitors (500 ppm chitosan, 0.5% yeast, and a non-elicitor (as control), and two organic fertilizers (20 g/m<sup>2</sup> moringa dry leaves, 20 g/m<sup>2</sup> fulvic acid, and 20 g/m<sup>2</sup> (NPK); the latter is a classic agrochemical). They show strong evidence for the potency of biotic elicitors chitosan > yeast > abiotic, gamma irradiation coupled with organic fertilizers moringa > fulvic acid > traditional agrochemical fertilizer NPK, as reliable CO-friendly solutions, significantly improving marjoram biomass, secondary metabolite production, and quality without the use of agrochemical pesticides and/or microbicides. In addition, chitosan > yeast > gamma irradiation in combination with organic fertilizers outperformed their integration with commercial NPK fertilizer (contribution 6).

Elsayed Salama, Dalal Aloraini, Sara El-Khateeb, and Mohamed Moustafa investigated the thermoluminescence properties of natural rhyolite. Dose response has been evaluated across a large dosage range of 0.5–2000 Gy. The minimum detectable dosage and the rate of thermal fading are calculated. After selecting the optimal read-out conditions, glow curve deconvolution was performed. The overlapping peaks were detected using the repeated initial rise (RIR) approach, and the thermoluminescence characteristics of rhyolite were extracted using a glow curve deconvolution procedure. A linear dose response up to 25 Gy was achieved, followed by supra linearity up to 2000 Gy. The TL properties of rhyolite revealed that it exhibits a linear dose response up to 25 Gy, followed by supra linearity up to 2000 Gy, and a comparatively high fading rate of 57% after two weeks with no further thermal fading seen. There is a low detection limit of around 0.5 Gy and a decent reproducibility of about 4% variance in subsequent measurements. These properties may qualify rhyolite as the sustainable natural material employed in this work for a range of radiation dose assessment applications (contribution 7).

Mohammad Khairul Azhar Abdul Razab, Norazlina Mat Nawi, Fara Hana Mohd Hadzuan, Nor Hakim Abdullah, Maimanah Muhamad, Rosidah Sunaiwi, Fathirah Ibrahim, Farah Amanina Mohd Zin and An'amt Mohamed Noor confirmed that the high sorption capacity and the ability to coagulate with any reactive elements at molecular structures, such as  $^{18}\text{F}$ -FDG, makes it a prime option for alternative radionuclides decontamination. The 'wax tissue' nanolayers and vast surface area have been shown to help graphene oxide (GO) wrap and adsorb radionuclides effectively. The adsorption rate was effective at a slow decay rate of  $^{18}\text{F}$ -FDG, where more available free electrons are ready for the adsorption interaction with GO functional groups. Graphene oxide nanoparticles are innovative approaches to the safe and sustainable preparation of radiopharmaceuticals. The use of graphene oxide nanoparticles can ensure the safe and sustainable preparation of radiopharmaceuticals, which may contaminate surface areas due to a spill during their preparation or an accident during their transportation from the laboratory to the treatment room. Graphene oxide nanoparticles show a high absorption affinity towards radionuclides, ensuring the safe and sustainable disposal of radioactive waste (Contribution 8).

Hosam Saleh, Ibrahim Bondouk, Elsayed Salama, Hazem Mahmoud, Khalid Omar, and Heba Esawii adopt environmentally friendly techniques to conserve the environment, such as recycling municipal or industrial waste, where the debris of polyvinyl chloride (PVC) pipes and asphaltene is used as cement additives to improve its mechanical properties while stabilizing radioactive waste resulting from the peaceful uses of nuclear materials, or enhancing its efficiency in radiation protection (Contribution 9).

Chelating agents for uranium mine residues: Chelating agents are innovative approaches to eliminating uranium mine residues. The use of chelating agents can remove uranium from mine residues and prevent soil pollution. This approach ensures the safe and

sustainable disposal of radioactive waste generated by uranium mining. Therefore, in their review, Yue You, Junfeng Dou, Yu Xue, Naifu Jin, and Kai Yang discussed the synthesis and application of chelating agents to assist in the phytoremediation of uranium-contaminated soils. The interactions between chelating agents and uranium ions were also demonstrated, in addition to presenting the mechanisms of plant extraction and the effectiveness of different chelating agents for the phytoremediation of soil contaminated with uranium. Furthermore, potential risks associated with chelating agents are discussed. The review also presented the synthesis and application of biodegradable slow-release chelating agents to slow mineral mobilization into the soil while reducing the risk of residual chelating agent leaching into groundwater (contribution 10).

### List of Contributions

1. Jae Jang, Y.; Hye Kwon, H.; Park, S.H.; Choi, Y.; Kim, K.B.; Kim, D.W.; Bhang, S.H., and Choi, S.H. Analysis of Activated Materials of Disposed Medical Linear Accelerators according to Clearance Level for Self-Disposal.
2. Abdelhamid, A.A.; Badr, M.H.; Mohamed, R.A. and Saleh, H.M. Using Agricultural Mixed Waste as a Sustainable Technique for Removing Stable Isotopes and Radioisotopes from the Aquatic Environment.
3. Sidique, E.; Hassan, S.H.A. and Dawoud, M.M. Natural Radioactivity Measurements and Radiological Hazards Evaluation for Some Egyptian Granites and Ceramic Tiles.
4. Ehab, M.; Salama, E.; Ashour, A.; Attallah, M. and Saleh, H.M. Optical Properties and Gamma Radiation Shielding Capability of Transparent Barium Borosilicate Glass Composite.
5. Raj, P.; Padiyath, N.; Semioshkina, N.; Foulon, F.; Voigt, A.K.A.G. and Addad, Y. Transfer of Natural Radionuclides from Soil to Abu Dhabi Date Palms.
6. Sayed, T. E. and Ahmed, E.S. Elicitation Promotability with Gamma Irradiation, Chitosan, and Yeast to Perform Sustainable and Inclusive Development for Marjoram under Organic Agriculture.
7. Salama, E.; Aloraini, D.A.; El-Khateeb, S.A. and Moustafa, M. Rhyolite as a Naturally Sustainable Thermoluminescence Material for Dose Assessment Applications.
8. Abdul Razab, M.K.A.; Nawwi, N.M.; Hadzuan, F.H.M.; Abdullah, N.H.; Muhammad, M.; Sunaiwi, R.; Ibrahim, F.; Zin, F.A.M. and Noor, A.M. Fluorine-18 Fluorodeoxyglucose Isolation Using Graphene Oxide for Alternative Radiopharmaceutical Spillage Decontamination in PET Scan.
9. Saleh, H.M.; Bondouk, I.I.; Salama, E.; Mahmoud, H.H.; Omar, K. and Esawii, H.A. Asphaltene or Polyvinylchloride Waste Blended with Cement to Produce a Sustainable Material Used in Nuclear Safety.
10. You, Y.; Dou, J.; Xue, Y.; Jin, N. and Yang, K. Chelating Agents in Assisting Phytoremediation of Uranium-Contaminated Soils: A Review.

**Conflicts of Interest:** The authors declare no conflict of interest.

### References

1. Hassan, A.I.; Saleh, H.M. Biological Effects of Hazardous Waste: Threshold Limits of Anomalies and Protective Approaches. In *Hazardous Waste Management and Health Risks*; Bentham Science Publishers: Potomac, MD, USA, 2020; pp. 62–96. [[CrossRef](#)]
2. Economou, G.; Kandarakis, I.; Panagiotakis, G.; Vlachos, I. PRINCIPLES OF X-RAY TECHNOLOGY IN MEDICAL IMAGING AND IMPROVEMENT OF RADIOLOGICAL IMAGES (2nd Part). *Paripex-Indian J. Res.* **2022**, *11*, 86–89. [[CrossRef](#)]
3. Saleh, H.M.; Moussa, H.R.; Mahmoud, H.H.; El-Saied, F.A.; Dawoud, M.; Abdel Wahed, R.S. Potential of the Submerged Plant *Myriophyllum Spicatum* for Treatment of Aquatic Environments Contaminated with Stable or Radioactive Cobalt and Cesium. *Prog. Nucl. Energy* **2020**, *118*, 103147. [[CrossRef](#)]
4. Hassan, A.I.; Saleh, H.M. Radioisotope Department, Nuclear Research Centre, Atomic Energy Authority, Giza, Egypt. In *Handbook of Greener Synthesis of Nanomaterials and Compounds: Volume 2: Synthesis at the Macroscale and Nanoscale*; Elsevier: Amsterdam, The Netherlands, 2021; p. 449.

5. Hassan, A.I.; Saleh, H.M. Chapter 7—Toxicity and Hazardous Waste Regulations. In *Hazardous Waste Management: An Overview of Advanced and Cost-Effective Solutions*; Yadav, D., Kumar, P., Singh, P., Vallerio, D.A.B.T.-H.W.M., Eds.; Elsevier: Amsterdam, The Netherlands, 2022; pp. 165–182; ISBN 978-0-12-824344-2.
6. Saleh, H.M.; Hassan, A.I. Medical Geochemistry. *Geochemistry* **2021**, 127–147. [[CrossRef](#)]
7. Saleh, H.M.; Eskander, S.B. Innovative Cement-Based Materials for Environmental Protection and Restoration. In *New Materials in Civil Engineering*; Elsevier: Amsterdam, The Netherlands, 2020; pp. 613–641.
8. Saleh, H.M.; Moussa, H.R.; El-Saied, F.A.; Dawoud, M.; Bayoumi, T.A.; Abdel Wahed, R.S. Mechanical and Physicochemical Evaluation of Solidified Dried Submerged Plants Subjected to Extreme Climatic Conditions to Achieve an Optimum Waste Containment. *Prog. Nucl. Energy* **2020**, 122, 103285. [[CrossRef](#)]
9. Eskander, S.B.; Saleh, H.M.; Tawfik, M.E.; Bayoumi, T.A. Towards Potential Applications of Cement-Polymer Composites Based on Recycled Polystyrene Foam Wastes on Construction Fields: Impact of Exposure to Water Ecologies. *Case Stud. Constr. Mater.* **2021**, 15, e00664. [[CrossRef](#)]
10. Rajkovic, S.; Bornhöft, N.A.; van der Weijden, R.; Nowack, B.; Adam, V. Dynamic Probabilistic Material Flow Analysis of Engineered Nanomaterials in European Waste Treatment Systems. *Waste Manag.* **2020**, 113, 118–131. [[CrossRef](#)]
11. Joseph, B.; James, J.; Kalarikkal, N.; Thomas, S. Recycling of Medical Plastics. *Adv. Ind. Eng. Polym. Res.* **2021**, 4, 199–208. [[CrossRef](#)]
12. Fuks, L.; Herdzik-Koniecko, I.; Kiegiel, K.; Miskiewicz, A.; Zakrzewska-Koltuniewicz, G. Methods of Thermal Treatment of Radioactive Waste. *Energies* **2022**, 15, 375. [[CrossRef](#)]
13. Muller, R.A.; Finsterle, S.; Grimsich, J.; Baltzer, R.; Muller, E.A.; Rector, J.W.; Payer, J.; Apps, J. Disposal of High-Level Nuclear Waste in Deep Horizontal Drillholes. *Energies* **2019**, 12, 2052. [[CrossRef](#)]
14. Juraku, K.; Sugawara, S.-E. Structural Ignorance of Expertise in Nuclear Safety Controversies: Case Analysis of Post-Fukushima Japan. *Nucl. Technol.* **2021**, 207, 1423–1441. [[CrossRef](#)]
15. Sharma, H.B.; Vanapalli, K.R.; Cheela, V.R.S.; Ranjan, V.P.; Jaglan, A.K.; Dubey, B.; Goel, S.; Bhattacharya, J. Challenges, Opportunities, and Innovations for Effective Solid Waste Management during and Post COVID-19 Pandemic. *Resour. Conserv. Recycl.* **2020**, 162, 105052. [[CrossRef](#)] [[PubMed](#)]
16. Kurniawan, T.A.; Othman, M.H.D.; Singh, D.; Avtar, R.; Hwang, G.H.; Setiadi, T.; Lo, W. Technological Solutions for Long-Term Storage of Partially Used Nuclear Waste: A Critical Review. *Ann. Nucl. Energy* **2022**, 166, 108736. [[CrossRef](#)]
17. Saleh, H.M.; Bondouk, I.I.; Salama, E.; Esawii, H.A. Consistency and Shielding Efficiency of Cement-Bitumen Composite for Use as Gamma-Radiation Shielding Material. *Prog. Nucl. Energy* **2021**, 137, 103764. [[CrossRef](#)]
18. Dawoud, M.M.A.; Hegazi, M.M.; Saleh, H.M.; El Helew, W.K. Removal of Stable and Radio Isotopes from Wastewater by Using Modified Microcrystalline Cellulose Based on Taguchi L16. *Int. J. Environ. Sci. Technol.* **2022**, 20, 1289–1300. [[CrossRef](#)]
19. Saleh, H.M.; Eskander, S.B. Long-Term Effect on the Solidified Degraded Cellulose-Based Waste Slurry in Cement Matrix. *Acta Montan. Slovaca* **2009**, 14, 291–297.
20. Bayoumi, T.A.; Reda, S.M.; Saleh, H.M. Assessment Study for Multi-Barrier System Used in Radioactive Borate Waste Isolation Based on Monte Carlo Simulations. *Appl. Radiat. Isot.* **2012**, 70, 99–102. [[CrossRef](#)]
21. Reda, S.M.; Saleh, H.M. Calculation of the Gamma Radiation Shielding Efficiency of Cement-Bitumen Portable Container Using MCNPX Code. *Prog. Nucl. Energy* **2021**, 142, 104012. [[CrossRef](#)]
22. Saleh, H.M.; El-Saied, F.A.; Salaheldin, T.A.; Hezo, A.A. Macro- and Nanomaterials for Improvement of Mechanical and Physical Properties of Cement Kiln Dust-Based Composite Materials. *J. Clean. Prod.* **2018**, 204, 532–541. [[CrossRef](#)]
23. Saleh, H.M.; El-Saied, F.A.; Salaheldin, T.A.; Hezo, A.A. Influence of Severe Climatic Variability on the Structural, Mechanical and Chemical Stability of Cement Kiln Dust-Slag-Nanosilica Composite Used for Radwaste Solidification. *Constr. Build. Mater.* **2019**, 218, 556–567. [[CrossRef](#)]
24. Eid, M.S.; Bondouk, I.I.; Saleh, H.M.; Omar, K.M.; Diab, H.M. Investigating the Effect of Gamma and Neutron Irradiation on Portland Cement Provided with Waste Silicate Glass. *Sustainability* **2022**, 15, 763. [[CrossRef](#)]
25. Eid, M.S.; Bondouk, I.I.; Saleh, H.M.; Omar, K.M.; Sayyed, M.I.; El-Khatib, A.M.; Elsafi, M. Implementation of Waste Silicate Glass into Composition of Ordinary Cement for Radiation Shielding Applications. *Nucl. Eng. Technol.* **2021**, 54, 1456–1463. [[CrossRef](#)]
26. Saleh, H.M. Some Applications of Clays in Radioactive Waste Management. In *Clays and Clay Minerals: Geological Origin, Mechanical Properties and Industrial Applications*; Wesley, L.R., Ed.; Nova Science Publishers, Inc.: New York, NY, USA, 2014; pp. 403–415; ISBN 978-1-63117-779-8.
27. Eskander, S.B.; Bayoumi, T.A.; Saleh, H.M. Leaching Behavior of Cement-Natural Clay Composite Incorporating Real Spent Radioactive Liquid Scintillator. *Prog. Nucl. Energy* **2013**, 67, 1–6. [[CrossRef](#)]
28. Senthilkumar, G.; Raghu, Y.; Sivakumar, S.; Chandrasekaran, A.; Anand, D.P.; Ravisankar, R. Natural Radioactivity Measurement and Evaluation of Radiological Hazards in Some Commercial Flooring Materials Used in Thiruvannamalai, Tamilnadu, India. *J. Radiat. Res. Appl. Sci.* **2014**, 7, 116–122. [[CrossRef](#)]

### Short Author Biography

**Hosam Saleh** is a professor of radioactive waste management at the Radioisotope Department, Atomic Energy Authority, Egypt. He was awarded MSc and Ph.D. degrees in Physical Chemistry from Cairo University. Saleh has more than 25 years of experience in hazardous waste management with an emphasis on treatment and developing new matrixes for the immobilization of these wastes. He is also interested in studying innovative economic and environment-friendly techniques for the management of hazardous and radioactive wastes. He authored many peer-reviewed scientific papers and chapters and served as a Book Editor of several books related to international publishers. He has been selected among the top 2% of scientists in the world according to the Stanford University report for 2020, 2021 and 2022. He is also a reviewer, an Editor in Chief or Associate Editor for different journals as well as a member of the Technical Program Committee for international conferences. He gained the Scientific Encouragement Award from Atomic Energy Authority (2013), Encouragement Prize in Advanced Technical Sciences from the Academy of Scientific Research (2014).

**Disclaimer/Publisher's Note:** The statements, opinions and data contained in all publications are solely those of the individual author(s) and contributor(s) and not of MDPI and/or the editor(s). MDPI and/or the editor(s) disclaim responsibility for any injury to people or property resulting from any ideas, methods, instructions or products referred to in the content.



## Article

# Analysis of Activated Materials of Disposed Medical Linear Accelerators according to Clearance Level for Self-Disposal

Young Jae Jang <sup>1,2,†</sup>, Na Hye Kwon <sup>3,4,†</sup>, Seong Hee Park <sup>2</sup>, Yona Choi <sup>2</sup>, Kum Bae Kim <sup>1</sup>, Dong Wook Kim <sup>3,4</sup>, Suk Ho Bhang <sup>5,\*</sup> and Sang Hyoun Choi <sup>1,\*</sup>

<sup>1</sup> Research Team of Radiological Physics & Engineering, Korea Institute of Radiological & Medical Sciences, Seoul 01812, Republic of Korea

<sup>2</sup> Department of Accelerator Science, Korea University, Sejong 30015, Republic of Korea

<sup>3</sup> Department of Radiation Oncology, Yonsei Cancer Center, Heavy Ion Therapy Research Institute, Yonsei University College of Medicine, Seoul 03722, Republic of Korea

<sup>4</sup> Medical Physics and Biomedical Engineering Lab (MPBEL), Yonsei University College of Medicine, Seoul 03722, Republic of Korea

<sup>5</sup> School of Chemical Engineering, Sungkyunkwan University, Suwon 16419, Republic of Korea

\* Correspondence: sukhobhang@skku.edu (S.H.B.); shchoi@kiram.s.re.kr (S.H.C.); Tel.: +82-31-290-7242 (S.H.B.); +82-2-970-1590 (S.H.C.)

† These authors contributed equally to this work.

**Abstract:** In Korea, when replacing or discarding parts of a medical linear accelerator (linac), self-disposal is required in the consideration of the activity, but there is no standard regulation to manage radioactive waste. The aim of this study is to check the activity of each part to determine the disposal time according to the clearance level for self-disposal. The results of measuring the components of the linac head parts of the disposed Varian, Elekta, and Siemens equipment were reflected in the Monte Carlo simulation to confirm the radionuclide change according to the presence or absence of impurities. To confirm the degree of activation of the linac, the main radionuclides according to the time after the linac shutdown, considering the workloads of 40/80 Gy/day of 10/15 MV linac irradiated with beams for 10 years in the results of the simulation of the linac parts, and the radionuclide concentration was confirmed. As a result of applying the clearance level for self-disposal in the notice of the Korean Nuclear Safety (KINS) to each linac head part, most parts of the 10 MV linac could be dismantled after 1 month, and 15 MV target and primary collimators were stored after a long period of time before being dismantled. Although additional radionuclides were identified according to the presence or absence of impurities, the disposal timing for each part did not change significantly. In this study, the clearance level for self-disposal for each radionuclide was applied to activated parts by three manufacturers to confirm the self-disposal timing and predict the timing at which workers are not exposed to radiation during dismantling/disposal.

**Keywords:** radioactive waste; medical linear accelerator; clearance level; radionuclide; Monte Carlo simulation

**Citation:** Jang, Y.J.; Kwon, N.H.; Park, S.H.; Choi, Y.; Kim, K.B.; Kim, D.W.; Bhang, S.H.; Choi, S.H. Analysis of Activated Materials of Disposed Medical Linear Accelerators according to Clearance Level for Self-Disposal. *Sustainability* **2023**, *15*, 4100. <https://doi.org/10.3390/su15054100>

Academic Editors: Hosam M. Saleh and Mohammad Mahmoud Dawoud

Received: 30 January 2023

Revised: 21 February 2023

Accepted: 21 February 2023

Published: 23 February 2023



**Copyright:** © 2023 by the authors. Licensee MDPI, Basel, Switzerland. This article is an open access article distributed under the terms and conditions of the Creative Commons Attribution (CC BY) license (<https://creativecommons.org/licenses/by/4.0/>).

## 1. Introduction

To meet the growing demand for radiotherapy, an increasing number of medical linear accelerators (hereinafter referred to as “linac”) are being installed in Korean hospitals every year ( $n = 185$  in 2022) [1]. Alongside new installations, an increasingly higher number of existing linacs has been replaced or disposed of in recent years. The service life of linacs ranges from 10 to 15 years, and they are replaced or disposed of for reasons such as the aging of parts, failure of major parts, and introduction of new treatment equipment [2]. According to the data from the Korean Institute of Nuclear Safety (KINS) in 2018 [3], two or more linacs are replaced or disposed of every year in Republic of Korea. It is recommended that the details of each case of replacement or disposal be reported to the KINS and major parts be subjected to self-disposal or storage for later disposal after evaluating their activity.



The Korean Nuclear Safety and Security Commission (NSSC) Notice No. 2020-6 stipulates the permissible standards for the self-disposal of radioactive waste according to the clearance level of each radionuclide [4]. In the case of medical linacs, however, no accurate information on radionuclides is available and standardized regulations allowing the flexible management of different workloads have yet to be established. Therefore, there is a major need for a management plan for dismantling radioactive parts of medical linear accelerators.

Various radionuclides generated through the activation process in a linac can cause problems to patients and related healthcare workers in general, and workers can be exposed to them during disposal/dismantling in particular. It is, hence, of paramount importance to quantify the radionuclides generated and compute the dose rates [5].

NCRP 79 specifies 10 MeV as the energy threshold for evaluation because only a negligible number of neutrons are generated at energies below 10 MeV, which defines the target, primary collimator, flattening filter, and head parts as the highest risks of activation [6]. In addition, IAEA-TECDOC-1183 suggested the possibility of the surrounding materials being activated by an accelerator using an energy of 10 MeV or greater, and clarified the necessity to assess the radiation hazard when dismantling the head of a medical linac used in radiation oncology [7].

A variety of studies have been conducted to identify and analyze radionuclides to ensure the safety of workers, concluding that radionuclides are mainly generated from the target, primary collimator, flattening filter, jaws, multileaf collimator (MLC), and bending magnet by high-energy photon beams [8,9]. These materials mainly consist of tungsten, gold, copper, and stainless steel. The target to produce photons is made of a high-density metal, such as tungsten or gold, and a primary collimator is made of tungsten, which is used to reduce the amount of scattered radiation. The flattening filter consisting of tungsten or brass is designed to generate a beam with a more uniform intensity across the field, and a jaw (MLC) made of tungsten is used to adjust the size and shape of the treatment beam. The properties of these components are carefully designed to ensure that the radiation beam is accurately directed towards the target area, while minimizing the dose to surrounding healthy tissue.

For the accurate assessment of radionuclides generated by the high-energy photon beams of each part when dismantling a linac, radionuclides emitted from each part should be identified using a gamma spectrometer or a Monte Carlo simulation method based on the data provided by the manufacturer and the component analysis of additional parts using laser-induced breakdown spectroscopy (LIBS) [10].

Adam Konefal et al. and Waller et al. identified and quantified activation products and their estimated activities generated by 18 MV Elekta and 15 MV Varian Truebeam using gamma-ray spectroscopy with HPGe [11,12]. Vichi et al. performed a Monte-Carlo-simulation-based activation study of a 15 MeV linear accelerator, investigating the production of radioactive isotopes and dose rates in various materials [9]. However, these studies did not evaluate the effect of radioactivity caused by impurities in the linear accelerator, nor did they study the change in nuclide and radioactivity over time after shutting down the linear accelerator.

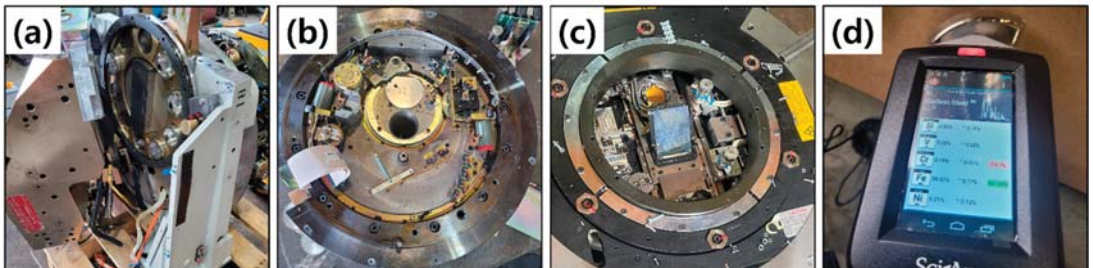
The presence of impurities in components can be a significant source of uncertainty in radiation measurements. Impurities in materials can produce additional gamma rays or other types of radiation that may not be accurately accounted for in the measurement process. There is a limit to studying the evaluation of radioactivity over time after the shutdown of the linear accelerator using HPGe. Even after the linear accelerator is turned off, the materials used in the construction of the accelerator and its components may continue to emit radiation owing to the residual activity of radioactive isotopes. This residual activity can persist for varying lengths of time depending on the specific isotopes involved, making it difficult to assess the radiation exposure levels in the surrounding environment accurately.

In this study, the degrees of activation of the components and impurities of each major part were assessed using LIBS for mapping out their composition in Varian, Elekta, and Siemens linacs, and by performing a Monte Carlo simulation. Based on the assessment results, it is intended to predict the timing of storage and disposal of each part taking into account its clearance level by determining the radionuclides emitted during the accelerator dismantling/disposal and the activation level over time.

## 2. Materials and Methods

### 2.1. Component Analysis of the Parts of Decommissioned Linacs by Manufacturer

Components, including the head of three decommissioned medical linacs, were analyzed. Particularly, the linacs investigated were Clinac iX (Varian), Agility™ (Elekta), and Oncor Expression (Siemens). The study focused on the parts of the linac head that are prone to activation in terms of the beam pathway, which included the target, primary collimator, ion chamber, jaw (MLC), and bending magnet. To confirm the components of each dismantled linac head part, laser-induced breakdown spectroscopy (LIBS) was used. Surface investigation was conducted at least three times for each part using a portable LIBS element analyzer (Z-300 GeoChem Pro, SciAps Inc., Woburn, MA, USA). The results of the measurements were then compared with the specifications provided by each manufacturer, and the levels of impurities were analyzed. Figure 1a–c shows the process of dismantling the linac head parts manufactured by Varian, Elekta, and Siemens, respectively. Figure 1d shows the portable LIBS device measuring the emission from each major component of the dismantled head parts.



**Figure 1.** Dismantled linac head parts of (a) Clinac iX (Varian); (b) Synergy platform (Elekta); (c) Oncor Expression (Siemens); and (d) LIBS measurement results of the components of their major parts.

### 2.2. Monte Carlo Simulation of Medical Linacs

Monte Carlo simulation was used to evaluate radionuclides generated by parts of the linear accelerator according to energy and workload. It is a computational method that uses random sampling to obtain numerical solutions to mathematical problems, and it is often used to model the behavior of particles (such as photons, electrons, or neutrons) as they interact with matter. It can simulate the behavior of particles in complex systems to study the effects of different materials, geometries, and other factors.

To perform a Monte Carlo simulation, we obtained the internal structures and specifications of different components of the medical linacs from their respective manufacturers, and devised three-dimensional models using AutoCAD software (Autodesk Inc., San Francisco, CA, USA). Specifically, parts such as target, primary collimator, ion chamber, jaw, and MLC of Varian, Elekta, and Siemens equipment were modeled based on the data provided by the manufacturers, and bending magnets and lead shields were modeled additionally based on the analysis data of the structures of decommissioned linacs. The SuperMC program (Super Monte Carlo simulation program, FDS team, Hefei, China) [13] was used to convert the modeled data into PHITS (Version 3.25) code written in Fortran [14]. The particle and heavy ion transport code system (PHITS) is a widely used general-purpose Monte Carlo simulation code that can handle the transport of all particles over a wide

range of energies using various nuclear reaction models and nuclear data libraries. It is used in numerous fields related to particle and heavy ion transport phenomena, including accelerator technology, radiotherapy, and space radiation. Using this code, radionuclides that can be generated for each part of the linear accelerator were simulated according to the energy of 10/15 MV and the workload of 40 and 80 Gy/day.

### 2.3. Time-Dependent Activity Level

The PHITS code, which was used to analyze radionuclides and their activity levels, was based on the nuclear data in the ENDF-6 format (ENDF-102), and the coding was performed to include all reactions in the 0.001 to 50 MeV energy band for gamma spectroscopic analysis by using source and tally. The source component in the PHITS code was specified as a transverse Gaussian distribution electron beam with energy levels of 10/15 MeV, which collided with a target to generate a photon beam. The nuclear physics module of PHITS included models for simulating nuclear reactions, such as scattering, fission, and fusion, as well as models to produce secondary particles, such as neutrons and gamma rays, in these reactions.

To calculate the neutron flux from the PHITS code, T-DCHAIN and T-Volume Tally were utilized. These include information such as cell number, beam amplitude, number of irradiations, cooling time steps, and the volume of each part to derive the neutron flux. To precisely determine the radionuclide concentration, time-dependent energy and current values were entered in the DCHAIN code, considering the linac's workload. The decay chain analysis code DCHAIN [15] was used to analyze all radionuclides of each component based on the neutron's flux results, whereby nuclear data were extracted from hybrid data libraries, such as JENDL/AD-2017, FENDL/A-3.0, JENDL-4.0, ENDF/B-VIII.0, and JEFF-3.3, to encompass all nuclides [16,17].

To assess the degree of activation of a medical linac, workloads of 80 Gy/day and 40 Gy/day were reflected in the DCHAIN code for equipment irradiated with beams for 10 years, and the time-dependent change in the activation level of radionuclides of each part was monitored by measuring it immediately after the linac shutdown and 6 h, 1 month, 3 months, 1 year, 5 years, and 10 years later. Major radionuclides were selected as those from the components whose activity level accounted for 0.01% or more of the total activity level among those with an activity level of  $10^{-6}$  Bq/g or higher immediately after linac shutdown and a half-life of 5 s or more.

## 3. Results

### 3.1. Component Analysis of the Parts of Decommissioned Linacs by Manufacturer

In Table 1, the elements of each of the main parts (target, primary collimator, flattening filter, ion chamber, mirror, jaw, and MLC) that affect major impurities and additional radionuclides, whose element composition ratios account for more than 0.5% of the total element composition, are listed along with the data provided by each manufacturer.

Among the parts with no data provided by the manufacturers and whose components were measured by LIBS, the bending magnet was found to be mainly composed of Fe, with the bending magnet provided by Varian containing large amounts of Cr and Ni, unlike those provided by Elekta and Siemens. In the LIBS measurement results, Varian's flattening filter 15 MV, Elekta's primary collimator, and Siemens' MLC were composed of 100% tungsten, with no impurities detected. As for the target, primary collimator, and jaw, the largest share of impurities was detected in those manufactured by Varian. Only the primary collimator manufactured by Siemens includes an absorber; therefore, it is annotated as Varian and Elekta in Table 1.

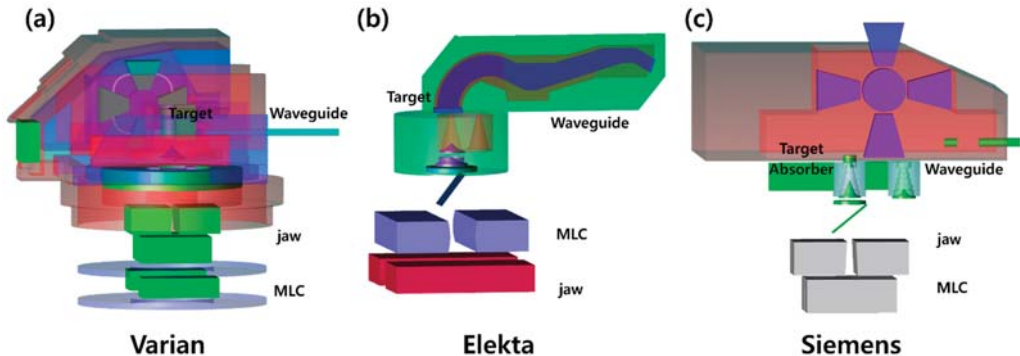
**Table 1.** Elements of the major parts of the medical linacs by manufacturer.

| Major Parts             | Varian                | Elekta                   | Siemens             |
|-------------------------|-----------------------|--------------------------|---------------------|
| Target                  | Cu W Zn *             | W Re Cu                  | Au Fe Cr Ni Cu *    |
| Bending magnet          | Fe * Cr * Ni *        | Fe * Si * Ni * Pb * Cu * | Fe * Mo *           |
| Primary collimator      | W Fe * Cr * Ni * Mn * | W Ni Fe                  | W                   |
| Absorber                | **                    | **                       | Al Ag * Cu * Mg *   |
| Flattening filter 15 MV | W                     | Fe Cr Mn Ni Mo *         | Fe Cr Mn Ni Mo *    |
| Flattening filter 10 MV | Cu O Zn *             |                          |                     |
| Ion chamber             | H C O N               | Al Si Fe Mn Mg           | Al O Mg * Ag * Cu * |
| Mirror                  | H C O                 | H C O                    | O Si Ca Na          |
| Jaw                     | W Ni * Cu * Nb * Mo * | W Ni Fe                  | W                   |
| MLC                     | W Ni Fe Cu            | W Ni Fe Cr * Mo *        | W                   |

\* Components additionally identified in LIBS measurements; \*\* head part components with no specifications provided by the manufacturers.

### 3.2. Medical Linac Modeling and Workload-Based Activation Evaluation

The schematic representations in Figure 2 are the results of modeling the main components and shield structures of the head parts of the three manufacturers. Siemens' target, unlike those of Varian and Elekta, is made of different materials, such as graphite, gold, and SST304, and is modeled in such a way that the absorber is placed inside the primary collimator; a beam of 10 MV or greater is applied. While the MLC of Varian is placed after the jaw, that of Elekta is placed before the jaw. For this reason, unlike other manufacturers, Elekta's MLC has a higher activity than the jaw. In addition to the main head part components, radiation shielding mainly composed of lead was additionally modeled to evaluate radionuclides and activity levels.



**Figure 2.** Medical linac modeling results of the three manufacturers: (a) Varian; (b) Elekta; and (c) Siemens.

No workload-dependent differences in the radionuclides were observed among the parts, and an analysis of the activity level revealed that the radiation of beams at a workload of 80 Gy/day was about twice as high as that of 40 Gy/day. In this study, radionuclides and their activity level analysis were analyzed based and compared on the workload of 80 Gy/day, taking a conservative approach. The main radionuclides from each manufacturer's parts are listed in Table 2. Radionuclides in Table 2 are the results of photonuclear reactions, such as  $(\gamma, n)$ ,  $(n, \gamma)$ ,  $(\gamma, 2n)$ , and  $(\gamma, np)$ . Nuclear reactions were confirmed through Monte Carlo simulations, including  $^{182}\text{W}(\gamma, n)^{181}\text{W}$ ,  $^{197}\text{Au}(\gamma, n)^{196}\text{Au}$ ,  $^{66}\text{Zn}(\gamma, n)^{65}\text{Zn}$ ,  $^{186}\text{W}(n, \gamma)^{187}\text{W}$ ,  $^{27}\text{Al}(n, \gamma)^{28}\text{Al}$ ,  $^{54}\text{Fe}(n, p)^{54}\text{Mn}$ , and  $^{58}\text{Ni}(n, p)^{58}\text{Co}$ . As additional radionuclides were contained in the parts with large proportions of impurities,  $^{94\text{m}}\text{Nb}$ ,  $^{58}\text{Co}$ , and  $^{99}\text{Mo}$  were detected in the jaw of Varian,  $^{99}\text{Mo}$  in the MLC of Elekta, and  $^{108}\text{Ag}$ ,  $^{65}\text{Zn}$ , and  $^{58}\text{Co}$  in the absorber of Siemens.

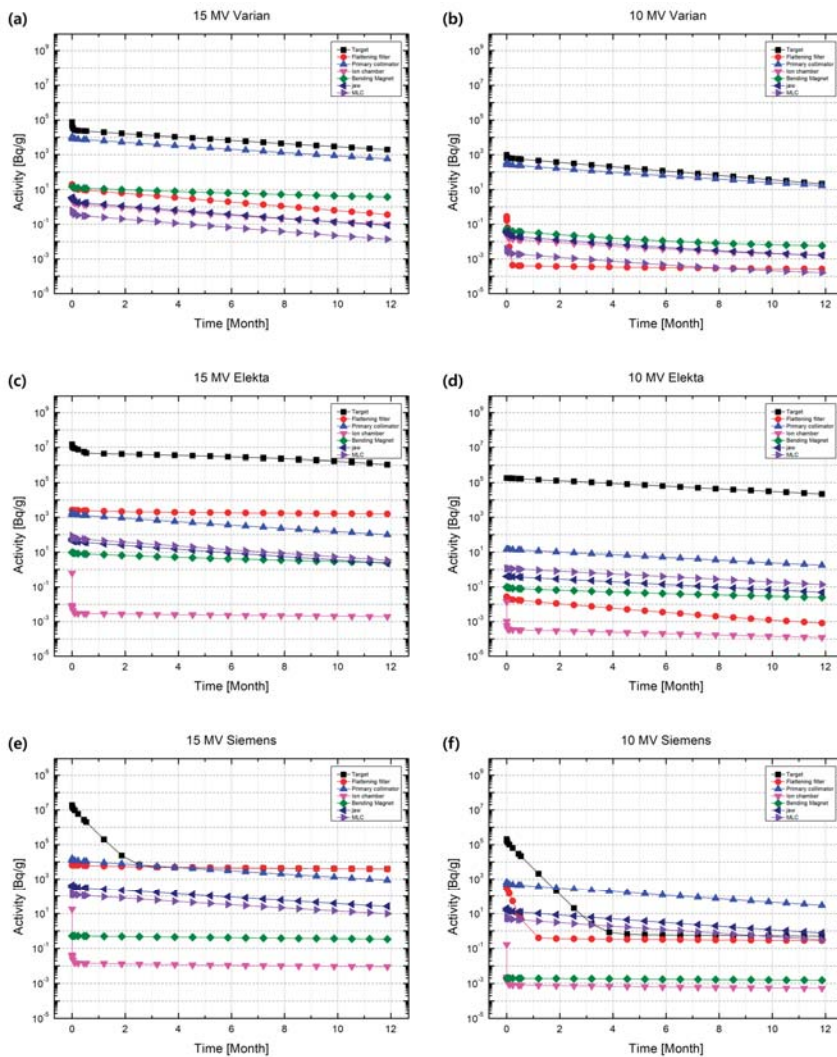
**Table 2.** List of major radionuclides in the parts of each manufacturer emitted at the workload of 80 Cy/day and activity in each part after shutdown.

| Major Parts        | Varian                        |                          | Elekta                   |                              | Siemens                  |                          |
|--------------------|-------------------------------|--------------------------|--------------------------|------------------------------|--------------------------|--------------------------|
|                    | Nuclide (T <sub>1/2</sub> )   | Activity [Bq/g]<br>15 MV | Activity [Bq/g]<br>10 MV | Nuclide (T <sub>1/2</sub> )  | Activity [Bq/g]<br>15 MV | Activity [Bq/g]<br>10 MV |
| Target             | <sup>64</sup> Cu (12.70 h)    |                          |                          | <sup>181</sup> W (121.18 d)  |                          |                          |
|                    | <sup>181</sup> W (121.18 d)   | 7.58 × 10 <sup>4</sup>   | 9.71 × 10 <sup>2</sup>   | <sup>64</sup> Cu (12.70 h)   | 1.47 × 10 <sup>7</sup>   | 1.84 × 10 <sup>5</sup>   |
|                    | <sup>187</sup> W (75.12 d)    |                          |                          | <sup>65</sup> Zn (243.98 d)  |                          |                          |
|                    | <sup>65</sup> Ni (101.15 y)   |                          |                          | <sup>38</sup> Co (70.86 d)   |                          |                          |
| Bending magnet     | <sup>55</sup> Fe* (2.75 y)    |                          |                          | <sup>55</sup> Fe* (2.75 y)   |                          |                          |
|                    | <sup>57</sup> Co* (271.76 d)  | 14.47                    | 5.26 × 10 <sup>-2</sup>  | <sup>54</sup> Mn* (312.04 d) | 9.65                     | 9.65 × 10 <sup>-2</sup>  |
|                    | <sup>58</sup> Co* (70.86 d)   |                          |                          | <sup>59</sup> Fe* (44.49 d)  |                          |                          |
|                    | <sup>57</sup> Ni* (1.48 d)    |                          |                          |                              |                          |                          |
| Primary collimator | <sup>187</sup> W (75.12 d)    |                          |                          | <sup>187</sup> W (75.12 d)   |                          |                          |
|                    | <sup>181</sup> W (121.18 d)   | 1.09 × 10 <sup>4</sup>   | 3.52 × 10 <sup>2</sup>   | <sup>181</sup> W (121.18 d)  | 1.88 × 10 <sup>3</sup>   | 14.46                    |
|                    | <sup>179</sup> Ta (1.82 y)    |                          |                          |                              |                          |                          |
|                    | <sup>55</sup> Fe* (2.75 y)    |                          |                          |                              |                          |                          |
| Absorber           |                               | **                       |                          |                              | **                       |                          |
|                    |                               |                          |                          |                              |                          | 0.48                     |
| Flattening filter  | <sup>181</sup> W (121.18 d)   |                          |                          | <sup>58</sup> Co (70.86 d)   |                          |                          |
|                    | <sup>187</sup> W (75.12 d)    | 19.12                    |                          | <sup>54</sup> Mn (312.04 d)  | 2.63 × 10 <sup>3</sup>   | 2.65 × 10 <sup>-2</sup>  |
|                    | <sup>66</sup> Cu (307.20 s)   |                          | 0.28                     | <sup>59</sup> Fe (2.75 y)    |                          |                          |
|                    | <sup>64</sup> Cu (12.70 h)    |                          |                          | <sup>99</sup> Mo* (2.75 d)   |                          |                          |
| Ion chamber        | <sup>3</sup> H (12.33 y)      |                          |                          | <sup>28</sup> Al (134.50 s)  |                          |                          |
|                    | <sup>14</sup> C (5704.59 y)   | 2.60                     | 2.49 × 10 <sup>-2</sup>  | <sup>56</sup> Mn (2.58 h)    | 0.62                     | 1.37 × 10 <sup>-2</sup>  |
|                    |                               |                          |                          | <sup>65</sup> Zn (243.98 d)  |                          |                          |
|                    |                               |                          |                          | <sup>65</sup> Ni (101.15 y)  |                          |                          |
| Mirror             | <sup>3</sup> H (12.33 y)      |                          |                          | <sup>3</sup> H (12.33 y)     |                          |                          |
|                    | <sup>14</sup> C (5704.59 y)   | 3.00 × 10 <sup>-7</sup>  | 4.32 × 10 <sup>-7</sup>  | <sup>14</sup> C (5704.59 y)  | 3.12 × 10 <sup>-4</sup>  | 4.12 × 10 <sup>-5</sup>  |
|                    |                               |                          |                          |                              |                          |                          |
| Jaw                | <sup>187</sup> W (75.12 d)    |                          |                          | <sup>187</sup> W (75.12 d)   |                          |                          |
|                    | <sup>94m</sup> Nb* (375.80 s) | 3.51                     | 3.82 × 10 <sup>-2</sup>  | <sup>181</sup> W (121.18 d)  | 58.29                    | 0.4                      |
|                    | <sup>38</sup> Co* (70.86 d)   |                          |                          | <sup>38</sup> Co (70.86 d)   |                          |                          |
| MLC                | <sup>187</sup> W (75.12 d)    |                          |                          | <sup>187</sup> W (75.12 d)   |                          |                          |
|                    | <sup>181</sup> W (121.18 d)   | 0.62                     | 3.82 × 10 <sup>-3</sup>  | <sup>181</sup> W (121.18 d)  | 87.44                    | 1.14                     |
|                    | <sup>64</sup> Cu (12.70 h)    |                          |                          | <sup>90m</sup> Nb (16.14 y)  |                          |                          |
|                    | <sup>55</sup> Fe (2.75 y)     |                          |                          | <sup>99</sup> Mo* (2.75 d)   |                          |                          |

\* Components additionally identified in LIBS measurements; \*\* head part components with no specifications provided by the manufacturers.

### 3.3. Time-Dependent Activity Level of Each Linac Part

The major radionuclides detected in the target after stopping the beam were  $^{185}\text{W}$ ,  $^{181}\text{W}$ , and  $^{64}\text{Cu}$  in Varian, with the highest activity level changing from  $^{64}\text{Cu}$  ( $2.69 \times 10^4$  Bq/g) immediately after the linac shutdown to  $^{185}\text{W}$  and  $^{181}\text{W}$  one day later. This change of the major radionuclide from  $^{64}\text{Cu}$  to tungsten isotopes can be explained by the former's half-life of 12.7 h (Figure 3a,b). In the target of Elekta, the major radionuclides changed from  $^{181}\text{W}$ ,  $^{64}\text{Cu}$ , and  $^{65}\text{Zn}$  immediately after the linac shutdown to  $^{181}\text{W}$  and  $^{64}\text{Cu}$  after one day. In particular, since  $^{181}\text{W}$ , which is a long half-life radionuclide, maintained a high concentration of  $1.83 \times 10^6$  Bq/g even after one year, not much lower than the initial concentration of  $1.47 \times 10^7$  Bq/g (Figure 3c,d).



**Figure 3.** Time-dependent changes in the activity levels of the linac major parts obtained by applying a workload of 80 Gy/day at the energy levels of 15 and 10 MV: (a) 15 MV Varian; (b) 10 MV Varian; (c) 15 MV Elekta; (d) 10 MV Elekta; (e) 15 MV Siemens; and (f) 10 MV Siemens.



Unlike Varian and Elekta, Siemens' target is composed of materials such as graphite, gold and SST304, giving rise to various radionuclide changes for each material. The main radionuclides detected immediately after stopping the beam were  $^3\text{H}$  and  $^{14}\text{C}$  in graphite,  $^{196}\text{Au}$  and  $^{198}\text{Au}$  in gold, and  $^{55}\text{Fe}$ ,  $^{51}\text{Cr}$ ,  $^{99}\text{Mo}$  in SST304. In particular,  $^{196}\text{Au}$  had a very high initial concentration of  $1.23 \times 10^7$  Bq/g, which fell to  $1 \times 10^3$  Bq/g two months later because it has a short half-life of 6.183 days (Figure 3e,f). From two months after the linac shutdown onward,  $^{55}\text{Fe}$ ,  $^{51}\text{Cr}$ , and  $^{58}\text{Co}$ , which are long half-life radionuclide in SST304, were identified as the major radionuclides. The highest time-dependent activity levels were found in the target up to two months after the linac shutdown in all three manufacturers (Figure 3).

On the other hand, although various radionuclides in impurities were additionally detected (Table 2), the content of the impurities in each part was negligibly low when their activity levels were checked against the composition of the components of the parts provided by the manufacturers. However, the bending magnet, for which no data were provided by the manufacturers, was found to have initial activity levels ranging from 0.1 to 10 Bq/g due to the long half-life radionuclides  $^{57}\text{Co}$  and  $^{58}\text{Co}$ .

#### 4. Discussion

Leprince assessed  $^{187}\text{W}$ ,  $^{183\text{m}}\text{W}$ ,  $^{185}\text{W}$ ,  $^{181}\text{W}$ , and  $^{178}\text{Ta}$  as major radionuclides in tungsten targets, with an activity level of  $4.03 \times 10^{17}$  Bq, using the MCNPX code, in equipment with a service life of five years [18]. Patil et al. identified radionuclides, such as  $^{198}\text{Au}$ ,  $^{196}\text{Au}$ ,  $^{181}\text{W}$ ,  $^{178}\text{W}$ ,  $^{60}\text{Co}$ ,  $^{58}\text{Co}$ ,  $^{57}\text{Co}$ ,  $^{54}\text{Mn}$ , and  $^{51}\text{Cr}$ , in gold and SST304 targets [19–22]. Roig et al. identified  $^{196}\text{Au}$ ,  $^{57}\text{Co}$ ,  $^{60}\text{Co}$ ,  $^{54}\text{Mn}$ , and  $^{58}\text{Ni}$  in Siemens KDS 18 MV, and specified a separate storage period of at least 30 days for  $^{196}\text{Au}$  radionuclide in the target pursuant in accordance with Spanish regulations (IS/05, 2003) until the activity level fell below  $10^6$  Bq [23]. While these results are consistent with those of this study, this study differentiates itself from others in that it also investigated the radionuclides additionally obtained by considering impurities.

To present, the allowable disposal time for each part of a dismantled linac, the clearance level of the radionuclides identified in each part should be applied. Regarding the self-disposal standards for radioactive waste, the United States use the technical standards published by the Department of Energy (DOE) for the disposal of radioactive waste from accelerators and accelerator facilities. Accordingly, Varian provides DOE-standards-based recommendations [24,25]. Japan has also established academic society standards for the management of radioactive materials of radiotherapy devices, specifying radioactive waste disposal procedures, parts subject to regulations, and measurement methods [26]. In the Korean notice, pursuant to the regulations on radioactive waste classification and self-disposal standards [4], clearance levels are indicated in Appendix 1 (related to Article 2 (2) and Article 3 (1)), and in the case of mixed radionuclides, the clearance level of each radionuclide should be calculated using Equation (1):

$$\sum_i \frac{C_i}{C_{L,i}} < 1 \quad (1)$$

$C_i$ : activity level (Bq/g) of radionuclide  $i$

$C_{L,i}$ : clearance level (Bq/g) of radionuclide  $i$

For the application of the clearance levels in compliance with the methods specified in the notice, the time-dependent concentrations of all radionuclides ( $C_{L,i}$ ) pertaining to each part obtained using the DCHAIN code were added, and the clearance level of a given radionuclide ( $C_i$ ) was checked, and a part calculated (using Equation (1)) to have a value exceeding its clearance level was analyzed to be stored until it reaches a value below the clearance level. Among the clearance level of the radionuclide specified by the NSSC notice, those on the radionuclides analyzed in this study are listed in Table 3. As recommended

in the notice, the concentration of 0.1 Bq/g was applied to radionuclides for which no clearance level is provided.

**Table 3.** Clearance level of each radionuclide detected in the medical linacs manufactured by Varian, Elekta, and Siemens.

| Radionuclides                                                                                                                                                                                                                               | Clearance Level (Bq/g) |
|---------------------------------------------------------------------------------------------------------------------------------------------------------------------------------------------------------------------------------------------|------------------------|
| <sup>24</sup> Na, <sup>28</sup> Al, <sup>31</sup> Si, <sup>37</sup> Ar, <sup>45</sup> Ca, <sup>54</sup> Mn, <sup>57</sup> Ni, <sup>65</sup> Zn, <sup>66</sup> Cu, <sup>108</sup> Ag, <sup>179</sup> Ta, <sup>183</sup> W, <sup>196</sup> Au | 0.1                    |
| <sup>14</sup> C, <sup>57</sup> Co, <sup>58</sup> Co, <sup>59</sup> Fe                                                                                                                                                                       | 1                      |
| <sup>56</sup> Mn, <sup>93m</sup> Nb, <sup>99</sup> Mo, <sup>181</sup> W                                                                                                                                                                     | 10                     |
| <sup>3</sup> H, <sup>51</sup> Cr, <sup>63</sup> Ni, <sup>64</sup> Cu                                                                                                                                                                        | 100                    |
| <sup>55</sup> Fe, <sup>185</sup> W                                                                                                                                                                                                          | 1000                   |

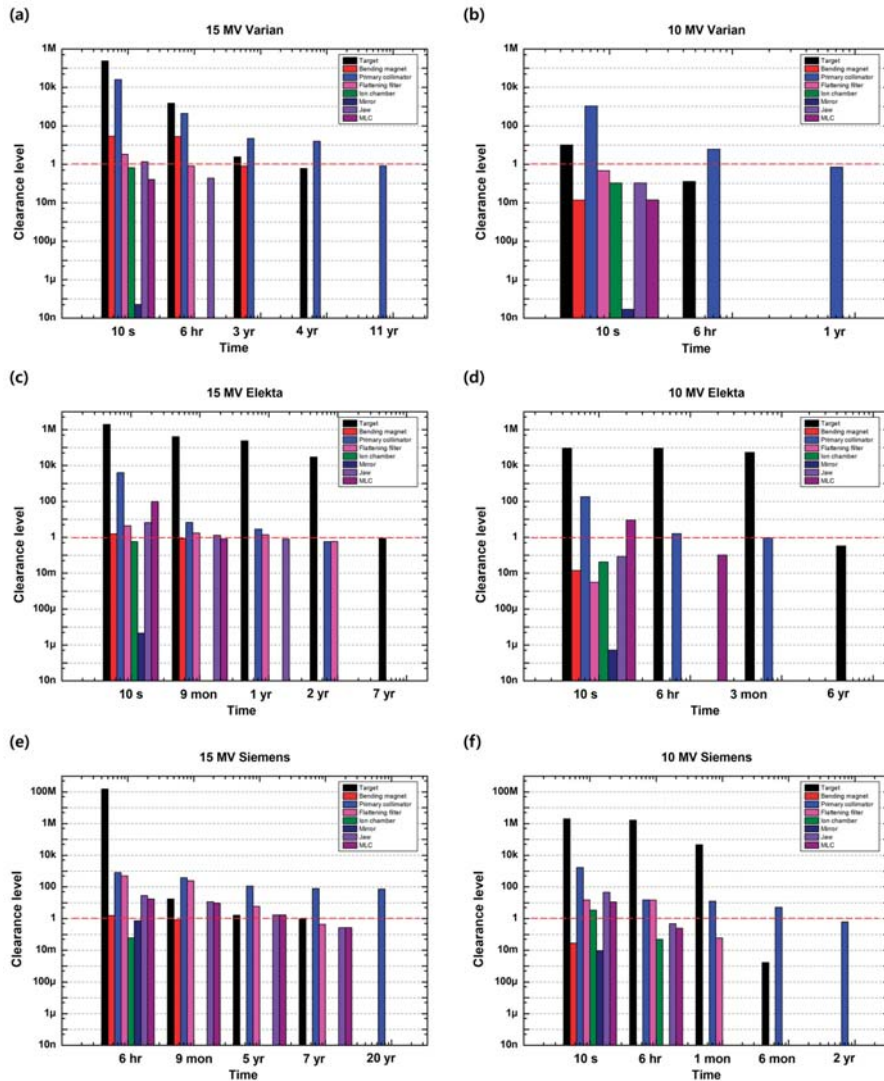
Radionuclide <sup>64</sup>Cu had the highest initial concentration ( $2.62 \times 10^4$  Bq/g) in Varian's target 15 MV, followed by <sup>185</sup>W ( $1.23 \times 10^4$  Bq/g). As mentioned in another study, <sup>64</sup>Cu and <sup>62</sup>Cu have very short half-lives, and the concentration of <sup>185</sup>W had to be considered for their self-disposal [27]. In Elekta's tungsten target 15 MV, <sup>181</sup>W had the highest initial concentration ( $1.47 \times 10^7$  Bq/g), followed by <sup>62</sup>Cu ( $2.99 \times 10^3$  Bq/g). Likewise, the concentration of <sup>181</sup>W was considered for their self-disposal. In Siemens' target, <sup>196</sup>Au pertaining to gold material had the highest initial concentration ( $1.23 \times 10^7$  Bq/g), followed by <sup>55</sup>Fe ( $3.17 \times 10^3$  Bq/g) among the non-gold materials. As shown in Figure 3e,f, after about 2 months, with major radionuclide changing from Au isotopes with short half-lives to Fe isotopes with long half-lives, the activity level is maintained, and the activity level of <sup>55</sup>Fe should be considered for self-disposal.

In Figure 4, Equation (1) and Table 3 were applied to indicate the clearance levels based on the activity levels assessed for the head parts of the equipment of the three manufacturers that operated at 10 and 15 MV energy for 10 years, applying the workload of 80 Gy/day.

Six hours after the linac shutdown, the activity levels of the ion chamber and mirror were found to be lower than the clearance level among all parts of the linacs using 10 and 15 MV energy (Figure 4). Most of the parts of the linacs of the three manufacturers using 10 MV energy were found to have an activity level below the clearance level after one month, but Siemens' 10 MV target reached the clearance level after two months, and Elekta's 10 MV target was found to have an activity level exceeding the clearance level even after one year. In particular, the 15 MV targets of the linacs of the three manufacturers maintained the activity level of  $10^3$  Bq/g or higher even after one year, exceeding the clearance level. The 15 MV flattening filter of Elekta and Siemens also had to be stored for one year or longer.

As regards the 15 MV primary collimator, which is composed mainly of tungsten, those of Elekta and Varian could be disposed after two and 11 years, respectively, but that of Siemens had an activity level in excess of the clearance level even after 20 years (Figure 4e). This is due to the fact that, unlike Elekta and Varian, Siemens' primary collimator has an absorber attached to it, and its clearance level exceeds 1 due to the radionuclide <sup>108m</sup>Ag identified as an impurity. <sup>108m</sup>Ag radionuclide has a significantly long half-life of 418 years and a high radionuclide concentration of 6.93 Bq/g immediately after the linac shutdown. Since the notice does not provide its clearance level, 0.1 Bq/g, which is recommended for radionuclides with an unspecified clearance level, was applied, and its activity level still exceeded the reference value of 1 even 20 years after linac shutdown. Since only the radionuclide <sup>28</sup>Al was detected in Siemens' absorber without impurities, its tungsten primary collimator could be disposed after 15 years.





**Figure 4.** Clearance level by part and by equipment (15 MV/10 MV linacs of three manufacturers), applying a workload of 80 Gy/day (dotted red line: reference clearance level of 1; self-disposal is allowed at the activity level below this line): (a) 15 MV Varian; (b) 10 MV Varian; (c) 15 MV Elekta; (d) 10 MV Elekta; (e) 15 MV Siemens; (f) 10 MV Siemens.

The parts that were analyzed to be stored for six months or longer until self-disposal, were those with radionuclides with mid-to-long half-lives ( $\geq 1 \times 10^6$  s) and high initial activity levels, such that their activity levels are still in excess of  $10^3$  Bq/g even after six months. Typical radionuclides with these attributes are  $^{51}\text{Cr}$ ,  $^{54}\text{Mn}$ ,  $^{55}\text{Fe}$ ,  $^{57}\text{Co}$ ,  $^{58}\text{Co}$ ,  $^{179}\text{Ta}$ ,  $^{181}\text{W}$ , and  $^{185}\text{W}$  generated from the SST304 and tungsten materials (Table 3).

When a workload of 40 Gy/day is applied, earlier disposal is possible because the activity levels of the parts are lower than when a workload of 80 Gy/day is applied. For the parts that require a long storage time ( $\geq 2$  years), i.e., target and primary collimator, no great changes occurred in the time for disposal when the workload was halved. However,

among those whose clearance level was reached after nine months, Elekta's MLC and bending magnet and Siemens' bending magnet could be disposed after one month when the workload was halved. As mentioned previously, a workload of 80 Gy/day was applied, adopting a conservative approach, and more accurate disposal time can be predicted by reflecting the energy and workload applied in actually decommissioned medical linacs.

## 5. Conclusions

This study was conducted to provide basic data for preparing regulations on the disposal of linear accelerators (linacs) by performing a component analysis of the linac parts of three manufacturers (Varian, Elekta, and Siemens), and assessing and analyzing the time-dependent activity levels of radionuclides using the Monte Carlo PHITS code and DCHAIN.

Although various radionuclides were additionally detected due to impurities, it was determined that their activity levels were negligible for the total activity level of each part and that the clearance level could be sufficiently examined using the Monte Carlo simulation results based on the data provided by the manufacturers. According to the clearance levels of the radionuclides specified in the pertinent Korean notice, the 15 MV targets of the three manufacturers should be stored at least for 3.5 to 7 years until they reach the clearance levels, whereas the 10 MV targets of Varian, Elekta, and Siemens can be disposed 6 h, 5.5 years, and 6 months after the linac shutdown, respectively. In order to avoid workers' exposure to radiation during dismantling/disposal, it is recommended to work after storing the parts until the clearance level (<1) is reached, as shown in Figure 4.

As demonstrated in this study, if values exceeding the clearance level can be computed through Monte Carlo simulation applying the workload until the dismantling/disposal of a linac, the storage period of each part after which workers can safely work on dismantling/disposal can be predicted. It is planned to perform a qualitative and quantitative analysis of radionuclides using HPGe-based gamma spectroscopy in addition to the Monte Carlo simulation with a view to providing a groundwork for clear safety management regulations for the disposal of decommissioned linacs.

**Author Contributions:** Conceptualization, Y.J.J. and S.H.C.; methodology, S.H.P. and D.W.K.; software, Y.C.; validation, K.B.K. and S.H.B.; formal analysis, N.H.K. and S.H.B.; investigation, Y.C. and K.B.K.; data curation, Y.J.J. and N.H.K.; writing—original draft, Y.J.J.; writing—review and editing, S.H.C.; supervision, S.H.P. and D.W.K.; funding acquisition, S.H.C. All authors have read and agreed to the published version of the manuscript.

**Funding:** This research was supported by the National Research Council of Science & Technology (NST) grant by the Korea government (MSIT) (No. CAP22041-000) & Korea Institute of Radiological & Medical Sciences(KIRAMS) grant funded by the Korea government (Ministry of Sciences and ICT) (No. 50572-2023).

**Institutional Review Board Statement:** Not applicable.

**Informed Consent Statement:** Not applicable.

**Data Availability Statement:** Not applicable.

**Conflicts of Interest:** The authors declare no conflict of interest.

## References

1. Kwon, N.H.; Jang, Y.J.; Kim, D.W.; Shin, D.O.; Kim, K.B.; Kim, J.S.; Choi, S.H. Trend Analysis on Korean and International Management for Activated Material Waste from Medical Linear Accelerator. *Prog. Med. Phys.* **2020**, *31*, 194–204. [[CrossRef](#)]
2. Kwon, N.H.; Shin, D.O.; Kim, J.S.; Yoo, J.; Park, M.S.; Kim, K.B.; Kim, D.W.; Choi, S.H. Current status of disposal and measurement analysis of radioactive components in linear accelerators in Korea. *Nucl. Eng. Technol.* **2022**, *54*, 507–513. [[CrossRef](#)]
3. Korea Institute of Nuclear Safety. *Improving Radiation Safety Management in the Medical Sector [Workshop]*; Korea Institute of Nuclear Safety: Daejeon, Republic of Korea, 2018.
4. Radioactive Waste Safety Division, Nuclear Safety and Security Commission. *Nuclear Safety and Security Commission No-Tification No. 2020-6, Regulations on Radioactive Waste Classification and Clearance Standards*; (Implementation and Revision in 2020.05.26); Radioactive Waste Safety Division, Nuclear Safety and Security Commission: Seoul, Republic of Korea, 2020.

5. MOTIE. *Radioactive Waste Control Act No. 15082*; (Implementation and Revision in 2017.11.28); Ministry of Trade Industry and Energy (MOTIE): Seoul, Republic of Korea, 2017.
6. Olsen, K.J. Neutron Contamination from Medical Electron Accelerators (NCRP Report No. 79). *Med. Phys.* **1986**, *13*, 968–969. [[CrossRef](#)]
7. International Atomic Energy Agency. *Management of Radioactive Waste from the Use of Radionuclides in Medicine*; IAEA-TECDOC-1183; IAEA: Vienna, Austria, 2000.
8. Naseri, A.; Mesbahi, A. A review on photoneutrons characteristics in radiation therapy with high-energy photon beams. *Rep. Pract. Oncol. Radiother.* **2010**, *15*, 138–144. [[CrossRef](#)] [[PubMed](#)]
9. Vichi, S.; Dean, D.; Ricci, S.; Zagni, F.; Berardi, P.; Mostacci, D. Activation study of a 15MeV LINAC via Monte Carlo simulations. *Radiat. Phys. Chem.* **2020**, *172*, 108758. [[CrossRef](#)]
10. Jang, Y.-J.; Kwon, N.H.; Park, S.H.; Choi, Y.; Yu, H.; Kim, K.B.; Kim, D.W.; Choi, S.H. Activation evaluation of Siemens linear accelerator using Monte Carlo simulation. *J. Korean Phys. Soc.* **2022**, *81*, 1107–1114. [[CrossRef](#)]
11. Konefał, A.; Bieniasiewicz, M.; Wendykier, J.; Adamczyk, S.; Wrońska, A. Additional radiation sources in a treatment and control room of medical linear accelerators. *Radiat. Phys. Chem.* **2021**, *185*, 109513. [[CrossRef](#)]
12. Waller, E.; Ram, R.; Steadman, I. Preliminary Determination of Activation Products for a Varian Truebeam Linear Accelerator. *Health Phys.* **2017**, *113*, 227–233. [[CrossRef](#)] [[PubMed](#)]
13. Wu, Y.; Song, J.; Zheng, H.; Sun, G.; Hao, L.; Long, P.; Hu, L. CAD-based Monte Carlo program for integrated simulation of nuclear system SuperMC. *Ann. Nucl. Energy* **2015**, *82*, 161–168. [[CrossRef](#)]
14. Sato, T.; Iwamoto, Y.; Hashimoto, S.; Ogawa, T.; Furuta, T.; Abe, S.-I.; Kai, T.; Tsai, P.-E.; Matsuda, N.; Iwase, H.; et al. Features of Particle and Heavy Ion Transport code System (PHITS) version 3.02. *J. Nucl. Sci. Technol.* **2018**, *55*, 684–690. [[CrossRef](#)]
15. Ratliff, H.N.; Matsuda, N.; Abe, S.-I.; Miura, T.; Furuta, T.; Iwamoto, Y.; Sato, T. Modernization of the DCHAIN-PHITS activation code with new features and updated data libraries. *Nucl. Instrum. Methods Phys. Res. Sect. B Beam Interact. Mater. Atoms* **2020**, *484*, 29–41. [[CrossRef](#)]
16. Zheng, L.; Huang, S.; Wang, K. Criticality benchmarking of ENDF/B-VIII.0 and JEFF-3.3 neutron data libraries with RMC code. *Nucl. Eng. Technol.* **2020**, *52*, 1917–1925. [[CrossRef](#)]
17. Shibata, K.; Iwamoto, H.; Nakagawa, T.; Iwamoto, N.; Ichihara, A.; Kunieda, S.; Chiba, S.; Furutaka, K.; Otuka, N.; Ohsawa, T.; et al. JENDL-4.0: A New Library for Nuclear Science and Engineering. *J. Nucl. Sci. Technol.* **2012**, *48*, 1–30. [[CrossRef](#)]
18. Leprince, A.; David, J.-C.; Ene, D.; Leray, S. Reliability and use of INCL4.6-Abla07 spallation model in the frame of European Spallation Source target design. *Prog. Nucl. Sci. Technol.* **2014**, *4*, 491–495. [[CrossRef](#)]
19. Patil, B.; Chavan, S.; Pethe, S.; Krishnan, R.; Bhoraskar, V.; Dhole, S. Estimation of neutron production from accelerator head assembly of 15MV medical LINAC using FLUKA simulations. *Nucl. Instrum. Methods Phys. Res. Sect. B Beam Interact. Mater. Atoms* **2011**, *269*, 3261–3265. [[CrossRef](#)]
20. Saeed, M.K.; Poppe, B.; Fischer, H. Direct air activation measurements at a 15-MV medical linear accelerator. *Radiat. Prot. Dosim.* **2015**, *163*, 233–237. [[CrossRef](#)] [[PubMed](#)]
21. Šagátová, A.; Fülöp, M.; Pavlovič, M.; Sedlačková, K.; Nečas, V. Electron-beam accelerator with conversion to X-rays: Optimal radiation type according to application. *Radiat. Phys. Chem.* **2020**, *172*, 108789. [[CrossRef](#)]
22. Długosz-Lisiecka, M.; Biegała, M.; Jakubowska, T. Activation of medical accelerator components and radioactive waste classification based on low beam energy model Clinac 2300. *Radiat. Phys. Chem.* **2023**, *205*, 110730. [[CrossRef](#)]
23. Roig, M.; Panettieri, V.; Ginjaume, M.; Sánchez-Reyes, A. Photonuclear isotope characterization of a Siemens KDS 18 MV linac head. *Phys. Med. Biol.* **2004**, *49*, N243–N246. [[CrossRef](#)]
24. U.S. Department of Energy. *Clearance and Release of Personal Property from Accelerator Facilities*; DOE-STD-6004-2016; U.S. Department of Energy: Washington, DC, USA, 2016.
25. U.S. Department of Energy. *Radiation Protection of the Public and the Environment*; DOE O 458.1; U.S. Department of Energy: Washington, DC, USA, 2013.
26. Japanese Society of Radiation Oncology. *Society Standard for the Management of Radioactive Substances in Radiotherapy Equipment*; Japanese Society of Radiation Oncology: Tokyo, Japan, 2014.
27. Dellepiane, G.; Casolaro, P.; Mateu, I.; Scampolli, P.; Braccini, S. Alternative routes for  $^{64}\text{Cu}$  production using an 18 MeV medical cyclotron in view of theranostic applications. *Appl. Radiat. Isot.* **2023**, *191*, 110518. [[CrossRef](#)] [[PubMed](#)]

**Disclaimer/Publisher's Note:** The statements, opinions and data contained in all publications are solely those of the individual author(s) and contributor(s) and not of MDPI and/or the editor(s). MDPI and/or the editor(s) disclaim responsibility for any injury to people or property resulting from any ideas, methods, instructions or products referred to in the content.

## Article

# Using Agricultural Mixed Waste as a Sustainable Technique for Removing Stable Isotopes and Radioisotopes from the Aquatic Environment

Arwa A. Abdelhamid <sup>1</sup>, Mogada H. Badr <sup>1</sup>, Ramadan A. Mohamed <sup>2,3</sup> and Hosam M. Saleh <sup>4,\*</sup><sup>1</sup> Department of Chemistry, Faculty of Science, Al-Azhar University, Nasr City 11884, Cairo, Egypt<sup>2</sup> Central Laboratory for Elemental and Isotopic Analysis-Nuclear Research Center, Egyptian Atomic Energy Authority, Nasr City 11787, Cairo, Egypt<sup>3</sup> Ion Sources and Accelerators Department, Nuclear Research Center, Egyptian Atomic Energy Authority, Nasr City 11787, Cairo, Egypt<sup>4</sup> Radioisotope Department, Nuclear Research Center, Egyptian Atomic Energy Authority, Nasr City 11787, Cairo, Egypt

\* Correspondence: hosam.saleh@eaea.org.eg or hosamsaleh70@yahoo.com; Tel.: +20-10051-91018; Fax: +20-23749-3042

**Abstract:** In the current study, dried ground mixed waste of olive waste and water hyacinth was subjected to the treatment of wastewater contaminated with stable or radioactive cobalt and cesium. Contact time, temperature, amount of adsorbent, metal ion concentration and pH-value were evaluated as the most potent factors that affect the adsorption process. Concentrations of Co and Cs ions before and after treatment are measured using ICP-OES technique. Moreover, kinetic and equilibrium isotherm parameters were investigated by explaining the equilibrium data by induction of two isotherms, “Langmuir” and “Freundlich”. Experimental results indicated that more than 85% of <sup>60</sup>Co and <sup>134</sup>Cs were efficiently removed from spiked wastewater after one hour of contact time by using 0.2 g of dried mixed waste. The optimal time to remove Cs<sup>+</sup> and Co<sup>2+</sup> was 50 and 90 min, respectively. The kinetic study showed that the adsorption of Cs<sup>+</sup> and Co<sup>2+</sup> were better suited to the second order. The most favorable pH value was at a range of 6–7 for Cs<sup>+</sup> and 5–6 for Co<sup>2+</sup>. R<sup>2</sup> values were higher at the Freundlich isotherm, indicating that the adsorption process was taking place according to Freundlich isotherm at all temperatures for Co<sup>2+</sup> and Cs<sup>+</sup> ions.

**Keywords:** olive waste; water hyacinth; cobalt; cesium; adsorption; kinetics; biomass; wastewater; ICP-OES spectroscopy

**Citation:** Abdelhamid, A.A.; Badr, M.H.; Mohamed, R.A.; Saleh, H.M. Using Agricultural Mixed Waste as a Sustainable Technique for Removing Stable Isotopes and Radioisotopes from the Aquatic Environment. *Sustainability* **2023**, *15*, 1600. <https://doi.org/10.3390/su15021600>

Academic Editor: Ferooz Sher

Received: 7 November 2022

Revised: 6 January 2023

Accepted: 10 January 2023

Published: 13 January 2023



**Copyright:** © 2023 by the authors. Licensee MDPI, Basel, Switzerland. This article is an open access article distributed under the terms and conditions of the Creative Commons Attribution (CC BY) license (<https://creativecommons.org/licenses/by/4.0/>).

## 1. Introduction

Water covers the vast majority of the Earth’s surface (71%), including only a small portion (3%) of freshwater that plays a vital role in the global economy. This natural essential resource became insufficient in numerous areas. The water scarcity was a major economic and social concern, especially in the agriculture sector, which consumes about 70% of the freshwater [1]. In many attempts in developing countries, 90% of the wastewater remains untreated in freshwater bodies, rendering it unsafe for human consumption, resulting in scarcity or toxic impact [2]. Clean soil and pure water are the most in-demand resources all over the world nowadays [3,4]; also in demand are more efficient selective methods for analysis [5,6].

Pollution is an important issue around the world, especially the contamination with chemical elements, including stable isotopes or radioisotopes. Chemical pollution is the most significant problem because of the easy dispersal of harmful metals, for example, it can be transferred into edibles; however, water contamination is considered a serious ecological problem around the world as well [7].

Physicochemical approaches, such as precipitation, redox-reaction, ion exchanging [8,9] and electrochemically [10], have been reported. Ultrafiltration [11], photocatalysis [12], reverse osmosis [13] and electro flotation [14] are some of the other important techniques. The disadvantages of these techniques are their cost and the production of secondary waste that requires extra treatment [15].

Developing sustainable, simple, efficient, and cost-effective techniques for removing different elements from wastewater is recent worldwide challenge. Because it is a straightforward means of removing metal ions from wastewater, phytoremediation [16,17], using aquatic plants, and adsorption process [18–20], using agricultural waste, become viable choices. For example, the cost of excavation and disposal of contaminated soil based on the Federal Remediation Technologies Roundtable (FRTR) data was in the range of 270 to 460 \$/ton, while the cost of phytoextraction, including plant selection and position, irrigation, soil amendment, field monitoring, harvesting, and residue management, could be in the range 10–35 \$/ton [21].

Although phytoremediation using aquatic plants achieved great effectiveness in the treatment process, the findings of the experiments revealed that dried plants are more effective than fresh plants, and consequently, adsorption techniques have recently been investigated in the management of contaminated wastewater spiked with arsenate, nitrate, phosphate, cadmium, and other heavy metals [7].

Increased cobalt concentrations injure humans, causing lung irritations, asthma, pneumonia, weight loss, paralysis, diarrhea, vomiting, thyroid hormones, liver damage, and nausea, due to the resemblance of cesium-134 to sodium; the ingestion of cesium causes its deposition in soft tissues throughout the body, posing internal hazards [22].

Physical procedures, such as adsorption by natural or manufactured materials, have been used to remove cesium and cobalt. As one of the traditional adsorbents, ion exchangers have limitations because of their competition with other monovalent cations found in liquid radioactive waste, such as sodium and potassium, which can inhibit the adsorption of cesium or other competing divalent cations capable of occupying cobalt adsorption sites [23]. Because the metal adsorption depends on cation exchange sites, it requires the development of new and more active materials with safe and sustainable features for the economical removal of stable or radio pollutants from wastewater.

Water hyacinth is an aquatic plant weed that grows quickly and floats freely in water. It has a reputation of having a very high metal tolerance. The adsorption of  $Pb^{2+}$  from liquid effluents was conducted using the dried biomass of *Eichhornia crassipes*. The performance of the adsorption mechanism was determined to be depended on pH and the adsorbent's uneven surface may aid in the adsorption of  $Pb^{2+}$  on the surface of the adsorbent [24].

The current study focuses on the utilization and effectiveness of biomass originated from dried ground mixed waste of water hyacinth and olive waste to remove cesium and cobalt from wastewater due to their high availability and low operating cost instead of traditional techniques, which are difficult to control and require primarily expensive requirements. Cobalt compounds should be considered genotoxic carcinogens with a practical threshold, and chronic inhalation of cobalt compounds can induce respiratory tumors [25], while the toxicity of cesium can induce gastrointestinal distress, hypotension, syncope, numbness or tingling of the lips [26]. Moreover, radiotoxicity was added on the chemical toxicity when in contact with radio cobalt or radio cesium.

In order to identify the ideal physicochemical conditions for the most effective sorption for treatment applications, the adsorption process was studied in terms of the impact of pH-value, adsorbent dose, metal ion, and interaction time. Additionally, the adsorption process followed the “Langmuir” and “Freundlich” adsorption models, and the kinetic studies were developed to describe the isothermal trend and constants of the adsorption process, with the pH-value being the most important factor. An experiment, using the nominated adsorbent to eliminate radiocobalt and radiocesium, was performed. These treatment processes generated secondary radioactive waste that had to be stabilized and



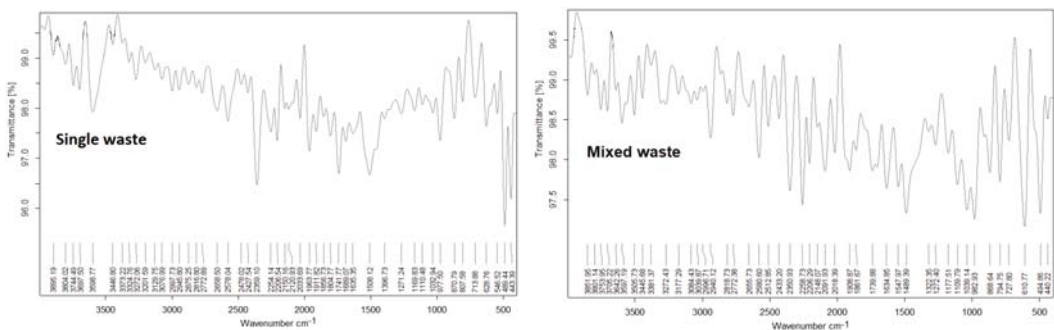
remediated for safe disposal, as reported in the previous literature, by using cement [27,28], cement polymer composite [29,30], and cement mixed with natural clay [31].

## 2. Experimental Approach

### 2.1. Materials

#### 2.1.1. Adsorptive Materials

Green plants of water hyacinth have been harvested from Egyptian waterways, dehydrated in a 70 °C oven for 2 days and ground to produce a fine powder using an electric mixer. Other types of unimportant materials, such as solid waste derived from the olive oil industry, were prepared by washing thoroughly with methanol, rinsing with pure water, and introducing them to drying at 70 °C. The dry matter was crushed and ground. The two dried ground plant wastes were mixed with a ratio of 50 to 50%. As shown in Figure 1, the chart of spectra confirmed the presence of major functional groups in ground dry single waste and mixed plant waste that were identified and characterized using FTIR spectroscopy with a Shimadzu FTIR-8201 PC. FTIR analysis was performed to identify the functional groups in the dried single waste and mixed waste using the KBr disc method. This investigation showed a strong broad absorption band of O-H stretching vibrations in the region of 3272–3177  $\text{cm}^{-1}$  and another peak at 3445  $\text{cm}^{-1}$ . Other peaks appeared at 1739  $\text{cm}^{-1}$  and 1322  $\text{cm}^{-1}$ , which corresponded to the C=O stretching vibrations and the phenolic hydroxyl groups, respectively. At 1547  $\text{cm}^{-1}$ , a stretching vibration regarding the C–N of the peptidic bond of proteins was present; a peak at around 1500  $\text{cm}^{-1}$  indicated C=C bending. The range 1130–1000  $\text{cm}^{-1}$  is a vibration of C–O–C and O–H of polysaccharides. The intensity of the adsorption bands confirmed no significant difference between olive waste alone and that mixed with water hyacinth; the functional groups were responsible for the adsorption of many elements.



**Figure 1.** FTIR spectra of single waste and mixed waste.

#### 2.1.2. Adsorbate Elements

Radioisotopes of  $^{134}\text{Cs}$  and  $^{60}\text{Co}$  were produced at the Egyptian Atomic Energy Authority, Egypt. The activity content of two radioisotopes was diluted to various activities in the range of (1400–4850 Bq). High purity and analytical-grade salts of stable cesium and cobalt were purchased from Sigma-Aldrich. To achieve a suitable value of concentration for the subsequent experimentations, dilution was used to adjust the concentration of stable elements in the range of (5–100 mg/L). Additionally, gradual addition of NaOH and 0.1 N of HCl were performed to adjust the acidity or alkalinity of the spiked solutions for various pH values.

### 2.2. Experimentation

#### 2.2.1. Adsorption Studies

All experiments have been performed in a bathwater with a constant shaking speed to investigate the influence of contact time, pH-value, adsorbent weight, concentration of  $\text{Cs}^+$  or  $\text{Co}^{2+}$  and temperature.

### Adsorption of Single Waste and Mixed Waste

A primary experiment was performed to evaluate adsorption efficiency using different weights of single waste (olive waste) and mixed waste (olive waste) to uptake Cs or Co elements for 2 h at the constant temperature of 25 °C, pH value of 7 and shaking speed of 100 rpm.  $q_e$  was performed according to the recent literature [32] and Equation (1).

$$q_e = \left( \frac{C_0 - C_e}{m} \right) \times V \quad (1)$$

$q_e$  is the adsorption capacity (mg/g),  $C_0$  is the initial concentration of ions (mg/L),  $C_e$  is the equilibrium concentration of ions (mg/L),  $m$  is the mass of biosorbent used in the process (g) and  $V$  is the volume of the solution (L).

### Contact Time

The effect of time on the adsorption of (50 mg/L)  $Cs^+$  or  $Co^{2+}$  on (0.1 g) mixed waste was evaluated at the constant temperature of 25 °C while maintaining the pH value at 7 and the shaking speed of 100 rpm at variable time during two hours (0, 1, 5, 10, 15, 20 and 30, 45, 60, 90 and 120 min). At each contact time, the concentration of non-adsorbed ions was determined by taking 1 mL of clear solution for subsequent analysis using atomic absorption spectroscopy.

### pH Effect

Under varying pH conditions, stable elements were adsorbed at the constant temperature and a shaking rate of 25 °C and 100 rpm, respectively. The pH of non-radioactive solutions was maintained by the addition of 0.1 N of HCl and NaOH to adjust the pH. The removal percentage of both ions (concentration, 50 mg/L) at various pH (3 to 8) by using 0.1 g of dry ground mixed waste was determined at 60 min.

### Adsorbent Dose

Six extended weights of dry mixed waste (0.025, 0.05, 0.1, 0.25, 0.5, and 1.0 g) were poured to six bottles including 100 mL of  $Cs^+$  or  $Co^{2+}$  at 25 °C, shaken at 100 rpm, with pH-value (7 for  $Cs^+$  and 6 for  $Co^{2+}$ ) for 60 min. Then, 1 mL of each bottle was collected and analyzed to determine the remaining concentration of each element after completing the process.

### 2.2.2. Inductively Coupled Plasma Optical Emissions Spectroscopy (ICP-OES)

ICP-OES, inductively coupled plasma optical emission spectroscopy (Prodigy High Dispersion ICP, Leeman in the United States) was used to evaluate the initial concentrations of Co and Cs, as well as the concentration of the remaining metal in the solution. The liquid was converted into an aerosol inside the instrument via a process known as nebulization. The sample aerosol was then transported to the plasma and desolvated, vaporized, atomized, excited, and/or ionized by the plasma. The excited atoms and ions emitted their characteristic radiation, which was collected and sorted by wavelength by a device [33].

The limit of detection (LOD) was primarily determined by instrumental sensitivity, spectral interferences, memory effects, digestion vessel cleanliness, and analytical reagent blank level, and it is possible to define the lowest concentrations that can be reliably detected and quantified.

The LODs for each element were calculated as the concentration equivalent of three times the standard deviation of the ion counts obtained from duplicate runs of reagent blank solutions (3% v/v  $HNO_3$  including the internal standard spikes) [34].

ICP-OES has the following features:

Available in radial, axial and dual view configurations;

Wavelength range from 165 to 1100 nm;

Resolution < 0.008 nm;

High precision elemental ratio measurements (0.01–0.02% RSD).

### 2.2.3. Adsorption Isotherms and Data Analysis

At various temperatures and constant pH and shaking speed (pH = 7, 100 rpm), adsorption isotherms were extrapolated for Cs and Co ions at the two contact times of 45 and 90 min, respectively. At 15, 25, 35, and 45 °C, 0.1 g of dried mixed waste was added to 100 mL of Cs or Co ions of various initial concentrations ( $C_0$ ), (5, 10, 20, 50, 75, and 100 mg/L), respectively, until equilibrium time was reached. A total of 1 mL of the remaining clear solution was analyzed by an atomic absorption apparatus to determine the non-adsorbed ions under various conditions.

Batch data from various contact times with variable initial concentrations of metal ions were analyzed using kinetic studies (pseudo-first order, pseudo-second order, and intra-particle diffusion).

Furthermore, different models of isothermal absorption, such as “Langmuir” and “Freundlich”, were applied to investigate the adsorption potential of different ions.

### 2.2.4. Adsorption of Radioisotopes ( $^{60}\text{Co}$ or $^{134}\text{Cs}$ )

Absorption processes at constant room temperature were followed by using 50 mL of  $^{60}\text{Co}$  or  $^{134}\text{Cs}$  solutions of various initial activity in the range of (1400 to 4350 Bq for  $^{134}\text{Cs}$ , and 3800 to 11000 Bq for  $^{60}\text{Co}$ ). In this experiment, extended doses of adsorbent (0.5, 1.0, 1.5, 2.0, 2.5 g) were mixed with  $^{60}\text{Co}$  and  $^{134}\text{Cs}$  for contact time (120 min.), constant shaking speed (100 rpm), and constant pH-value (7). The removal of radionuclides was assessed by periodically recording the radioactivity content of the remaining solution using a multichannel analyzer of a NaI detector, PCAP, USA.

### 2.2.5. Statistical Analysis

All results are expressed as means  $\pm$  SEM and regression models with the SPSS software (Statistical Package for the Social Sciences), version 24 (IBM SPSS Statistics for Windows, Armonk, NY, USA: IBM Corp.). Comparisons made between more than two groups were performed using multifactorial analysis of variance (ANOVA) followed by the Least Significant Difference (LSD) test. Differences were considered statistically significant when the alpha probability was  $\leq 0.05$ .

## 3. Results and Discussions

### 3.1. Single Waste and Mixed Waste

The potential of agricultural waste has been conducted in recent decades according to its ability to accumulate some elements from contaminated water or soil [35]. At least the same potential, such as terrestrial plants, can eliminate heavy metal contaminants that are commonly found in the environment, such as Cd, Cr, Cu, Hg, Pb, Ni, Zn and Fe [36].

Some of these elements are essential for plants but the others are toxic or still have unknown biological effects. A primary experiment was performed to evaluate the efficiency of using single waste, such as dry olive waste, and mixed waste of the same waste with dry water hyacinth to uptake Cs or Co elements after 2 h of contact. Figure 2 shows the superiority of mixed waste in the accumulation of constant concentration of Cs and Co by different amounts of adsorbents. According to the observed results, it is confirmed that mixed waste has a tendency to accumulate more than single waste, especially in the case of Co. From the statistical analysis, it is clear that  $F$  for treatment = 19.336 at  $p = 0.00$  ( $< 0.05$ ) and this confirms the statistically significant differences between the averages in the case of treatment. Consequently, in this study, the mixed waste of olive waste and water hyacinth was selected to evaluate its efficiency to eliminate cobalt and cesium elements from artificial contaminated water. This result is consistent with the recently published literature conducted to evaluate the use of mixed biomass (*Aspergillus campestris* and agro waste) [37].



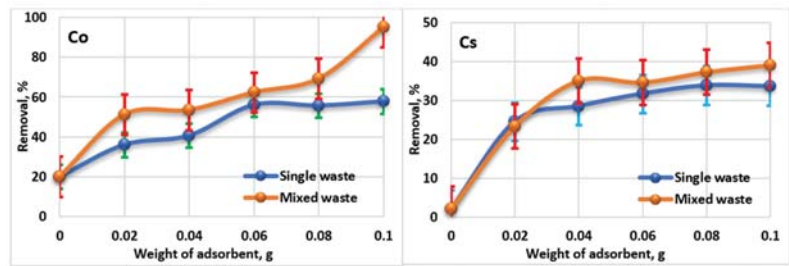


Figure 2. Adsorption of both ions separately on dry single waste and mixed waste.

### 3.2. Contact Time

Contact time acts as a vital key for determining the equilibrium point at the highest adsorption value. The optimal contact time is the time spent to achieve the highest removal percent with respect to different adsorption concentrations by evaluating the biosorption kinetics [38]. In this experiment, the statistical analysis confirmed that  $F$  for time = 70.681 when  $p = 0.000$  ( $<0.05$ ) and this confirms the statistically significant differences between the averages in the case of the time factor.

At a constant pH (7) and constant temperature ( $25\text{ }^{\circ}\text{C}$ ), the adsorption capacities of both ions ( $\text{Cs}^+$  or  $\text{Co}^{2+}$ ) onto dry biowaste was evaluated. As shown in Figure 3, as the contact time increases, the rate of adsorption first increases and then becomes constant due to the aggregation of adsorbed ions that diffuse deeper into the adsorbent structure at higher energy sites with time. This aggregation negates the influence of contact time as the pores get filled up and start offering resistance to the diffusion of aggregated ions in the adsorbents [39]. However, the elimination efficiency was increased and maximum biosorption capacity was achieved in 50 and 90 min, respectively.

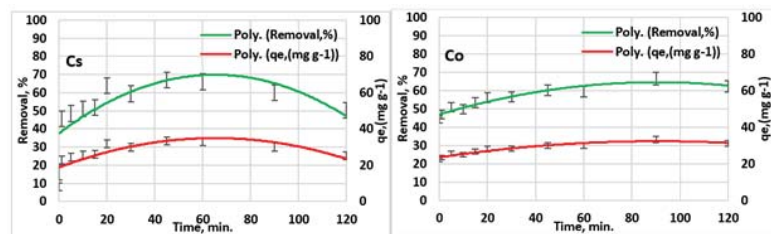


Figure 3. Removal (%) and adsorption capacity( $q_e$ ) of both ions separately using dry mixed waste during contact time.

The data are means  $\pm$  SE ( $n = 5$ ). ANOVA followed by LSD's multiple comparison post hoc test; the differences were considered significant at  $p \leq 0.05$ . A statistically significant difference  $F$  (contact time) was 70.681 at  $p = 0.000$  ( $<0.05$ ).

The calculated data of adsorption/time were employed to both kinetic models; pseudo-first order as shown in Equation (2) and pseudo-second order as shown in Equation (3).

$$\text{Log}(q_e - q_t) = \text{log } q_e - (k_1/2.303) t \quad (2)$$

$$\frac{t}{q_t} = \frac{1}{k_2 q_e^2} + \frac{1}{q_e} \quad (3)$$

where  $k_1$  ( $\text{min}^{-1}$ ) is the pseudo-first order rate constant of adsorption,  $q_e$  and  $q_t$  ( $\text{mg/g}$ ) refer to amount of ions adsorbed at equilibrium and at time  $t$ , respectively.  $K_2$  ( $\text{g mg}^{-1} \text{min}^{-1}$ ) is the pseudo-second order rate constant of adsorption.

The suitable model was investigated by computing the correction coefficient value of straight line ( $R^2$ ). As indicated in Figure 4, the adsorption of  $\text{Cs}^+$  ion processes were in pseudo second order greater than in pseudo-first order because the high regression coefficient ( $R^2$ ) of the pseudo-second order model was higher than that in the pseudo-first order model. Similarly, the adsorption of  $\text{Co}^{2+}$  ion processes fit the second-order model more than the first-order model according to the higher value of regression coefficient ( $R^2$ ) in the case of the pseudo-second order model, as shown in Figure 5 [40]. The adsorption kinetics of  $\text{Cs}^+$  and  $\text{Co}^{2+}$  suited the pseudo-second order model, indicating that the key step in the adsorption mechanism was the ion exchange by electrostatic interactions.

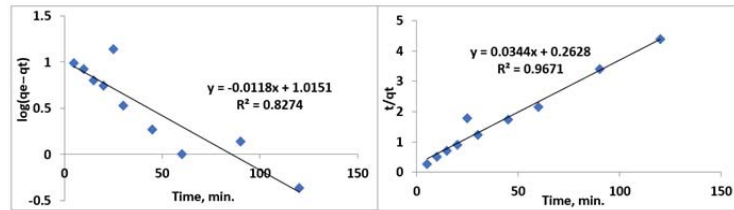


Figure 4. Adsorption kinetics modeled using pseudo-first and pseudo-second orders for  $\text{Cs}^+$ .

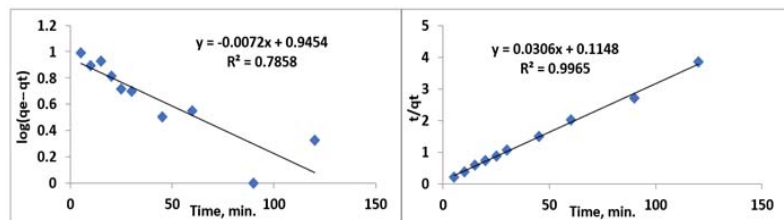
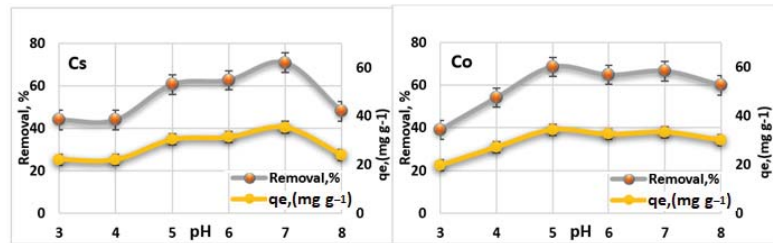


Figure 5. Adsorption kinetics modeled using pseudo-first and pseudo-second orders for  $\text{Co}^{2+}$ .

### 3.3. pH Effect

pH is one of the most important factors that largely affects the adsorption processes due to the effect of  $\text{H}^+$  ions on the biosorption of  $\text{Cs}^+$  and  $\text{Co}^{2+}$  ions by using dry plant mixed waste [41]. The potential of changing the pH from 3 to 8 was evaluated and presented in Figure 6, significantly pH could change the relative distribution of ions in the solution, as well as the surface properties of the adsorbent. The adsorption of the mixed waste was clearly affected by the varying solution pH values, which considerably increased by enhancing the solution's pH from 2 to 5, and basically remained unchanged in the case of the Co solution. In the case of the Cs solution, at pH 7, the removal capacity reached maximum value; however, afterwards rapidly decreased at a solution pH of more than 7.0. This behavior can be explained by the fact that at lower pH values, excess  $\text{H}^+$  ions compete with  $\text{Cs}^+$  and  $\text{Co}^{2+}$  for free adsorption sites, reducing their adsorption. With low pH, the solubility of some heavy elements in water increases, which causes an increase in their spread; pH plays a critical role in the transfer of heavy metals between the liquid and solid phases [42]. Another factor that could contribute to enhancing metal ion adsorption is the increasing pH, which encourages metal ion precipitation from the solution in the form of hydroxides [43]. From the statistical analysis it is clear that the F value (for pH) was 7.274 when  $p = 0.016$  ( $<0.05$ ) and this confirms the statistically significant differences between the averages in the case of this factor.

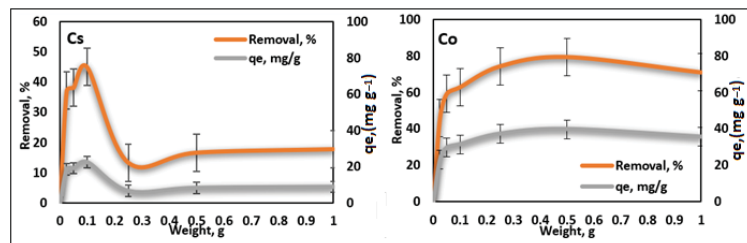


**Figure 6.** Removal (%) and adsorption capacity( $q_e$ ) of both ions separately in dry mixed waste at different pH-values.

The data are means  $\pm$  SE ( $n = 5$ ). ANOVA followed by LSD's multiple comparison post hoc test; the differences were considered significant at  $p \leq 0.05$ . A statistically significant difference F (pH) was 7.274 at  $p = 0.016$  ( $< 0.05$ ).

### 3.4. Dosage Weight of Dried Mixed Waste

Knowledge of the effect of the adsorbent dose on adsorption is critical for optimal adsorbent use. Figure 7 shows that batch studies with varying quantities of mixed waste were carried out to determine the best adsorbent dose. The adsorption capacity ( $q_e$ ) was increased by increasing the adsorbent dose and then proceeded steadily at a high level in the case of Co, while in case of Cs it increased with the increasing the dose, then dropped suddenly, and then settled at a low level. The rise in removal with the dose is associated with the increased number of active sites, it is readily understood that the number of available adsorption sites and the surface area increase by increasing the adsorbent dose [44].



**Figure 7.** Removal (%) and adsorption capacity( $q_e$ ) of both ions separately at different loading weights of mixed waste.

The steady removal thereafter is an indication of the adsorption equilibrium, and the decline in removal at a high dose could have resulted from the aggregation of adsorbent particles [45]. At low adsorbent dosages, however, the adsorbed amount ( $q_e$ ) reduced dramatically in the case of Cs. The optimum adsorbent doses of  $\text{Cs}^+$  and  $\text{Co}^{2+}$  were 0.1 g for  $\text{Cs}^+$  and 0.5 g for  $\text{Co}^{2+}$  ions. Statistically, F (for weight) was 0.041 at  $p = 0.998$  ( $> 0.05$ ) non-significant.

The data are means  $\pm$  SE ( $n = 5$ ). A significant difference F (loading weight) was 0.041 at  $p = 0.998$  ( $> 0.05$ ) non-significant.

### 3.5. Comparison of the Study Findings with Other Similar Published Work

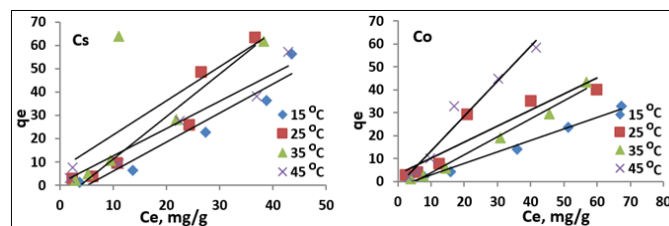
The economic and ecological features of the adsorption technique, various adsorbents have been studied in the literature. Some of these adsorbents have been collected in Table 1, where they are compared with the mixed waste used in the current study to evaluate the adsorption capacity.

**Table 1.** Adsorption capacity of mixed waste relative to other adsorbents for both ions separately.

| Material                            | Adsorption Capacity ( $q_e$ ) of Co | Literature    |
|-------------------------------------|-------------------------------------|---------------|
| Kaolinite                           | 0.92                                | [46]          |
| Soil                                | 1.50                                | [47]          |
| Marine bacterium                    | 4.38                                | [48]          |
| Nedalco sludge                      | 11.71                               | [49]          |
| Eerbeek sludge                      | 12.34                               | [49]          |
| Coir pith                           | 12.82                               | [50]          |
| Brown seaweed                       | 20.63                               | [51]          |
| <i>Myriophyllum spicatum</i>        | 43.40                               | [18]          |
| Mixed waste                         | 37.45                               | Current study |
| Adsorption Capacity ( $q_e$ ) of Cs |                                     |               |
| Ceiling tiles                       | 0.21                                | [52]          |
| Coal and chitosan                   | 3.00                                | [53]          |
| Bure mudrock                        | 13.30                               | [54]          |
| Modified akadama clay               | 16.10                               | [55]          |
| Kaolinite clay                      | 17.10                               | [56]          |
| Coir pith                           | 32.00                               | [57]          |
| Bentonite                           | 40.00                               | [55]          |
| <i>Myriophyllum spicatum</i>        | 58.00                               | [18]          |
| Mixed waste                         | 48.30                               | Current study |

### 3.6. Adsorption Isotherm at Different Temperatures

At various temperatures, the adsorption behavior attained a maximum uptake value of 35 mg/g at 25 °C and 45 mg/g at 45 °C for both elements Cs<sup>+</sup> or Co<sup>2+</sup>, respectively, as shown in Figure 8. Due to the ratio of the interaction energies of the cations with water molecules between the layers and with the charges on the surface of the biomass layer, ions with a small radius, (Co), have lower competitive advantages over those with a large radius, (Cs) [58]. However, the change in the cation diffusion coefficient with increasing temperature is slightly indicated in the case of Cs.

**Figure 8.** Adsorption capacity ( $q_e$ ) of both ions separately on dry mixed waste at various temperatures.

The Langmuir adsorption isotherm implies the presence of a homogenous monolayer at all sorbent surface sites with no adsorbed molecules interacting with nearby adsorption sites. The Langmuir model was applied by Equation (4).

$$\frac{1}{q_e} = \frac{1}{k_L q_{\max}} \frac{1}{C_e} + \frac{1}{q_{\max}} \quad (4)$$

where  $q_e$  (mg/g) is the uptake at equilibrium concentration,  $C_e$  (mg/L), and  $q_{max}$  (mg/g) is the maximum number of ions required to create a monolayer. The linearized Langmuir adsorption isotherm was used to examine the equilibrium data, as shown in Figures 9 and 10. Table 2 shows the Langmuir constants,  $k_L$ , and monolayer sorption capacity,  $q_{max}$ , which were computed using the slope and intercept of the curve between  $1/q_e$  and  $1/C_e$ . The  $q_{max}$  values obtained from “Langmuir” plots do not agree with the experimental result [59].

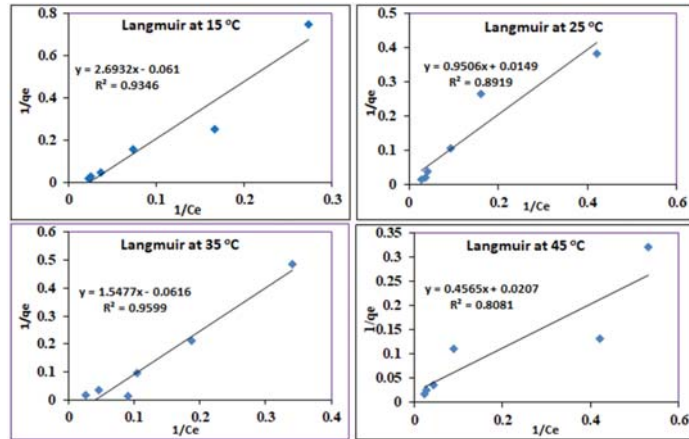


Figure 9. Adsorption of  $Cs^+$  ions on mixed waste at different temperatures (Langmuir isotherm).

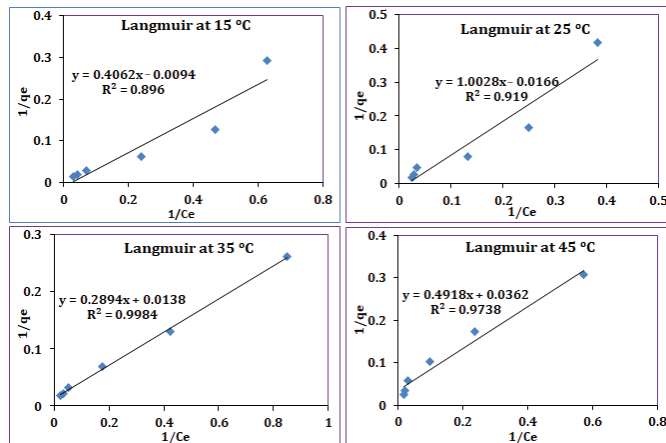


Figure 10. Adsorption of  $Co^{2+}$  ions on mixed waste at different temperatures (Langmuir isotherm).

Table 2. Value of Langmuir parameters for adsorption of both ions separately on mixed waste.

| Temp. | $Cs^+$ |           |       |       | $Co^{2+}$ |           |       |       |
|-------|--------|-----------|-------|-------|-----------|-----------|-------|-------|
|       | $q_e$  | $q_{max}$ | $k_L$ | $R^2$ | $q_e$     | $q_{max}$ | $k_L$ | $R^2$ |
| 15 °C | 43     | 16.3      | 0.022 | 0.934 | 67        | 21.55     | 0.021 | 0.896 |
| 25 °C | 36     | 67.0      | 0.015 | 0.891 | 59        | 37.45     | 0.029 | 0.919 |
| 35 °C | 38     | 16.2      | 0.039 | 0.959 | 56        | 21.23     | 0.013 | 0.998 |
| 45 °C | 42     | 48.3      | 0.045 | 0.808 | 41        | 14.80     | 0.034 | 0.973 |

An empirical equation used to define heterogeneous schemes is the Freundlich isotherm. The "Freundlich" equation is represented as

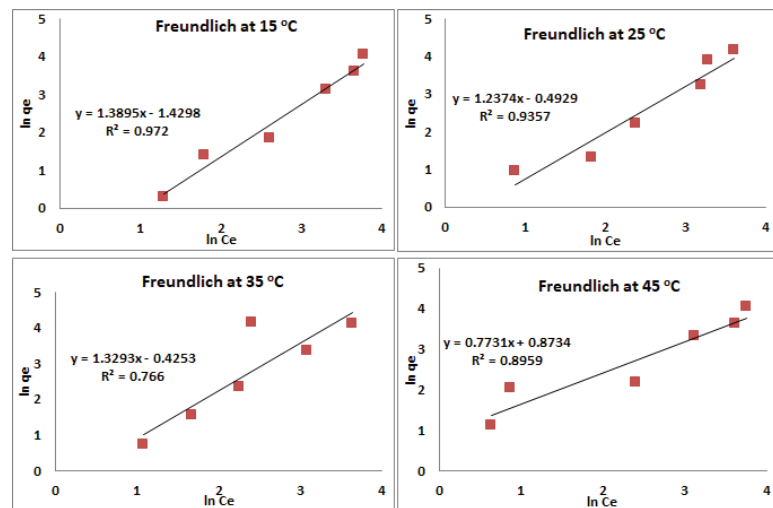
$$\ln q_e = \ln K_f + \frac{1}{n} \ln C_e \quad (5)$$

The Freundlich equation's linear formula is given in Equation (5), where  $K_f$  and  $n$  are Freundlich constants, with  $K_f$  (mg/g (L/mg)<sup>1/n</sup>) denoting the adsorption capability and  $n$  denoting how beneficial the adsorption progression is. The adsorption favorability is determined by the extent of the exponent,  $1/n$ .  $n > 1$ , which indicates that the adsorption conditions are good. The intercept and slope of the curve illustrated in Figures 11 and 12 are used to estimate  $K_f$  and  $n$ , which are provided in Table 3.

The explanation behind the isotherm's compatibility with the Freundlich isotherm model rather than the Langmuir isotherm model is that  $R^2$  was higher at Freundlich, which indicates that the adsorption process were taking place according to the Freundlich isotherm at all temperatures for  $\text{Co}^{2+}$  and  $\text{Cs}^+$  ions. In this study, the Freundlich model is more significantly correlated with high  $R^2$  than the Langmuir model, assuming that the stronger binding sites are occupied first and that binding strength decreases with the increasing degree of site occupation [60].

**Table 3.** Value of Freundlich parameters for adsorption of both ions separately on mixed waste.

| Temp. | $\text{Cs}^+$ |       |       | $\text{Co}^{2+}$ |       |       |
|-------|---------------|-------|-------|------------------|-------|-------|
|       | $n$           | $K_f$ | $R^2$ | $n$              | $K_f$ | $R^2$ |
| 15 °C | 0.719         | 0.239 | 0.972 | 0.926            | 0.298 | 0.957 |
| 25 °C | 0.935         | 0.951 | 0.935 | 1.048            | 0.953 | 0.926 |
| 35 °C | 0.750         | 0.653 | 0.766 | 0.734            | 0.166 | 0.995 |
| 45 °C | 1.29          | 2.3   | 0.895 | 0.703            | 0.372 | 0.970 |



**Figure 11.** Adsorption of  $\text{Cs}^+$  ions on mixed waste at different temperatures (Freundlich isotherm).

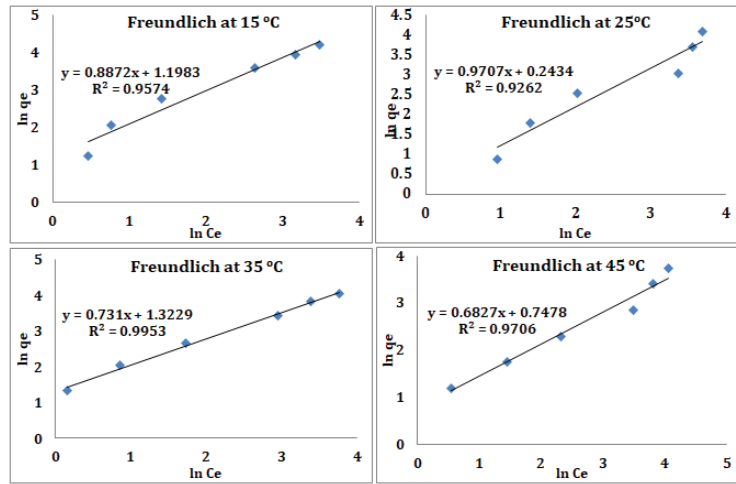


Figure 12. Adsorption of  $\text{Co}^{2+}$  ions on mixed waste at different temperatures (Freundlich isotherm).

To acquire the thermodynamic parameters of the adsorption reaction,  $k_f$  values were processed at different temperatures according to van't Hoff Equation (6):

$$\ln k_f = \frac{-\Delta H^0}{RT} + \frac{\Delta S^0}{R} \quad (6)$$

where  $\Delta H^0$  ( $\text{KJ}\cdot\text{mol}^{-1}$ ) and  $\Delta S^0$  ( $\text{KJ}\cdot\text{mol}\cdot\text{k}^{-1}$ ) are enthalpy and entropy changes, respectively, R is gas constant. Plotting  $k_f$  against  $1/T$ , as shown in Figure 13, gives a straight line with a slope and intercept  $-\Delta H^0/R$  and  $\Delta S^0/R$ , respectively. The value of  $\Delta H^0$  and  $\Delta S^0$  were calculated and listed in Table 4.

The positive value of  $\Delta H^0$  corresponds to the endothermic adsorption process of  $\text{Cs}^+$  and the negative value of  $\Delta H^0$  corresponds to the exothermic adsorption process  $\text{Co}^{2+}$  ions. The Gibbs free energy of adsorption was estimated from the following relation Equation (7) Table 4.

$$\Delta G^0 = \Delta H^0 - T\Delta S^0 \quad (7)$$

Table 4 indicated that little change in  $T\Delta S^0$  has been conducted at all temperatures for  $\text{Cs}^+$  ion and  $T\Delta S^0 < \Delta H^0$ . This finding implied that enthalpy, rather than entropic change, is the driving force of adsorption. These findings are consistent with prior research indicating that the adsorption process is non-spontaneous due to positive  $\Delta G^0$  values obtained [40]. Result for  $\text{Co}^{2+}$  show that  $T\Delta S^0 > \Delta H^0$  suggest an entropic rather than an enthalpic change in the adsorption process. The positive value of  $\Delta G^0$  obtained indicated that the adsorption process of  $\text{Cs}^+$  ion is nonspontaneous.

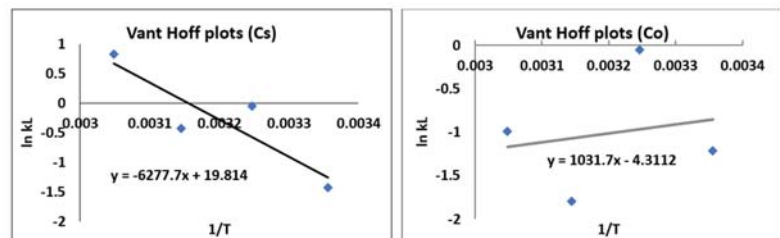


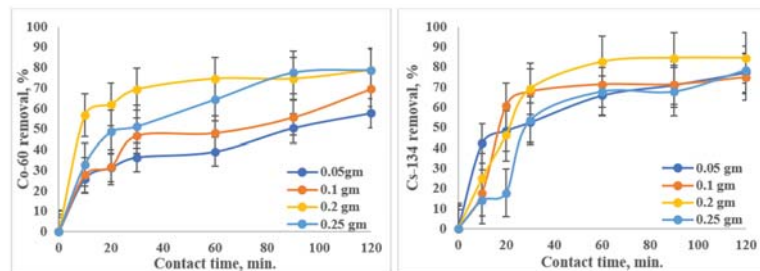
Figure 13. Van't Hoff plots related to adsorption of both ions separately on mixed waste.

**Table 4.** Thermodynamic parameters of adsorption of both ions on mixed waste.

| Element          | $\Delta S$ | $\Delta H$ | T(K) | $T\Delta S$ | $\Delta G$ |
|------------------|------------|------------|------|-------------|------------|
| $\text{Co}^{2+}$ | −0.035     | −8.5       | 288  | −10.08      | 1.58       |
|                  |            |            | 298  | −10.43      | 1.39       |
|                  |            |            | 308  | −10.78      | 2.28       |
|                  |            |            | 318  | −11.13      | 2.63       |
| $\text{Cs}^+$    | 0.16       | 52.1       | 288  | 46.08       | 6.02       |
|                  |            |            | 298  | 47.68       | 4.42       |
|                  |            |            | 308  | 49.28       | 2.82       |
|                  |            |            | 318  | 50.88       | 1.22       |

### 3.7. Adsorption of Radioisotopes ( $^{60}\text{Co}$ and $^{134}\text{Cs}$ ) on Dry Mixed Waste

Figure 14 depicts the adsorption of radioactive cesium and cobalt; the removal efficiency increases with time until it reaches a constant value at equilibrium. The removal percentage of  $^{60}\text{Co}$  after 120 min with different weights of dried mixed waste (0.05, 0.1, 0.2, and 0.25 g) was 55, 70, 80, and 80%, respectively. While the removal percentage of  $^{134}\text{Cs}$  after 120 min with different weights of dried mixed waste (0.05, 0.1, 0.2, and 0.25 g) was between 78.5 and 84.6%. Because there are no chemical differences between stable and radioactive elements, the same adsorption pattern was produced as in a previously reported study of the stable and radioisotopes [18]. With the difference in the radii of cesium and cobalt elements, the ability to impact diffusion mobility and to improve the adsorption process is different, and consequently, the diffusive mobility of the large radius of  $^{134}\text{Cs}$  from the solution to the surface of the biosorbent in aqueous media is lower than the diffusive mobility of the small radius of  $^{60}\text{Co}$  [61].

**Figure 14.** Adsorption of  $^{134}\text{Cs}$  and  $^{60}\text{Co}$  separately on mixed waste.

## 4. Conclusions

The novelty in this study lies in a sustainable treatment technology because it employs dry biomass from mixed waste to demonstrate its synergistic benefits, such as high efficiency and cost effectiveness.

In this study, the removal of stable and radioisotopes of cobalt and cesium from aqueous solutions by biosorption in dried mixed waste of olive waste and water hyacinth as a low-cost and natural available sorbent was investigated. The results show that the natural biomass of mixed waste is an excellent biosorbent for the examined isotopes. The pH experiments showed that the significant biosorption takes place in the acidic range in the case of Co and in the neutral medium in case of Cs. Contact times of 50 and 90 min were the optimal times for the maximum biosorption efficiency of  $\text{Cs}^+$  or  $\text{Co}^{2+}$ . Generally, the increase in mass biosorbent leads to the increase in biosorption due to an increase in the number of biosorption sites. Experimental data were better described by the pseudo-second



order model. The adsorption isotherm could be well-fitted to the Freundlich isotherm model. The biosorption capacity decreases with an increase in solution temperature.

Based on the experimental and mathematical data obtained, mixed dry waste of water hyacinth and olive waste could be nominated as a sustainable low cost and efficient natural adsorbent material suggested for the efficient remediation of radio or stable cobalt and cesium ions from wastewater. However, this technology is predicted to achieve the successful decontamination of hazardous metals and radionuclides in an environmentally friendly and sustainable manner with the extensively decreasing the cost of wastewater treatment.

**Author Contributions:** Conceptualization, H.M.S.; Methodology, A.A.A., R.A.M. and H.M.S.; Writing—original draft, H.M.S.; Writing—review & editing, H.M.S.; Supervision, M.H.B. and H.M.S. All authors have read and agreed to the published version of the manuscript.

**Funding:** This research received no external funding.

**Institutional Review Board Statement:** Not applicable.

**Informed Consent Statement:** Not applicable.

**Data Availability Statement:** Not applicable.

**Conflicts of Interest:** The authors declare no conflict of interest.

## References

- Baroni, L.; Cenci, L.; Tettamanti, M.; Berati, M. Evaluating the Environmental Impact of Various Dietary Patterns Combined with Different Food Production Systems. *Eur. J. Clin. Nutr.* **2007**, *61*, 279–286. [[CrossRef](#)]
- Corcoran, E. *Sick Water?: The Central Role of Wastewater Management in Sustainable Development: A Rapid Response Assessment*; UNEP/Earthprint: Geneva, Switzerland, 2010; ISBN 8277010753.
- Saleh, H.M.; Mahmoud, H.H.; Abdou, M.I.; Eskander, S.B. Health Risk Assessment Based on Metal Analysis of Soil and Crops in Al-Dakhla Oasis. *Arab. J. Geosci.* **2021**, *14*, 260. [[CrossRef](#)]
- Saleh, H.M.; Eskander, S.B.; Mahmoud, H.H.; Abdou, M.I. Groundwater Quality and Health Assessments Based on Heavy Metals and Trace Elements Content in Dakhla Oasis, New Valley Governorate, Egypt. *Water Sci.* **2022**, *36*, 1–12. [[CrossRef](#)]
- Aglan, R.F.; Saleh, H.M.; Mohamed, G.G. Potentiometric Determination of Mercury (II) Ion in Various Real Samples Using Novel Modified Screen-Printed Electrode. *Appl. Water Sci.* **2018**, *8*, 141. [[CrossRef](#)]
- Aglan, R.F.; Mahmoud, H.H.; Rashad, A.M.; Saleh, H.M. Novel Coated Wire Potentiometric Sensor for Selective Determination of Mn (II) Ions in Various Authentic Samples. *J. Iran. Chem. Soc.* **2021**, *18*, 1567–1579. [[CrossRef](#)]
- Al Nagggar, Y.; Khalil, M.S.; Ghorab, M.A. Environmental Pollution by Heavy Metals in the Aquatic Ecosystems of Egypt. *Open Acc. J. Toxicol.* **2018**, *3*, 555603.
- Dąbrowski, A.; Hubicki, Z.; Podkościelny, P.; Robens, E. Selective Removal of the Heavy Metal Ions from Waters and Industrial Wastewaters by Ion-Exchange Method. *Chemosphere* **2004**, *56*, 91–106. [[CrossRef](#)]
- Shaidan, N.H.; Eldemerdash, U.; Awad, S. Removal of Ni (II) Ions from Aqueous Solutions Using Fixed-Bed Ion Exchange Column Technique. *J. Taiwan Inst. Chem. Eng.* **2012**, *43*, 40–45. [[CrossRef](#)]
- Dermentzis, K.; Christoforidis, A.; Valsamidou, E. Removal of Nickel, Copper, Zinc and Chromium from Synthetic and Industrial Wastewater by Electrocoagulation. *Int. J. Environ. Sci.* **2011**, *1*, 697–710.
- Molinari, R.; Poerio, T.; Argurio, P. Selective Separation of Copper (II) and Nickel (II) from Aqueous Media Using the Complexation-Ultrafiltration Process. *Chemosphere* **2008**, *70*, 341–348. [[CrossRef](#)]
- Shirzad Siboni, M.; Samadi, M.T.; Yang, J.K.; Lee, S.M. Photocatalytic Reduction of Cr (VI) and Ni (II) in Aqueous Solution by Synthesized Nanoparticle ZnO under Ultraviolet Light Irradiation: A Kinetic Study. *Environ. Technol.* **2011**, *32*, 1573–1579. [[CrossRef](#)] [[PubMed](#)]
- Mohsen-Nia, M.; Montazeri, P.; Modarress, H. Removal of Cu<sup>2+</sup> and Ni<sup>2+</sup> from Wastewater with a Chelating Agent and Reverse Osmosis Processes. *Desalination* **2007**, *217*, 276–281. [[CrossRef](#)]
- Belkacem, M.; Khodir, M.; Abdelkrim, S. Treatment Characteristics of Textile Wastewater and Removal of Heavy Metals Using the Electroflotation Technique. *Desalination* **2008**, *228*, 245–254. [[CrossRef](#)]
- Saeed, A.; Iqbal, M.; Akhtar, M.W. Removal and Recovery of Lead (II) from Single and Multimetal (Cd, Cu, Ni, Zn) Solutions by Crop Milling Waste (Black Gram Husk). *J. Hazard. Mater.* **2005**, *117*, 65–73. [[CrossRef](#)] [[PubMed](#)]
- Saleh, H.M.; Aglan, R.F.; Mahmoud, H.H. Ludwigia Stolonifera for Remediation of Toxic Metals from Simulated Wastewater. *Chem. Ecol.* **2019**, *35*, 164–178. [[CrossRef](#)]
- Saleh, H.M.; Mahmoud, H.H.; Aglan, R.F.; Bayoumi, T.A. Biological Treatment of Wastewater Contaminated with Cu(II), Fe(II) and Mn(II) Using Ludwigia Stolonifera Aquatic Plant. *Environ. Eng. Manag. J.* **2019**, *18*, 1327–1336. [[CrossRef](#)]

18. Saleh, H.M.; Moussa, H.R.; El-Saied, F.A.; Dawoud, M.; Nouh, E.S.A.; Abdel Wahed, R.S. Adsorption of Cesium and Cobalt onto Dried *Myriophyllum Spicatum* L. from Radio-Contaminated Water: Experimental and Theoretical Study. *Prog. Nucl. Energy* **2020**, *125*, 103393. [[CrossRef](#)]
19. Dawoud, M.M.A.; Hegazy, M.M.; Saleh, H.M.; El Helew, W.K. Removal of Stable and Radio Isotopes from Wastewater by Using Modified Microcrystalline Cellulose Based on Taguchi L16. *Int. J. Environ. Sci. Technol.* **2022**, 1–12. [[CrossRef](#)]
20. Dawoud, M.M.A.; Hegazy, M.M.; Helew, W.K.; Saleh, H.M. Overview of Environmental Pollution and Clean Management of Heavy Metals and Radionuclides by Using Microcrystalline Cellulose. *J. Nucl. Energy Sci. Power Gener. Technol.* **2021**, *3*, 2.
21. Chen, W.; Li, H. Cost-Effectiveness Analysis for Soil Heavy Metal Contamination Treatments. *Water Air Soil Pollut.* **2018**, *229*, 126. [[CrossRef](#)]
22. Ghaly, M.; Metwally, S.S.; El-Sherief, E.A.; Saad, E.A.; Abdel Rahman, R.O. Utilization of Synthetic Nano-Cryptomelane for Enhanced Scavenging of Cesium and Cobalt Ions from Single and Binary Solutions. *J. Radioanal. Nucl. Chem.* **2022**, *331*, 1821–1838. [[CrossRef](#)]
23. Avery, S.V.; Codd, A.; Gadd, M. Caesium Accumulation and Interactions with Other Monovalent Cations in the Cyanobacterium *Synechocystis* PCC 6803. *Microbiology* **1991**, *137*, 405–413. [[CrossRef](#)]
24. Singh, A.; Kumar, S. Application of Aquatic Plants Dead Biomass in Remediation of Heavy Metals Pollution by Adsorption: A Review. *Indian J. Sci. Technol.* **2022**, *15*, 729–735. [[CrossRef](#)]
25. Lison, D.; Van Den Brûle, S.; Van Maele-Fabry, G. Cobalt and Its Compounds: Update on Genotoxic and Carcinogenic Activities. *Crit. Rev. Toxicol.* **2018**, *48*, 522–539. [[CrossRef](#)] [[PubMed](#)]
26. Melnikov, P.; Zanon, L.Z. Clinical Effects of Cesium Intake. *Biol. Trace Elem. Res.* **2010**, *135*, 1–9. [[CrossRef](#)]
27. Saleh, H.M.; Moussa, H.R.; El-Saied, F.A.; Dawoud, M.; Bayoumi, T.A.; Abdel Wahed, R.S. Mechanical and Physicochemical Evaluation of Solidified Dried Submerged Plants Subjected to Extreme Climatic Conditions to Achieve an Optimum Waste Containment. *Prog. Nucl. Energy* **2020**, *122*, 103285. [[CrossRef](#)]
28. Saleh, H.M.; Aglan, R.F.; Mahmoud, H.H. Qualification of Corroborated Real Phytoremediated Radioactive Wastes under Leaching and Other Weathering Parameters. *Prog. Nucl. Energy* **2020**, *119*, 103178. [[CrossRef](#)]
29. Saleh, H.M.; Eskander, S.B. Toxicity and Remediation of Radioactive Pollutants. *J. Nucl. Energy Sci. Power Gener. Technol.* **2020**, *9*, 197. [[CrossRef](#)]
30. Saleh, H.; Salman, A.; Faheim, A.; El-Sayed, A. Polymer and Polymer Waste Composites in Nuclear and Industrial Applications. *J. Nucl. Energy Sci. Power Gener. Technol.* **2020**, *9*, 1000199.
31. Saleh, H.M. Some Applications of Clays in Radioactive Waste Management. In *Clays and Clay Minerals: Geological Origin, Mechanical Properties and Industrial Applications*; Wesley, L.R., Ed.; Nova Science Pub. Inc.: Hauppauge, NY, USA, 2014; pp. 403–415; ISBN 9781631177804.
32. Aijaz, M.O.; Yang, S.B.; Karim, M.R.; Naseer, I.A.; Alahmari, A.D.; Mubaddel, F.A.; Assaifan, A.K. Preparation and Characterization of Electrospun Poly (Lactic Acid)/Poly (Ethylene Glycol)-b-Poly (Propylene Glycol)-b-Poly (Ethylene Glycol)/Silicon Dioxide Nanofibrous Adsorbents for Selective Copper (II) Ions Removal from Wastewater. *Membranes* **2023**, *13*, 54. [[CrossRef](#)]
33. Boss, C.B.; Fredeen, K.J. *Concepts, Instrumentation and Techniques in Inductively Coupled Plasma Optical Emission Spectroscopy*; Perkin Elmer: Waltham, MA, USA, 1999.
34. Liu, Y.; Diwu, C.; Zhao, Y.; Liu, X.; Yuan, H.; Wang, J. Determination of Trace and Rare-Earth Elements in Chinese Soil and Clay Reference Materials by ICP-MS. *Chin. J. Geochem.* **2014**, *33*, 95–102. [[CrossRef](#)]
35. Bhatnagar, A.; Sillanpää, M.; Witek-Krowiak, A. Agricultural Waste Peels as Versatile Biomass for Water Purification—A Review. *Chem. Eng. J.* **2015**, *270*, 244–271. [[CrossRef](#)]
36. He, Z.L.; Yang, X.E.; Stoffella, P.J. Trace Elements in Agroecosystems and Impacts on the Environment. *J. Trace Elem. Med. Biol.* **2005**, *19*, 125–140. [[CrossRef](#)] [[PubMed](#)]
37. Saravanan, A.; Sundararaman, T.R.; Jeevanantham, S.; Karishma, S.; Kumar, P.S.; Yaashikaa, P.R. Effective Adsorption of Cu (II) Ions on Sustainable Adsorbent Derived from Mixed Biomass (*Aspergillus campestris* and Agro Waste): Optimization, Isotherm and Kinetics Study. *Groundw. Sustain. Dev.* **2020**, *11*, 100460. [[CrossRef](#)]
38. Fubara, A.G.; Uche, C.C.; Nwoko, C.O.; Tony-Njoku, R.F.; Ojiaku, A.A.; Edo, F.A. Assessment of the Effectiveness of Water Hyacinth (*E. Crassipes*) in the Biosorption of Heavy Metals from Aluminium Extruding Company Effluents. *J. Appl. Sci. Environ. Manag.* **2022**, *26*, 37–46. [[CrossRef](#)]
39. Sharma, P.; Kaur, H. Sugarcane Bagasse for the Removal of Erythrosin B and Methylene Blue from Aqueous Waste. *Appl. Water Sci.* **2011**, *1*, 135–145. [[CrossRef](#)]
40. Ghanavati, B.; Bozorgian, A.; Ghanavati, J. Removal of Copper (II) Ions from the Effluent by Carbon Nanotubes Modified with Tetrahydrofuran. *Chem. Rev. Lett.* **2022**, *5*, 68–75.
41. Xu, Z.; Xing, Y.; Ren, A.; Ma, D.; Li, Y.; Hu, S. Study on Adsorption Properties of Water Hyacinth-Derived Biochar for Uranium (VI). *J. Radioanal. Nucl. Chem.* **2020**, *324*, 1317–1327. [[CrossRef](#)]
42. Hanaf, R.A.-K. Effect of Salinity and PH on the Absorption of Cadmium in Lemna Minor. *Int. J. Aquat. Biol.* **2021**, *9*, 383–387.
43. Adeolu, A.T.; Okareh, O.T.; Dada, A.O. Adsorption of Chromium Ion from Industrial Effluent Using Activated Carbon Derived from Plantain (*Musa Paradisiaca*) Wastes. *Am. J. Env. Prot.* **2016**, *4*, 7–20.

44. Sartape, A.S.; Mandhare, A.M.; Jadhav, V.V.; Raut, P.D.; Anuse, M.A.; Kolekar, S.S. Removal of Malachite Green Dye from Aqueous Solution with Adsorption Technique Using Limonia Acidissima (Wood Apple) Shell as Low Cost Adsorbent. *Arab. J. Chem.* **2017**, *10*, S3229–S3238. [[CrossRef](#)]
45. Azam, M.G.; Kabir, M.H.; Shaikh, M.A.A.; Ahmed, S.; Mahmud, M.; Yasmin, S. A Rapid and Efficient Adsorptive Removal of Lead from Water Using Graphene Oxide Prepared from Waste Dry Cell Battery. *J. Water Process Eng.* **2022**, *46*, 102597. [[CrossRef](#)]
46. Yavuz, Ö.; Altunkaynak, Y.; Güzel, F. Removal of Copper, Nickel, Cobalt and Manganese from Aqueous Solution by Kaolinite. *Water Res.* **2003**, *37*, 948–952. [[CrossRef](#)] [[PubMed](#)]
47. Rawat, J.P.; Iraqi, S.M.U.; Singh, R.P. Sorption Equilibria of Cobalt (II) on Two Types of Indian Soils—The Natural Ion Exchangers. *Colloids Surfaces A Physicochem. Eng. Asp.* **1996**, *117*, 183–188. [[CrossRef](#)]
48. Iyer, A.; Mody, K.; Jha, B. Biosorption of Heavy Metals by a Marine Bacterium. *Mar. Pollut. Bull.* **2005**, *50*, 340–343. [[CrossRef](#)]
49. van Hullebusch, E.D.; Peerbolte, A.; Zandvoort, M.H.; Lens, P.N.L. Sorption of Cobalt and Nickel on Anaerobic Granular Sludges: Isotherms and Sequential Extraction. *Chemosphere* **2005**, *58*, 493–505. [[CrossRef](#)]
50. Parab, H.; Joshi, S.; Shenoy, N.; Lali, A.; Sarma, U.S.; Sudersanan, M. Determination of Kinetic and Equilibrium Parameters of the Batch Adsorption of Co (II), Cr (III) and Ni (II) onto Coir Pith. *Process Biochem.* **2006**, *41*, 609–615. [[CrossRef](#)]
51. Vijayaraghavan, K.; Jegan, J.; Palanivelu, K.; Velan, M. Biosorption of Cobalt (II) and Nickel (II) by Seaweeds: Batch and Column Studies. *Sep. Purif. Technol.* **2005**, *44*, 53–59. [[CrossRef](#)]
52. Miah, M.Y.; Volchek, K.; Kuang, W.; Tezel, F.H. Kinetic and Equilibrium Studies of Cesium Adsorption on Ceiling Tiles from Aqueous Solutions. *J. Hazard. Mater.* **2010**, *183*, 712–717. [[CrossRef](#)]
53. Wang, T.-H.; Li, M.-H.; Yeh, W.-C.; Wei, Y.-Y.; Teng, S.-P. Removal of Cesium Ions from Aqueous Solution by Adsorption onto Local Taiwan Laterite. *J. Hazard. Mater.* **2008**, *160*, 638–642. [[CrossRef](#)]
54. Melkior, T.; Yahiaoui, S.; Motellier, S.; Thoby, D.; Tevissen, E. Cesium Sorption and Diffusion in Bure Mudrock Samples. *Appl. Clay Sci.* **2005**, *29*, 172–186. [[CrossRef](#)]
55. Ding, D.; Lei, Z.; Yang, Y.; Zhang, Z. Efficiency of Transition Metal Modified Akadama Clay on Cesium Removal from Aqueous Solutions. *Chem. Eng. J.* **2014**, *236*, 17–28. [[CrossRef](#)]
56. Rani, R.D.; Sasidhar, P. Sorption of Cesium on Clay Colloids: Kinetic and Thermodynamic Studies. *Aquat. Geochem.* **2012**, *18*, 281–296. [[CrossRef](#)]
57. Parab, H.; Sudersanan, M. Engineering a Lignocellulosic Biosorbent—Coir Pith for Removal of Cesium from Aqueous Solutions: Equilibrium and Kinetic Studies. *Water Res.* **2010**, *44*, 854–860. [[CrossRef](#)] [[PubMed](#)]
58. Wang, C.; Myshkin, V.F.; Khan, V.A.; Poberezhnikov, A.D.; Baraban, A.P. Effect of Temperature on the Diffusion and Sorption of Cations in Clay Vermiculite. *ACS Omega* **2022**, *7*, 11596–11605. [[CrossRef](#)] [[PubMed](#)]
59. Elemile, O.O.; Akpor, B.O.; Ibitogbe, E.M.; Afolabi, Y.T.; Ajani, D.O. Adsorption Isotherm and Kinetics for the Removal of Nitrate from Wastewater Using Chicken Feather Fiber. *Cogent Eng.* **2022**, *9*, 2043227. [[CrossRef](#)]
60. Anah, L.; Astrini, N. Isotherm Adsorption Studies of Ni (II) Ion Removal from Aqueous Solutions by Modified Carboxymethyl Cellulose Hydrogel. In *Proceedings of the IOP Conference Series: Earth and Environmental Science*; IOP Publishing: Bristol, England, 2018; Volume 160, p. 12017.
61. Dakrouy, G.A.R.; Abo-Zahra, S.F.; Hassan, H.S.; Ali, H.E.A. Improvement of the Sorption Behavior of Aluminum Silicate Composite toward <sup>134</sup>Cs and <sup>60</sup>Co Radionuclides by Non-Living Biomass of *Chlorella Vulgaris*. *Environ. Sci. Pollut. Res.* **2020**, *27*, 21109–21125. [[CrossRef](#)]

**Disclaimer/Publisher's Note:** The statements, opinions and data contained in all publications are solely those of the individual author(s) and contributor(s) and not of MDPI and/or the editor(s). MDPI and/or the editor(s) disclaim responsibility for any injury to people or property resulting from any ideas, methods, instructions or products referred to in the content.

## Article

# Natural Radioactivity Measurements and Radiological Hazards Evaluation for Some Egyptian Granites and Ceramic Tiles

Essam Sidique <sup>1,\*</sup>, Sedky H. A. Hassan <sup>2,3</sup> and Mohammad Mahmoud Dawoud <sup>4,\*</sup><sup>1</sup> Physics Department, Faculty of Science, New Valley University, El-Kharga 72511, Egypt<sup>2</sup> Biology Department, College of Science, Sultan Qaboos University, Muscat 123, Oman<sup>3</sup> Botany & Microbiology Department, Faculty of Science, New Valley University, El-Kharga 72511, Egypt<sup>4</sup> Radioisotopes Department, Nuclear Research Center, Egyptian Atomic Energy Authority, Giza 12311, Egypt

\* Correspondence: esamsadik@yahoo.com (E.S.); mohammed.h.aea@gmail.com (M.M.D.)

**Abstract:** All over the world, people widely use granites and ceramic tiles in their residential establishments. Information concerning the radiological properties of such materials reveals how to ensure the sustainability of their safe use in terms of these properties. In the present work, the distribution of the terrestrial radioisotopes U-238 (Ra-226), Th-232, and K-40 for 23 different brands of Egyptian commercial granites and ceramic tiles samples (widely used domestically and exported) was determined using gamma radiation spectroscopy. This process pinpoints the possible radiological health risks related to gamma ray exposure and radon gas resulting from the use of these materials indoors. The concentration values of the aforementioned radioisotopes in the examined samples were compared to the corresponding global average values (GAVs) of the UNSCEAR and to those available in other countries. The overall average concentrations for U-238, Th-232, and K-40 in the total samples were observed to be  $46.17 \pm 2.81$  (less than its GAV),  $51.65 \pm 2.35$  (slightly above its GAV), and  $701.62 \pm 40.60$  Bq/kg (1.4 times greater than the GAV), respectively. The related radiological parameters and indices were calculated and compared to the prescribed limits set by commissions and organizations concerned with radiation protection (the WHO, ICRP, UNSCEAR, and EC) to ensure the safe use of the investigated granites and ceramic tiles. The assessed indices and parameters fall within the recommended values and safety limits. In conclusion, there is no risk from using the granites and ceramic tiles under investigation in residential facilities.

**Keywords:** natural radioactivity; gamma rays; radon gas; radiation exposure; building materials; granites; ceramic

**Citation:** Sidique, E.; Hassan, S.H.A.; Dawoud, M.M. Natural Radioactivity Measurements and Radiological Hazards Evaluation for Some Egyptian Granites and Ceramic Tiles. *Sustainability* **2022**, *14*, 14611. <https://doi.org/10.3390/su142114611>

Academic Editor: Changhyun Roh

Received: 24 September 2022

Accepted: 30 October 2022

Published: 7 November 2022

**Publisher's Note:** MDPI stays neutral with regard to jurisdictional claims in published maps and institutional affiliations.



**Copyright:** © 2022 by the authors. Licensee MDPI, Basel, Switzerland. This article is an open access article distributed under the terms and conditions of the Creative Commons Attribution (CC BY) license (<https://creativecommons.org/licenses/by/4.0/>).

## 1. Introduction

For humans, exposure to natural ionizing radiation is unavoidable. Exposure arises primarily from both terrestrial and cosmogenic radioisotopes. Terrestrial radioisotopes (K-40, U-238, and Th-232) exist naturally in all different environmental media, including air, water, food, soil, rock, building materials, etc. [1–3]. The existence of the abovementioned radioisotopes in building materials is responsible for delivering about 85% of the radiation dosage to the world's population [3,4]. Accordingly, providing information on terrestrial radioisotope concentrations and distributions in building materials is essential and it is required to monitor contamination originating from their radioactivity in residential environments.

The natural radioactivity level in building materials is confined in the terrestrial radionuclide concentrations in the geological materials from which they are derived [4,5], i.e., it varies according to the geological origin and geochemical characteristics of the constituent materials. Additionally, the radiation dose received is controlled by several factors, including residences places ventilation, and kinds [1].

In fact, gamma rays and radon gas (Rn-222 and Rn-220) are the most significant products of the terrestrial radioisotopes' radioactivity in building materials, in light of the

radiological hazards to the population [6]. Gamma rays are responsible for the external exposure of populations and their dose comes mainly from Tl-208 and Ac-228 of the Th-232 disintegration chain, from Pb-214 and Bi-214 derived from Rn-226 of the U-238 disintegration chain, and from K-40. On the other hand, radon gas (specifically Rn-222) which originates as a result of radium disintegration (Ra-226 of the U-238 chain), is responsible for the internal exposure [7]. According to the UNSCEAR [6], the average yearly external exposure indoors due to gamma rays was assessed as 0.41 mSv, while the internal exposure from Rn-222 inhalation was about 1.15 mSv. It is worth mentioning that several epidemiological investigations conducted in many countries have demonstrated substantial evidence linking raised levels of radon exposure in houses to an increased risk of lung cancer [8–10].

Construction materials that typically come from the soil and rocks of the earth may be categorized into three groups: structural materials, covering materials, and additive raw materials. Structural materials such as cement, concrete, mortar, and clay bricks, etc., are primarily used for building structures. The covering materials (granite, ceramic, marble, etc.) are employed for ornamentation and insulation purposes, whereas fly ash, bauxite, phosphogypsum, etc., are the additive raw materials used as optional components for modifying certain properties of building materials [1]. In light of global recommendations, determining the natural radioactivity levels of construction materials is crucial for assessing the radiological risks owing to radiation exposures as well as for developing national standards and guidelines for these materials. Recently, as a result of rising social concern, there has been a high worldwide interest in studying the natural radioactivity of construction materials as well as investigating their impact on the public (e.g., [4,5,11–20]). To the best of the authors' knowledge, important international studies on natural radioactivity measurements and radiological hazards evaluation for granites and ceramic tiles were published in the Refs. [1,2,9,18,19,21–39], just to name a few. Nevertheless, although granites and ceramic tiles of various brands are widely used in residences for interior and exterior ornamentation and decoration purposes in Egypt, no detailed studies have been conducted to determine the activity levels of terrestrial radioisotopes in these materials.

The present work investigates in depth the natural radioactivity of twenty-three well-known Egyptian brands of commercial granites and ceramic tiles samples widely used in Egypt and abroad, as well as the potential health risks associated with their use indoors. Moreover, its overall goal is to complete a radiometric study on some sample Egyptian commercial granites and ceramic tiles which have not been previously covered. Hopefully, the findings of the present work and the accompanying assessments will establish baseline data for monitoring radioactive pollution in residential environments and will provide adequate public protection recommendations.

## 2. Experimental Arrangements

### 2.1. Sample Preparation

A total of 107 tile samples (42 granite samples plus 65 ceramic samples) from 23 different brands were purchased from Egyptian building materials markets and suppliers. The commercial ceramics and granites studied are among the best widely used decorative building materials brands in Egypt. Before transporting the samples to the lab, they were properly catalogued, labeled, and named according to their popular names known in both the global and domestic markets (Table 1). More detailed information, particularly for granite, is available at ([www.stonecontact.com](http://www.stonecontact.com), accessed on 19 June 2022). The samples have been given identification numbers in brackets, which are (1 to 42) for granites, and (43 to 107) for ceramic tiles. Then, each sample was individually ground to a powder, to avoid contamination between samples, and sieved through a sieve (200  $\mu\text{m}$  mesh). All the samples were oven-dried for 5 h at 105 °C to remove the moisture content. These prepared samples were subsequently weighed (between 600 g and 850 g) and sealed in plastic cylindrical beakers (48 mm radius, 82 mm height, and 0.5 mm thickness) for more than 4 weeks to guarantee access to the secular equilibrium between parent radioisotopes and daughters in the natural disintegration series ( $^{232}\text{Th}$  and  $^{238}\text{U}$ ).



**Table 1.** Granites and ceramic tiles of various brands used in Egypt.

| Tiling Material       | Brand Name         | Brand ID | Sample Size | Sample Origin                          |                                      |
|-----------------------|--------------------|----------|-------------|----------------------------------------|--------------------------------------|
| Granite               | Bianco Halayeb     | GBiHa    | 3           | Abu Ghusun, Red Sea, Egypt             |                                      |
|                       | Brown Hurgada      | GBrHu    | 3           | Hurghada, Egypt                        |                                      |
|                       | Imperial Red       | GIR      | 3           | Aswan, South of Egypt                  |                                      |
|                       | Karnak Grey        | GKG      | 3           | Aswan, South of Egypt                  |                                      |
|                       | Negro Aswan        | GNA      | 4           | Aswan, South of Egypt                  |                                      |
|                       | Rosa Aswan Dark    | GRAD     | 3           | Aswan, South of Egypt                  |                                      |
|                       | Rosa El Hody Light | GRHL     | 3           | Aswan, South of Egypt                  |                                      |
|                       | Rosa Abu Simble    | GRAS     | 4           | Wadi Halfa, Aswan, Egypt               |                                      |
|                       | Rosa Sardo Sinai   | GRSS     | 3           | Sinai, Egypt                           |                                      |
|                       | Red Aswan          | GRA      | 3           | Aswan, South of Egypt                  |                                      |
|                       | Red Nefertary      | GRN      | 4           | Aswan, South of Egypt                  |                                      |
|                       | Red Forsan         | GRF      | 3           | Wadi Forsan, northeastern Egypt        |                                      |
|                       | Yellow Ghazal      | GYG      | 3           | Sinai, Egypt                           |                                      |
|                       | Ceramic            | Alfa     | CAL         | 7                                      | 6th of October City (2), Giza, Egypt |
|                       |                    | Art      | CAR         | 7                                      | 6th of October City (2), Giza, Egypt |
| Cleopatra             |                    | CCL      | 5           | 10th of Ramadan City (1), Cairo, Egypt |                                      |
| Gemma (Al-Jawhara)    |                    | CGE      | 7           | El Sadat City Desert, Menoufia, Egypt  |                                      |
| Gloria                |                    | CGL      | 6           | Nasr City, Cairo, Egypt                |                                      |
| Labotie               |                    | CLA      | 6           | 10th of Ramadan City, Sharqia, Egypt   |                                      |
| Pharaohs (Alfaraeina) |                    | CPH      | 7           | Al Azbakeya, Cairo, Egypt              |                                      |
| Prima                 |                    | CPR      | 7           | 5th Industrial zone, Menoufia, Egypt   |                                      |
| Royal                 |                    | CRO      | 6           | Al Obour, Al Qalyubia, Egypt           |                                      |
| Venezia               |                    | CVE      | 7           | 6th of October City (2), Giza, Egypt   |                                      |

## 2.2. Gamma Spectrometric Analysis

To measure the activity concentrations of the radioisotopes ( $\gamma$ -emitters) in the samples, a low-background  $\gamma$ -rays spectroscopy system consisting of a semiconductor HPGe (Hyper-Pure Germanium) detector (Model GR4020, Canberra, Meriden, CT, USA) with a 40% relative efficiency and energy resolution (FWHM) of 2 keV at the 1332 keV  $\gamma$ -line (Co-60) was used. In addition, the system contains a suitable lead shield (Model 747E, Canberra, USA) surrounding the detector to prevent more than 98% of the external background radiation from reaching the detector during the analysis. The gamma spectrums were acquired and analyzed utilizing the Genie-2000 software (Version 3.3, Canberra, USA) [40] coupled with a multichannel analyzer (Model DAS-1000, Canberra, USA). For calibrating the detector's energy and efficiency, the LabSOCS (Laboratory Sourceless Calibration Software) designed using the features of geometry composer and gamma analysis within the Genie-2000 software, was used. The Genie-2000 software also contains the detector's characterization files created based on the system manufacturer's fundamental calibration tests (Canberra). To authenticate the efficiency data provided by LabSOCS, measurements were completed in our laboratory with a set of gamma calibration sources (Co-60, Cs-137, Ba-133, Mn-54, Zn-65, and Na-22), which revealed a significant agreement (90%) between empirical and mathematical peak efficiency.

Each prepared sample was put on the detector for a time period no less than 12 h in order to obtain an accurate counting statistic for gamma lines (photo-peaks) of importance. Additionally, the background level in the laboratory was measured using an empty beaker in similar conditions. The K-40 radionuclide was determined directly by its own gamma line intensity (1460.8 keV). As for U-238 (Ra-226), it was specified through its progeny Bi-214 (1764.5, 1120.3, and 609.3 keV) and Pb-214 (351.9 and 295.2 keV). On the other hand, Th-232 was identified via its daughters Ac-228 (968.9, 911.2, and 338.3 keV), Tl-208 (2614.5 and 583.2 keV), and Pb-212 (238.6 keV). The activity concentration (AC) and the uncertainty in activity concentration ( $U_{AC}$ ) of the previously mentioned radionuclides in each sample were calculated from their corresponding gamma line intensities taking into account the sample mass, counting time, gamma decay transition probabilities, and detector efficiencies [41–43].

### Activity Concentrations Estimation

The activity concentration (AC) in the granites and ceramic tiles samples under investigation was estimated as follows [41]:

$$AC[\text{Bq/kg}] = \frac{N_{c,E}}{P_{\gamma,E} \cdot \epsilon_E \cdot M_s} \quad (1)$$

where  $N_{c,E}$  is the net count rate resulting from subtracting the count rate of the peak at energy  $E$  in the sample spectrum minus that of the background spectrum at the same energy  $E$ ,  $P_{\gamma,E}$  denotes the probability of emitting gamma radiation with energy  $E$  for the radioisotope of interest,  $\epsilon_E$  is the detector absolute efficiency at energy  $E$ , and  $M_s$  refers to the sample mass. Moreover, using the equation below, the uncertainty in activity concentration,  $U_{AC}$ , was calculated based on uncertainties in  $N_{c,E}$ ,  $P_{\gamma,E}$ ,  $\epsilon_E$ , and  $M_s$  [43]:

$$U_{AC} = AC \sqrt{\left[\frac{U_{N_{c,E}}}{N_{c,E}}\right]^2 + \left[\frac{U_{P_{\gamma,E}}}{P_{\gamma,E}}\right]^2 + \left[\frac{U_{\epsilon_E}}{\epsilon_E}\right]^2 + \left[\frac{U_{M_s}}{M_s}\right]^2} \quad (2)$$

### 3. Estimation of Radiological Risks

For understanding the effect of radiological hazards on human health when using the investigated granites and ceramic tiles as tiling materials in buildings, several radiation hazard indices were estimated. The radium equivalent activity ( $Ra_{eq}$ ), gamma index ( $I_\gamma$ ), indoor absorbed gamma dose rate ( $D_{in}$ ), yearly effective gamma dose rate ( $E_{in}$ ), and excess lifetime cancer risk (ELCR) were used to investigate gamma radiation risks, while the alpha index ( $I_\alpha$ ), radon exhalation rate (RX), radon concentration ( $C_{Rn}$ ), and yearly effective dose due to radon ( $E_{Rn}$ ) were evaluated in order to investigate the potential radon risks.

#### 3.1. Radium Equivalent Activity ( $Ra_{eq}$ )

The  $Ra_{eq}$  is one of the most effective radiological indices for determining gamma radiation hazards due to the radioisotopes K-40, U-238 and Th-232 content in tiling materials, considering the non-uniform distribution of these radioisotopes in matter. As per Beretka et al. [44],  $Ra_{eq}$  is described by the following equation:

$$Ra_{eq} [\text{Bq kg}^{-1}] = \left( \frac{AC_U}{370} + \frac{AC_{Th}}{259} + \frac{AC_K}{4810} \right) \times 370 \quad (3)$$

where  $AC_U$ ,  $AC_{Th}$ , and  $AC_K$  are the specific activity concentrations of the radioisotopes U-238 (Ra-226), Th-232, and K-40, respectively. In fact, the  $Ra_{eq}$  reflects the weighted total of the abovementioned three radioisotopes' concentrations within materials under the premise that gamma dose rates from 4810 Bq/kg of K-40, 259 Bq/kg of Th-232, and 370 Bq/kg of U-238 (Ra-226) are almost equal.

From a radiation protection perspective, the ceramic and granite tiles studied herein are safe provided that their  $Ra_{eq}$  levels are not above 370 Bq/kg [44] (permissible limit) corresponding to a yearly effective dosage of 1.5 mSv [41,45].

#### 3.2. Gamma Index ( $I_\gamma$ )

The  $I_\gamma$  is taken into consideration as a monitoring tool specifying whether construction materials are safe to use or not. Considering that the external exposure due to gamma radiation from the tiling (superficial or covering) materials has a limit of 1 mSv/year, the  $I_\gamma$  is adopted by the European Commission [46] to be estimated via the following equation:

$$I_\gamma = \frac{AC_U}{300 \text{ Bq kg}^{-1}} + \frac{AC_{Th}}{200 \text{ Bq kg}^{-1}} + \frac{AC_K}{3000 \text{ Bq kg}^{-1}} \quad (4)$$

According to the European Commission [46], for covering materials such as the ceramic and granite tiles under investigation, if they have a  $I_\gamma \leq 2$ , this leads to an increase



in the annual gamma dose rate with an amount  $\leq 0.3$  mSv/y resulting from these materials. In other words, these materials fall within the exemption level for building materials from all limitations about their radioactivity. Furthermore, if materials achieve criteria  $2 < I_\gamma \leq 6$ , they will contribute to the annual gamma dose rate with an amount  $\leq 1$  mSv/y and fall within the recommended action level. Eventually, materials with  $I_\gamma > 6$  are not suitable for safe use in buildings [46].

### 3.3. Indoor Absorbed Gamma Dose Rate ( $D_{in}$ ) and Yearly Effective Dose ( $E_{in}$ )

Estimation of the indoor absorbed gamma dose rate ( $D_{in}$ ) and its associated yearly effective dose ( $E_{in}$ ) are significant mechanisms for determining the external exposure caused by terrestrial radioisotopes (Th-232, U-238, and K-40). According to the European Commission [46], Equations (5) and (6) can be used to estimate the  $D_{in}$  and  $E_{in}$  in the air within rooms as a result of using the investigated granites and ceramic tiles as superficial construction materials:

$$D_{in} \left[ \text{nGy h}^{-1} \right] = (12AC_{Ra} + 14AC_{Th} + 0.96AC_K) \times 10^{-2} \quad (5)$$

$$E_{in} \left[ \text{mSvy}^{-1} \right] = D_{in} \left[ \text{nGy h}^{-1} \right] \times F_1 \times F_2 \times F_3 \times 10^{-6} \quad (6)$$

where  $F_1$  (=0.7 Sv/Gy),  $F_2$  (=0.8), and  $F_3$  (=8766 h) represent the conversion factor from the absorbed dose to the effective dose in the air, indoor residency factor, and hours of the year, respectively.

### 3.4. Excess Lifetime Cancer Risk (ELCR)

The ELCR is an important quantity through which the incidence of cancer for an individual exposed to a low gamma radiation dose over their lifetime (66-years) can be figured out. Depending on the  $E_{in}$  incurred by individuals from the studied ceramic and granite tiles (superficial building materials) when used in buildings, the ELCR can be estimated as follows [4,41]:

$$\text{ELCR} = E_{in} [\text{Sv/y}] \times C_1 \times C_2 \quad (7)$$

where  $C_1$  (=66 y [47]) and  $C_2$  (=0.05  $\text{Sv}^{-1}$  for the general population) stand for life expectancy on average and fatal cancer risk, respectively [42,48].

### 3.5. Alpha Index ( $I_\alpha$ )

The  $I_\alpha$  given by the equation below [41] is used for estimating the risk of exposure to internal alpha radiation owing to the inhalation of radon. The estimation of  $I_\alpha$  is fundamentally dependent on the U-238 (Ra-226) activity concentration ( $AC_{Ra}$ ) in construction materials, considering that materials with a concentration of  $^{226}\text{Ra} < 200$  Bq  $\text{kg}^{-1}$  cannot emit an indoor radon concentration  $>200$  Bq  $\text{m}^{-3}$ , i.e., these materials come within the range of the recommended action level of indoor radon exposure for buildings, as previously agreed upon by the European Commission [46] and ICRP [49].

$$I_\alpha = \frac{AC_{Ra}}{200 \text{Bq kg}^{-1}} \leq 1 \quad (8)$$

### 3.6. Radon Concentration ( $C_{Rn}$ ) and Yearly Effective Dose Resulting Therefrom ( $E_{Rn}$ )

In this study, the parallelepiped room model ( $4 \times 5 \times 2.8$  m) is taken into account to assess the concentration of radon and the associated absorbed dose rate delivered to residents, assuming the floor is made of the investigated ceramic or granite tiles. Thus, Equation (9) is applied, according to the European Commission [46], to determine the

increase in indoor radon concentration ( $C_{Rn}$ ) brought on by the radon exhalation rate (RX) from the investigated ceramic or granite tiles used in buildings:

$$C_{Rn} \left[ \text{Bq m}^{-3} \right] = \frac{RX \cdot S}{(\lambda + \lambda_0) \cdot V} \quad (9)$$

where  $RX$  [ $\text{Bq m}^{-2} \text{h}^{-1}$ ],  $\lambda$  ( $=0.0076 \text{ h}^{-1}$ ),  $\lambda_0$  [ $\text{h}^{-1}$ ],  $S$  [ $\text{m}^2$ ], and  $V$  [ $\text{m}^3$ ] represent the radon exhalation rate per unit area, Ra-226 decay constant, ventilation rate, tiled floor surface, and volume of the room, respectively. Based on the determined Ra-226 concentration ( $AC_{Ra}$ ), Equation (10) can be applied to estimate the RX for the investigated tiles with thickness  $d$  ( $=3 \text{ cm}$  and  $1 \text{ cm}$  for granites and ceramic tiles, respectively), density  $\rho$  ( $=2600 \text{ kg/m}^3$ ), and emanation coefficient  $\eta$  ( $=0.45$ ), as reported in Refs. [20,41,50]:

$$RX = AC_{Ra} \cdot \lambda \cdot \rho \cdot \eta \cdot d \cdot 0.5 \quad (10)$$

It is worth noting that the room ventilation rate ( $\lambda_0$ ) was chosen with  $0.5 \text{ h}^{-1}$  for normal ventilation and  $0.1 \text{ h}^{-1}$  for poor ventilation. [9,41]. Furthermore, the ( $S/V$ ) ratio of the room surface tiled with the investigated ceramic and granite tiles was chosen to be  $2 \text{ m}^{-1}$  [41].

As per the UNSCEAR [6] report, the yearly effective dose ( $E_{Rn}$ ) that dwellers obtain from the indoor radon concentration ( $C_{Rn}$ ) was estimated by the following formula:

$$E_{Rn} \left[ \text{mSv y}^{-1} \right] = C_{Rn} \left[ \text{Bq m}^{-3} \right] \times C_1 \times 8766 \left[ \text{h y}^{-1} \right] \times C_2 \times C_3 \times 10^{-6} \quad (11)$$

where  $C_1$  ( $=9 \text{ nSv per Bq m}^{-3} \text{ h}$ ),  $C_2$  ( $=0.8$ ), and  $C_3$  ( $=0.4$ ) stand for the factors of dose conversion, dwellers' indoor residency, and equilibrium equivalent radon concentration indoors, respectively [6,51].

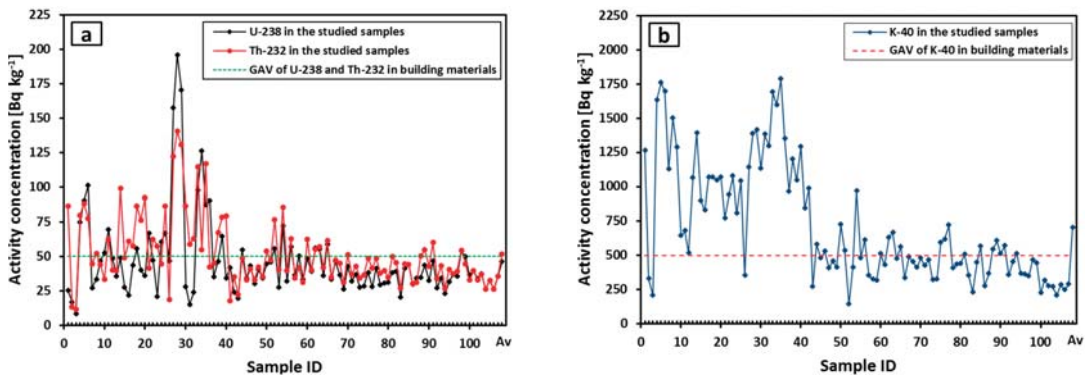
## 4. Results and Discussion

### 4.1. Radioisotope ( $^{238}\text{U}$ , $^{232}\text{Th}$ , and $^{40}\text{K}$ ) Concentrations

Table 2 displays the ranges and averages, as well as standard errors, for the estimated concentrations values of U-238 (Ra-226), Th-232, and K-40 in the granites and ceramic tiles collected. Furthermore and by way of illustration, Figure 1 depicts the variations of the abovementioned radioisotopes concentrations in the samples under examination. Evidently, Figure 1 and Table 2 show that the concentrations of the considered radioisotopes fluctuate from  $8.40 \pm 2.09$  in GBiH (sample No. 3) to  $196.01 \pm 37.84 \text{ Bq kg}^{-1}$  in GRSS (sample No. 28),  $11.62 \pm 1.28$  in GBiH (sample No. 3) to  $140.32 \pm 27.41 \text{ Bq kg}^{-1}$  in GRSS (sample No. 28), and  $141.01 \pm 12.83$  in CAR (sample No. 52) to  $1785.78 \pm 125.00 \text{ Bq kg}^{-1}$  in GRN (sample No. 35) for  $^{238}\text{U}$ ,  $^{232}\text{Th}$ , and  $^{40}\text{K}$ , respectively. Conceivably, the observed variations in radioisotopes' concentrations could be attributed to the samples' various origins and compositions. Evidently, most of the ceramic samples (samples No. 43 to 107) have lower concentrations of the three radioisotopes (U-238, Th-232, and K-40) than those of the granite samples (samples No. 1 to 42). This materializes the granite's naturally high level of terrestrial radioisotopes [3].

**Table 2.** Mean concentrations of  $^{238}\text{U}$  ( $^{226}\text{Ra}$ ),  $^{232}\text{Th}$ , and  $^{40}\text{K}$  (mean value  $\pm$  standard error) in the investigated samples of the considered granite and ceramic brands, compared to their global average values (AGVs) in building materials.

| Tiling Material                          | Brand ID | Sample Size | Activity Concentration [ $\text{Bq kg}^{-1}$ ] |                    |                  |                   |                    |                      |                    |
|------------------------------------------|----------|-------------|------------------------------------------------|--------------------|------------------|-------------------|--------------------|----------------------|--------------------|
|                                          |          |             | Ra-226                                         |                    | Th-232           |                   | K-40               |                      |                    |
|                                          |          |             | Range                                          | Mean $\pm$ SE      | Range            | Mean $\pm$ SE     | Range              | Mean $\pm$ SE        |                    |
| Granite                                  | GBiHa    | 3           | 8.40–25.37                                     | 16.95 $\pm$ 4.90   | 11.62–86.75      | 37.31 $\pm$ 24.73 | 207.21–1260.66     | 598.67 $\pm$ 332.83  |                    |
|                                          | GBrHu    | 3           | 75.12–101.20                                   | 88.90 $\pm$ 7.56   | 77.66–88.53      | 82.05 $\pm$ 3.31  | 1631.50–1760.39    | 1695.38 $\pm$ 37.21  |                    |
|                                          | GIR      | 3           | 27.20–47.05                                    | 35.93 $\pm$ 5.85   | 44.37–52.01      | 46.99 $\pm$ 2.51  | 1124.02–1500.22    | 1302.47 $\pm$ 109.03 |                    |
|                                          | GKG      | 3           | 48.81–69.49                                    | 56.98 $\pm$ 6.35   | 33.32–62.66      | 45.38 $\pm$ 8.86  | 516.76–678.58      | 612.54 $\pm$ 49.02   |                    |
|                                          | GNA      | 4           | 21.65–48.85                                    | 33.49 $\pm$ 5.88   | 39.69–99.06      | 62.28 $\pm$ 13.02 | 827.73–1391.41     | 1044.82 $\pm$ 125.30 |                    |
|                                          | GRAD     | 3           | 40.01–55.74                                    | 46.55 $\pm$ 4.73   | 57.57–86.32      | 73.44 $\pm$ 8.43  | 1045.65–1068.33    | 1060.42 $\pm$ 7.39   |                    |
|                                          | GRHL     | 3           | 35.98–67.08                                    | 50.06 $\pm$ 9.10   | 41.40–92.11      | 65.34 $\pm$ 14.71 | 771.84–1065.73     | 925.86 $\pm$ 85.13   |                    |
|                                          | GRAS     | 4           | 21.13–67.08                                    | 48.99 $\pm$ 10.19  | 18.67–86.71      | 51.89 $\pm$ 14.15 | 350.61–1073.63     | 817.88 $\pm$ 166.70  |                    |
|                                          | GRSS     | 3           | 157.24–196.01                                  | 174.55 $\pm$ 11.38 | 122.33–140.32    | 131.07 $\pm$ 5.20 | 1139.85–1411.17    | 1311.92 $\pm$ 86.37  |                    |
|                                          | GRA      | 3           | 15.31–28.13                                    | 22.46 $\pm$ 3.78   | 58.88–86.32      | 69.42 $\pm$ 8.54  | 1128.03–1380.24    | 1267.88 $\pm$ 74.09  |                    |
|                                          | GRN      | 4           | 87.24–126.01                                   | 100.37 $\pm$ 8.82  | 42.37–116.83     | 82.22 $\pm$ 19.52 | 1346.94–1785.78    | 1604.53 $\pm$ 94.24  |                    |
|                                          | GRF      | 3           | 35.03–64.76                                    | 48.78 $\pm$ 8.65   | 45.05–78.71      | 63.70 $\pm$ 9.89  | 962.71–1198.79     | 1067.69 $\pm$ 69.39  |                    |
|                                          | GYG      | 3           | 24.08–41.92                                    | 33.48 $\pm$ 5.17   | 17.74–79.20      | 44.09 $\pm$ 18.28 | 842.65–1291.41     | 1039.86 $\pm$ 132.37 |                    |
|                                          | Ceramic  | CAL         | 7                                              | 19.65–54.90        | 36.77 $\pm$ 4.18 | 22.25–49.10       | 36.59 $\pm$ 3.25   | 268.80–580.00        | 447.99 $\pm$ 37.90 |
|                                          |          | CAR         | 7                                              | 27.67–72.44        | 47.97 $\pm$ 5.83 | 39.71–85.67       | 58.16 $\pm$ 6.75   | 141.01–967.61        | 553.36 $\pm$ 97.53 |
|                                          |          | CCL         | 5                                              | 33.67–50.24        | 41.70 $\pm$ 3.32 | 31.00–62.56       | 41.93 $\pm$ 5.51   | 314.01–508.89        | 385.20 $\pm$ 36.68 |
|                                          |          | CGE         | 7                                              | 33.25–58.88        | 46.13 $\pm$ 4.10 | 34.57–61.48       | 48.98 $\pm$ 3.59   | 332.64–667.11        | 515.68 $\pm$ 43.22 |
| CGL                                      |          | 6           | 26.41–42.62                                    | 32.37 $\pm$ 2.60   | 31.18–51.31      | 38.88 $\pm$ 2.94  | 318.72–480.82      | 404.54 $\pm$ 28.08   |                    |
| CLA                                      |          | 6           | 28.05–41.58                                    | 33.26 $\pm$ 2.22   | 34.78–48.75      | 41.87 $\pm$ 2.34  | 407.88–719.45      | 535.22 $\pm$ 51.80   |                    |
| CPH                                      |          | 7           | 20.50–44.17                                    | 35.47 $\pm$ 3.06   | 27.04–49.82      | 38.96 $\pm$ 3.45  | 230.25–565.65      | 391.33 $\pm$ 45.91   |                    |
| CPR                                      |          | 7           | 23.11–46.87                                    | 34.64 $\pm$ 3.19   | 26.84–60.17      | 44.59 $\pm$ 4.38  | 354.45–606.42      | 506.75 $\pm$ 31.46   |                    |
| CRO                                      |          | 6           | 31.46–53.77                                    | 40.73 $\pm$ 3.64   | 32.94–54.47      | 41.58 $\pm$ 3.02  | 222.48–467.20      | 366.72 $\pm$ 35.20   |                    |
| CVE                                      |          | 7           | 26.40–39.61                                    | 33.09 $\pm$ 1.92   | 26.11–39.63      | 32.96 $\pm$ 1.94  | 206.35–317.18      | 269.36 $\pm$ 13.15   |                    |
| Total                                    | 107      | 8.40–196.01 | 46.17 $\pm$ 2.81                               | 11.62–140.32       | 51.65 $\pm$ 2.35 | 141.01–1785.78    | 701.62 $\pm$ 40.60 |                      |                    |
| GAV (Global Average Value) UNSCEAR [52]) |          |             | —                                              | 50                 | —                | 50                | —                  | 500                  |                    |



**Figure 1.** U-238, Th-232 and K-40 concentrations in the investigated granites and ceramic tiles samples.

Regarding the mean values of the radioisotope concentrations inserted in Table 2 and plotted in Figure 2, it is clear that CVE samples contain the lowest mean concentrations of both K-40 and Th-232, with levels of  $269.36 \pm 13.15$  and  $32.96 \pm 1.94$  Bq/kg, respectively, while GBiHa samples have the lowest mean concentration of U-238 with a level of  $16.95 \pm 4.90$  Bq/kg. In contrast, GRSS samples appear to have the highest mean concentrations of both U-238 and Th-232, with levels of  $174.55 \pm 11.38$  and  $131.07 \pm 5.20$  Bq/kg, respectively, whereas, GBrHu samples have the highest mean concentration of K-40, with a level of  $1695.38 \pm 37.21$  Bq/kg.

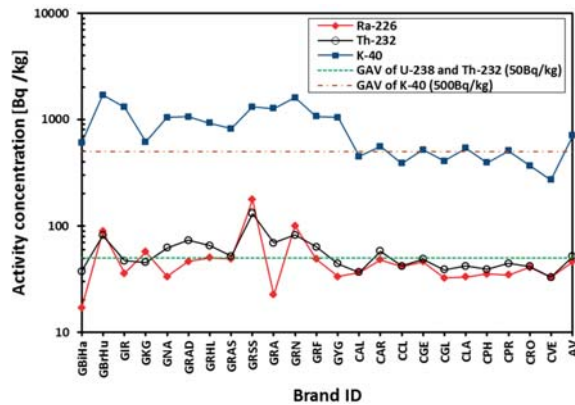


Figure 2. Comparison of the average values of U-238 (Ra-226), Th-232 and K-40 in the investigated ceramic and granites tiles to their corresponding GAVs in the building materials.

Figure 2 and Table 2 also display the mean values of the aforementioned radioisotope concentrations in the materials under investigation against their corresponding global average values (GAVs) in building materials as given by the UNSCEAR [52]. Notably, the GAVs for U-238, Th-232, and K-40 in building materials are 50, 50, and 500 Bq/kg, respectively, according to the UNSCEAR [52]. Apparently, the mean concentration of U-238 in all granites and ceramic tiles samples herein, except for GBrHu, GKG, GRHL, GRSS, and GRN samples, is lower than its GAV of 50 Bq/kg in building materials [52], (Figure 2 and Table 2). Similarly, the average concentration of Th-232 in the investigated samples, except for the GBrHu, GNA, GRAD, GRHL, GRAS, GRSS, GRA, GRN, GRF, and CAR samples, is lower than its GAV in building materials of 50 Bq/kg [52]. However, the average concentration of K-40 for all of the granite and ceramic brands, except for the CAL, CCL, CGL, CPH, CRO, and CVE samples, is greater than the GAV (500 Bq/kg) of building materials [52], (Figure 2 and Table 2).

The overall average concentrations for U-238, Th-232, and K-40 of the total samples were observed to be  $46.17 \pm 2.81$  (less than its GAV),  $51.65 \pm 2.35$  (slightly above its GAV), and  $701.62 \pm 40.60$  Bq/kg (1.4 times greater than the GAV), respectively, as demonstrated in Table 2 and Figure 2. Moreover, in all of the investigated brands' samples (Figure 2), the K-40 concentration is the greatest among the concentrations of the three studied radionuclides, as the granites contain about 33% potash feldspar minerals [21]. Moreover, it was found that the K-40 concentration is the largest contributor to the total concentration for all samples (Figure 3). Both U-238 and Th-232 contribute roughly the same percentage (6%), to the overall concentration of samples, while K-40 contributes a larger percentage (88%), as shown in Figure 3.

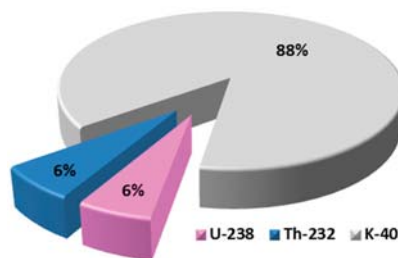
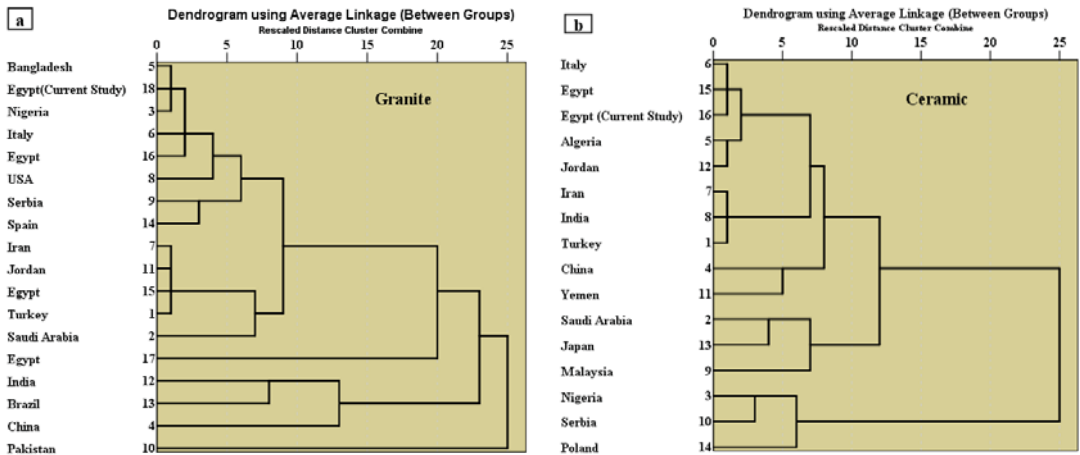


Figure 3. Contributions of the three radioisotopes, <sup>238</sup>U, <sup>232</sup>Th, and <sup>40</sup>K, to the studied samples' overall concentration.

A comparison between the radioactivity levels in the studied samples and those in other previous relevant studies on granites and ceramics used in Egypt and other countries is illustrated in Table 3. From Table 3, one can deduce that many of the data from the relevant literature are comparable to our findings. This can be confirmed using the dendrogram (Figure 4) derived from the hierarchical cluster analysis (HCA) based on the three variables (U-238, Th-232, and K-40 concentrations). In HCA, the cluster method between-groups linkage is used coupled with the square Euclidean distance. Accordingly, the countries in which the studies were accomplished have been divided into homogeneous groups based on the similarity in concentrations of the three radionuclides (U-238, Th-232, and K-40) (Figure 4). Figure 4a shows that the Egyptian granite tiles studied herein come close to the granites used in Bangladesh [22] and Nigeria [2] in terms of the content of the three aforementioned radionuclides, as they were grouped into a homogeneous group. However, they are far from those used in Pakistan [25], as illustrated in Figure 4a. Likewise, Figure 4b exhibits that the ceramic tiles examined herein are matched to the ceramics used in Italy [23] and Egypt [30] but are very different to those used in Poland [37], Serbia [9], and Nigeria [2] in terms of radionuclide content.

**Table 3.** The radioisotopes concentrations (present study) in comparison to other similar previous international research.

| Tiling Materials | Countries' Names | Concentrations [Bq/kg] |        |         | References    |
|------------------|------------------|------------------------|--------|---------|---------------|
|                  |                  | U-238                  | Th-232 | K-40    |               |
| Granite          | Turkey           | 45.40                  | 82.30  | 931.60  | [1]           |
|                  | Saudi Arabia     | 54.50                  | 43.40  | 677.70  | [21]          |
|                  | Nigeria          | 74                     | 100    | 1098    | [2]           |
|                  | China            | 355.9                  | 317.9  | 1636.5  | [19]          |
|                  | Bangladesh       | 49.51                  | 75.50  | 1122.15 | [22]          |
|                  | Italy            | 81.33                  | 129    | 1065    | [23]          |
|                  | Iran             | 38                     | 47     | 917     | [18]          |
|                  | USA              | 31                     | 61     | 1210    | [24]          |
|                  | Serbia           | 200                    | 77     | 1280    | [9]           |
|                  | Pakistan         | 659                    | 598    | 1218    | [25]          |
|                  | Jordan           | 41.52                  | 58.42  | 897     | [26]          |
|                  | India            | 82                     | 112    | 1908    | [27]          |
|                  | Brazil           | 31                     | 73     | 1648    | [28]          |
|                  | Spain            | 101                    | 48     | 1293    | [29]          |
|                  | Egypt            | 65                     | 60     | 885     | [30]          |
|                  | Egypt            | 137                    | 82     | 1082    | [31]          |
|                  | Egypt            | 15.25                  | 15.35  | 399.39  | [38]          |
| Ceramic          | Egypt            | 58.46                  | 65.76  | 1107.55 | Current study |
|                  | Turkey           | 43.5                   | 37.9   | 310.9   | [1]           |
|                  | Saudi Arabia     | 47.18                  | 80.70  | 590.2   | [21]          |
|                  | Nigeria          | 85                     | 77     | 877     | [2]           |
|                  | China            | 172.35                 | 135.5  | 351.4   | [19]          |
|                  | Algeria          | 55                     | 41     | 410     | [32]          |
|                  | Italy            | 52                     | 42.5   | 450     | [23]          |
|                  | Iran             | 32                     | 27     | 292     | [18]          |
|                  | India            | 17.52                  | 38.93  | 298.59  | [33]          |
|                  | Malaysia         | 92                     | 68     | 673     | [34]          |
|                  | Serbia           | 67                     | 61     | 828     | [9]           |
|                  | Yemen            | 131.88                 | 83.55  | 400.7   | [35]          |
|                  | Jordan           | 33.86                  | 28.82  | 411     | [26]          |
|                  | Japan            | 82.7                   | 63.9   | 527     | [36]          |
|                  | Poland           | 50                     | 50     | 963     | [37]          |
|                  | Egypt            | 52                     | 33     | 450     | [30]          |
|                  | Egypt            | 38.23                  | 42.54  | 439.33  | Current study |



**Figure 4.** The dendrogram for comparing the Egyptian granites and ceramic tiles investigated herein with those used in Egypt and other countries in terms of the natural radioactivity.

Evidently, in many of the investigated granite and ceramic samples, the radioisotopes' displayed concentrations were more elevated than the GAVs (Figure 2). For instance, in granites of “Rosa Sardo Sinai” (GRSS) samples, concentrations of uranium, thorium, and potassium exceed their corresponding GAVs by about three times, confirming the previous study on the granite of the Sinai area by Fares [39]. Therefore, it was crucial to assess the likely radiological risks to peoples' health owing to the use of these materials in buildings.

#### 4.2. Gamma Radiation Impact Estimation

Table 4 displays some of the evaluated radiological variables for the granite and ceramic samples under consideration. Through the estimated  $R_{eq}$ ,  $I_\gamma$ ,  $D_{in}$ ,  $E_{in}$ , and ELCR (Table 4), the gamma ray hazards posed by the materials under investigation when used as tiling in buildings can be judged. It was found that all  $R_{eq}$  values in the samples of ceramic tiles fell within ranges below the threshold standard of 370 Bq/kg [44]. Similarly, the  $R_{eq}$  values for all the samples of the investigated granite tiles were in ranges lower than the criterion limitation of 370 Bq/kg, with the exception of three samples (No. 27 to 29) of GRSS and two samples (No. 33 and 35) from GRN samples. Furthermore, the mean  $R_{eq}$  values varied between 100.96 Bq/kg in the CVE samples and 463 Bq/kg in the GRSS samples, with an overall mean of 174.06 Bq/kg. Accordingly, the granites and ceramic tiles of the different brands herein don't constitute any considerable radiological risks for individuals when used as tiling materials, except for the GRSS samples which may be a cause for concern due to the mean value of  $R_{eq}$  going beyond 370 Bq/kg (recommended value) (Figure 5a).

**Table 4.** Ranges and mean values of the radiological parameters showing the gamma impact of the studied granite and ceramic brands.

| Tiling Material        | Brand ID | Sample Size     | Parameters Showing Gamma Impact |                |                                    |                                     |                      |
|------------------------|----------|-----------------|---------------------------------|----------------|------------------------------------|-------------------------------------|----------------------|
|                        |          |                 | Ra <sub>eq</sub> [Bq/kg]        | I <sub>γ</sub> | D <sub>in</sub> [nGy/h]            | E <sub>in</sub> [mSv/y]             | ELCR/10 <sup>3</sup> |
| Granite                | GBiHa    | 3               | (40.97–246.48)                  | (0.16–0.94)    | (4.62–27.29)                       | (0.02–0.13)                         | (0.07–0.44)          |
|                        |          |                 | 116.39                          | 0.44           | 13.00                              | 0.06                                | 0.21                 |
|                        | GBrHu    | 3               | (315.09–352.52)                 | (1.19–1.33)    | (35.87–40.14)                      | (0.18–0.20)                         | (0.58–0.65)          |
|                        |          |                 | 336.77                          | 1.27           | 38.43                              | 0.19                                | 0.62                 |
|                        | GIR      | 3               | (177.53–223.44)                 | (0.69–0.87)    | (20.30–25.71)                      | (0.10–0.13)                         | (0.33–0.42)          |
|                        |          |                 | 203.42                          | 0.79           | 23.39                              | 0.11                                | 0.38                 |
|                        | GKG      | 3               | (146.02–211.34)                 | (0.54–0.77)    | (16.44–23.63)                      | (0.08–0.12)                         | (0.27–0.38)          |
|                        |          |                 | 169.04                          | 0.62           | 19.07                              | 0.09                                | 0.31                 |
|                        | GNA      | 4               | (167.45–297.64)                 | (0.64–1.12)    | (18.86–33.09)                      | (0.09–0.16)                         | (0.31–0.54)          |
|                        |          |                 | 202.99                          | 0.77           | 22.77                              | 0.11                                | 0.37                 |
|                        | GRAD     | 3               | (208.47–261.36)                 | (0.79–0.97)    | (23.58–29.02)                      | (0.12–0.14)                         | (0.38–0.47)          |
|                        |          |                 | 233.22                          | 0.88           | 26.05                              | 0.13                                | 0.42                 |
|                        | GRHL     | 3               | (185.71–249.75)                 | (0.69–0.94)    | (21.25–27.44)                      | (0.10–0.12)                         | (0.34–0.44)          |
|                        |          |                 | 214.78                          | 0.80           | 24.04                              | 0.12                                | 0.39                 |
|                        | GRAS     | 4               | (100.68–271.20)                 | (0.37–1.00)    | (11.62–30.18)                      | (0.06–0.15)                         | (0.19–0.49)          |
|                        |          |                 | 186.17                          | 0.70           | 20.99                              | 0.10                                | 0.34                 |
|                        | GRSS     | 3               | (419.94–503.29)                 | (1.52–1.82)    | (46.94–56.46)                      | (0.23–0.28)                         | (0.76–0.91)          |
|                        |          |                 | 463.00                          | 1.67           | 51.89                              | 0.25                                | 0.84                 |
|                        | GRA      | 3               | (205.78–238.43)                 | (0.81–0.90)    | (23.33–26.29)                      | (0.11–0.13)                         | (0.38–0.43)          |
|                        |          |                 | 219.35                          | 0.84           | 24.59                              | 0.12                                | 0.40                 |
| GRN                    | 4        | (254.79–391.81) | (0.96–1.47)                     | (29.72–44.00)  | (0.15–0.22)                        | (0.48–0.71)                         |                      |
|                        |          | 341.48          | 1.28                            | 38.96          | 0.19                               | 0.63                                |                      |
| GRF                    | 3        | (173.58–257.52) | (0.66–0.96)                     | (19.75–28.79)  | (0.10–0.14)                        | (0.32–0.47)                         |                      |
|                        |          | 222.08          | 0.84                            | 25.02          | 0.12                               | 0.41                                |                      |
| GYG                    | 3        | (132.17–247.14) | (0.51–0.94)                     | (15.60–27.62)  | (0.08–0.14)                        | (0.25–0.45)                         |                      |
|                        |          | 176.59          | 0.68                            | 20.17          | 0.10                               | 0.33                                |                      |
| Ceramic                | CAL      | 7               | (72.17–169.77)                  | (0.27–0.62)    | (8.05–19.03)                       | (0.04–0.09)                         | (0.13–0.31)          |
|                        |          |                 | 123.58                          | 0.45           | 13.83                              | 0.07                                | 0.22                 |
|                        | CAR      | 7               | (117.76–269.45)                 | (0.43–0.99)    | (12.99–29.98)                      | (0.06–0.15)                         | (0.21–0.49)          |
|                        |          |                 | 173.75                          | 0.64           | 19.21                              | 0.09                                | 0.31                 |
|                        | CCL      | 5               | (102.18–177.47)                 | (0.37–0.65)    | (11.39–19.50)                      | (0.06–0.1)                          | (0.18–0.32)          |
|                        |          |                 | 131.31                          | 0.48           | 14.57                              | 0.07                                | 0.24                 |
|                        | CGE      | 7               | (108.30–190.11)                 | (0.39–0.69)    | (12.02–21.07)                      | (0.06–0.1)                          | (0.19–0.34)          |
|                        |          |                 | 155.88                          | 0.57           | 17.34                              | 0.09                                | 0.28                 |
|                        | CGL      | 6               | (101.24–153.02)                 | (0.37–0.56)    | (11.18–16.91)                      | (0.05–0.08)                         | (0.18–0.27)          |
|                        |          |                 | 119.11                          | 0.44           | 13.21                              | 0.06                                | 0.21                 |
|                        | CLA      | 6               | (114.95–166.65)                 | (0.42–0.62)    | (12.76–18.72)                      | (0.06–0.09)                         | (0.21–0.30)          |
|                        |          |                 | 134.34                          | 0.50           | 14.99                              | 0.07                                | 0.24                 |
|                        | CPH      | 7               | (76.90–151.06)                  | (0.28–0.56)    | (8.46–16.93)                       | (0.04–0.08)                         | (0.14–0.27)          |
|                        |          |                 | 121.31                          | 0.44           | 13.47                              | 0.07                                | 0.22                 |
|                        | CPR      | 7               | (100.94–176.82)                 | (0.38–0.65)    | (11.41–19.52)                      | (0.06–0.10)                         | (0.18–0.32)          |
|                        |          |                 | 137.43                          | 0.51           | 15.27                              | 0.07                                | 0.25                 |
|                        | CRO      | 6               | (100.61–167.64)                 | (0.36–0.61)    | (11.11–18.56)                      | (0.05–0.09)                         | (0.18–0.30)          |
|                        |          |                 | 128.42                          | 0.47           | 14.23                              | 0.07                                | 0.23                 |
|                        | CVE      | 7               | (80.21–120.70)                  | (0.29–0.44)    | (8.86–13.35)                       | (0.04–0.07)                         | (0.14–0.22)          |
|                        |          |                 | 100.96                          | 0.36           | 11.17                              | 0.05                                | 0.18                 |
| Total                  | 107      | (40.97–503.29)  | (0.16–1.82)                     | (4.62–56.46)   | (0.02–0.28)                        | (0.07–0.91)                         |                      |
|                        |          | 174.06          | 0.65                            | 19.51          | 0.10                               | 0.32                                |                      |
| Allowable Value or GAV |          |                 | 370 <sup>a</sup>                | 2 <sup>b</sup> | 84 <sup>a</sup> or 70 <sup>b</sup> | 0.41 <sup>a</sup> or 1 <sup>b</sup> | 1.16 <sup>c</sup>    |

<sup>a</sup> GAV given by the UNSCEAR [3], <sup>b</sup> GAV reported by the European Commission [46], <sup>c</sup> GAV indicated by Sidique et al. [41] and Qureshi et al. [53].



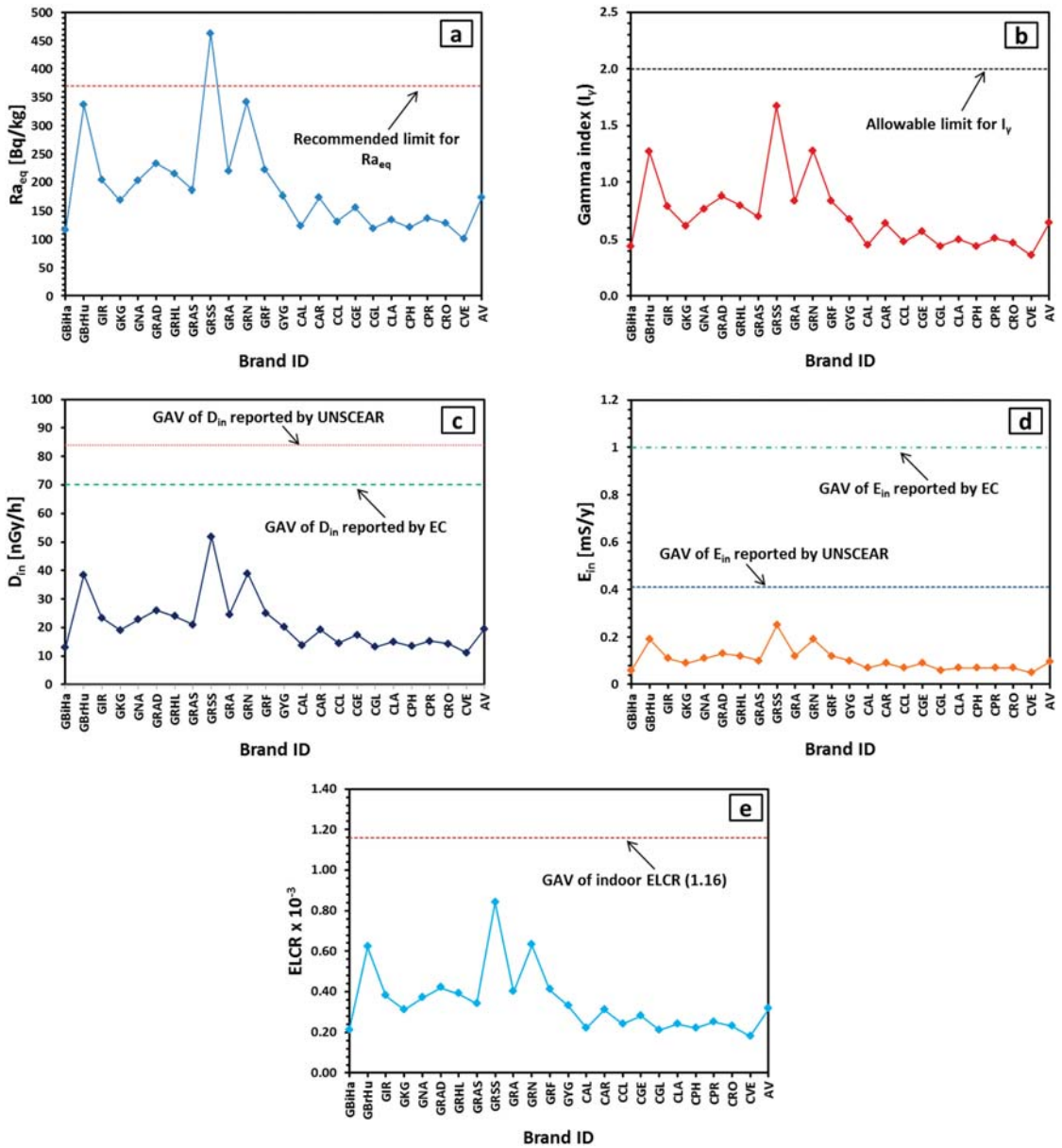


Figure 5. The radiological parameters showing the gamma impact from the ceramic and granite tiles of the brands under investigation.

According to the calculated values of  $I_\gamma$  (Table 4), none of the values in the samples under investigation go beyond the exemption limit of 2. This implies that the yearly effective gamma dose resulting from the investigated materials herein when used as covering or superficial building materials indoors is less than 0.3 mSv/y (exemption limit indicated by the European Commission [46]). Thus, the granites and ceramic tiles of the brands under investigation are suitable for use without any restrictions. Furthermore, and

by way of illustration, Figure 5b displays the estimated mean values of  $I_\gamma$  for the granites and ceramic tiles where they do not go beyond their allowable limit, indicating that all of the investigated materials do not raise any cause for concern when used in buildings.

Considering the estimated  $D_{in}$  and  $E_{in}$  values for the samples under investigation (Table 4), neither the granites nor the ceramic samples of the various brands examined herein had  $D_{in}$  and  $E_{in}$  values going beyond their corresponding worldwide average values of 84 nGy/h and 0.41 mSv/y [3] and of 70 nGy/h and 1 mSv/y [46]. Notably, the mean values of  $D_{in}$  and  $E_{in}$  for the studied granites and ceramic tiles compared with the corresponding global average values (GAVs) are illustrated in Figs. 5c and 5d, where they are below the adopted limits, reflecting their safe use.

The indoor ELCR values based on  $E_{in}$ , as well as their mean values in the granites and ceramics under investigation, are shown in Table 4 and plotted in Figure 5e. Evidently, all the ELCR values are within the range of 0.07 to 0.91, with an overall mean of 0.32. Namely, the mean ELCR values in all the brands of tiling materials are less than their corresponding GAV of 1.16 indicated by Sidique et al. [41] and Qureshi et al. [53], as shown in Figure 5e. Thus, in buildings where the materials under investigation are used, over a 66-year lifespan, their residents are at a very insignificant risk of developing cancer resulting from exposure to gamma rays emitted by these materials.

#### 4.3. Radon Impact Assessment

The potential radon (Rn-222) risks posed by the studied materials when used as tiles in buildings can be investigated through the estimated  $I_\alpha$ , RX,  $C_{Rn}$ , and  $E_{Rn}$ . For the samples of each brand, Table 5 displays ranges and averages of  $I_\alpha$ , RX,  $C_{Rn}$ , and  $E_{Rn}$  values, while Figure 6 compares averages of these parameters with their corresponding allowable limits. Table 5 reveals that the  $I_\alpha$  values oscillate between 0.04 and 0.98, with an overall mean value of 0.23. Furthermore, no mean value of  $I_\alpha$  for any of the brands' samples under investigation goes beyond the unity, as shown in Figure 6a. Thus, arguably, the materials under consideration come under the range of the indoor radon safe exposure action level for buildings, as indicated by the European Commission [46] and ICRP [49].

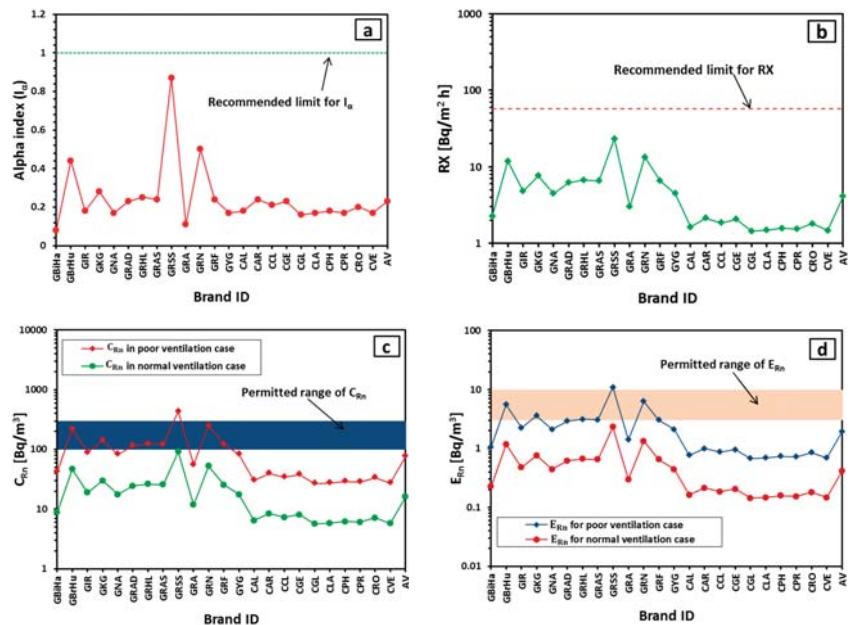


Figure 6. The radiological parameters showing the Rn impact from the studied ceramic and granite tiles.

**Table 5.** Ranges and mean values of the radiological parameters showing the Rn impact of the studied granite and ceramic brands.

| Tiling Material        | Brand ID | Sample Size | $I_{\alpha}$   | RX<br>[Bq/m <sup>2</sup> h] | Poor Ventilation Case         |                     | Normal Ventilation Case       |                     |
|------------------------|----------|-------------|----------------|-----------------------------|-------------------------------|---------------------|-------------------------------|---------------------|
|                        |          |             |                |                             | $C_{Rn}$ [Bq/m <sup>3</sup> ] | $E_{Rn}$ [mSv/y]    | $C_{Rn}$ [Bq/m <sup>3</sup> ] | $E_{Rn}$ [mSv/y]    |
| Granite                | GBiHa    | 3           | (0.04–0.13)    | (1.12–3.38)                 | (20.81–62.88)                 | (0.53–1.59)         | (4.41–13.33)                  | (0.11–0.34)         |
|                        |          |             | 0.08           | 2.26                        | 42.01                         | 1.06                | 8.91                          | 0.22                |
|                        | GBrHu    | 3           | (0.38–0.51)    | (10.02–13.50)               | (186.24–250.89)               | (4.70–6.33)         | (39.48–53.18)                 | (1.00–1.34)         |
|                        |          |             | 0.44           | 11.86                       | 220.39                        | 5.56                | 46.72                         | 1.18                |
|                        | GIR      | 3           | (0.14–0.24)    | (3.63–6.28)                 | (67.43–116.65)                | (1.70–2.94)         | (14.29–24.73)                 | (0.36–0.62)         |
|                        |          |             | 0.18           | 4.79                        | 89.09                         | 2.25                | 18.88                         | 0.48                |
|                        | GKG      | 3           | (0.24–0.35)    | (6.51–9.27)                 | (121.01–172.28)               | (3.05–4.35)         | (25.65–36.52)                 | (0.65–0.92)         |
|                        |          |             | 0.28           | 7.60                        | 141.27                        | 3.57                | 29.95                         | 0.76                |
|                        | GNA      | 4           | (0.11–0.24)    | (2.89–6.52)                 | (53.67–121.11)                | (1.36–3.06)         | (11.38–25.67)                 | (0.29–0.65)         |
|                        |          |             | 0.17           | 4.47                        | 83.02                         | 2.10                | 17.60                         | 0.44                |
|                        | GRAD     | 3           | (0.20–0.28)    | (5.34–7.43)                 | (99.19–138.19)                | (2.50–3.49)         | (21.03–29.29)                 | (0.53–0.74)         |
|                        |          |             | 0.23           | 6.21                        | 115.39                        | 2.91                | 24.46                         | 0.62                |
|                        | GRHL     | 3           | (0.18–0.34)    | (4.80–8.95)                 | (89.20–166.29)                | (2.25–4.20)         | (18.91–35.25)                 | (0.48–0.89)         |
|                        |          |             | 0.25           | 6.68                        | 124.10                        | 3.13                | 26.31                         | 0.66                |
|                        | GRAS     | 4           | (0.11–0.34)    | (2.82–8.95)                 | (52.38–166.29)                | (1.32–4.20)         | (11.10–35.25)                 | (0.28–0.89)         |
|                        |          |             | 0.24           | 6.53                        | 121.45                        | 3.07                | 25.75                         | 0.65                |
|                        | GRSS     | 3           | (0.79–0.98)    | (20.97–26.14)               | (389.83–485.94)               | (9.84–12.27)        | (82.63–103.01)                | (2.09–2.60)         |
|                        |          |             | 0.87           | 23.28                       | 432.75                        | 10.93               | 91.73                         | 2.32                |
|                        | GRA      | 3           | (0.08–0.14)    | (2.04–3.75)                 | (37.94–69.74)                 | (0.96–1.76)         | (8.04–14.78)                  | (0.20–0.37)         |
|                        |          |             | 0.11           | 3.00                        | 55.67                         | 1.41                | 11.80                         | 0.30                |
| GRN                    | 4        | (0.44–0.63) | (11.64–16.81)  | (216.28–312.40)             | (5.46–7.89)                   | (45.85–66.22)       | (1.16–1.67)                   |                     |
|                        |          | 0.50        | 13.39          | 248.83                      | 6.28                          | 52.75               | 1.34                          |                     |
| GRF                    | 3        | (0.18–0.32) | (4.67–8.64)    | (86.85–160.55)              | (2.19–4.05)                   | (18.41–34.03)       | (0.46–0.86)                   |                     |
|                        |          | 0.24        | 6.51           | 120.93                      | 3.05                          | 25.63               | 0.65                          |                     |
| GYG                    | 3        | (0.12–0.21) | (3.21–5.59)    | (59.69–103.91)              | (1.51–2.62)                   | (12.65–22.03)       | (0.32–0.56)                   |                     |
|                        |          | 0.17        | 4.47           | 83.00                       | 2.10                          | 17.59               | 0.44                          |                     |
| Ceramic                | CAL      | 7           | (0.10–0.27)    | (0.87–2.44)                 | (16.24–45.37)                 | (0.41–1.15)         | (3.44–9.62)                   | (0.09–0.24)         |
|                        |          |             | 0.18           | 1.63                        | 30.38                         | 0.77                | 6.44                          | 0.16                |
|                        | CAR      | 7           | (0.14–0.36)    | (1.23–3.22)                 | (22.87–59.86)                 | (0.58–1.51)         | (4.85–12.69)                  | (0.12–0.32)         |
|                        |          |             | 0.24           | 2.13                        | 39.64                         | 1.00                | 8.40                          | 0.21                |
|                        | CCL      | 5           | (0.17–0.25)    | (1.50–2.23)                 | (27.82–41.52)                 | (0.70–1.05)         | (5.90–8.80)                   | (0.15–0.22)         |
|                        |          |             | 0.21           | 1.85                        | 34.46                         | 0.87                | 7.30                          | 0.18                |
|                        | CGE      | 7           | (0.17–0.29)    | (1.48–2.62)                 | (27.48–48.66)                 | (0.69–1.23)         | (5.82–10.31)                  | (0.15–0.26)         |
|                        |          |             | 0.23           | 2.05                        | 38.12                         | 0.96                | 8.08                          | 0.20                |
|                        | CGL      | 6           | (0.13–0.21)    | (1.17–1.89)                 | (21.83–35.22)                 | (0.55–0.89)         | (4.63–7.47)                   | (0.12–0.19)         |
|                        |          |             | 0.16           | 1.44                        | 26.75                         | 0.68                | 5.67                          | 0.14                |
|                        | CLA      | 6           | (0.14–0.21)    | (1.25–1.85)                 | (23.18–34.36)                 | (0.59–0.87)         | (4.91–7.28)                   | (0.12–0.18)         |
|                        |          |             | 0.17           | 1.48                        | 27.48                         | 0.69                | 5.83                          | 0.15                |
|                        | CPH      | 7           | (0.10–0.22)    | (0.91–1.96)                 | (16.94–36.50)                 | (0.43–0.92)         | (3.59–7.74)                   | (0.09–0.20)         |
|                        |          |             | 0.18           | 1.58                        | 29.31                         | 0.74                | 6.21                          | 0.16                |
|                        | CPR      | 7           | (0.12–0.23)    | (1.03–2.08)                 | (19.10–38.73)                 | (0.48–0.98)         | (4.05–8.21)                   | (0.10–0.21)         |
|                        |          |             | 0.17           | 1.54                        | 28.63                         | 0.72                | 6.07                          | 0.15                |
|                        | CRO      | 6           | (0.16–0.27)    | (1.4–2.39)                  | (26.00–44.44)                 | (0.66–1.12)         | (5.51–9.42)                   | (0.14–0.24)         |
|                        |          |             | 0.20           | 1.81                        | 33.66                         | 0.85                | 7.13                          | 0.18                |
|                        | CVE      | 7           | (0.13–0.20)    | (1.17–1.76)                 | (21.82–32.73)                 | (0.55–0.83)         | (4.62–6.94)                   | (0.12–0.18)         |
|                        |          |             | 0.17           | 1.47                        | 27.35                         | 0.69                | 5.80                          | 0.15                |
| Total                  | 107      | (0.04–0.98) | (0.87–26.14)   | (16.24–485.94)              | (0.41–12.27)                  | (3.44–103.01)       | (0.09–2.60)                   |                     |
|                        |          | 0.23        | 4.09           | 76.08                       | 1.92                          | 16.13               | 0.41                          |                     |
| Allowable Value or GAV |          |             | 1 <sup>a</sup> | 57.6 <sup>b</sup>           | (100–300) <sup>c</sup>        | (3–10) <sup>a</sup> | (100–300) <sup>c</sup>        | (3–10) <sup>a</sup> |

<sup>a</sup> GAV reported by the ICRP [49]. <sup>b</sup> GAV declared by the UNSCEAR [3]. <sup>c</sup> GAV recommended by the WHO (World Health Organization) [8].

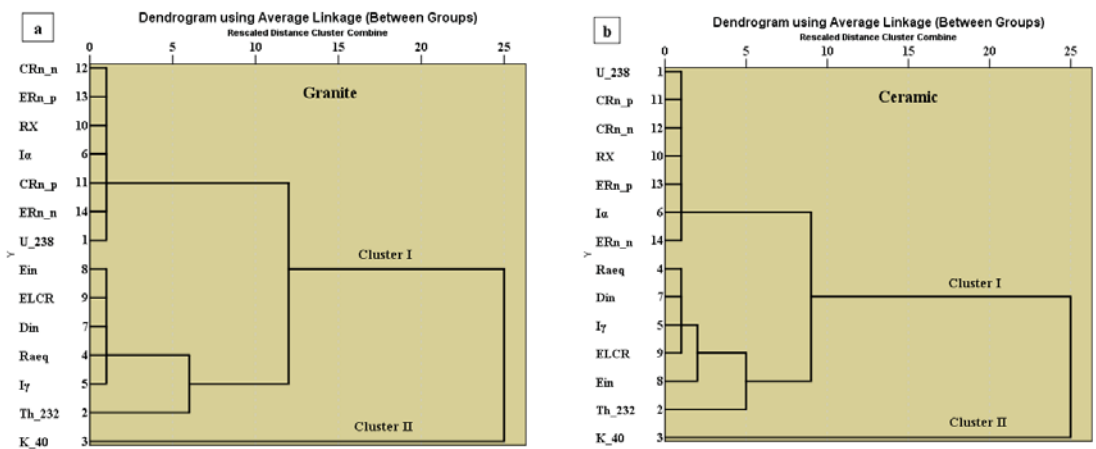
Regarding the mean values of the radon exhalation rate (RX) for the samples under investigation (Table 5 and Figure 6b), they stretch between 1.44 Bq/m<sup>2</sup> h in the CGL samples and 23.28 Bq/m<sup>2</sup> h in the GRSS samples, with an overall mean value of 4.09 Bq/m<sup>2</sup> h.

Moreover, no mean value of RX for samples of any brand of ceramic or granite exceeds the global average value (GAV) of  $57.6 \text{ Bq/m}^2 \text{ h}$  ( $0.016 \text{ Bq/m}^2 \text{ s}$ ) as declared by the UNSCEAR [3], as shown in Figure 6b. It is therefore expected that the materials under investigation do not constitute any health risks to dwellers.

Based on the RX values, the indoor radon concentration ( $C_{Rn}$ ) was assessed from the indirect mathematical model of a typical residence room tiled by the studied ceramics and granites in both poor and normal ventilation cases as per Equation (9). Accordingly, for the room model with normal ventilation, the mean values of  $C_{Rn}$  of granites and ceramics from the different brands under investigation fluctuate between  $5.67 \text{ Bq/m}^3$  in the CGL samples to  $91.73 \text{ Bq/m}^3$  in the GRSS samples, with an overall mean value of  $16.13 \text{ Bq/m}^3$  (Table 5 and Figure 6c). Consequently, for the normal ventilation case, none of the mean values of  $C_{Rn}$  in the studied brands of granites and ceramic tiles, as shown in Figure 6c, go beyond the acceptable range ( $100\text{--}300 \text{ Bq/m}^3$ ) declared by the WHO (World Health Organization) [8]. On the other hand, for the room model with poor ventilation, the mean values of the  $C_{Rn}$  of granites and ceramics from the brands under examination oscillate between  $26.75 \text{ Bq/m}^3$  in the CGL samples and  $432.75 \text{ Bq/m}^3$  in the GRSS samples, with an overall mean value of  $76.08 \text{ Bq/m}^3$  (Table 5 and Figure 6c). Thus, for the poor ventilation case, none of the mean values of  $C_{Rn}$  in the studied brands of ceramics and granites, as shown in Figure 6c, exceed the acceptable range ( $100\text{--}300 \text{ Bq/m}^3$ ) declared by the WHO [8], except for GRSS which as a result is not recommended for poorly ventilated buildings.

Regarding the yearly effective dose rate ( $E_{Rn}$ ) due to radon concentration (Table 5 and Figure 6d), the mean values span a range from  $0.14 \text{ mSv/y}$  in the CGL samples to  $2.32 \text{ mSv/y}$  in the GRSS samples, with an overall mean value of  $0.41 \text{ mSv/y}$  in the case of normal ventilation. Moreover, all of these values fluctuated below the acceptable range of  $3\text{--}10 \text{ mSv/y}$  documented by ICRP [49], (Figure 6d). On the other hand, for the poor ventilation case, the mean values of  $E_{Rn}$  for the granites and ceramics from the different brands under investigation stretch between  $0.68 \text{ mSv/y}$  in the CGL samples to  $10.93 \text{ mSv/y}$  in the GRSS samples, with an overall mean value of  $1.92 \text{ mSv/y}$ . Furthermore, as shown in Figure 6d for poor ventilation, the granite from the brand GRSS is the only one that has a mean value of  $C_{Rn}$  going beyond the recommended range of  $3\text{--}10 \text{ mSv/y}$  [49]. Therefore, it is not recommended for poorly ventilated rooms.

The hierarchical cluster analysis (HCA) coupled with the Pearson correlation method was performed to effectively prove the relationship among all considered radiological variables. The dendrogram obtained from the HCA shows the relationship between the radionuclide concentrations and the relevant radiological parameters (Figure 7). Depending on the similarities in existence, all considered variables are gathered into two principal clusters. Cluster I comprised U-238 and Th-232 concentrations as well as all radiological parameters with a highly similar correlation (Figure 7). This reflects that the slight radioactivity level arising in both of the examined granites or ceramic tiles is ascribable to U-238 and Th-232 concentrations. On the other hand, cluster II is only comprised K-40, reflecting the weak relationship of K-40 with the radiological parameters, i.e., despite the high concentration of K-40 in the examined granites and ceramic tiles, K-40 contributes very little to the radioactivity level.



**Figure 7.** The dendrogram for exhibiting the relationship among the studied radiological variables of the granites and ceramic tiles under consideration.

## 5. Conclusions

A radiological evaluation for 23 well-known brands of Egyptian commercial granites and ceramic tile samples was performed for hazard and dose estimations. A total of 107 samples representative of the materials under investigation were analyzed using a HPGe detector. The terrestrial radionuclides (U-238 (Ra-226), Th-232, and K-40) concentrations in the investigated samples together with their radiological indices ( $R_{eq}$ ,  $I_\gamma$ ,  $D_{in}$ ,  $E_{in}$ , ELCR,  $I_\alpha$ ,  $C_{Rn}$ ,  $E_{Rn}$ ) were determined. It was found that the concentrations of the aforementioned radioisotopes were higher in most of the granite samples than in the ceramic samples. Furthermore, the concentration values of the terrestrial radionuclides indicated significant differences in the granite and ceramic tile samples collected from the different brands. This is significant in differentiating between the considered brands. K-40 concentration was found to be the biggest contributor to the total concentration for all samples, followed by Th-232 and U-238. Generally, the terrestrial radioisotope concentrations in the materials under investigation are comparable to many of those from the relevant literature and come within the worldwide range. Although the average concentration values for K-40 and Th-232 were higher than their GAVs, the obtained results for the majority of the radiological parameters showed that the studied granites and ceramic tiles are safe to use indoors except “Rosa Sardo Sinai” granite (GRSS). The GRSS samples go beyond the recommended values in terms of their high radium equivalent ( $R_{eq}$ ) mean values, and indoor radon concentration ( $C_{Rn}$ ), as well as their associated yearly effective dose rate ( $E_{Rn}$ ) in poorly ventilated buildings, which may be a cause for concern. Therefore, it is not recommended for poorly ventilated buildings. In line with the HCA conducted herein, it reflects the weak relationship of K-40 with all different radiological parameters without exception. In other words, the insignificant risk levels originating from the use of the concerned granites and ceramic tiles are principally due to Th-232 and U-238, with only a weak contribution of K-40.

Our data herein are important for two reasons: firstly, they may raise awareness among the general population of the natural radioactivity of the materials under investigation, and secondly, they are required for developing the standards, rules, and management of tiling materials used in Egypt and in any other country to which such materials are exported.

**Author Contributions:** All the authors contributed to the conception of the study, study design, methodology, data analysis, validation, writing of the original draft, revision of the manuscript, and final publication. All authors have read and agreed to the published version of the manuscript.

**Funding:** This research received no external funding.

**Institutional Review Board Statement:** Not applicable.

**Informed Consent Statement:** Not applicable.

**Data Availability Statement:** Not applicable.

**Acknowledgments:** The authors sincerely thank Mervat A. Elhaddad, Department of Geology, Faculty of Science, Assiut University, Egypt, for her support during the editing and revision of this research article.

**Conflicts of Interest:** The authors declare that they have no competing interest.

## References

1. Turhan, Ş.; Kurnaz, A.; Karataşlı, M. Evaluation of natural radioactivity levels and potential radiological hazards of common building materials utilized in Mediterranean region, Turkey. *Environ. Sci. Pollut. Res.* **2022**, *29*, 10575–10584. [[CrossRef](#)] [[PubMed](#)]
2. Aladeniyi, K.; Arogunjo, A.M.; Pereira, A.J.S.C.; Khandaker, M.U.; Bradley, D.A.; Sulieman, A. Evaluation of radiometric standards of major building materials used in dwellings of South-Western Nigeria. *Radiat. Phys. Chem.* **2021**, *178*, 109021. [[CrossRef](#)]
3. UNSCEAR. *Sources and Effects of Ionizing Radiation: UNSCEAR 2000 Report to the General Assembly, with Scientific Annexes*; United Nations: New York, NY, USA, 2000; Volume 1.
4. Abdullahi, S.; Ismail, A.F.; Samat, S. Determination of indoor doses and excess lifetime cancer risks caused by building materials containing natural radionuclides in Malaysia. *Nucl. Eng. Technol.* **2019**, *51*, 325–336. [[CrossRef](#)]
5. Al-Sulaiti, H.; Alkhomashi, N.; Al-Dahan, N.; Al-Dosari, M.; Bradley, D.A.; Bukhari, S.; Matthews, M.; Regan, P.H.; Santawamaitre, T. Determination of the natural radioactivity in Qatari building materials using high-resolution gamma-ray spectrometry. *Nucl. Instrum. Methods Phys. Res. Sect. A* **2011**, *652*, 915–919. [[CrossRef](#)]
6. UNSCEAR. *Sources and Effects of Ionizing Radiation, United Nations Scientific Committee on the Effects of Atomic Radiation (UNSCEAR) 2008 Report*; United Nations: New York, NY, USA, 2010; Volume I. [[CrossRef](#)]
7. Aykamuş, A.Ş.; Turhan, Ş.; Aysun Ugur, F.; Baykan, U.N.; Kılıç, A.M. Natural radioactivity, radon exhalation rates and indoor radon concentration of some granite samples used as construction material in Turkey. *Radiat. Prot. Dosim.* **2013**, *157*, 105–111. [[CrossRef](#)] [[PubMed](#)]
8. WHO; Zeeb, H. *WHO Handbook on Indoor Radon: A Public Health Perspective*; World Health Organization: Geneva, Switzerland, 2009.
9. Kuzmanović, P.; Todorović, N.; Filipović Petrović, L.; Mrđa, D.; Forkapić, S.; Nikolov, J.; Knežević, J. Radioactivity of building materials in Serbia and assessment of radiological hazard of gamma radiation and radon exhalation. *J. Radioanal. Nucl. Chem.* **2020**, *324*, 1077–1087. [[CrossRef](#)]
10. Axelsson, G.; Andersson, E.M.; Barregard, L. Lung cancer risk from radon exposure in dwellings in Sweden: How many cases can be prevented if radon levels are lowered? *Cancer Causes Control* **2015**, *26*, 541–547. [[CrossRef](#)]
11. Higgy, R.H.; El-Tahawy, M.S.; Abdel-Fattah, A.T.; Al-Akabawy, U.A. Radionuclide content of building materials and associated gamma dose rates in Egyptian dwellings. *J. Environ. Radioact.* **2000**, *50*, 253–261. [[CrossRef](#)]
12. Rizzo, S.; Brai, M.; Basile, S.; Bellia, S.; Hauser, S. Gamma activity and geochemical features of building materials: Estimation of gamma dose rate and indoor radon levels in Sicily. *Appl. Radiat. Isot.* **2001**, *55*, 259–265. [[CrossRef](#)]
13. Moghazy, N.M.; El-Tohamy, A.M.; Fawzy, M.M.; Awad, H.A.; Zakaly, H.M.H.; Issa, S.A.M.; Ene, A. Natural Radioactivity, Radiological Hazard and Petrographical Studies on Aswan Granites Used as Building Materials in Egypt. *Appl. Sci.* **2021**, *11*, 6471. [[CrossRef](#)]
14. Kumar, A.; Kumar, M.; Singh, B.; Singh, S. Natural activities of <sup>238</sup>U, <sup>232</sup>Th and <sup>40</sup>K in some Indian building materials. *Radiat. Meas.* **2003**, *36*, 465–469. [[CrossRef](#)]
15. Roy, S.; Alam, M.S.; Begum, M.; Alam, B. Radioactivity in building materials used in and around Dhaka city. *Radiat. Prot. Dosim.* **2005**, *114*, 527–532. [[CrossRef](#)] [[PubMed](#)]
16. Al-Zahrani, J.H. Estimation of natural radioactivity in local and imported polished granite used as building materials in Saudi Arabia. *J. Radiat. Res. Appl. Sci.* **2017**, *10*, 241–245. [[CrossRef](#)]
17. Çetinkaya, H.; Manisa, K.; Işık, U. Radioactivity content of building materials used in kutahya province, turkey. *Radiat. Prot. Dosim.* **2022**, *198*, 167–174. [[CrossRef](#)] [[PubMed](#)]
18. Imani, M.; Adelikhah, M.; Shahrokhi, A.; Azimpour, G.; Yadollahi, A.; Kocsis, E.; Toth-Bodrogi, E.; Kovács, T. Natural radioactivity and radiological risks of common building materials used in Semnan Province dwellings, Iran. *Environ. Sci. Pollut. Res.* **2021**, *28*, 41492–41503. [[CrossRef](#)] [[PubMed](#)]
19. Tuo, F.; Peng, X.; Zhou, Q.; Zhang, J. Assessment of natural radioactivity levels and radiological hazards in building materials. *Radiat. Prot. Dosim.* **2020**, *188*, 316–321. [[CrossRef](#)]



20. Kuzmanović, P.; Todorović, N.; Nikolov, J.; Hansman, J.; Vraničar, A.; Knežević, J.; Miljević, B. Assessment of radiation risk and radon exhalation rate for granite used in the construction industry. *J. Radioanal. Nucl. Chem.* **2019**, *321*, 565–577. [[CrossRef](#)]
21. Al-Hamarnah, I.F. Radiological hazards for marble, granite and ceramic tiles used in buildings in Riyadh, Saudi Arabia. *Environ. Earth Sci.* **2017**, *76*, 516. [[CrossRef](#)]
22. Asaduzzaman, K.; Khandaker, M.; Amin, Y.; Bradley, D. Natural radioactivity levels and radiological assessment of decorative building materials in Bangladesh. *Indoor Built Environ.* **2016**, *25*, 541–550. [[CrossRef](#)]
23. Righi, S.; Bruzzi, L. Natural radioactivity and radon exhalation in building materials used in Italian dwellings. *J. Environ. Radioact.* **2006**, *88*, 158–170. [[CrossRef](#)]
24. Kitto, M.E.; Haines, D.K.; Menia, T.A. Assessment of gamma-ray emissions from natural and manmade decorative stones. *J. Radioanal. Nucl. Chem.* **2009**, *282*, 409. [[CrossRef](#)]
25. Asghar, M.; Tufail, M.; Sabiha, J.; Abid, A.; Waqas, M. Radiological implications of granite of northern Pakistan. *J. Radiol. Prot.* **2008**, *28*, 387–399. [[CrossRef](#)]
26. Sharaf, J.M.; Hamideen, M.S. Measurement of natural radioactivity in Jordanian building materials and their contribution to the public indoor gamma dose rate. *Appl. Radiat. Isot.* **2013**, *80*, 61–66. [[CrossRef](#)] [[PubMed](#)]
27. Sonkawade, R.G.; Kant, K.; Muralithar, S.; Kumar, R.; Ramola, R.C. Natural radioactivity in common building construction and radiation shielding materials. *Atmos. Environ.* **2008**, *42*, 2254–2259. [[CrossRef](#)]
28. Anjos, R.M.; Veiga, R.; Soares, T.; Santos, A.M.A.; Aguiar, J.G.; Frascá, M.H.B.O.; Brage, J.A.P.; Uzêda, D.; Mangia, L.; Facure, A.; et al. Natural radionuclide distribution in Brazilian commercial granites. *Radiat. Meas.* **2005**, *39*, 245–253. [[CrossRef](#)]
29. Guillén, J.; Tejado, J.J.; Baeza, A.; Corbacho, J.A.; Muñoz, J.G. Assessment of radiological hazard of commercial granites from Extremadura (Spain). *J. Environ. Radioact.* **2014**, *132*, 81–88. [[CrossRef](#)]
30. Medhat, M.E. Assessment of radiation hazards due to natural radioactivity in some building materials used in Egyptian dwellings. *Radiat. Prot. Dosim.* **2009**, *133*, 177–185. [[CrossRef](#)]
31. Amin, R.M. Gamma radiation measurements of naturally occurring radioactive samples from commercial Egyptian granites. *Environ. Earth Sci.* **2012**, *67*, 771–775. [[CrossRef](#)]
32. Amrani, D.; Tahtat, M. Natural radioactivity in Algerian building materials. *Appl. Radiat. Isot.* **2001**, *54*, 687–689. [[CrossRef](#)]
33. Rajamannan, B.; Viruthagiri, G.; Suresh Jawahar, K. Natural radionuclides in ceramic building materials available in Cuddalore district, Tamil Nadu, India. *Radiat. Prot. Dosim.* **2013**, *156*, 531–534. [[CrossRef](#)]
34. Abdullahi, S.; Ismail, A.F.; Mohd Fadzil, S.; Samat, S. Assessment of the long-term possible radiological risk from the use of ceramic tiles in Malaysia. *Nucl. Sci. Tech.* **2019**, *30*, 19. [[CrossRef](#)]
35. Amin, S.A.; Naji, M. Natural radioactivity in different commercial ceramic samples used in Yemeni buildings. *Radiat. Phys. Chem.* **2013**, *86*, 37–41. [[CrossRef](#)]
36. Iwaoka, K.; Hosoda, M.; Suwankot, N.; Omori, Y.; Ishikawa, T.; Yonehara, H.; Tokonami, S. Natural radioactivity and radon exhalation rates in man-made tiles used as building materials in Japan. *Radiat. Prot. Dosim.* **2015**, *167*, 135–138. [[CrossRef](#)] [[PubMed](#)]
37. Zalewski, M.; Tomczak, M.; Kapala, J. Radioactivity of building materials available in northeastern Poland. *Pol. J. Environ. Stud.* **2001**, *10*, 183–188.
38. Shohda, A.M.; Draz, W.M.; Ali, F.A.; Yassien, M.A. Natural radioactivity levels and evaluation of radiological hazards in some Egyptian ornamental stones. *J. Radiat. Res. Appl. Sci.* **2018**, *11*, 323–327. [[CrossRef](#)]
39. Fares, S. Natural Radioactivity Emitted from Granite and Marble Samples Collected from Sinai Area Egypt and Excess Lifetime Cancer Risk. *Int. J. Sci. Eng. Res.* **2016**, *7*, 432–444.
40. Canberra. *The Genie-2000 Operations Manual, Including the S501 Gamma Analysis Option*; Canberra Industries: Canberra, Australia, 2013.
41. Sidique, E.; Elhaddad, M.A.; Abdelwahab, S.F.; El Hadek, H.H. Health Hazards Assessment and Geochemistry of ElSibai-Abu ElTiyur Granites, Central Eastern Desert, Egypt. *Appl. Sci.* **2021**, *11*, 12002. [[CrossRef](#)]
42. El-Gamal, H.; Sidique, E.; El-Haddad, M.; Farid, M.E.-A. Assessment of the natural radioactivity and radiological hazards in granites of Mueilha area (South Eastern Desert, Egypt). *Environ. Earth Sci.* **2018**, *77*, 691. [[CrossRef](#)]
43. El-Gamal, H.; Sidique, E.; El-Haddad, M. Spatial Distributions and Risk Assessment of the Natural Radionuclides in the Granitic Rocks from the Eastern Desert, Egypt. *Minerals* **2019**, *9*, 386. [[CrossRef](#)]
44. Beretka, J.; Matthew, P.J. Natural radioactivity of Australian building materials, industrial wastes and by-products. *Health Phys.* **1985**, *48*, 87–95. [[CrossRef](#)]
45. NEA-OECD. *Exposure to Radiation from Natural Radioactivity in Building Materials*; Report by NEA Group of Experts of the Nuclear Energy Agency; OECD: Paris, France, 1979.
46. European Commission. Radiological protection principles concerning the natural radioactivity of building materials. *Radiat. Prot.* **1999**, *112*, 5–16.
47. Khan, A.R.; Rafique, M.; Jabbar, A.; Rahman, S.U.; Shahzad, M.I.; Khan, M.E.; Yasin, M. Radionuclide concentrations in sand samples from riverbanks of Muzaffarabad, Azad Kashmir. *Nucl. Sci. Tech.* **2018**, *29*, 93. [[CrossRef](#)]
48. ICRP. *ICRP Publication 60: 1990 Recommendations of the International Commission on Radiological Protection*; SAGE Publications: Southend Oaks, CA, USA, 1990.
49. ICRP. *ICRP Publication 65: Protection Against Radon-222 at Home and at Work*; SAGE Publications: Southend Oaks, CA, USA, 1994.



50. Papadopoulos, A.; Christofides, G.; Koroneos, A.; Papadopoulou, L.; Papastefanou, C.; Stoulos, S. Natural radioactivity and radiation index of the major plutonic bodies in Greece. *J. Environ. Radioact.* **2013**, *124*, 227–238. [[CrossRef](#)] [[PubMed](#)]
51. Salaheldin, G.; Elhaddad, M.; Sidique, E. Radon concentration and exhalation rate for granitic rocks, Central Eastern Desert, Egypt. *Arab. J. Geosci.* **2022**, *15*, 1221. [[CrossRef](#)]
52. UNSCEAR. *Sources and Effects of Ionizing Radiation: UNSCEAR 1993 Report to the General Assembly, with Scientific Annexes*; United Nations: New York, NY, USA, 1993.
53. Qureshi, A.A.; Tariq, S.; Din, K.U.; Manzoor, S.; Calligaris, C.; Waheed, A. Evaluation of excessive lifetime cancer risk due to natural radioactivity in the rivers sediments of Northern Pakistan. *J. Radiat. Res. Appl. Sci.* **2014**, *7*, 438–447. [[CrossRef](#)]



## Article

# Optical Properties and Gamma Radiation Shielding Capability of Transparent Barium Borosilicate Glass Composite

Mohamed Ehab <sup>1,\*</sup>, Elsayed Salama <sup>2,\*</sup>, Ahmed Ashour <sup>1</sup>, Mohamed Attallah <sup>3</sup> and Hosam M. Saleh <sup>4</sup>

<sup>1</sup> Engineering Mathematics and Physics Department, Faculty of Engineering and Technology, Future University in Egypt (FUE), New Cairo 11845, Egypt

<sup>2</sup> Basic Science Department, Faculty of Engineering, The British University in Egypt (BUE), El Sherouk City 11837, Egypt

<sup>3</sup> Basic Science Department, Higher Technological Institute, 10th of Ramadan City 44629, Egypt

<sup>4</sup> Radioisotope Department, Nuclear Research Center, Egyptian Atomic Energy Authority, Cairo 11787, Egypt

\* Correspondence: mehab@fue.edu.eg (M.E.); elsayed.salama@bue.edu.eg (E.S.); Tel.: +20-1223870849 (E.S.); Fax: +20-2-24665630 (E.S.)

**Abstract:** In this study, both radiation shielding capability and optical properties of prepared SiO<sub>2</sub>-ZnO-Na<sub>2</sub>CO<sub>3</sub>-H<sub>3</sub>BO<sub>3</sub>-BaCO<sub>3</sub> glass composite with different concentrations of barium carbonate (0–30 mol%) have been studied. Gamma attenuation properties, such as the mass attenuation coefficient (MAC), mean free path (MFP), and exposure build-up factor (EBF), are experimentally and theoretically investigated. The detected XRD patterns for the prepared glass composites confirm their amorphous nature. It is evident from the obtained data that all tested parameters, such as mass density, molar volume, refractive index, dielectric constant, refraction loss (%), and molar refraction, have been increased as BaCO<sub>3</sub> mol% increased. At the same time, the results of the optical bandgap show a gradual decrease with increasing barium concentration. It was also found that the mass attenuation coefficients increased with BaCO<sub>3</sub> concentration from 0.078 at zero mol% BaCO<sub>3</sub> to 0.083 cm<sup>2</sup>/g at 30 mol%. Moreover, the half-value layer (HVL) and the exposure build-up factor (EBF) up to 40 mfp penetration depth were investigated in addition to the effective atomic number (Z<sub>eff</sub>) and the corresponding equivalent atomic number (Z<sub>eq</sub>) at the energy range of 0.015–15 MeV. The produced glass composite might be considered for many shielding applications based on the obtained results that require a transparent shielding material.

**Keywords:** mass attenuation coefficient; effective atomic number; build-up factor; borosilicate glass; radiation shielding

**Citation:** Ehab, M.; Salama, E.; Ashour, A.; Attallah, M.; Saleh, H.M. Optical Properties and Gamma Radiation Shielding Capability of Transparent Barium Borosilicate Glass Composite. *Sustainability* **2022**, *14*, 13298. <https://doi.org/10.3390/su142013298>

Academic Editor: Changhyun Roh

Received: 7 July 2022

Accepted: 9 October 2022

Published: 16 October 2022

**Publisher's Note:** MDPI stays neutral with regard to jurisdictional claims in published maps and institutional affiliations.



**Copyright:** © 2022 by the authors. Licensee MDPI, Basel, Switzerland. This article is an open access article distributed under the terms and conditions of the Creative Commons Attribution (CC BY) license (<https://creativecommons.org/licenses/by/4.0/>).

## 1. Introduction

Shielding materials have a significant role in radiation protection during the wide medical use of radioactive isotopes and X-ray machines and in many industrial applications, such as petroleum and gas extraction [1]. The shielding of ionizing radiation has significantly changed over the last 60 years. As a result of these ongoing developments in anti-ionizing radiation technology, the significance of composite materials for radiation shielding has been acknowledged. In shielding applications, composite materials are desirable because secondary radiation must be considered in radiation shielding design. Therefore, a functional shield's composition must be such that it can efficiently absorb both primary and secondary radiation rays. In addition to their ability to absorb all primary and likely secondary radiation, other properties might restrict the use of particular materials for radiation shielding, such as space, cost, mechanical strength, chemical stability, and thermal stability.

There is a continuing need for new materials to be employed as shielding materials under testing nuclear radiation exposure circumstances [2–5]. The most often utilized protective material so far is concrete [5–10], which is cement mixed with various additives,

such as cellulosic waste [11,12], bitumen [13,14], glass [15], polymers [16–18], nanomaterials [19,20], and cement wastes [21,22]. However, the trouble in accomplishing homogeneity, the presence of water and the need for transparency of the shield have persuaded scientists to use glass rather than concrete [23–27]. Borate glasses are used for their exceptionally high transparency, low melting point, and thermal stability. The role of glass additives is different depending on the kind of the enhancement property. Adding sodium carbonate ( $\text{Na}_2\text{CO}_3$ ) to the borate glass improves its glass nature characterizations by changing the coordination of the boron coordination group [19], while zinc oxide (ZnO) is added to borate glass to boost its thermal stability, reduce crystallization, and enhance the glass matrix's chemical resistance [28–32]. Heavy elements, such as lead, barium, bismuth, and tungsten are used to increase the borate glass density, which in turn greatly enhancing their radiation-shielding abilities [5,27,33,34]. Borated glasses doped with lead and other specific elements to enhance their densities and radiation attenuation characteristics are successfully produced [32,35–37]. Borosilicate glasses have further advantages, such as chemical durability, better heat stability, extremely low thermal expansion coefficients, and high capacities for substantial visible light transmission [38–41].

Due to its high atomic number and good attenuation coefficient, barium-based glasses have a very promising gamma radiation attenuation coefficient. Several borosilicate glass systems were tested as gamma-ray shielding materials doped with different metal oxides, such as  $\text{PbO}$ ,  $\text{BaO}$ ,  $\text{Bi}_2\text{O}_3$ ,  $\text{BaO}$ ,  $\text{TiO}_2$ , and  $\text{SrO}$  at different concentrations, showed better shielding efficiencies compared with those previously used in the industry [26,27,42–46]. Adding iron (III) oxide to sodium-barium-vanadate glass has an impact on its physical, optical, mechanical, and radiation absorption features where significant effect on the interaction parameters of thermal neutrons and gamma radiation absorption are observed [47]. The prepared titanium borosilicate glass modified with various ratios of barium oxide showed that adding barium increased the attenuation parameters and enhanced the durability of the prepared sample [48]. The density of sodium zinc borate glasses doped with dysprosium and barium oxide was observed to increase from  $2.30$  to  $4.02 \text{ g/cm}^3$ , and the glass's hygroscopic property considerably decreased with the addition of barium [49]. The addition of  $\text{BaO}$  to zinc barium tellurite glasses enhances its polarization by increasing the bond length, hence the glass network expansion resulting in volume.

The current work aims to prepare and investigate highly transparent, lead-free barium borosilicate glass composite to be used for gamma shielding applications.

## 2. Materials and Methods

The glass composite of  $10 \text{ Na}_2\text{CO}_3 - 20 \text{ SiO}_2 - 10 \text{ ZnO} - (60 - x) \text{ H}_3\text{BO}_3 - x \text{ BaCO}_3$  (where  $x = 0, 5, 10, 20$ , and  $30 \text{ mol}\%$ ) was fabricated using the conventional fast melt-quenching technique. High purity grade powders of  $\text{Na}_2\text{CO}_3$ ,  $\text{SiO}_2$ ,  $\text{ZnO}$ ,  $\text{H}_3\text{BO}_3$ , and  $\text{BaCO}_3$  were utilized as a starting material, as shown in Table 1. The compositions were mashed in an agate mortar and melted at  $1100 \text{ }^\circ\text{C}$  for one hour in a porcelain crucible and twirled a lot until a homogenous bubble-free liquid was formed. The melts were poured into preheated stainless-steel molds and annealed at  $\sim 400 \text{ }^\circ\text{C}$  for 4 h to reduce the cracking and thermal stresses of the samples and then left to cool to room temperature. The photos of the obtained samples before polishing are shown in Figure 1. The samples were then manually polished to obtain maximum flatness.

**Table 1.** Samples compositions (mol%).

| Sample | $\text{Na}_2\text{CO}_3$ | $\text{SiO}_2$ | $\text{ZnO}$ | $\text{H}_3\text{BO}_3$ | $\text{BaCO}_3$ |
|--------|--------------------------|----------------|--------------|-------------------------|-----------------|
| S0     | 10                       | 20             | 10           | 60                      | 0               |
| S1     | 10                       | 20             | 10           | 55                      | 5               |
| S2     | 10                       | 20             | 10           | 50                      | 10              |
| S3     | 10                       | 20             | 10           | 40                      | 20              |
| S4     | 10                       | 20             | 10           | 30                      | 30              |



Figure 1. Photos of the prepared samples.

X-ray diffraction (XRD) was accomplished for the prepared glass powders by utilizing a Philips X'pert Pro X-ray powder diffractometer (Malvern Panalytical, Almelo, The Netherlands) at room temperature. The X-ray diffraction patterns were analyzed in  $2\theta$  scan from  $10^\circ$  to  $90^\circ$  with  $\text{CuK}\alpha$  as a target and Ni as a filter ( $\lambda = 1.5418 \text{ \AA}$ ) at 40 KV and 30 mA with a speed of scanning reaching to 0.3 s.

Fourier transformation of the infrared absorption spectra (FTIR) of the produced samples were measured in the spectral region  $400\text{--}4000 \text{ cm}^{-1}$  using a JASCOFT-IR6200 spectrometer with the KBr pellet method.

The densities of the prepared glass specimens were measured at room temperature by a simple Archimedes technique that utilizes xylene as a submerged liquid according to the following formula [50]:

$$\rho = \frac{W_a}{W_a - W_b} \rho_b \quad (1)$$

where  $W_a$  is the sample's weight in air,  $W_b$  represents its weight in xylene, and  $\rho_b$  is xylene's density ( $\rho_b = 0.863 \text{ g/cm}^3$ ). Using the results of the mass density, the molar volume of the glasses can be calculated according to the following formula [51]:

$$V_m = M_W / \rho \quad (2)$$

where  $M_W$  is the molecular weight, and  $\rho$  is the glass sample density. Subsequently, the refractive index of the prepared samples can be calculated by the following relation [39,51]:

$$n = \left( \frac{\rho + 10.4}{8.6} \right) \quad (3)$$

Other features depending on the refractive index can be acquired, such as the dielectric constant, which can be calculated according to the following formula [52]:

$$\varepsilon = n^2 \quad (4)$$

Additionally, the reflection loss (R) has been calculated by using the following Fresnel's formula [53]:

$$R = \left( \frac{n - 1}{n + 1} \right)^2 \quad (5)$$

The ratio of molar volume to molar refractivity ( $R_M$ ), which is acquired and calculated via the following equation [52], is another structural correlation that can be used to forecast glass propensity that would be metallic or insulating.

$$R_M = V_m \left( \frac{n^2 - 1}{n^2 + 2} \right) \quad (6)$$

A recording double beam UV-VIS spectrophotometer (type JASCO Crop., V-770, Japan) encompassing the wavelength range from 200 to 1100 nm was used to evaluate the optical absorption spectra of the polished samples. The absorption coefficient and optical bandgap

of the samples were determined according to the optical absorption data. The optical absorption coefficient  $\alpha(\nu)$  was calculated utilizing the following equation [52]:

$$\alpha(\nu) = 2.303A/d \quad (7)$$

where A is the absorbance, and d is the thickness of the glass sample. Then, the optical bandgap ( $E_{opt}$ ) is determined through the well-known relation [54]:

$$\alpha(\nu) = B \frac{(h\nu - E_{opt})^n}{h\nu} \quad (8)$$

where  $h\nu$  is the incident photon energy, and B is a constant relating to the band tailing's extent.

For direct allowed, indirect allowed, direct forbidden, and indirect forbidden transitions, respectively, the index n has the values 1/2, 2, 3/2, and 3. Since there is no transition symmetry in the case of indirect transitions, the electron's wave vector might change during the optical transition, and phonons will either take or give up the momentum shift. [55]. In the above-mentioned case,  $(\alpha h\nu)^{0.5}$  renders a linear relation with the photon energy. Extrapolating of the linear part of the overhead relation shows the optical bandgap  $E_{opt}$  where  $(\alpha h\nu)^{0.5} = 0$  in case of indirect transition.

A NaI (TI) scintillation detector (Teledyne Isotopes "2 × 2" NaI (TI) Scintillation Detector, AL, USA) with an energy resolution of 8% at 662 keV was used to test the gamma-ray shielding properties of the set glass samples. The generated glass samples were measured at four distinct gamma energies under the correct geometrical constraints: 0.662 MeV from a Cs-137-point source, 0.239 MeV, 0.911 MeV from a <sup>232</sup>Th point source, and 1.332 MeV from a Co-60-point source. All these sources are provided by a spectrum techniques company. The investigated samples were polished and formed to have cylindrical shape of about 2 cm diameter and 1 cm thickness. During the measurements of the gamma attenuation coefficients, the sample was in contact with the point source, and the distance between the source and the detector was fixed at about 10 cm.

### 3. Theoretical Background

Modified Lambert-Beer law was utilized for the calculation of the linear attenuation coefficients as follows [23]:

$$I = I_0 \times B \times e^{-\mu x} \quad (9)$$

where  $I_0$  and I are the initial and transmitted photon intensities, respectively,  $\mu$  is a linear attenuation coefficient ( $\text{cm}^{-1}$ ), and B (E, x) is the build-up factor depending on the thickness x (cm) of the used material and the energy E of the incident photon. The mass attenuation coefficient ( $\mu_m$ ) can be determined utilizing the measured linear attenuation coefficient and the mass density ( $\rho$ ) values by the following relationship [36]:

$$\mu_m = \frac{\mu}{\rho} \quad (10)$$

The following formula can be used to determine  $\mu_m$  for a compound or mixture [54]:

$$\mu_m = \sum_i w_i (\mu_m)_i \quad (11)$$

where  $(\mu_m)_i$  is the mass attenuation coefficient of the examined mixture's ith element and  $w_i$  stands for its weight percentage. The half-value layer (HVL) of the prepared glasses can be calculated by the following formula [53,56]:

$$\text{HVL} = \frac{0.693}{\mu} \quad (12)$$

where  $\mu$  is the material's linear attenuation coefficient, which obviously relies on the material's type, mass density, and beam energy.

The National Institute of Standard and Technology (NIST) created a photon cross-sections database called XCOM that contains the attenuation coefficients of all elements in the periodic table at various energies in order to calculate the values of the mass attenuation coefficients for the glass samples over a broad range of energies from 0.015 to 15 MeV [57]. The following equation was used to compute the mean free path (MFP) values using the linear attenuation coefficient [58]:

$$\text{MFP} = \frac{1}{\mu} \quad (13)$$

The effective atomic number of a material ( $Z_{\text{eff}}$ ) is defined as the ratio of an object's electronic cross-section ( $\sigma_a$ ) to its effective atomic cross-section ( $\sigma_e$ ). For the produced glass samples, the following relationship may be used to estimate the values of  $Z_{\text{eff}}$  based on the obtained data of  $\mu_m$  [33]:

$$Z_{\text{eff}} = \frac{\sigma_a}{\sigma_e} = \frac{\sum_i f_i A_i (\mu_m)_i}{\sum_i f_i \frac{A_i}{Z_i} (\mu_m)_i} \quad (14)$$

where  $A_i$  is the atomic weight,  $Z_i$  is the atomic number,  $(\mu_m)_i$  is the mass attenuation coefficient for the  $i$ th element, and  $f_i$  represents  $i$ th element fractional abundance concerning the number of atoms. To calculate the build-up factor, we must first obtain the Compton partial attenuation coefficient ( $(\mu_m)_{\text{comp}}$ ) and total attenuation coefficient ( $(\mu_m)_{\text{total}}$ ) values for the constituent elements and compounds of the examined glass samples in the energy range of 0.015–15.0 MeV. The values of the equivalent atomic number ( $Z_{\text{eq}}$ ) for the produced glass samples may then be computed by comparing the ratio  $(\mu_m)_{\text{comp}}/(\mu_m)_{\text{total}}$  at a certain energy with comparable ratios of elements at the same energy. The interpolation of the equivalent atomic number was determined using the following logarithmic interpolation algorithm [59] where the ratio  $(\mu_m)_{\text{comp}}/(\mu_m)_{\text{total}}$  lies between two subsequent ratios of elements:

$$Z_{\text{eq}} = \frac{Z_1(\log R_2 - \log R) + Z_2(\log R - \log R_1)}{\log R_2 - \log R_1} \quad (15)$$

where the atomic numbers of the pure elements corresponding to the ratios  $R_1$  and  $R_2$  are  $Z_1$  and  $Z_2$ , respectively, and  $R$  is the ratio for studied glass samples at certain energy [60]. Using the general progressive (G-P) interpolation in the energy range of 0.015–15 MeV up to 40 mfp, the exposure build-up factors EBF were calculated for the prepared above-mentioned glass samples utilizing the following equations as mentioned in Harima et al. (1993) [6,61,62]:

$$B(E, X) = 1 + \frac{b-1}{K-1}(K^X - 1) \text{ for } K \neq 1 \quad (16)$$

$$B(E, X) = 1 + (b-1)X \text{ for } K = 1 \quad (17)$$

$$K(E, X) = cX^a + d \frac{\tanh\left(\frac{X}{X_K} - 2\right) - \tanh(-2)}{1 - \tanh(-2)} \quad (18)$$

where  $E$  is the photon energy,  $X$  is the separation between the detector and the source as a function of MFP,  $B$  is the EBF value at 1 MFP,  $K(E, X)$  is the dosage multiplicative factor, and  $b$ ,  $c$ ,  $a$ ,  $X_K$  and  $d$  are the calculated G-P fitting parameters that rely on the attenuating medium and source energy. The prepared glasses'  $b$ ,  $c$ ,  $a$ ,  $X_K$  and  $d$  G-P fitting parameters can be interpolated logarithmically using the following equation-like method for the 0.015–15 MeV gamma-ray energy range up to 40 mfp [63,64].

$$P = \frac{P_1(\log \log Z_2 - \log \log Z_{\text{eq}}) + P_2(\log \log Z_{\text{eq}} - \log \log Z_1)}{\log \log Z_2 - \log \log Z_1} \quad (19)$$

$P_1$  and  $P_2$  are the values of the G-P fitting parameters that correspond to the  $Z_1$  and  $Z_2$  atomic numbers at the specified energy, respectively. The American Nuclear Society's study criteria for G-P fit for the elements were used [65].



## 4. Results and Discussion

### 4.1. XRD Analysis and FTIR

The XRD patterns for the prepared glass samples were obtained and are shown in Figure 2. The absence of sharp peaks in the XRD results demonstrates that the prepared specimens have an amorphous nature. The two humps seen at  $2\theta$  equal  $25^\circ$  and  $45^\circ$  for each sample and serve as a strong piece of evidence for the constructive interferences at variance of two and the aggregation of atoms in the glass matrix in two separate ways. A typical peak for borosilicate matrices was previously seen in several publications [45,66,67].

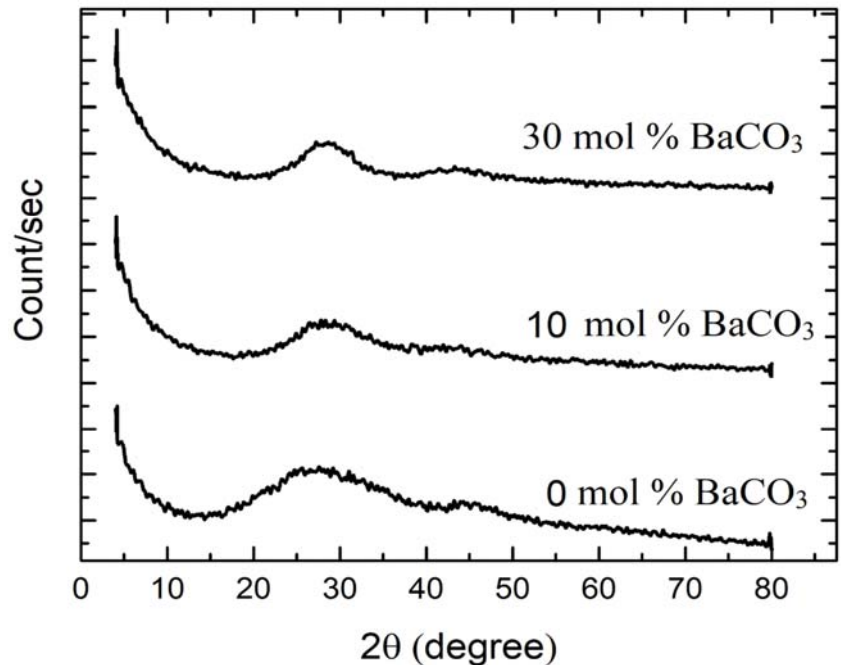


Figure 2. Patterns of X-ray diffraction for ZnO borosilicate glasses doped with  $\text{BaCO}_3$ .

The FTIR transmission spectra of ZnO borosilicate glasses doped with different concentrations of  $\text{BaCO}_3$  are shown in Figure 3. Table 2 displays the results of the FTIR absorption bands and the associated vibrational modes.

Four distinct bands can be found in the observed data. The band located between  $800$  and  $1200\text{ cm}^{-1}$  represented the  $\text{BO}_4$  structural units. Two more bands were visible in the range of  $600$  and  $800\text{ cm}^{-1}$  and  $1200$  to  $1600\text{ cm}^{-1}$  and were returned to  $\text{BO}_3$  structural units. Finally, the band of metal ion vibrations was observed at  $400$  to  $600\text{ cm}^{-1}$ . The stretching relaxation modes of B–O bonds of trigonal  $\text{BO}_3$  band centered at  $1364\text{ cm}^{-1}$  is observed with a small shoulder edge around  $1260\text{ cm}^{-1}$  [68]. While the strong broad band from  $1176$ – $755\text{ cm}^{-1}$  centered at  $955\text{ cm}^{-1}$  are attributed to asymmetric stretching of B–O bonds of tetrahedral  $\text{BO}_4$  units. The higher intensity observed may be due to the formation of Si–O–Si and B–O–Si bonds, which contribute vibrational modes at the  $\text{BO}_4$  band [70–72]. A moderate band centered around  $700\text{ cm}^{-1}$  may be due to bending vibrations of B–O–B of linkages in a borate network [73,74]. The band centered at  $440\text{ cm}^{-1}$  and the shoulder noticed at  $500\text{ cm}^{-1}$  may be attributed to vibrational modes of all metal cations  $\text{Ba}^{+2}$  and  $\text{Zn}^{+2}$  [75–77]. It is noticed that the increase in the  $\text{BaCO}_3$  mol% in the composite shifts the bands to a lower wavenumber, which denotes a reduction in the  $\text{BO}_3$  group and formation

of the  $\text{BO}_4$  in the glass structure. As a result, an increase in non-bridging oxygens (NBO) and a decrease in the degree of localization of electrons are produced.

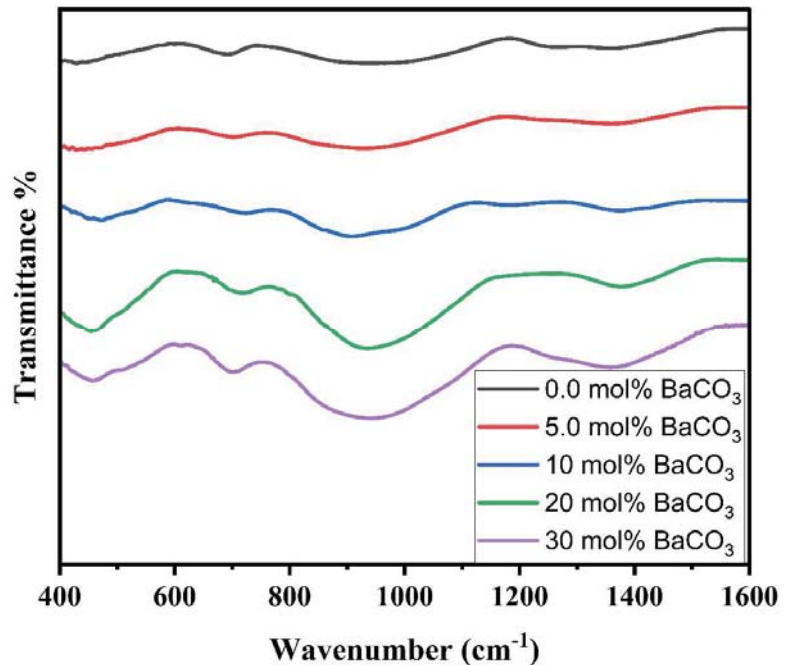


Figure 3. FTIR for ZnO borosilicate glasses doped with  $\text{BaCO}_3$ .

Table 2. The assigned infrared bands to the produced glass samples' spectra.

| Peak Position ( $\text{cm}^{-1}$ ) | Assignment                                                             | Reference Range     |
|------------------------------------|------------------------------------------------------------------------|---------------------|
| 1364                               | Stretching relaxation of B–O bonds of trigonal $\text{BO}_3$ units     | 1170–1600 [68,69]   |
| 950                                | Stretching vibrations of B–O–Si linkages                               | 950–1050 [70,71]    |
| 926                                | Stretching vibrations of B–O bonds of tetrahedral $\text{BO}_4$ units. | 800–1200 [43,71,72] |
| 705                                | B–O–B vibrations of linkages in a borate network                       | ~700 [73,74]        |
| 451                                | Vibrations of the metal cations $\text{Ba}^{+2}$ and $\text{Zn}^{+2}$  | 400–600 [75,77]     |

#### 4.2. Density and Molar Volume

Figure 4 displays the mass densities and molar volumes of the produced glasses. Both the density and the molar volume show an equivalent trend increase with increasing the  $\text{BaCO}_3$  mol% in the composites. By increasing the  $\text{BaCO}_3$  mol% in the composite, the structure becomes more compact. The larger molecular weight of  $\text{BaCO}_3$  relative to the other elements may have contributed to the rise in density. On the contrary, the increases in molar volume may be related to the creation of non-bridging oxygen ions (NBOs), which tend to increase the randomizer in the network and convert triangular ( $\text{BO}_3$ ) structure units into tetrahedral ( $\text{BO}_4$ ) structure units [46,78].

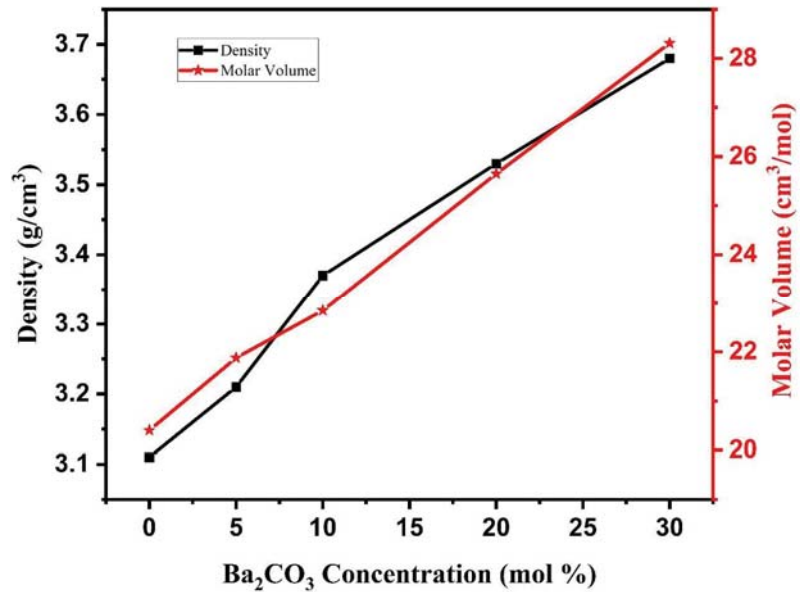


Figure 4. Density and molar volume for ZnO borosilicate glasses doped with BaCO<sub>3</sub>.

#### 4.3. Optical Absorption Spectra

A powerful technique used to express the optical transitions and electronic band configuration of the amorphous materials is the absorption edge in the region of UV-Vis. Therefore, the optical absorption spectra for set glass samples are shown in Figure 5. The consistency of each sample has been kept as small as possible to evade the inherent absorbance resulted from the long optical path length.

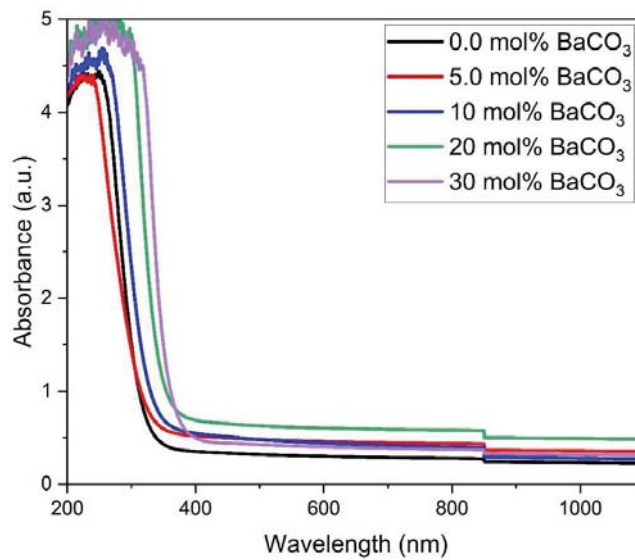


Figure 5. Absorbance versus wavelength for ZnO borosilicate glasses as a function of BaCO<sub>3</sub> mol%.

The linear relation between  $(\alpha h\nu)^{0.5}$  and the photon energy is shown in Figure 6. Extrapolating of the linear part of the overhead relation shows the optical bandgap  $E_{opt}$  energies of 3.55, 3.42, 3.29, 3.21, and 3.13 eV. The values of optical bandgap performance show a gradual decrease with increasing barium concentration. The observed decrease in bandgap with improved  $BaCO_3$  mole% concentration could be attributable to potential flaws in the glass network as non-bridging oxygen (NBO) ranges rise. It also indicates the formation of new localized states formed between the valence and conductive bands. Finally, because of the usage of  $BaCO_3$  rather than boron oxide, the glass matrix is densified, which is well compatible with the resulting density and changes in the optical bandgap.

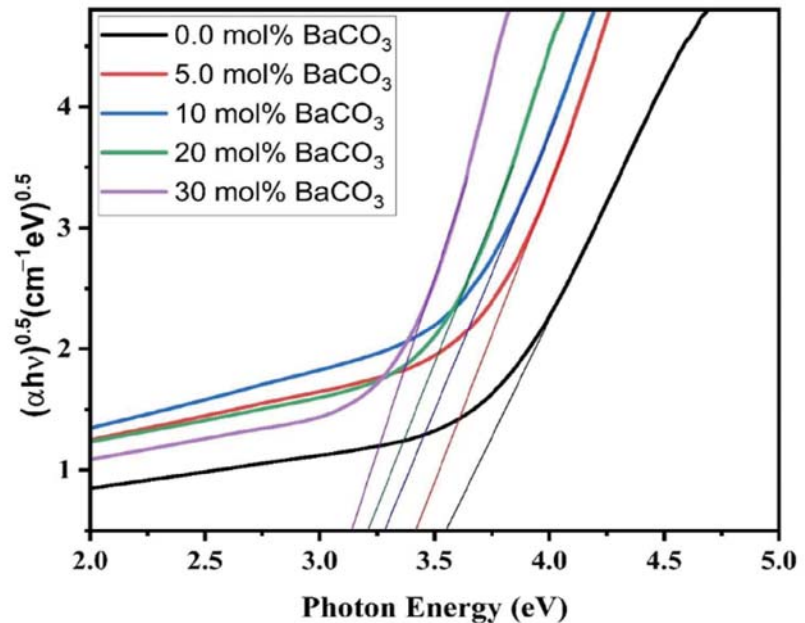


Figure 6. Optical bandgap for ZnO borosilicate glasses as a function of  $BaCO_3$  mol%.

The received data of the refractive index and its related parameters are summarized in Table 3. It is evident from the obtained data that all these parameters have the same trend. With increasing  $BaCO_3$  mol%, the parameters grew linearly. All estimated parameters confirm the role of barium oxide in the glass network. It has been observed that the refractive index increases as the  $BaCO_3$  mol% increases inside the structure grow. The compactness that rises in the glass samples can be linked to this boom in the refractive index.

#### 4.4. Mass Attenuation Coefficient

Table 4 compares the values of the mass attenuation coefficient ( $\mu_m$ ) that were derived theoretically and experimentally. It has been established that there is a close correlation between experimental and theoretical values. Figure 7 displays the fluctuation of  $m$  for the produced glass samples with photon energies ranging from 0.015 to 15 MeV. The obtained values of  $\mu_m$  significantly boost the growth in  $BaCO_3$  concentration at the same photon energy while mimicking the chemical composition and photon energy. Based on the interaction of gamma radiation with the examined material, it is possible to explain the inverse relationship between  $m$  and the rise in energy for all samples. The photoelectric effect is the most common interaction at low photon energies ( $E$ ), with an interaction probability proportional to  $E^{-3.5}$ . While Compton scattering is the dominant interaction at

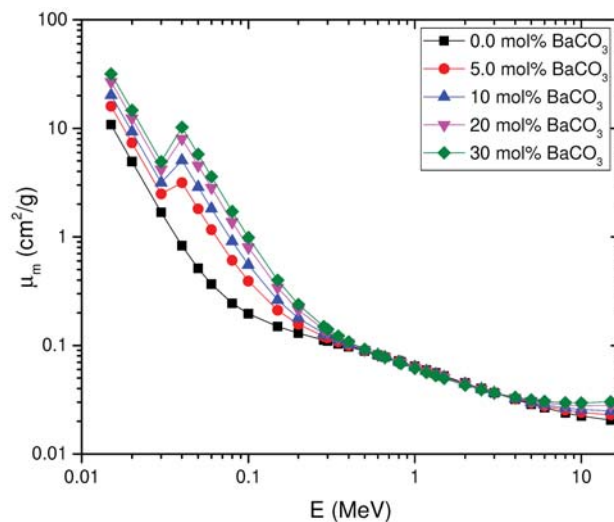
intermediate energies, its probability of interaction is proportional to  $E^{-1}$ . Pair production is most prevalent at very high photon energies over 1.022 MeV, where the chance of contact is proportional to  $E^2$ . The little variation in the mass density of the prepared glass samples with an increase in BaCO<sub>3</sub> concentration from 0 to 30 mol% is what causes the Compton mass attenuation fraction to remain constant. As a result, the mass attenuation coefficient of the produced glass samples has been significantly increased in low-energy areas where x-ray shielding applications are advantageous. The K-absorption edge of barium is what causes the observed peak at around 0.04 MeV (0.037 MeV).

**Table 3.** Physical parameters of the prepared glass system.

| Physical Parameter                                | BaCO <sub>3</sub> mol% |       |       |       |       |
|---------------------------------------------------|------------------------|-------|-------|-------|-------|
|                                                   | 0                      | 5     | 10    | 20    | 30    |
| Density (g/cm <sup>3</sup> )                      | 3.11                   | 3.21  | 3.37  | 3.53  | 3.68  |
| Molar volume (cm <sup>3</sup> mol <sup>-1</sup> ) | 33.69                  | 33.77 | 33.91 | 33.96 | 34.52 |
| Refractive index                                  | 1.57                   | 1.58  | 1.59  | 1.61  | 1.63  |
| Dielectric constant                               | 2.46                   | 2.5   | 2.54  | 2.62  | 2.68  |
| Refraction loss (%)                               | 0.049                  | 0.050 | 0.052 | 0.055 | 0.058 |
| Molar refraction (cm <sup>3</sup> )               | 11.07                  | 11.29 | 11.51 | 11.91 | 12.39 |
| The optical bandgap (eV)                          | 3.55                   | 3.42  | 3.29  | 3.21  | 3.13  |

**Table 4.** The mass attenuation coefficients (cm<sup>2</sup>/g) of the created glass samples, both theoretically and experimentally.

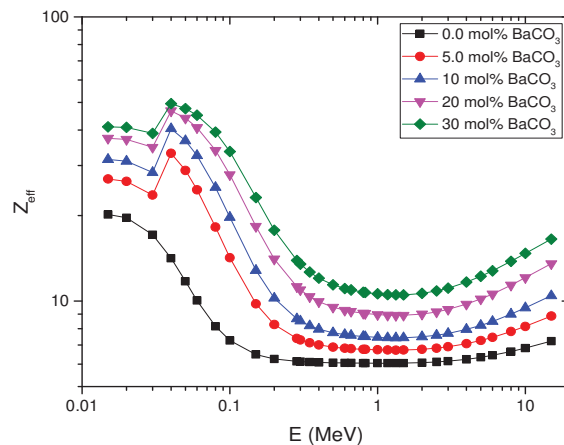
| BaCO <sub>3</sub> (mol%) | 0.662 MeV     |       |         | 1.173 MeV     |       |         | 1.332 MeV     |       |         |
|--------------------------|---------------|-------|---------|---------------|-------|---------|---------------|-------|---------|
|                          | Exp.          | Theo. | % Diff. | Exp.          | Theo. | % Diff. | Exp.          | Theo. | % Diff. |
| 0                        | 0.078 ± 0.006 | 0.078 | 0.0     | 0.056 ± 0.006 | 0.059 | 5.4     | 0.055 ± 0.003 | 0.056 | 1.8     |
| 5                        | 0.078 ± 0.006 | 0.078 | 0.0     | 0.059 ± 0.004 | 0.059 | 0.0     | 0.054 ± 0.002 | 0.055 | 1.9     |
| 10                       | 0.078 ± 0.006 | 0.078 | 0.0     | 0.049 ± 0.004 | 0.058 | 17      | 0.056 ± 0.003 | 0.054 | 3.6     |
| 20                       | 0.079 ± 0.006 | 0.078 | 1.3     | 0.054 ± 0.004 | 0.057 | 5.6     | 0.054 ± 0.002 | 0.053 | 1.9     |
| 30                       | 0.083 ± 0.005 | 0.078 | 6.0     | 0.051 ± 0.004 | 0.056 | 7.8     | 0.054 ± 0.002 | 0.053 | 1.9     |



**Figure 7.** Mass attenuation coefficients of 10 Na<sub>2</sub>CO<sub>3</sub> – 20 SiO<sub>2</sub> – 10 ZnO – (60 – x) H<sub>3</sub>BO<sub>3</sub> – x BaCO<sub>3</sub> glass system in the energy ranges from 0.015–15 MeV and x = 0, 5, 10, 20, 30.

#### 4.5. Half Value Layer (VL) and Effective Atomic Number ( $Z_{\text{eff}}$ )

Figure 8 depicts the fluctuation in the produced glass composite's effective atomic number ( $Z_{\text{eff}}$ ) at energies between 0.015 and 15 MeV and at various concentrations of  $\text{BaCO}_3$ . The observed increase in the  $Z_{\text{eff}}$  with the increase in the barium concentration can be attributed to the higher atomic number for barium compared with boron (barium is added on the expense of boron) while the change in  $Z_{\text{eff}}$  of the prepared glass composite in the investigated energy range 0.015–15 MeV can be explained based on the probability of gamma radiation interaction at each energy photon. At low energy range, photoelectric reaction dominates, with the probability proportional to  $Z^4$ . As the incident photon energy increases, photo electric interaction probability will decrease, and therefore,  $Z_{\text{eff}}$  will also decrease. At the intermediate energy range, Compton interaction dominates, with the probability proportional to  $Z$ . As the incident photon energy increases, Compton interaction probability will decrease (Compton interaction probability proportional with  $E^{-1}$ ), and therefore,  $Z_{\text{eff}}$  will also decrease. At the higher energy range, more than 1.022 MeV pair production interaction dominates, with the probability proportional to  $Z^2$ . As the incident photon energy increases, pair production interaction probability will increase, and therefore,  $Z_{\text{eff}}$  will also increase [79]. At about 0.04 MeV, the ultimate  $Z_{\text{eff}}$  value was detected in all the prepared glass samples. As discussed in the attenuation curve, maximum absorption occurred at the K-absorption edge of barium at about 0.037 MeV.



**Figure 8.**  $Z_{\text{eff}}$  results of  $10 \text{ Na}_2\text{CO}_3 - 20 \text{ SiO}_2 - 10 \text{ ZnO} - (60 - x) \text{ H}_3\text{BO}_3 - x \text{ BaCO}_3$  glass system.

The results of the calculated values of the half value layer (HVL) at the same energy range 0.015–15 MeV are shown in Figure 9. The discussion of these results is the same as mentioned in the case of the mass attenuation coefficients.

#### 4.6. The Exposure Build-Up Factor (EBF)

As shown in Figure 10, the exposure build-up factor (EBF) values for the prepared glass samples (S0–S4) were calculated using the geometrical progression (G-P) method with depth penetration of up to 40 mfp and photon energies of up to 15 MeV. The picture also demonstrates that, according to the photoelectric effect interaction mechanism, the EBF values of the produced glass samples are negligible at low photon energies. Additionally, within the intermediate energy range when numerous scatterings about the Compton interactions has happened, the samples' EBF significances rise with the energy of the photons. The calculated EBF values for the pair formation process increase at high photon energies. Additionally, strong peaks can be seen at 0.04 MeV in Figure 8 due to the K-absorption edge of barium (0.037 MeV).

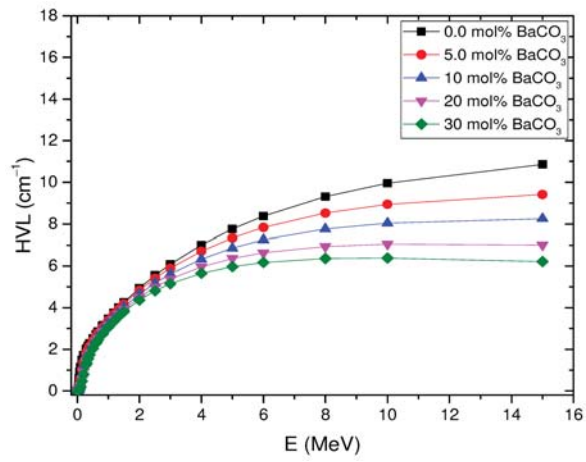
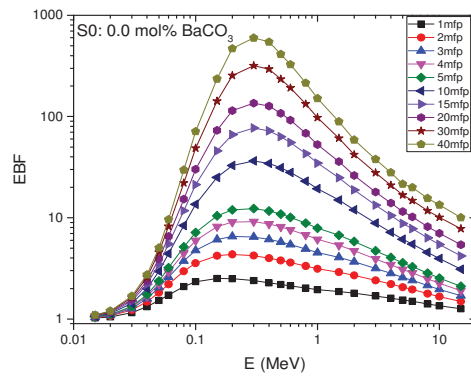
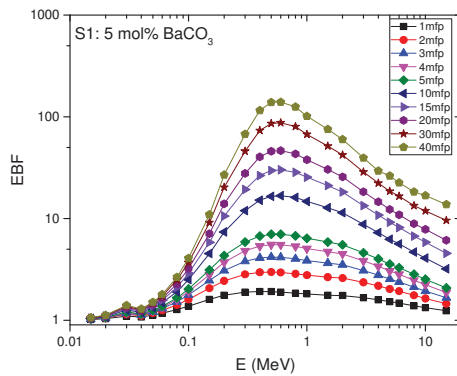


Figure 9. HVL results of 10 Na<sub>2</sub>CO<sub>3</sub> – 20 SiO<sub>2</sub> – 10 ZnO – (60 – x) H<sub>3</sub>BO<sub>3</sub> – x BaCO<sub>3</sub> glass system.



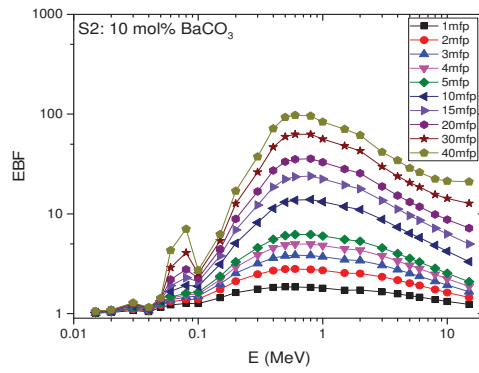
(a)



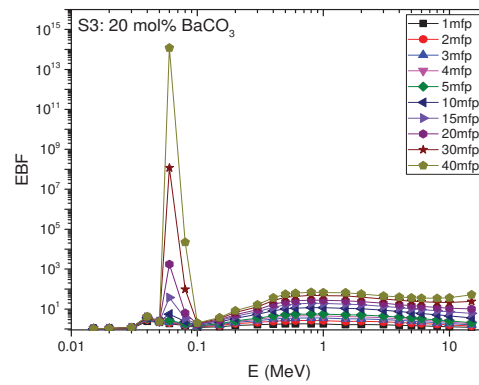
(b)

Figure 10. Cont.

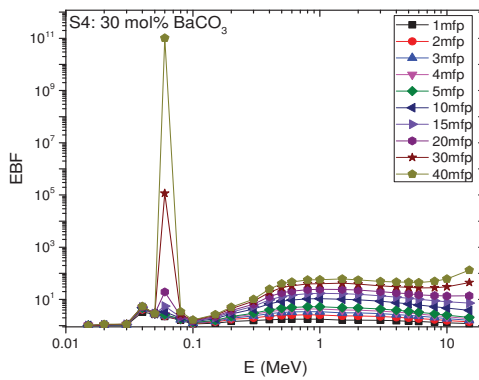




(c)



(d)



(e)

**Figure 10.** EBF of the produced borosilicate glass composite at 0.015 to 15 MeV up to 40 mfp photon energies with (a) 0 mol% BaCO<sub>3</sub>, (b) 5 mol% BaCO<sub>3</sub>, (c) 10 mol% BaCO<sub>3</sub>, (d) 20 mol% BaCO<sub>3</sub>, and (e) 30 mol% BaCO<sub>3</sub>.

## 5. Conclusions

The glass composites  $10 \text{ Na}_2\text{CO}_3 - 20 \text{ SiO}_2 - 10 \text{ ZnO} - (60 - x) \text{ H}_3\text{BO}_3 - x \text{ BaCO}_3$  in the current study have been made using the traditional melting procedure, where  $x = 0, 5, 10, 20, 30$ . The parameters for structural, optical, and gamma attenuation are established. With the addition of  $\text{BaCO}_3$ , the molar volume and mass density measurements revealed an improvement in compactness. Different vibrational bonding modes, including B–O, B–O–B, and B–O–Si, were seen in the produced glasses according to the FTIR data. The effective atomic number ( $Z_{\text{eff}}$ ), mass attenuation coefficients (MAC), and exposure build-up factors (EBF) of the previously described prepared glass samples were computed at various photon energies between 0.015 and 15 MeV. The findings attained may recommend the manufactured glasses for applications requiring transparent shielding.

**Author Contributions:** Formal analysis, E.S.; Methodology, M.E., E.S., A.A. and M.A.; Supervision, E.S. and H.M.S.; Writing—original draft, M.E. and M.A.; Writing—review & editing, E.S. All authors have read and agreed to the published version of the manuscript.

**Funding:** This research received no external funding.

**Institutional Review Board Statement:** Not applicable.

**Informed Consent Statement:** Not applicable.

**Data Availability Statement:** Not applicable.

**Conflicts of Interest:** The authors declare no conflict of interest.

## References

- Majeed, K.F.; Salama, E.; Elfiki, S.A.; Al-Bakhat, Y.M.Z. Natural radioactivity assessment around the petroleum-producing areas of The-Qar province, Iraq. *Environ. Earth Sci.* **2021**, *80*, 64. [[CrossRef](#)]
- Farah, K.; Mejri, A.; Hosni, F.; Ben Ouada, H.; Fuochi, P.G.; Lavallo, M.; Kovács, A. Characterization of a silicate glass as a high dose dosimeter. *Nucl. Instrum. Methods Phys. Res. Sect. A Accel. Spectrometers Detect. Assoc. Equip.* **2010**, *614*, 137–144. [[CrossRef](#)]
- DWK Life Sciences Glassware Technical Information. *Glas. Types Prop.* **2022**, 12–19.
- Jubier, N.J. Estimation of Radiation Shielding Properties for Composites Material Based Unsaturated Polyester Filled with Granite and Iron Particles. *J. Multidiscip. Eng. Sci. Stud.* **2017**, *3*, 1309–1316.
- Khanna, A.; Bhatti, S.S.; Singh, K.J.; Thind, K.S. Gamma-ray attenuation coefficients in some heavy metal oxide borate glasses at 662 keV. *Nucl. Instrum. Methods Phys. Res. Sect. B Beam Interact. Mater. Atoms* **1996**, *114*, 217–220. [[CrossRef](#)]
- Oto, B.; Gür, A.; Kavaz, E.; Çakır, T.; Yaltay, N. Determination of gamma and fast neutron shielding parameters of magnetite concretes. *Prog. Nucl. Energy* **2016**, *92*, 71–80. [[CrossRef](#)]
- Mesbahi, A.; Ghiasi, H. Shielding properties of the ordinary concrete loaded with micro-and nano-particles against neutron and gamma radiations. *Appl. Radiat. Isot.* **2018**, *136*, 27–31. [[CrossRef](#)]
- Shimizu, A.; Onda, T.; Sakamoto, Y. Calculation of gamma-ray buildup factors up to depths of 100 mfp by the method of invariant embedding, (III). *J. Nucl. Sci. Technol.* **2004**, *41*, 413–424. [[CrossRef](#)]
- Singh, K.; Singh, H.; Sharma, V.; Nathuram, R.; Khanna, A.; Kumar, R.; Singh Bhatti, S.; Singh Sahota, H. Gamma-ray attenuation coefficients in bismuth borate glasses. *Nucl. Instrum. Methods Phys. Res. Sect. B Beam Interact. Mater. Atoms* **2002**, *194*, 1–6. [[CrossRef](#)]
- Durani, L. Update to ANSI/ANS-6.4.3-1991 for Low-Z and Compound Materials and Review of Particle Transport Theory. Master's Thesis, University of Nevada, Las Vegas, NV, USA, 2009.
- Dawoud, M.M.A.; Hegazi, M.M.; Saleh, H.M.; El Helew, W.K. Removal of stable and radio isotopes from wastewater by using modified microcrystalline cellulose based on Taguchi L16. *Int. J. Environ. Sci. Technol.* **2022**, 1–12. [[CrossRef](#)]
- Dawoud, M.M.A.; Hegazy, M.M.; Helew, W.K.; Saleh, H.M. Overview of Environmental Pollution and Clean Management of Heavy Metals and Radionuclides by using Microcrystalline Cellulose. *J. Nucl. Energy Sci. Power Gener. Technol.* **2021**, *3*, 2.
- Saleh, H.M.; Bondouk, I.I.; Salama, E.; Esawii, H.A. Consistency and shielding efficiency of cement-bitumen composite for use as gamma-radiation shielding material. *Prog. Nucl. Energy* **2021**, *137*, 103764. [[CrossRef](#)]
- Reda, S.M.; Saleh, H.M. Calculation of the gamma radiation shielding efficiency of cement-bitumen portable container using MCNPX code. *Prog. Nucl. Energy* **2021**, *142*, 104012. [[CrossRef](#)]
- Eid, M.S.; Bondouk, I.I.; Saleh, H.M.; Omar, K.M.; Sayyed, M.I.; El-Khatib, A.M.; Elsafi, M. Implementation of waste silicate glass into composition of ordinary cement for radiation shielding applications. *Nucl. Eng. Technol.* **2021**, *54*, 1456–1463. [[CrossRef](#)]
- Eskander, S.B.; Saleh, H.M.; Tawfik, M.E.; Bayoumi, T.A. Towards potential applications of cement-polymer composites based on recycled polystyrene foam wastes on construction fields: Impact of exposure to water ecologies. *Case Stud. Constr. Mater.* **2021**, *15*, e00664. [[CrossRef](#)]

17. Saleh, H.; Salman, A.; Faheim, A.; El-Sayed, A. Polymer and polymer waste composites in nuclear and industrial applications. *J. Nucl. Energy Sci. Power Gener. Technol.* **2020**, *9*, 1000199.
18. Saleh, H.M.; Eskander, S.B. Impact of water flooding on hard cement-recycled polystyrene composite immobilizing radioactive sulfate waste simulate. *Constr. Build. Mater.* **2019**, *222*, 522–530. [[CrossRef](#)]
19. Saleh, H.M.; El-Saied, F.A.; Salaheldin, T.A.; Hezo, A.A. Influence of severe climatic variability on the structural, mechanical and chemical stability of cement kiln dust-slag-nanosilica composite used for radwaste solidification. *Constr. Build. Mater.* **2019**, *218*, 556–567. [[CrossRef](#)]
20. Saleh, H.M.; El-Sheikh, S.M.; Elshereafy, E.E.; Essa, A.K. Performance of cement-slag-titanate nanofibers composite immobilized radioactive waste solution through frost and flooding events. *Constr. Build. Mater.* **2019**, *223*, 221–232. [[CrossRef](#)]
21. Saleh, H.M.; Salman, A.A.; Faheim, A.A.; El-Sayed, A.M. Sustainable composite of improved lightweight concrete from cement kiln dust with grated poly (styrene). *J. Clean. Prod.* **2020**, *277*, 123491. [[CrossRef](#)]
22. Saleh, H.M.; Salman, A.A.; Faheim, A.A.; El-Sayed, A.M. Influence of aggressive environmental impacts on clean, lightweight bricks made from cement kiln dust and grated polystyrene. *Case Stud. Constr. Mater.* **2021**, *15*, e00759. [[CrossRef](#)]
23. Singh, V.P.; Badiger, N.M.; Kaewkhao, J. Radiation shielding competence of silicate and borate heavy metal oxide glasses: Comparative study. *J. Non-Cryst. Solids* **2014**, *404*, 167–173. [[CrossRef](#)]
24. Sayyed, M.I.; Tekin, H.O.; Kilicoglu, O.; Agar, O.; Zaid, M.H.M. Shielding features of concrete types containing sepiolite mineral: Comprehensive study on experimental, XCOM and MCNPX results. *Results Phys.* **2018**, *11*, 40–45. [[CrossRef](#)]
25. Hanumantharayappa, C. Study of gamma, X-ray and neutron shielding parameters of some alloys. *IJPAP* **2018**, *56*, 631–634.
26. Abouhaswa, A.S.; Tekin, H.O.; Ahmed, E.M.; Kilicoglu, O.; Rammah, Y.S. Synthesis, physical, linear optical and nuclear radiation shielding characteristics of B<sub>2</sub>O<sub>3</sub>–BaO–PbO–SrO<sub>2</sub> glasses. *J. Mater. Sci. Mater. Electron.* **2021**, *32*, 18163–18177. [[CrossRef](#)]
27. Al-Hadeethi, Y.; Sayyed, M.I. Analysis of borosilicate glasses doped with heavy metal oxides for gamma radiation shielding application using Geant4 simulation code. *Ceram. Int.* **2019**, *45*, 24858–24864. [[CrossRef](#)]
28. Zaid, M.H.M.; Matori, K.A.; Abdul Aziz, S.H.; Zakaria, A.; Ghazali, M.S.M. Effect of ZnO on the physical properties and optical band gap of soda lime silicate glass. *Int. J. Mol. Sci.* **2012**, *13*, 7550–7558. [[CrossRef](#)]
29. Dong, M.G.; Sayyed, M.I.; Lakshminarayana, G.; Çelikbilek Ersundu, M.; Ersundu, A.E.; Nayar, P.; Mahdi, M.A. Investigation of gamma radiation shielding properties of lithium zinc bismuth borate glasses using XCOM program and MCNP5 code. *J. Non-Cryst. Solids* **2017**, *468*, 12–16. [[CrossRef](#)]
30. Tekin, H.O.; Altunsoy, E.E.; Kavaz, E.; Sayyed, M.I.; Agar, O.; Kamislioglu, M. Photon and neutron shielding performance of boron phosphate glasses for diagnostic radiology facilities. *Results Phys.* **2019**, *12*, 1457–1464. [[CrossRef](#)]
31. Sayyed, M.I.; Rammah, Y.S.; Abouhaswa, A.S.; Tekin, H.O.; Elbashir, B.O. ZnO–B<sub>2</sub>O<sub>3</sub>–PbO glasses: Synthesis and radiation shielding characterization. *Phys. B Condens. Matter* **2018**, *548*, 20–26. [[CrossRef](#)]
32. Hussein, K.I.; Alqahtani, M.S.; Alzahrani, K.J.; Alqahtani, F.F.; Zahran, H.Y.; Alshehri, A.M.; Yahia, I.S.; Reben, M.; Yousef, E.S. The Effect of ZnO, MgO, TiO<sub>2</sub>, and Na<sub>2</sub>O Modifiers on the Physical, Optical, and Radiation Shielding Properties of a TeTaNb Glass System. *Materials* **2022**, *15*, 1844. [[CrossRef](#)]
33. Tijani, S.A.; Kamal, S.M.; Al-Hadeethi, Y.; Arib, M.; Hussein, M.A.; Wageh, S.; Dim, L.A. Radiation shielding properties of transparent erbium zinc tellurite glass system determined at medical diagnostic energies. *J. Alloys Compd.* **2018**, *741*, 293–299. [[CrossRef](#)]
34. Shams, T.; Eftekhar, M.; Shirani, A. Investigation of gamma radiation attenuation in heavy concrete shields containing hematite and barite aggregates in multi-layered and mixed forms. *Constr. Build. Mater.* **2018**, *182*, 35–42. [[CrossRef](#)]
35. Kindrat, I.I.; Padlyak, B.V.; Drzewiecki, A. Intrinsic luminescence of un-doped borate glasses. *J. Lumin.* **2017**, *187*, 546–554. [[CrossRef](#)]
36. Singh, N.; Singh, K.J.; Singh, K.; Singh, H. Comparative study of lead borate and bismuth lead borate glass systems as gamma-radiation shielding materials. *Nucl. Instrum. Methods Phys. Res. Sect. B Beam Interact. Mater. Atoms* **2004**, *225*, 305–309. [[CrossRef](#)]
37. AlBuriah, M.S.; Hegazy, H.H.; Alresheedi, F.; Olanoye, I.O.; Algarni, H.; Tekin, H.O.; Saudi, H.A. Effect of CdO addition on photon, electron, and neutron attenuation properties of boro-tellurite glasses. *Ceram. Int.* **2021**, *47*, 5951–5958. [[CrossRef](#)]
38. Kaur, R.; Singh, S.; Pandey, O.P. Structural variation in gamma ray irradiated PbO–Na<sub>2</sub>O–B<sub>2</sub>O<sub>3</sub>–SiO<sub>2</sub> glasses. *Solid State Commun.* **2014**, *188*, 40–44. [[CrossRef](#)]
39. Marzouk, S.Y.; Seoudi, R.; Said, D.A.; Mabrouk, M.S. Linear and non-linear optics and FTIR characteristics of borosilicate glasses doped with gadolinium ions. *Opt. Mater.* **2013**, *35*, 2077–2084. [[CrossRef](#)]
40. Bootjomchai, C.; Laopaiboon, J.; Yenchai, C.; Laopaiboon, R. Gamma-ray shielding and structural properties of barium-bismuth-borosilicate glasses. *Radiat. Phys. Chem.* **2012**, *81*, 785–790. [[CrossRef](#)]
41. Salama, E.; Soliman, H.A.; Youssef, G.M.; Hamad, S. Thermoluminescence Properties of Borosilicate Glass Doped with ZnO Thermoluminescence properties of borosilicate glass doped with ZnO. *J. Lumin.* **2018**, *186*, 164–169. [[CrossRef](#)]
42. Alajerami, Y.S.M.; Hashim, S.; Ghoshal, S.K.; Bradley, D.A.; Mhareb, M.; Saleh, M.A. Copper doped borate dosimeters revisited. *J. Lumin.* **2014**, *155*, 141–148. [[CrossRef](#)]
43. Mhareb, M.H.A.; Alqahtani, M.; Alshahri, F.; Alajerami, Y.S.M.; Saleh, N.; Alonizan, N.; Sayyed, M.I.; Ashiq, M.G.B.; Ghrib, T.; Al-Dhafar, S.I.; et al. The impact of barium oxide on physical, structural, optical, and shielding features of sodium zinc borate glass. *J. Non-Cryst. Solids* **2020**, *541*, 120090. [[CrossRef](#)]

44. Rammah, Y.S.; Tekin, H.O.; Sriwunkum, C.; Olanroye, I.; Alalawi, A.; Al-Buriah, M.S.; Nutaro, T.; Tonguc, B.T. Investigations on borate glasses within SBC-Bx system for gamma-ray shielding applications. *Nucl. Eng. Technol.* **2021**, *53*, 282–293. [\[CrossRef\]](#)
45. Aly, P.; El-Kheshen, A.A.; Abou-Gabal, H.; Agamy, S. Structural investigation and measurement of the shielding effect of borosilicate glass containing PbO, SrO, and BaO against gamma irradiation. *J. Phys. Chem. Solids* **2020**, *145*, 109521. [\[CrossRef\]](#)
46. Sayed El-Ahll, L.; Salama, E.; Saudi, H.A.; Alazab, H.A.; Ghany, H.A.A. The Effect of Barium on the Nuclear Radiation Shielding Capabilities of Nickel-Reinforced Borosilicate Glasses. *Silicon* **2022**, *14*, 8909–8917. [\[CrossRef\]](#)
47. Kavas, T.; Alsufyani, S.J.; Alrowaili, Z.A.; Tamam, N.; Kurtulus, R.; Olanroye, I.O.; Al-Buriah, M.S. Influence of iron (III) oxide on the optical, mechanical, physical, and radiation shielding properties of sodium-barium-vanadate glass system. *Optik* **2022**, *257*. [\[CrossRef\]](#)
48. Mhareb, M.H.A.; Alqahtani, M.; Alajerami, Y.S.M.; Alshahri, F.; Sayyed, M.I.; Mahmoud, K.A.; Saleh, N.; Alonizan, N.; Al-Buriah, M.S.; Kaky, K.M. Ionizing radiation shielding features for titanium borosilicate glass modified with different concentrations of barium oxide. *Mater. Chem. Phys.* **2021**, *272*, 125047. [\[CrossRef\]](#)
49. Aboalatta, A.; Asad, J.; Humaid, M.; Musleh, H.; Shaat, S.K.K.; Ramadan, K.; Sayyed, M.I.; Alajerami, Y.; Aldahoudi, N. Experimental investigation of zinc sodium borate glass systems containing barium oxide for gamma radiation shielding applications. *Nucl. Eng. Technol.* **2021**, *53*, 3058–3067. [\[CrossRef\]](#)
50. Abdel-Baki, M.; Salem, A.M.; Abdel-Wahab, F.A.; El-Diasty, F. Bond character, optical properties and ionic conductivity of  $\text{Li}_2\text{O}/\text{B}_2\text{O}_3/\text{SiO}_2/\text{Al}_2\text{O}_3$  glass: Effect of structural substitution of  $\text{Li}_2\text{O}$  for  $\text{LiCl}$ . *J. Non-Cryst. Solids* **2008**, *354*, 4527–4533. [\[CrossRef\]](#)
51. Singh, D.; Singh, K.; Singh, G.; Manupriya; Mohan, S.; Arora, M.; Sharma, G. Optical and structural properties of  $\text{ZnO-PbO-B}_2\text{O}_3$  and  $\text{ZnO-PbO-B}_2\text{O}_3\text{-SiO}_2$  glasses. *J. Phys. Condens. Matter* **2008**, *20*, 075228. [\[CrossRef\]](#)
52. Rammah, Y.S.; Sayyed, M.I.; Ali, A.A.; Tekin, H.O.; El-Mallawany, R. Optical properties and gamma-shielding features of bismuth borate glasses. *Appl. Phys. A Mater. Sci. Process.* **2018**, *124*, 832. [\[CrossRef\]](#)
53. Rammah, Y.S.; Sayyed, M.I.; Abohaswa, A.S.; Tekin, H.O. FTIR, electronic polarizability and shielding parameters of  $\text{B}_2\text{O}_3$  glasses doped with  $\text{SnO}_2$ . *Appl. Phys. A Mater. Sci. Process.* **2018**, *124*, 650. [\[CrossRef\]](#)
54. Bashter, I.I. Calculation of radiation attenuation coefficients for shielding concretes. *Ann. Nucl. Energy* **1997**, *24*, 1389–1401. [\[CrossRef\]](#)
55. Thakur, S.; Thakur, V.; Kaur, A.; Singh, L. Structural, optical and thermal properties of nickel doped bismuth borate glasses. *J. Non-Cryst. Solids* **2019**, *512*, 60–71. [\[CrossRef\]](#)
56. Gaafar, I.; El-Shershaby, A.; Zeidan, I.; El-Ahll, L.S. Natural radioactivity and radiation hazard assessment of phosphate mining, Quseir-Safaga area, Central Eastern Desert, Egypt. *NRIAG J. Astron. Geophys.* **2016**, *5*, 160–172. [\[CrossRef\]](#)
57. Umar, S.A.; Halimah, M.K.; Chan, K.T.; Amirah, A.A.; Azlan, M.N.; Grema, L.U.; Hamza, A.M.; Ibrahim, G.G. Optical and structural properties of rice husk silicate incorporated borotellurite glasses doped with erbium oxide nanoparticles. *J. Mater. Sci. Mater. Electron.* **2019**, *30*, 18606–18616. [\[CrossRef\]](#)
58. Sayyed, M.I.; Qashou, S.I.; Khattari, Z.Y. Radiation shielding competence of newly developed  $\text{TeO}_2\text{-WO}_3$  glasses. *J. Alloys Compd.* **2017**, *696*, 632–638. [\[CrossRef\]](#)
59. Sathiyaraj, P.; Samuel, E.J.J.; Valeriano, C.C.S.; Kurudirek, M. Effective atomic number and buildup factor calculations for metal nano particle doped polymer gel. *Vacuum* **2017**, *143*, 138–149. [\[CrossRef\]](#)
60. Kavaz, E.; Yorgun, N.Y. Gamma ray buildup factors of lithium borate glasses doped with minerals. *J. Alloys Compd.* **2018**, *752*, 61–67. [\[CrossRef\]](#)
61. El-Kameesy, S.U.; Youssef, G.M.; El-Zaiat, S.Y.; Saudi, H.A.; Abd El-Kawy, F.S. Gamma Rays Attenuation Properties and the Associated Optical and Mechanical Behavior of Development (70-x)  $\text{B}_2\text{O}_3\text{-}10\text{Al}_2\text{O}_3\text{-}10\text{Na}_2\text{O-}10\text{ZnO-x PbO}$  Glasses. *Silicon* **2018**, *10*, 1881–1886. [\[CrossRef\]](#)
62. Harima, Y. An historical review and current status of buildup factor calculations and applications. *Radiat. Phys. Chem.* **1993**, *41*, 631–672. [\[CrossRef\]](#)
63. Kaplan, M.F. *Concrete Radiation Shielding: Nuclear Physics, Concrete Properties, Design and Construction*; Longman Scientific & Technical: New York, NY, USA, 1989; ISBN 0470213388.
64. Singh, V.P.; Badiger, N.M. Gamma ray and neutron shielding properties of some alloy materials. *Ann. Nucl. Energy* **2014**, *64*, 301–310. [\[CrossRef\]](#)
65. ANSI/ANS-6.4.3; Gamma-Ray Attenuation Coefficients and Buildup Factors for Engineering Materials. American Nuclear Society: La Grange Park, IL, USA, 1991.
66. Gomaa, H.M.; Yahia, I.S.; Zahren, H.Y.; Saudi, H.A.; El-Dosokey, A.H. Effect of replacement of  $\text{SiO}_2$  with  $\text{BaTiO}_3$  on the cadmium calcium-borate glass: Aiming to obtain an active glass for optical and shielding applications. *Radiat. Phys. Chem.* **2022**, *193*, 109955. [\[CrossRef\]](#)
67. Huang, W.J.; Wen, Z.X.; Li, L.J.; Ashraf, G.A.; Chen, L.P.; Lei, L.; Guo, H.; Li, X.M. Photoluminescence and X-ray excited scintillating properties of  $\text{Tb}^{3+}$ -doped borosilicate aluminate glass scintillators. *Ceram. Int.* **2022**, *48*, 17178–17184. [\[CrossRef\]](#)
68. Shajan, D.; Murugasen, P.; Sagadevan, S. Analysis on the structural, spectroscopic, and dielectric properties of borate glass. *Dig. J. Nanomater. Biostruct.* **2016**, *11*, 177–183.
69. Mustafa, I.S.; Kamari, H.M.; Wan Yusoff, W.M.D.; Aziz, S.A.; Rahman, A.A. Structural and optical properties of lead-boro-tellurite glasses induced by Gamma-ray. *Int. J. Mol. Sci.* **2013**, *14*, 3201–3214. [\[CrossRef\]](#)

70. Yadav, A.K.; Gautam, C.R. Structural and optical studies of Fe<sub>2</sub>O<sub>3</sub> doped barium strontium titanate borosilicate glasses. *Indian J. Pure Appl. Phys.* **2015**, *53*, 42–48.
71. Rani, S.; Sanghi, S.; Agarwal, A.; Seth, V.P. Study of optical band gap and FTIR spectroscopy of Li<sub>2</sub>O-Bi<sub>2</sub>O<sub>3</sub>-P<sub>2</sub>O<sub>5</sub> glasses. *Spectrochim. Acta—Part A Mol. Biomol. Spectrosc.* **2009**, *74*, 673–677. [[CrossRef](#)]
72. Yadav, A.K.; Gautam, C.R. Synthesis, structural and optical studies of barium strontium titanate borosilicate glasses doped with ferric oxide. *Spectrosc. Lett.* **2015**, *48*, 514–520. [[CrossRef](#)]
73. Gautam, C.; Yadav, A.K.; Mishra, V.K.; Vikram, K. Synthesis, IR and Raman Spectroscopic Studies of (Ba,Sr)TiO<sub>3</sub> Borosilicate Glasses with Addition of La<sub>2</sub>O<sub>3</sub>. *Open J. Inorg. Non-Metallic Mater.* **2012**, *2*, 47–54. [[CrossRef](#)]
74. Gautam, C.R.; Kumar, D.; Parkash, O. IR study of Pb-Sr titanate borosilicate glasses. *Bull. Mater. Sci.* **2010**, *33*, 145–148. [[CrossRef](#)]
75. Mandal, A.K.; Agrawal, D.; Sen, R. Preparation of homogeneous barium borosilicate glass using microwave energy. *J. Non-Cryst. Solids* **2013**, *371–372*, 41–46. [[CrossRef](#)]
76. Study, S.; Consumption, L.E.; Part, D.U.; Utilization, D.; Yoshizawa, N.; Harimoto, K.; Ichihara, M.; Miki, Y.; Takase, K.; Inoue, T. Synthesis, Characterization and Bioactive Study of Borosilicate Sol-Gel Glass Khairy. *Nat. Sci.* **2015**, *13*, 475–476.
77. Rada, S.; Dehelean, A.; Culea, E. FTIR and UV-VIS spectroscopy investigations on the structure of the europium-lead-tellurate glasses. *J. Non-Cryst. Solids* **2011**, *357*, 3070–3073. [[CrossRef](#)]
78. Saudi, H.A.; Abd-Allah, W.M.; Shaaban, K.S. Investigation of gamma and neutron shielding parameters for borosilicate glasses doped europium oxide for the immobilization of radioactive waste. *J. Mater. Sci. Mater. Electron.* **2020**, *31*, 6963–6976. [[CrossRef](#)]
79. Alzahrani, J.S.; Alrowaili, Z.A.; Olarinoye, I.O.; Alothman, M.A.; Al-Baradi, A.M.; Kebaili, I.; Al-Buriah, M.S. Nuclear shielding properties and buildup factors of Cr-based ferroalloys. *Prog. Nucl. Energy* **2021**, *141*, 103956. [[CrossRef](#)]



## Article

# Transfer of Natural Radionuclides from Soil to Abu Dhabi Date Palms

Prasoon Raj <sup>1,\*</sup>, Nemeer Padiyath <sup>1</sup>, Natalia Semioshkina <sup>2</sup>, Francois Foulon <sup>1</sup>, Ahmed K. Alkaabi <sup>1</sup>, Gabriele Voigt <sup>2</sup> and Yacine Addad <sup>1</sup>

<sup>1</sup> Emirates Nuclear Technology Center (ENTC), Department of Nuclear Engineering, Khalifa University (KU), Abu Dhabi P.O. Box 127788, United Arab Emirates

<sup>2</sup> Cognitive Radioecology, r.e.m. GbR, Liebigstr. 3, 80538 Munich, Germany

\* Correspondence: prason.raj@ku.ac.ae or prason.raj@outlook.com

**Abstract:** Nuclear power and modern agriculture are two crucial sectors for sustainable development in the United Arab Emirates (UAE). As these industries mature rapidly in the country, their long-term inter-compatibility needs monitoring with local data on transfer of radionuclides from arid sandy soils to farm products. Date palms, main crop from the Arabian Peninsula, remain largely unstudied for radioecological impact assessments. This paper reports the first measurement of soil to UAE date palms concentration ratios for natural radionuclides. Representative samples of soils, fruits, and leaves from seven palms in Abu Dhabi have been studied using gamma-spectrometry. Average activity concentrations in the soils are around 278.9 Bq kg<sup>-1</sup> for <sup>40</sup>K, 15.5 Bq kg<sup>-1</sup> for <sup>238</sup>U, and 8.3 Bq kg<sup>-1</sup> for <sup>232</sup>Th. The latter two decay chains, in the plant samples, are close to detection limits, signifying their lower levels in the UAE flora and the need for upgrading analytical techniques. The geometric means of soil to fruit concentration ratios are 1.12 for <sup>40</sup>K, but negligibly low for the others—approximately 0.08 for <sup>238</sup>U and 0.17 for <sup>232</sup>Th chains. The respective ratios for the leaves are approximately 0.13, 0.36, and 0.77. Personal radiation doses due to soils and dates are very low, posing no danger to the public.

**Keywords:** radioecology; nuclear power; soil radioactivity; plant sciences; agricultural sustainability; energy studies; arid land; impact assessment; NORM; potassium; middle east

**Citation:** Raj, P.; Padiyath, N.; Semioshkina, N.; Foulon, F.; Alkaabi, A.K.; Voigt, G.; Addad, Y. Transfer of Natural Radionuclides from Soil to Abu Dhabi Date Palms. *Sustainability* **2022**, *14*, 11327. <https://doi.org/10.3390/su141811327>

Academic Editors: Hosam M. Saleh and Mohammad Mahmoud Dawoud

Received: 18 July 2022

Accepted: 3 September 2022

Published: 9 September 2022

**Publisher's Note:** MDPI stays neutral with regard to jurisdictional claims in published maps and institutional affiliations.



**Copyright:** © 2022 by the authors. Licensee MDPI, Basel, Switzerland. This article is an open access article distributed under the terms and conditions of the Creative Commons Attribution (CC BY) license (<https://creativecommons.org/licenses/by/4.0/>).

## 1. Introduction

### 1.1. Radioecology vis-à-vis Nuclear Power in the Arabian Peninsula

In wake of the increasing energy demands in the Arab countries, nuclear power programs are being accelerated in the region, towards a more sustainable future energy mix [1]. Legacy and future nuclear activities are known to put risks of trace radioactivity releases in the environments [2]. The so-released radionuclides may undergo a complex, long-term transport to human food, via wind, rain, waterbodies, soil, plants, animals, etc., as studied under a collective science called radioecology. It is critical to conduct thorough radiological impact assessments (RIA) [3] and to develop nuclear emergency-preparedness systems, for combatting adverse bioecological impacts of such a transfer chain. To that end, at Emirates Nuclear Technology Center (ENTC), we are undertaking baseline radioecological studies in the United Arab Emirates (UAE). A particularly novel challenge is present in the UAE's modern agriculture sector, which is simultaneously progressing to address the food self-sufficiency concerns of the Arab nations [4].

In agricultural farms, radionuclides deposited on the soil are absorbed by plants through their roots [2]. This transfer process is termed as root uptake and is characterized by the radionuclide activity concentrations (AC, units: Bq kg<sup>-1</sup>) in plant parts and rhizosphere soils, as well as their relative value, i.e., the *plant:soil* concentration ratio (CR). The AC and CR parameters are important inputs for computational prediction of the radioisotope



phytoextraction efficiencies following a radioactivity release scenario. Such a calculation assists in predicting cumulative doses to the humans and biota, and furthermore, in optimizing the immediate and long-term mitigation solutions. It also supports the future land decontamination and waste management efforts using phytoremediation. In this regard, the soil–plant bio-transfer kinetics of native plants is crucial to investigate further, but remains severely understudied for arid lands [5,6].

Arid region radioecology (ARRE) is a developing subject to gather more radionuclide transfer factor (TF) data, such as CR, specific to crops, climates, and practices prevalent in arid nations, which are substantially different from temperate regions [7]. It attends to the less explored features [6], such as the physiochemistry of sandy soils, bio-saline growth media, perennial crops such as date palms, heavy irrigation, large usage of chemicals, etc. ARRE not only supports the Arab nations, but also the drylands globally, covering around half of the earth's territory. Moreover, it equips us for better decision-making under changing climatic conditions, which may push many more regions towards aridity in the years to come. The ARRE knowledge will help establish the long-term inter-compatibility of nuclear power and modern agriculture, advocate safety of the nuclear operations and waste management plans to the experts and the public, and finally, support the wider adoption of nuclear electricity for sustainable development.

### 1.2. Soil and Date Palm Studies in the UAE

Having made substantial progress in nuclear energy through the Barakah Nuclear Power Plant (BNPP) [8], as well as arid agriculture, the UAE serves as a great platform for radioecological activities. Presently, the focus sources of environmental radionuclides in the UAE are naturally occurring radioactive materials (NORM) from fossil fuel industries, and artificial radionuclides (ARN) from the global fallout (mainly  $^{137}\text{Cs}$ ) [9]. For emergency-preparedness, academic consideration of reactor emissions is also warranted in future activities, especially radionuclides such as  $^{134,137}\text{Cs}$ ,  $^{89,90}\text{Sr}$ ,  $^{58,60}\text{Co}$ ,  $^{131}\text{I}$ , etc.

In the UAE's agriculture, date palms (*Phoenix dactylifera* L.) make the main crop, topmost exported entity, and most traditional food. Native date palms are systematically propagated for sustainable land and biodiversity managements. Palm cultivars occupy more than 390 km<sup>2</sup> of land, amounting to an annual produce of approximately 340 kton, valued at USD 500–800 million [10]. With about 40 million trees of over 100 gene-varieties, the UAE's dates constitute 12% of the world's total supply [11]. Besides the fruits, its leaves, pits, wood, and other parts are also used for consumer products [12]. So, we have identified the root uptake CR and bioaccumulation of natural radionuclides from soil to the date palms as an important baseline data to measure in the UAE [6].

Past studies on the UAE soils report approximately mean activity concentrations of the key NORMs; of  $^{238}\text{U}$  as 17.8 Bq kg<sup>-1</sup>, of  $^{232}\text{Th}$  as 5.2 Bq kg<sup>-1</sup>, and of  $^{40}\text{K}$  as 182 Bq kg<sup>-1</sup> [9]. Limited measurements of the date fruits from the UAE's commercial producers have concluded low activities of NORMs, with mean values ~0.66 Bq kg<sup>-1</sup> for  $^{226}\text{Ra}$  ( $^{238}\text{U}$  series), ~0.15 Bq kg<sup>-1</sup> for  $^{228}\text{Ra}$  ( $^{232}\text{Th}$  series), and 277 Bq kg<sup>-1</sup> for  $^{40}\text{K}$  [9,13,14]. However, *plant:soil* CR estimates of any kind are practically absent from the UAE's literature. For the date palms, CR values are scarce even from the worldwide literature, except for a few cases [15,16].

### 1.3. Objectives of the Research

This paper reports a pilot field experiment to estimate baseline *plant:soil* CR of the UAE date palms. The research aims to develop and assess an internationally traceable procedure for CR experiments in arid areas, to obtain the first comprehensive estimates of CRs of natural gamma-emitting radionuclides, to document the farm practices unique to the arid geographies such as the UAE, and, to improve understanding of the NORM migration kinetics in date palms. Seven different palm samples with their surrounding soils have been collected and gamma-assayed in Abu Dhabi (the capital city of the UAE). As the first of its kind, this paper details the consistent and reproducible protocols for sample

processing, specific logistical challenges, as well as a detailed analysis of the measured data on soil physiochemistry and CRs. It discusses some essential correlations between soil characteristics and radionuclide speciation and provides conservative risk factors due to background radioactivity in soils and date fruits. Finally, a future program to create a database of radioecological parameters for the UAE agricultural crops is outlined, to complete gaps of the existing global ARRE databases [7].

## 2. Materials and Methods

The pilot study on date palm CR measurements was conducted in the *Sas-al-Nakhl* locality (SAN in short, the term literally translated from Arabic stands for ‘village of the date palms’) of Abu Dhabi (UAE) (Figure 1A). Date palms are perennial, woody trees, living up to 60 years, fruiting from as early as 4 years of age, and are particularly tolerant towards very harsh summer temperatures as well as high soil salinities [17]. Date fruits are rich in nutrients, and often, particularly in urban settings, are allowed to ripen on the tree. Trees can grow to 10–20 m in height. They have compound leaves, 2–4 m long, comprised of a thick midrib, and green-coloured pinnae, also known as leaflets. Depending on the location, the roots extend in soil to a depth of 50–60 cm. Date palms, prime among the few native trees, hold an indispensable position in the Arabic food and traditions, and are important for soil, land, and biodiversity conservation. For their safe cultivation and propagation alongside the radioisotope remnants in environments, detailed research is needed in the UAE on date palm phytoremediation capabilities.



**Figure 1.** (A) Sampling location with tree spots (numbered I–VII) in KU SAN Campus, and the nearby Abu Dhabi landmarks in inset; (B) a sampled date palm tree with soil sampling spots (yellow circles); (C) canopy of a sampled tree with fruit bunches and compound leaves; (D) method of soil sampling using a manual Auger; (E) photographs of the representative portions of date fruit samples. Several species varieties could be seen in the photographs in (E).

### 2.1. Sampling

The sampling location is in the SAN campus of Khalifa University (KU), south-east of the Abu Dhabi city (Figure 1A), which has around 100 date palms. Soils are primarily

Torripsaments [18] transported from agricultural areas of the UAE, treated monthly with bio compost and macronutrient fertilizers, and watered daily with drip irrigation. These are common practices in the commercial farms as well. Due to saline infertile soil cover in the city, artificial assembly of desert soil layers is done in most of the date palm farms. This makes the KU locations representative for the baseline data measurements.

Date palms typically follow a long growth period, from pollination in February–March to final harvest in July–August. Because of the COVID-19 related restrictions in 2020, the harvests were delayed. In September 2020, 14 palm trees were sampled. Fruits were plucked in their tamr stage (fully ripe), but some kimri and khalal stages (mature but unripe) could also be collected. From 2 kg to 4 kg fresh bunches were carefully detached, from two directions of the tree. Two large leaves with midribs were sampled from two directions. For the barks, around 20 cm long pieces were sliced from surface, but deeper layers could not be sampled to avoid damage to the palms. For each tree, soil was collected at 4–6 randomized spots under the canopy (Figure 1B), to an average depth of 22 cm, using a 10 cm diameter soil Auger (Figure 1D), and mixed to make one composite sample per tree.

## 2.2. Sample Processing

Date fruits were detached from the pedicels (see Figure 1C,E). Likewise, green leaflets were separated from the thick midribs of each compound leaf. A sample processing methodology was developed following the internationally acclaimed technique for radionuclide measurements in biological samples [3], and a careful adaptation of similar studies conducted elsewhere on fruits and vegetables [19,20]. In the end, for each of the 14 palms under study, 1 sample each of fruit (pulp with skin), pit/seed, pedicel, leaflet, leaf midrib, upper bark, and soil were obtained. In this phase of the experiment, fruit, leaflet, and soil samples from only seven of the palm trees were completed and reported. Numbered I to VII, in Figure 1, samples with fully ripe fruits were selected. In this paper, only ripe edible pulp (with skin) of the dates are referred to as ‘fruit’, and the green leaflets as ‘leaf’. Quantities of fruit pits, midribs and barks are relatively more difficult to analyse in the current setting of detector-sample geometry and are postponed for the next phase of this study.

Fruits were gently washed 2–3 times under tap water to remove dust and dirt. Then they were washed with distilled water and left on paper towels to air-dry for one night. The following day, they were cut lengthwise into multiple 1–2 cm wide pieces. Date-pits were separated and stored, while the fruit pieces were spread on steel plates and allowed to dry to a constant weight, in a forced-air convection oven at 100–105 °C. For the seven fruit samples, the net weight reduction due to heating, which amounts to the water content of the fruits, varied between 24% and 34%, and averaged around 26%. Dried fruit pieces were ground using a heavy-duty centrifugal mill. For some samples, the fruits were too sticky because of their high sugar-content. Those samples were briefly embrittled by dipping in liquid nitrogen bath, then immediately ground, and re-dried for the removal of any additional moisture absorbed during air-condensation [21]. Leaves were cleaned multiple times, cut, oven-dried, ground, and packed in the same manner as the fruits. The average moisture content in the leaves was found to be around 38%. Finally, the dried ground powders of fruits and leaves were sieved to <2 mm grain size and packed in 1 L polyethylene bottles. Homogenous and tight pack geometry was ensured. The average net weight of fruits packed in a bottle was about 704 g, while that of leaves was about 382 g. The bottles were properly capped. A two-layer air-tight sealing was done for the caps using aluminium-backed tapes topped with two rounds of polyvinyl tapes.

Soil samples were at first sieved to remove larger chunks of rocks, debris, roots, etc. Then they were thoroughly homogenized by mixing in large plastic drums. Around 1 kg units of wet soil were packed in air-tight zip lock bags for physiochemical analyses. The rest were oven dried like the plant samples, sieved to <2 mm, and packed in 1 L tin cans, each typically packing 1.2 kg to 1.5 kg of dried soils. After securing the caps, a thin ~5 mm layer of molten wax was applied to seal the containers. All the sealed sample bottles and

cans were stored for around one month (time > ten half-lives of  $^{222}\text{Rn}/^{224}\text{Ra}$ ) to ensure radioactivity secular equilibrium between  $^{226}\text{Ra}$  and its progenies [22].

### 2.3. Analytical Techniques

Wet (homogenized, unprocessed) soil samples were studied for their physiochemical properties (Table 1) such as pH, organic matter content (OM), cation exchange capacity (CEC), electrical conductivity (EC), moisture content, and USDA texture class [23], using standardized soil analysis techniques [24,25].

**Table 1.** Minimum (Min.), maximum (Max.) and AM (Avg.) of the physicochemical characteristics of the soil samples. Parameters include pH, electrical conductivity (EC, unit:  $\text{dS m}^{-1}$ ), organic matter content (OM, unit: weight %), percent moisture content (Mois.), cation exchange capacity (CEC, unit:  $\text{meq (100 g)}^{-1}$ ), and soil texture, i.e., the percentage contents of clay, silt, and sand.

|                 | pH                                                                      | EC   | OM  | Mois. | CEC | Clay | Silt | Sand |
|-----------------|-------------------------------------------------------------------------|------|-----|-------|-----|------|------|------|
|                 | Aggregate of Sample Numbers I to V and VII (excluding Sample number VI) |      |     |       |     |      |      |      |
| Min.            | 7.4                                                                     | 1.2  | 1.8 | 2.0   | 4.8 | 1.6  | 1.2  | 91.3 |
| Max.            | 7.6                                                                     | 2.8  | 2.8 | 16.0  | 8.2 | 3.9  | 4.9  | 96.5 |
| Avg.            | 7.5                                                                     | 1.9  | 2.2 | 9.6   | 6.8 | 2.7  | 2.6  | 94.4 |
|                 | Aggregate of all seven samples                                          |      |     |       |     |      |      |      |
| Sample# VI      | 7.5                                                                     | 52.3 | 2.0 | 6.9   | 5.8 | 4.8  | 7.8  | 87.3 |
| Avg. (I to VII) | 7.5                                                                     | 9.1  | 2.1 | 9.2   | 6.6 | 3.0  | 3.3  | 93.4 |

The processed samples of soils, fruits and leaves were assayed for their gamma spectra using two cylindrical high-purity germanium (HPGe) detectors, located at the Emirates Nuclear Energy Corporation (ENEC) [8] Environmental Radiochemistry Laboratory (ERL). The detectors' relative efficiencies are 40% and 60%, and the energy resolution is 1.9 keV at 1332 keV. They are calibrated for energy and efficiency using a calibration standard containing 105 kBq mixed gamma radionuclides (EZAG 8503 mixture), in the same geometries as the sample containers. Counting times on HPGe detectors were limited to 4 h for soil samples in tin cans and 16 h for plant samples in plastic bottles. The measurement characteristics are optimized for higher processing speeds as per the program requirements of the ERL. Quality assurance for natural radionuclide quantification in environmental matrices is achieved by frequent comparison with certified reference materials, successful participation in standardized proficiency tests (PT) conducted by International Atomic Energy Agency (IAEA) and other top bodies.

NORM measurement protocols as per Ref. [22] were followed. A wide range of radionuclides with progenies from each series were set to be identified, including but not limited to  $^{235/238}\text{U}$ ,  $^{228/232/234}\text{Th}$ ,  $^{224/226/228}\text{Ra}$ ,  $^{210/212/214}\text{Pb}$ ,  $^{212/214}\text{Bi}$ ,  $^{228}\text{Ac}$ ,  $^{208}\text{Tl}$ , and  $^{40}\text{K}$ . A priori minimum detectable activities (MDA), in units of  $\text{Bq kg}^{-1}$ , for the five key radionuclides are: [ $^{40}\text{K}$ : 2.41,  $^{214}\text{Bi}$ : 1.53,  $^{214}\text{Pb}$ : 1.65,  $^{228}\text{Ac}$ : 2.72, and  $^{208}\text{Tl}$ : 2.23] in 1 L plastic bottles used for plant samples, while [ $^{40}\text{K}$ : 11.7,  $^{214}\text{Bi}$ : 2.61,  $^{214}\text{Pb}$ : 2.85,  $^{228}\text{Ac}$ : 4.65, and  $^{208}\text{Tl}$ : 3.70] in 1 L tin cans used for soil samples. The spectra were further analysed using GENIE 2000 [26] to obtain the nuclide's activity concentrations, along with the necessary corrections as needed, such as interference and coincidence summing, background and Compton corrections, etc.

### 2.4. Data Treatment

To establish a benchmark for multivariate analyses necessary for the TF experiments in the UAE, the data on soil characteristics were employed in non-parametric Kendall's  $\tau_B$  Rank Correlation tests [27,28]. The results were studied in terms of coefficients of correlation ( $r$ ) and statistical significance ( $p$ ), where  $r > 0.7$  and  $p < 0.05$  have been taken as a measure of strong correlation. This partially helps in understanding radionuclide speciation and fate in the UAE soils, as further nuclear activities and waste remediation efforts are implemented.

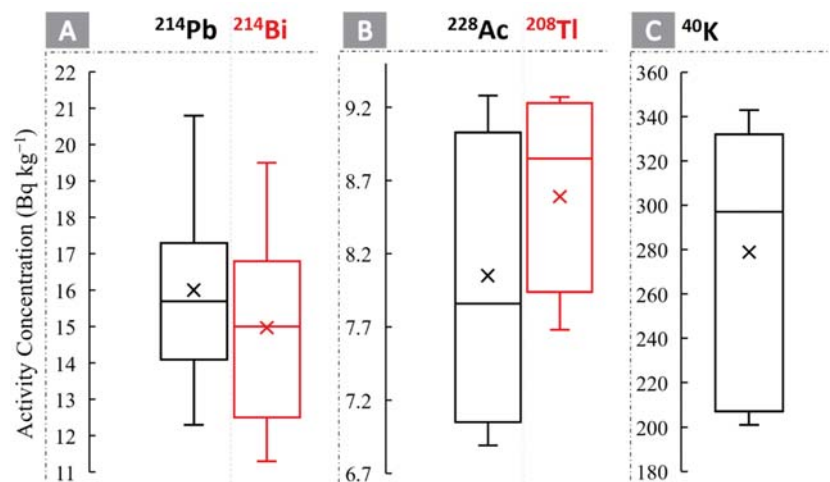
Based on theoretical considerations, biogeological distributions such as the CRs often follow lognormal statistics. Therefore, central tendencies are reported alternatively as arithmetic means (AM) with  $1\sigma$  standard deviations (SD), as well as geometric means (GM) with geometric standard deviations (GSD) [2,7].

### 3. Results and Discussion

#### 3.1. Physiochemistry and Radioactivity of Soils

Table 1 reports the range (minimum and maximum) and average values (excluding sample number VI) of the main characteristics for the six soil samples (I–V and VII). Preliminary studies have concluded that sample number VI has higher salinity due to disposal of wastewater and construction debris in the sampling position. So, in Table 1, characteristics of soil sample VI are reported separately, along with the respective averages for all seven samples. A major difference can be noted in the average values of electrical conductivities. Overall, the sampled soils are slightly alkaline, but near neutral, with an average pH of about 7.5. Their organic matter content is between 1.8% and 2.8%, and moisture is between 2% and 16% of the weight. They have been classified under the USDA texture class: sandy (with an average sand content of 93.4%).

Gamma-spectrometry of the soil samples (each one assayed for about 4 h) yielded clear measurements of all the NORM chains. Box-whisker plots in Figure 2 depict variations of the respective radionuclides over the seven soil samples. For  $^{238}\text{U}$  chain,  $^{214}\text{Pb}$  and  $^{214}\text{Bi}$  have been consistently recorded and their activity concentrations agree with each other very well. Likewise, for the  $^{232}\text{Th}$  chain, progeny radionuclides measured accurately are  $^{228}\text{Ac}$  and  $^{208}\text{Tl}$ , again with excellent inter-agreement. The weighted AM  $\pm$  SD values for activity concentrations of the soils in units  $\text{Bq kg}^{-1}$  are:  $15.5 \pm 2.8$  for  $^{238}\text{U}$ ,  $8.3 \pm 0.8$  for  $^{232}\text{Th}$ , and  $278.9 \pm 57.7$  for  $^{40}\text{K}$ .



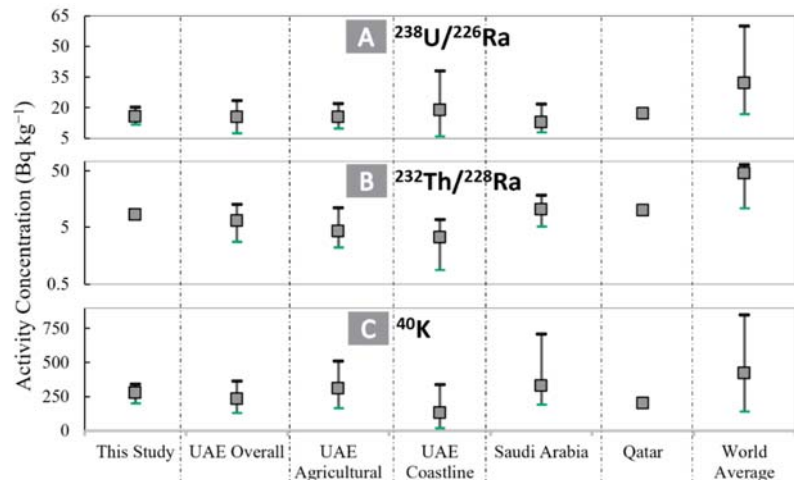
**Figure 2.** Box-whisker plots showing variabilities of activity concentrations (in unit:  $\text{Bq kg}^{-1}$ ) in the seven soil samples for the main measured radionuclides under NORM decay chains of (A)  $^{238}\text{U}$ , (B)  $^{232}\text{Th}$ , and (C)  $^{40}\text{K}$ . X shows the AM of the data.

Radionuclide speciation in soil solids vs. in aqueous solutions in a plant growing soil–water system, are known to be associated with the soil's physiochemical properties [29]. However, such relationships have rarely been established for soils primarily composed of desert sands, as we encountered in this study. A cross-correlation test between various reported parameters have provided some interesting observations, albeit with a very limited number of samples in a small population. There is a clear relationship between



concentrations of  $^{40}\text{K}$  and  $^{214}\text{Bi}$ . The former is also impacted by moisture content in the soil. Moisture, furthermore, has a strong correlation with the organic matter/carbon retention in the soils. Finally, electrical conductivity is found to be positively associated with silt content of the soils, also observable for sample VI in Table 1.

Figure 3 compares the ranges and mean values NORM activity concentrations between various soil studies in the UAE, nearby countries, and world average. Soil NORM activities as measured in this study agrees well with previous measurements conducted in the UAE, with samples specifically from agricultural lands [30], from coastlines [31], as well as those averaging over all territories within the UAE [9].



**Figure 3.** Range (shown with error bars, black dash showing maximum and green the minimum) and AMs (square markers) of soil activity concentrations for (A)  $^{238}\text{U}$ -series, (B)  $^{232}\text{Th}$ -series, and (C)  $^{40}\text{K}$ , as measured in this study, and compared with other measurements in the region. **Sources:** UAE overall [9], UAE agricultural [30], UAE coastline [31], Saudi Arabia [16], Qatar [32], and World [33].

The eastern and western coastlines on the UAE feature some differences, due to differences in geologies, soil makeup [10,18], more rains on the east, and gradient of salinity between the two seas (Arabian Gulf on west, and Arabian Sea on east). The averaging across all coastlines in Ref. [31] has led to relatively lower potassium and thorium contents than urban soils. Abu Dhabi soil radioactivity is very similar to those in Saudi Arabia and Qatar, within the uncertainty margins.

Compared to the world average [33], the activity concentrations of the NORMs in the UAE soils are consistently lower, and well within the recommended limits. Low retention behaviour of sandy soils can be a reason behind the low U and Th values. A comparatively higher content of potassium can be attributed to large-scale application of potassium-containing fertilizers [2,34] in farms, gardens, etc. However, the mean  $^{40}\text{K}$  in soils in the UAE and nearby countries such as Qatar, are lower than the global average. Because caesium and potassium uptakes are known to compete [2], in scenarios of large  $^{137}/^{134}\text{Cs}$  depositions in the local soils, it is probable that low K-levels in soils can promote the uptake of radiocaesium by plants [35].

### 3.2. NORM Concentrations in Date Palms

Unlike the soils, the fruit and the leaf samples from date palms have considerably lower concentrations of NORM radionuclides, except for  $^{40}\text{K}$ . Gamma-spectrometry has quantified the activity concentrations for  $^{238}\text{U}$  and  $^{232}\text{Th}$  in only 3–5 samples each of fruits and leaves. This is based on the weighted means of the same progenies as in Figure 2 and as shown in Table 2. AM of  $^{238}\text{U}$  and  $^{232}\text{Th}$  activity concentrations in both leaves and

fruits vary between 1.1 and 3.2 Bq kg<sup>-1</sup>, with the average concentrations in leaves greater than those in fruits. In general, <sup>232</sup>Th measures slightly higher than <sup>238</sup>U for the plant samples. One of the progenies of <sup>238</sup>U chain, <sup>210</sup>Pb, has been consistently found in 6/7 of the leaf samples, with AM ± SD as 30.3 ± 5.7 Bq kg<sup>-1</sup>, an order of magnitude higher than the weighted mean of the decay chain's radioactivity. This can be due to the superficial contamination of leaves with lead contained in the aerial pollutants, but it requires further experimental verification.

**Table 2.** Measured ranges and averages (in parentheses) of activity concentrations of NORMs radionuclides in leaf and fruit samples from this study. BDL stands for below detection limit. A comparison (bottom part) is shown with similar studies on date fruits in the UAE and Saudi Arabia.

| Ref.                    | Country      | <sup>238</sup> U/ <sup>226</sup> Ra | <sup>232</sup> Th | <sup>40</sup> K  |
|-------------------------|--------------|-------------------------------------|-------------------|------------------|
| <i>Date palm leaf</i>   |              |                                     |                   |                  |
| This study <sup>a</sup> | UAE          | BDL–2.85 (2.05)                     | BDL–4.04 (3.18)   | 75.2–393 (234.2) |
| <i>Date palm fruit</i>  |              |                                     |                   |                  |
| This study <sup>a</sup> | UAE          | BDL–1.47 (1.06)                     | BDL–1.79 (1.43)   | 277–370 (308)    |
| [9] <sup>b</sup>        | UAE          | BDL                                 | BDL               | 173–302 (219)    |
| [14]                    | UAE          | BDL–0.8 (0.66)                      | BDL–0.23 (0.15)   | 191–362 (277)    |
| [13]                    | UAE          | BDL                                 | 0.31–0.62         | 244.8–302.3      |
| [16] <sup>c</sup>       | Saudi Arabia | 1.3–7 (5.6)                         | 1.4–6.3 (2.8)     | 89.5–252 (181)   |
| [36]                    | Saudi Arabia | 1.3–1.4 (1.3)                       | 0.5–0.7 (0.6)     | 137–198 (163)    |
| [15]                    | Saudi Arabia | 1.1–1.5 (1.37)                      | 1.15–1.3 (1.22)   | 123–131 (127)    |

<sup>a</sup> weighted averages of respective progenies are reported. <sup>b</sup> values reported for fresh dates; <sup>c</sup> values reported for date-pits.

The measured concentrations of <sup>40</sup>K are much higher (average of leaves and fruits around 271 Bq kg<sup>-1</sup>) than the other two NORMs. This is due to the large appetite of desert plantations towards macronutrients such as potassium. It is also enhanced by the frequent fertigation using NPK supplements in the soils and waters to sustain the growth and improve yields [10,34]. It is worthwhile to reiterate the competition between the Cs and K uptakes in plants [2]. Larger extraction of potassium, even at <sup>40</sup>K soil concentrations lower than the world average, could mean much higher risks of <sup>137/134</sup>Cs transfers to date palms and other trees in the UAE and nearby countries [35]. Furthermore, phosphates from the fertilizers, depending on their original production process, are known to add considerable amounts of uranium to the soil. This must impact uptake concentrations, which requires a detailed study in future projects.

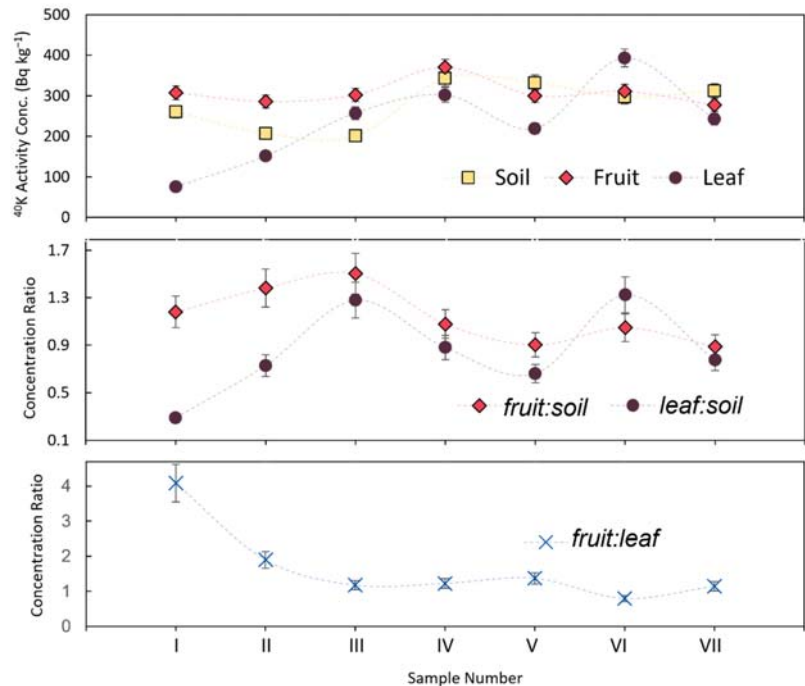
A pragmatic approach has been taken in estimating the low levels of U and Th concentrations in plant samples. These radionuclides have often suffered with large relative uncertainties in the primary gamma-ray peak area (going to 200%). As they are extremely important data to evaluate, all detected cases providing relative uncertainty up to 50–60%, and within gamma line MDA limits have been accepted, to generate at least their rough estimates. In the future, either much higher efficiency gamma-detection setups should be employed, or alternative techniques with lower limits of detection should be developed. However, it is important to point out that the natural contents of NORMs in the UAE's dates have been verified to be extremely low in other works as well (see Table 2). The literature has merely a few instances of the UAE's date fruits gamma-assays, and the U- and Th-series are often below detection limit (BDL) and difficult to quantify. No measurements on leaves are available for comparison. However, for the fruits, averages of previously measured values are consistently lower than the ones reported in this study, although within the statistical variance margins.

### 3.3. Concentration Ratio Estimations

Soil to plant NORM CRs for date palm fruits and leaves have been estimated by taking the ratios of the activity concentrations (Bq kg<sup>-1</sup>) in the plant part to that in the



corresponding soil. After calculating the ratios for each sample, GM and GSD values are calculated to provide central tendencies for each NORM. A complete demonstration of the process is shown for  $^{40}\text{K}$  in Figure 4, with sample-wise variation of  $\text{Bq kg}^{-1}$  in soils, fruits, and leaves, along with CR values for *fruit:soil* and *leaf:soil*, as well as the *fruit:leaf* translocation factor.



**Figure 4.** Sample wise distribution of  $^{40}\text{K}$  measurements: (top) activity concentrations in soil, fruit, and leaf, (middle) CR values *fruit:soil* and *leaf:soil*; and (bottom) CR *fruit:leaf*. The connecting lines are for guidance only.

For the fruits,  $^{40}\text{K}$  CR has a GM of  $1.12 \pm 1.2$ , and for leaves it is  $0.77 \pm 1.6$  (see Table 3). This indicates a preferential bioconcentration of  $^{40}\text{K}$  in the fruits. Dates and nuts are typically potassium-rich fruits [19], which is a possible explanation for  $\text{CR} > 1$ . A comparison has been done for the CR values from this study with the much lower ones available in the literature in Table 3. Ref. [16] cites a recorded  $\text{CR} \sim 0.22$ , while Ref. [15] gives  $\text{CR} \sim 0.55$  for  $^{40}\text{K}$ . A main driver for potassium uptake in the urban Abu Dhabi date palms is the larger application of NPK fertilizers (with potassium in concentrations of 22 kton [11]—much higher than the global average). This observation highlights the need for a detailed study of the impact of fertilizers on the CR values.

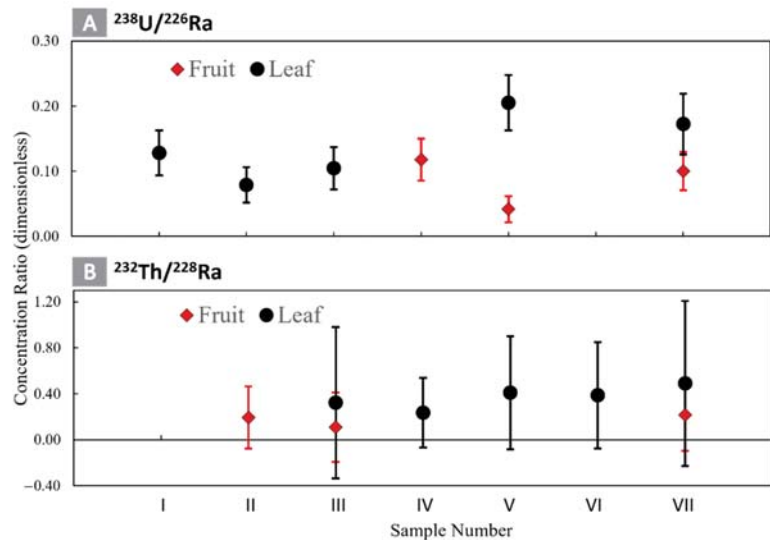
Estimation of CRs for the U- and Th-chains has been difficult due to the low activity concentrations of the corresponding radionuclides in the plant samples. For all the available cases, the measured CRs with  $1\sigma$  uncertainties are plotted in Figure 5. Regarding both of these decay chains, five samples could provide estimates for *leaf:soil* CR, three for *fruit:soil* CR, and two for *fruit:leaf* CR. The mean values of all CRs are reported in Table 3, and are compared with the two literature cases of date palm CR measurements [15,16]. The *fruit:soil* CR for  $^{238}\text{U}$  ( $\text{GM} = 0.08 \pm 1.6$ ) is only 20% deviant from the literature value on Saudi dates. The same comparison is more pronounced for CR of  $^{232}\text{Th}$ , which deviates by more than 40%. Uncertainties in the case of Th chain are much higher than the U chain (see Figure 5). This is mainly because the inherent thorium content in UAE soils (see Figure 2)

is lower by an order of magnitude than uranium, adversely impacting the transfer factor measurements. For some samples, the large uncertainty margins render the  $^{232}\text{Th}$  CR < 0, which is a physically impossible extreme. This brings us to the caveat that the estimated CRs for Th- and U-decay chains in date palms are indicative only.

**Table 3.** Overall values expressed using frequency of observations ( $n$ ), GM and GSD, for the soil-to-plant CRs for leaf and fruit, with fruit:leaf CR. Literature CR value are also shown for comparison.

| Ref.       | CR type    | $^{238}\text{U}/^{226}\text{Ra}$ |                   |                  | $^{232}\text{Th}/^{228}\text{Ra}$ |                   |                  | $^{40}\text{K}$ |      |     |
|------------|------------|----------------------------------|-------------------|------------------|-----------------------------------|-------------------|------------------|-----------------|------|-----|
|            |            | $n$                              | GM                | GSD              | $n$                               | GM                | GSD              | $n$             | GM   | GSD |
| This Study | leaf:soil  | 5                                | 0.13              | 1.4              | 5                                 | 0.36              | 1.3              | 7               | 0.77 | 1.6 |
|            | fruit:soil | 3                                | 0.08              | 1.6              | 3                                 | 0.17              | 1.3              | 7               | 1.12 | 1.2 |
|            | fruit:leaf | 2                                | 0.39 <sup>a</sup> | 0.3 <sup>b</sup> | 2                                 | 0.39 <sup>a</sup> | 0.1 <sup>b</sup> | 7               | 1.46 | 1.6 |
| [15]       | fruit:soil | 5                                | 0.10              | 1.4              | 5                                 | 0.07              | 1.2              | 5               | 0.22 | 1.1 |
| [16]       | pits:soil  | 9                                | 0.33              | 2.1              | 9                                 | 0.22              | 1.8              | 9               | 0.51 | 2.0 |

<sup>a,b</sup> arithmetic mean and arithmetic standard deviation are reported, as  $n \leq 2$ .



**Figure 5.** Sample wise variation of *fruit:soil* CR and *leaf:soil* CR values for (top)  $^{238}\text{U}$  and (bottom)  $^{232}\text{Th}$ . Unlike  $^{40}\text{K}$  in Figure 4, these NORMs were observed in a few samples only. For some cases, very high  $1\sigma$  uncertainties yield CR < 0 as (meaningless) limits.

### 3.4. Aggregated Risk Factors

Obtained average activity concentrations of the soils and plant samples have been used for estimating the conservative ranges of radiation exposure 1 m above the earth surface using the standard methods proposed in Refs. [33,36,37]. For soil and date palm (leaf and fruit), the radium equivalent ( $\text{Ra}_{\text{eq}}$ ), internal hazard index ( $\text{H}_{\text{in}}$ ), absorbed dose ( $\text{D}_{\text{abs}}$ ), and effective dose equivalent ( $\text{D}_{\text{eff}}$ ) are reported in Table 4.

For the fruits, additional calculations are done for per capita annual radioactivity intake based on the measured indicative activity concentrations. This is further used to evaluate the associated committed effective doses. For the risk factors due to fruits, FAOSAT data on the total annual production of dates in the UAE and total population have been employed [11], adding up to give the maximum committed effective dose from consumption of the studied dates, providing conservative risk estimates. All the aggregated dose factors and hazard indices are well within the UAE national [9] and global

limits [33] and pose no risks to the public, as specified in the table. This demonstrates that the phytoextraction of natural radionuclides in the Abu Dhabi date palms are below the safety limits, promising its large-scale propagation in agriculture and landscaping.

**Table 4.** Summary of aggregated doses and risk factors from exposure to NORM baseline radioactivity in soil, leaf, and fruit of date palms, with (bottom part) ingested doses from date fruits, presented with respective global control limits for comparison.

|       | Average Activity Concentration (Bq kg <sup>-1</sup> ) |                                      |                 |                                     |                                                   | D <sub>abs</sub>       | D <sub>eff</sub>       |
|-------|-------------------------------------------------------|--------------------------------------|-----------------|-------------------------------------|---------------------------------------------------|------------------------|------------------------|
|       | <sup>226</sup> Ra/ <sup>238</sup> U                   | <sup>228</sup> Ra/ <sup>232</sup> Th | <sup>40</sup> K | Ra <sub>eq</sub>                    | H <sub>in</sub>                                   | (nGy h <sup>-1</sup> ) | (μSv y <sup>-1</sup> ) |
| Soil  | 15.5                                                  | 8.3                                  | 278.9           | 48.9                                | 0.17                                              | 24.0                   | 29.4                   |
| Leaf  | 2.0                                                   | 3.2                                  | 234.2           | 24.6                                | 0.07                                              | 12.7                   | 15.6                   |
| Fruit | 1.1                                                   | 1.4                                  | 307.6           | 26.8                                | 0.08                                              | 14.2                   | 17.4                   |
|       | Global Limit                                          |                                      |                 | [370]                               | [1]                                               | [55]                   | [1000]                 |
|       | Per Capita Intake Radioactivity (Bq y <sup>-1</sup> ) |                                      |                 |                                     | Committed D <sub>eff</sub> (μSv y <sup>-1</sup> ) |                        |                        |
|       | <sup>226</sup> Ra/ <sup>238</sup> U                   | <sup>228</sup> Ra/ <sup>232</sup> Th | <sup>40</sup> K | <sup>226</sup> Ra/ <sup>238</sup> U | <sup>228</sup> Ra/ <sup>232</sup> Th              | <sup>40</sup> K        | Total                  |
| Fruit | 35.1                                                  | 47.5                                 | 10,220.9        | 9.8                                 | 32.8                                              | 63.4                   | 106.0                  |
|       | Global Limit                                          |                                      |                 | [120]                               | [120]                                             | [170]                  | [290]                  |

### 3.5. Perspectives and Possible Expansions

This experiment has strengthened the avenues for future CR measurements in the UAE, but it has also highlighted the necessary developments in our laboratory capabilities. A major shortcoming for measurements of low levels of NORMs in UAE plants is the high detector counting uncertainties. Improved gamma-spectrometry setups, and alternative radioanalytical techniques such as liquid scintillation counting, gross alpha/beta spectrometry, and sequential extraction based isotopic analyses, need to be employed to fill the gaps and improve the confidence in measurements. Using counting times much longer than the one employed in this study (16 h), will also improve the uncertainties and detection limits greatly. Our sample processing steps require longer instrument times and can work with larger quantities (few kg) of samples only. This reduces the speed of our studies, increases manual work, and leads to higher instrumental expenses. Experimental setups adaptable to various quantities and geometries of samples are under development, to reduce the time and expenditure for all steps, from sampling to analysis.

In this pilot study, a limited geographical distribution and statistically smaller number of samples could provide only indicative values of activity concentrations and CRs. In the following stages, many more locations will be sampled, with better focus on the representative, large-scale, commercial farms. An important aspect is to include local agricultural practices in hyper-arid countries, such as the use of modern greenhouses/net houses. Dedicated sampling efforts are necessary to account for the factors capable of systematically impacting the average CR estimates such as the species of fruits sampled, age of trees, seasonal dependency, irrigation, and fertigation practices in the fields, etc. The impact of fertilizers is a highly significant research topic for root uptake studies in UAE farms. More fieldwork is demanded to ascertain the detailed biochemical kinetics of transfer/translocation of radionuclides in date palms, with full-body studies on multiple tree samples. Further sophistication of experiments is expected for the CR estimation for other major crops of the UAE, viz.: vegetables (cucumber, tomato, capsicum, etc.), animal fodder (maize, Rhodes grass, Alfalfa mixture, etc.) and desert plants (Rimth, Ghaf, etc.). Studies addressing the above issues have been planned under the ENTC's coordinated project with IAEA [38].

## 4. Conclusions

This paper describes the development and results of a field experiment towards the first estimation of natural radionuclides' soil to plant concentration ratios (CR) in the

date palms in the UAE. Date palms are one of the topmost crops, exported entities, and traditional foods of Arab nations. Native date palms have been adopted for enhanced cultivation and propagation with modern agriculture and are utilized in sustainable land and biodiversity managements in arid lands. Upcoming nuclear power development in the region raises the risks of radioactivity release to the environments. In this regard, date palms have not been studied thoroughly, making it a critical subject for obtaining the associated radioecological transfer factors and phytoextraction safety limits.

As part of a pilot study in Abu Dhabi (UAE), seven date palm trees were sampled. Samples of their rootzone soils, fruits and leaves were processed and assayed for gamma-emitting NORM radionuclide activities. The soil samples have high concentrations of  $^{40}\text{K}$ , but values for  $^{238}\text{U}$  and  $^{232}\text{Th}$  are much lower. The measured soil radioactivity is below the global averages. The uptake of  $^{40}\text{K}$  is considerably high in the dates, leading to GM of CR  $\sim 1.12$ . Only rough estimates of  $^{238}\text{U}$  ( $\sim 0.08$ ) and  $^{232}\text{Th}$  ( $\sim 0.17$ ) could be obtained due to their very low inherent contents in the local dates. The experiment also recorded the uptake to leaf, also a consumer product, as 0.77 for  $^{40}\text{K}$ , 0.13 for  $^{238}\text{U}$  and 0.36 for  $^{232}\text{Th}$ . The values obtained here compare very well with the limited literature measurements but makes a novel and complementary input to the global arid region radioecology database. The developed protocol will be replicated for more accurate estimations of date palm CRs, which can be further utilized in national exercises of risk prediction, radioactive waste management, and nuclear emergency-preparedness. Preliminary calculations suggest negligible personal dose factors due to the baseline radioactivity in Abu Dhabi soils and date palms. More detailed experiments and computational impact assessments are planned based on this experience, expanding to new geographies in the country, as well as new measurement techniques, and other important crops.

**Author Contributions:** Conceptualization, formal analysis, investigation, software, P.R.; methodology, P.R., N.P., N.S. and G.V.; resources, P.R., N.P., Y.A. and A.K.A.; writing—original draft preparation, P.R.; writing—review and editing, N.P., N.S., G.V. and Y.A.; visualization, P.R.; supervision, F.F. and Y.A.; project administration, F.F.; funding acquisition, F.F. and Y.A. All authors have read and agreed to the published version of the manuscript.

**Funding:** This research was sponsored by Khalifa University and received no external funding.

**Institutional Review Board Statement:** Not applicable.

**Data Availability Statement:** All relevant data are included in the article.

**Acknowledgments:** The authors would like to thank the Research and Development team of Emirates Nuclear Energy Corporation (ENEC) for providing access to the radioanalytical instruments in the Environmental Radiochemistry Laboratory, located outside Al Ruwais. Their scientists Michael Millinor and Andrew Maddison are dearly acknowledged for their involvement in the gamma spectrometry and for their several discussions and comments. Likewise, the authors extend their gratitude to the Soil Analysis Laboratory of the International Centre for Biosaline Agriculture (ICBA) Dubai for their support in physiochemical analysis of the soil samples. Sincere thanks are due to Greendreams Landscaping for participation in the field surveys and sampling campaigns.

**Conflicts of Interest:** The authors declare no conflict of interest.

## References

1. Bollino, C.A.; Asdrubali, F.; Polinori, P.; Bigerna, S.; Micheli, S.; Guattari, C.; Rotili, A. A Note on Medium- and Long-Term Global Energy Prospects and Scenarios. *Sustainability* **2017**, *9*, 833. [[CrossRef](#)]
2. IAEA TRS 472. In *Handbook of Parameter Values for the Prediction of Radionuclide Transfer in Terrestrial and Freshwater Environments*; Technical Reports Series; International Atomic Energy Agency: Vienna, Austria, 2010; ISBN 978-92-0-113009-9.
3. IAEA TRS 486. In *Guidelines on Soil and Vegetation Sampling for Radiological Monitoring*; Technical Reports Series; International Atomic Energy Agency: Vienna, Austria, 2019; ISBN 978-92-0-102218-9.
4. Hameed, M.; Moradkhani, H.; Ahmadalipour, A.; Moftakhari, H.; Abbaszadeh, P.; Alipour, A. A Review of the 21st Century Challenges in the Food-Energy-Water Security in the Middle East. *Water* **2019**, *11*, 682. [[CrossRef](#)]
5. Semioshkina, N.; Voigt, G. Soil—Plant Transfer of Radionuclides in Arid Environments. *J. Environ. Radioact.* **2021**, *237*, 106692. [[CrossRef](#)]

6. Raj, P.; Padiyath, N.; Semioshkina, N.; Addad, Y.; Foulon, F.; Francis, D.; Voigt, G. Conceptualization of Arid Region Radioecology Strategies for Agricultural Ecosystems of the United Arab Emirates (UAE). *Sci. Total Environ.* **2022**, *832*, 154965. [CrossRef]
7. IAEA TECDOC 1979. In *Soil-Plant Transfer of Radionuclides in Non-Temperate Environments*; Technical Document; International Atomic Energy Agency: Vienna, Austria, 2021; ISBN 978-92-0-129121-9.
8. ENEC Emirates Nuclear Energy Corporation. Available online: <https://www.enec.gov.ae/> (accessed on 25 May 2022).
9. Conatser, R.L.; Abdouli, A.A.; Sallam, A.; Bosc, E.; Nuaimi, F.A.; Ameri, H.A.; Zaabi, M.A.; Al-Hasani, S.; Mansour, T. Radiological Environmental Monitoring in the United Arab Emirates, First Report, 1 January—31 December 2015; Federal Authority for Nuclear Regulations (FANR). Available online: <https://bit.ly/2DhwvVQ> (accessed on 25 August 2022).
10. UAE MOCCA Open Data | UAE Ministry of Climate Change and Environment. Available online: <https://www.moccae.gov.ae/en/open-data.aspx#page=1> (accessed on 25 May 2022).
11. FAOSTAT, U.N.O. Food and Agriculture Data; Food and Agriculture Organization (FAO) of the United Nations. Available online: <https://www.fao.org/faostat/en/#data> (accessed on 25 May 2022).
12. Naushad, M.; Lichtfouse, E. (Eds.) *Sustainable Agriculture Reviews 34: Date Palm for Food, Medicine and the Environment*; Sustainable Agriculture Reviews; Springer International Publishing: Cham, Switzerland, 2019; Volume 34, ISBN 978-3-030-11344-5.
13. Alrefae, T. Long-Lived Gamma Emitting Radionuclides in Palm Dates and Estimates of Annual Effective Doses. *Health Phys.* **2015**, *108*, 547–550. [CrossRef]
14. Rahman, R.; Solodov, A. Analysis of Natural and Anthropogenic Radionuclide Content in Palm Date Fruit of the United Arab Emirates: A Baseline Study. *Health Phys.* **2016**, *111*, 465–470. [CrossRef]
15. El-Taher, A. A Study on Transfer Factors of Radionuclides from Soil to Plant. *Life Sci. J.* **2013**, *10*, 532–539.
16. Shayeb, M.A.; Alharbi, T.; Baloch, M.A.; Rahman Alsamhan, O.A. Transfer Factors for Natural Radioactivity into Date Palm Pits. *J. Environ. Radioact.* **2017**, *167*, 75–79. [CrossRef]
17. Al-Alawi, R.A.; Al-Mashiqri, J.H.; Al-Nadabi, J.S.M.; Al-Shihi, B.I.; Baqi, Y. Date Palm Tree (*Phoenix dactylifera* L.): Natural Products and Therapeutic Options. *Front. Plant Sci.* **2017**, *8*, 845. [CrossRef]
18. Emirates Soil Museum, U.A.E. International Center for Biosaline Agriculture (ICBA), Dubai. Available online: <https://www.emiratessoilmuseum.org/> (accessed on 25 May 2022).
19. Napier, B.A.; Fellows, R.J.; Krupka, K.M. *Soil-to-Plant Concentration Ratios for Assessing Food Chain Pathways in Biosphere Models*; NUREG/CR-6941, 926965; Pacific Northwest National Laboratory (PNNL): Richland, WA, USA, 2007; p. PNNL-16741.
20. Duong Van, H.; Nguyen, T.D.; Peka, A.; Hegedus, M.; Csordas, A.; Kovacs, T. Study of Soil to Plant Transfer Factors of <sup>226</sup>Ra, <sup>232</sup>Th, <sup>40</sup>K and <sup>137</sup>Cs in Vietnamese Crops. *J. Environ. Radioact.* **2020**, *223–224*, 106416. [CrossRef]
21. Karam, M.C.; Petit, J.; Zimmer, D.; Baudelaire Djantou, E.; Scher, J. Effects of Drying and Grinding in Production of Fruit and Vegetable Powders: A Review. *J. Food Eng.* **2016**, *188*, 32–49. [CrossRef]
22. Gilmore, G. *Practical Gamma-Ray Spectrometry*, 2nd ed.; Wiley: Chichester, UK; Hoboken, NJ, USA, 2008; ISBN 978-0-470-86196-7.
23. Shirazi, M.A.; Boersma, L. A Unifying Quantitative Analysis of Soil Texture. *Soil Sci. Soc. Am. J.* **1984**, *48*, 142–147. [CrossRef]
24. USDA Handbook No. 60 Handbook No. 60: Diagnosis and Improvement of Saline and Alkali Soils. Available online: <https://www.ars.usda.gov/pacific-west-area/riverside-ca/agricultural-water-efficiency-and-salinity-research-unit/docs/publications/handbook-no-60/> (accessed on 25 May 2022).
25. Day, P.R. Particle Fractionation and Particle-Size Analysis. In *Methods of Soil Analysis*; John Wiley & Sons, Ltd.: Hoboken, NJ, USA, 1965; pp. 545–567, ISBN 978-0-89118-203-0.
26. Genie 2000 Genie™ 2000 Gamma Analysis Software. Available online: <https://www.mirion.com/products/genie-2000-gamma-analysis-software> (accessed on 25 May 2022).
27. Kendall, M.G. A New Measure of Rank Correlation. *Biometrika* **1938**, *30*, 81–93. [CrossRef]
28. Chandrasekaran, A.; Ravisankar, R.; Rajalakshmi, A.; Eswaran, P.; Vijayagopal, P.; Venkatraman, B. Assessment of Natural Radioactivity and Function of Minerals in Soils of Yelagiri Hills, Tamilnadu, India by Gamma Ray Spectroscopic and Fourier Transform Infrared (FTIR) Techniques with Statistical Approach. *Spectrochim. Acta Part A Mol. Biomol. Spectrosc.* **2015**, *136*, 1734–1744. [CrossRef] [PubMed]
29. Nisbet, A.F.; Woodman, R.F.M. Soil-to-Plant Transfer Factors for Radiocesium and Radiostrontium in Agricultural Systems. *Health Phys.* **2000**, *78*, 279–288. [CrossRef] [PubMed]
30. Ajaj, R.M.B. Determination of Primordial and Anthropogenic Radionuclide Concentrations in Agricultural Soil of the United Arab Emirates Using Gamma-Ray Spectrometry. Ph.D. Thesis, United Arab Emirates University, Al Ain, United Arab Emirates, 2017.
31. Al-Ali, Y.A.M. Natural Radioactivity of UAE Coastal Areas. Master's Thesis, United Arab Emirates University, Al Ain, United Arab Emirates, 2003.
32. Ahmad, A.Y.; Al-Ghouti, M.A.; AlSadig, I.; Abu-Dieyeh, M. Vertical Distribution and Radiological Risk Assessment of <sup>137</sup>Cs and Natural Radionuclides in Soil Samples. *Sci. Rep.* **2019**, *9*, 12196. [CrossRef] [PubMed]
33. *Sources and Effects of Ionizing Radiation: United Nations Scientific Committee on the Effects of Atomic Radiation: UNSCEAR 2000 Report to the General Assembly, with Scientific Annexes*; United Nations: New York, NY, USA, 2000; ISBN 978-92-1-142238-2.
34. Ibrahim, M.M.; El-Beshbeshy, R.T.; Kamh, N.R.; Abou-Amer, A.I. Effect of NPK and Biofertilizer on Date Palm Trees Grown in Siwa Oasis, Egypt. *Soil Use Manag.* **2013**, *29*, 315–321. [CrossRef]
35. Vandenhove, H.; Smolders, E.; Cremers, A. Potassium Bentonites Reduce Radiocaesium Availability to Plants. *Eur. J. Soil Sci.* **2003**, *54*, 91–102. [CrossRef]

36. Khandaker, M.U.; Shuaibu, H.K.; Alklabi, F.A.A.; Alzimami, K.S.; Bradley, D.A. Study of Primordial  $^{226}\text{Ra}$ ,  $^{228}\text{Ra}$ , and  $^{40}\text{K}$  Concentrations in Dietary Palm Dates and Concomitant Radiological Risk. *Health Phys.* **2019**, *116*, 789–798. [[CrossRef](#)] [[PubMed](#)]
37. Prasad, N.G.S.; Nagaiah, N.; Ashok, G.V.; Karunakara, N. Concentrations of  $^{226}\text{Ra}$ ,  $^{232}\text{Th}$ , AND  $^{40}\text{K}$  in the Soils of Bangalore Region, India. *Health Phys.* **2008**, *94*, 264–271. [[CrossRef](#)] [[PubMed](#)]
38. IAEA CRP K41022 New CRP: Transfer of Radionuclides in Arid and Semi-Arid Environments for Radiological Environmental Impact Assessment (K41022). Available online: <https://www.iaea.org/newscenter/news/new-crp-transfer-of-radionuclides-in-arid-and-semi-arid-environments-for-radiological-environmental-impact-assessment-k41022> (accessed on 25 May 2022).

## Article

# Elicitation Promoability with Gamma Irradiation, Chitosan and Yeast to Perform Sustainable and Inclusive Development for Marjoram under Organic Agriculture

Tarek E. Sayed \* and El-Sayed S. Ahmed

Radioisotope Department, Egyptian Atomic Energy Authority, Cairo 11787, Egypt

\* Correspondence: dr.tarekelsayed64@gmail.com

**Abstract:** Sweet marjoram (*Majorana hortensis*) is an important aromatic herbal plant that has long been used and well managed in the traditional and general medical, pharmaceutical, food, cosmetic, and perfume industries. Thus, the increase in its productivity appears to be of great value since there is a large number of bioactive secondary metabolites as well as an increase in the demand in domestic or foreign markets. The purpose of this study is the possibility of promoting the sustainable development of marjoram in the framework of organic farming through gamma irradiation, chitosan and yeast. Field experiments were conducted in a factorial split-plot design with three iterations over two consecutive seasons (2019 and 2020). The main plot is an abiotic elicitor (15 Gy gamma irradiation), two biotic elicitors 500 ppm chitosan, 0.5% yeast, and a non-elicitor (as control), while in the sub-main plot, there were two organic fertilizers, water extract of moringa 20 g/m<sup>2</sup> dry leaves, 20 g/m<sup>2</sup> fulvic acid, and 20 g/m<sup>2</sup> (NPK); the latter is a traditional agrochemical. Statistical analysis of all characteristics of production and quality of biomass and biologically active secondary metabolites revealed that the use of organic fertilizers helped in increasing the yield of marjoram, both qualitatively and quantitatively, and significantly outperformed the chemical fertilizer. The experiment enhances the comprehensive and integrated development of marjoram under organic cultivation and achieves a promising alternative to traditional cultivation without the use of microbicides and/or agrochemical pesticides.

**Keywords:** elicitation; gamma irradiation; organic agriculture; secondary metabolites; yeast

**Citation:** Sayed, T.E.; Ahmed, E.-S.S. Elicitation Promoability with Gamma Irradiation, Chitosan and Yeast to Perform Sustainable and Inclusive Development for Marjoram under Organic Agriculture. *Sustainability* **2022**, *14*, 9608. <https://doi.org/10.3390/su14159608>

Academic Editors: Hosam M. Saleh and Mohammad Mahmoud Dawoud

Received: 3 June 2022

Accepted: 1 August 2022

Published: 4 August 2022

**Publisher's Note:** MDPI stays neutral with regard to jurisdictional claims in published maps and institutional affiliations.



**Copyright:** © 2022 by the authors. Licensee MDPI, Basel, Switzerland. This article is an open access article distributed under the terms and conditions of the Creative Commons Attribution (CC BY) license (<https://creativecommons.org/licenses/by/4.0/>).

## 1. Introduction

Sustainability is currently a global issue that has provoked significant challenges for modern economic technologies and researchers, especially in using plants to solve major environmental problems worldwide [1,2]. With great application of nuclear technologies, the risk for humans and the environment has been considered of significant importance. In concert with sustainability and nuclear applications, green and dry plants [3,4] have an important role in the remediation of wastewater contaminated with stable and radioisotopes then followed by sustainable stabilization in cement [5,6]. Moreover, plants could be used in treatment such as aiding the recovery of the workers at the Chernobyl accident site using a daily oral dose of *G. Biloba* [7]. Medicinal plants and their constituents can alter radiolabeling and biodistribution via several mechanisms [8]. On the other hand, nuclear radiation can be used to improve the efficiency and performance of medicinal plants used in modern and traditional medicinal applications [9].

Sweet marjoram (*Majorana hortensis*) is a precious herbaceous aromatic plant native to the Mediterranean region that belongs to the *Lamiaceae* family [10]. In addition, it is a medicinal plant that is widely applied in domestic medical systems. Sweet marjoram is grown in numerous Asian, North African, and European nations, including Tunisia, Egypt, India, France, Hungary, Germany, Spain, Hungary, Portugal, Poland, and France [11].



Egypt has been internationally known for the cultivation and export of quality marjoram fresh or dry tender stems and the leaves are used for condiments and spices [12].

The leaves and flowers of the plant contain delicate fragrant essential oils that are widely used in traditional medicinal including, but not limited to, lotions, perfumes, creams, and soap [13]. The use of the plant has been documented to treat many ailments such as headaches, asthma, ear problems, and others. Additionally, cramps, depression, dizziness, gastrointestinal disorders, migraine, headache, paroxysmal cough, and a diuretic are all treated with *O. majorana*. Its essential oil is used in perfumery, the pharmaceutical industry, and cosmetics.

Recent studies have shown the vital role of marjoram in the treatment of cancer and as an active anti-fungal, antioxidant and cytotoxic agent. The antioxidant properties of marjoram have been studied extensively [14]. However, it is used mainly as a spice and natural preservative for foods, especially meat.

Elicitors are described as herbal or synthetic (organic or non-biological) substances, and while they are permeable to plants at low levels, they stimulate stress responses in plants and aid in the synthesis of secondary metabolites [15]. Elicitors serve as signals, and elicitation begins with signal perception by eliciting specific receptors on the plant cell membrane, which is followed by the initiation of a signal transduction cascade, which subsequently changes the expression levels of different governance transcription genes of secondary metabolic pathways [16,17]. Elicitation is a successful and commonly used biotechnological method for inducing new secondary metabolites in plants [18].

Elicitors' innate plant resistance mechanisms are induced using biotic and abiotic factors. Elicitation can be an important strategy for producing bioactive secondary metabolites (BSMs). It has been suggested that foliar application of these compounds' (abiotic & biotic elicitors) under normal and stressful conditions improved phytochemicals and biosynthetic pathways of secondary metabolite (BSM) content in plants, including medicinal and aromatic plants [18,19].

Elicitors improve the quality and quantity of BSMs that promote health [17,19,20]. Changes in elicitor growth and development can affect morphological, physiological, and biochemical properties and improve biomass production and quality [21,22].

Attention to agriculture has become imperative over time and implementation of sustainability in this field is crucial. To move forward towards sustainability involves maintaining modern technology and rationing the use of pesticides of various kinds to increase production. These pesticides have been selectively used on medicinal and aromatic plants as well as cereals and horticulture. Pesticides have a negative impact on the environment and hinder long-term growth [23], and several studies have linked the increased use of these pesticides to health issues [24,25]. Organic farming has grown in popularity in recent years, as has pharmaceutical production of organic medicinal and aromatic plants as an alternative to regular agriculture [26]. Considering the above facts according to recent trends and future prospects of various strategies to direct increased productivity of biomass and bioactive secondary metabolites in medicinal and aromatic plants are highlighted. It is notwithstanding works dealing with these aspects are scarce. Hence, the present article highlights elicitation coupled with organic fertilizer mediating biomass and bioactive secondary metabolites production and quality to promote the achievement of sustainable development for marjoram under organic agriculture.

## 2. Materials and Methods

### 2.1. Practical Field Experiment

Two consecutive seasons of field experiment trials, 2019 and 2020, were constructed as split-plot design with three replications based on randomized full block design.

The primary plot had three elicitors: 15 G gamma irradiation (GI), 500 ppm chitosan (CH), and 0.5 g/L (YS) solution in water with 0.1 percent (*v/v*) Tween 20 as a surfactant. The sub-main plot contained three fertilizers, two organic fertilizers, Moringa dry leaves

water- extract 20 g/m<sup>2</sup> (MO), fulvic acid 20 g/m<sup>2</sup> (FA), and traditional chemical fertilizer NPK, 20 g/m<sup>2</sup>.

Gamma irradiated and non-irradiated marjoram seeds on 1st February for both seasons were planted in trays containing soil, sand, beat mixed (1:1:1) ratio (*v/v*) subsequently established in a greenhouse. Seedlings 4 weeks of age were transplanted to the field in plots 4 × 4 m in row 50 cm interspacing that contain 64 plants/plot. At such seasons, plants' leaves were sprayed with water, (Zero elicitor), (NA)CH, and YS a non-elicitor or solution two times 1st April, 1st May before 1st harvesting on 1st June. They were also sprayed on 1st July and 1st August before harvesting on 1st September.

## 2.2. Biomass Yield Production

The fresh weight of leaves was determined pre-plot and per m<sup>2</sup> for the 2019 and 2020 seasons.

## 2.3. Bioactive Secondary Metabolites Production (BSMs)

### 2.3.1. Phenolics (TPC)

The Folin–Ciocalteu reagent was used to determine total phenol content, as described in [27]. A diluted sample extract (1 mg/mL) aliquot was mixed with 125 L of Folin-Clocaiteu reagent and 500 L of water. The mixture was stirred and left for 5 min before adding 125 g of 7% of Na<sub>2</sub>CO<sub>3</sub>. A 1 mL quantity of distilled water was added and well mixed. After 90 min in the dark, the absorbance at 760 nm was compared to a blank. Using a gallic acid solution, a calibration curve was constructed. Equations drawn from the standard gallic acid diagram are used to create content.

### 2.3.2. Flavonoids (TFC)

Flavonoid content was determined according to [28]. *Sechium edule* (jacq.) antioxidant activity of Swartz extract. Food Chemistry, 97:452:458. Each extract was dissolved in 1 mL of ethanol. One mL of the extract was combined with 1 mL of a 2% methanolic AlCl<sub>3</sub> solution. After 15 min of incubation at room temperature, the absorbance at 430 nm was measured, and the total flavonoids in the sample extract were quantified using a calibration curve (quercetin).

### 2.3.3. Flavonols (TFL)

The total flavonoids in *O. majorana* ethanolic extracts were calculated using the method described by [29]. Two mL AlCl<sub>3</sub> (2%) ethanol and 3 mL of sodium acetate solution (50 g/L) were mixed together. The blend was mixed before being incubated at 20 °C for 2 h. At 440 nm, the absorbance was measured. The amount of total flavonoids was measured in mg of quercetin equivalents per gram of dry weight (mg EQ/g DW).

### 2.3.4. Tannins (TAE)

Total tannins were calculated using a procedure devised by [30] based on the protein bovine serum albumin precipitation. The approach works by measuring the absorption of colored compound Fe<sup>2+</sup> phenols at 510 nm using spectrophotometry. The results were calculated in milligrams of tannic acid equivalent per gram of dry weight (mg TA/g DW).

### 2.3.5. Essential Oils (EO)

Fresh leaf samples from the plots were subjected to hydrodistillation for three hours to obtain content. The extracted essential oil was concentrated using sodium sulphate (anhydrous Na<sub>2</sub>SO<sub>4</sub>) and reserved in an amber glass sealed with Teflon kept at 4 °C even analysis as the following:

$$\begin{aligned} 1\text{-EO}\% &= \text{Extracted EO, g/ground leaves sample} \times 100\text{-moisture} \\ 2\text{-EOY, Kg/m}^2 &= \text{EO}\% \times \text{FLY, Kg/m}^2 \text{ EO} \end{aligned}$$

Essential oil contents (EOC), analyzed by GC/MS using Shimadzu-HPLC System (Shimadzu Co., Kyoto, Japan) prepared with a CBM-20 AH controller, and LC20 AP Pump and an SPD-M<sub>2</sub>OA Photo Diode Array (FDA) detector.

### 3. Statistical Analysis

Using a statistical analysis method, the data sets were first checked for normality using the Anderson and Darling normality tests (SAS, 2003). There are no statistically significant differences in the data from the two seasons. As a result, the pooled mean values of two seasons for all attributes examined were statistically analyzed. LSD at the 1% level was used to compare the significant means.

### 4. Results and Discussion

Statistical analysis revealed that solitary application with elicitors and fertilizers achieved a significant positive impact for such lasted trait as, chitosan (CH) > yeast (YS) >  $\gamma$ - irradiation (GI) under Moringa (MO) > fulvic acid (FA) > NPK for both two seasons. However, the drenches between the two seasons were insignificant.

#### 4.1. Biomass Yield Production

Pooled fresh leaves yield (FLY), 6.060 KG/m<sup>2</sup> as control (NE.NPK), was increased significantly, expressed as % of control (0) as the following:

CH.MO, CH.FA, and CH.NPK were 27, 22, and 19 respectively. In addition, YS.MO, YS.FA, YS.NPK were 24, 21, and 17 respectively and GI.MO, GI.FA, GI.NPK were 20, 17, and 11 respectively. Additionally, NE.MO, NE.FA, NE.NPK were 11, 8, and 0 (control 6.060 Kg/m<sup>2</sup>) respectively as listed in Table 1 and represented in Figure 1.

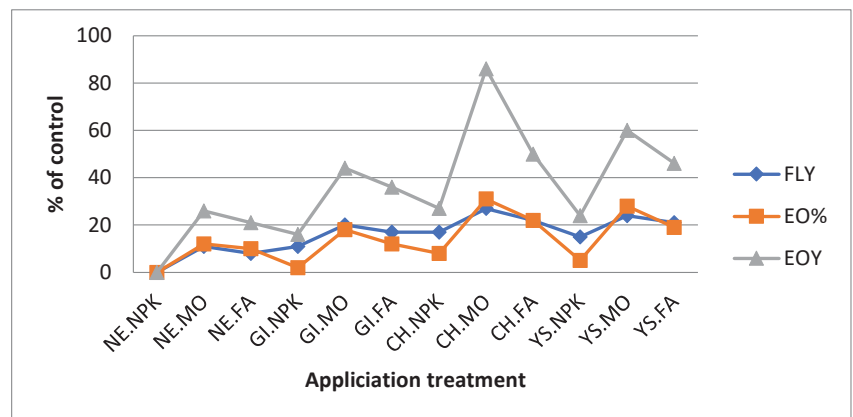


Figure 1. FLY, EO%, EOY.

#### 4.2. Essential oils % (EO%)

PM EO %, 0.532% (control NE Significant, as % of control according to the following: CH.MO, CH.FA, CH.NPK were 3122, and 8, respectively. As well as, YS.MO, YS.FA, YS.NPK were 28, 19, and 5 respectively, and GI.MO, GI.FA, GI.NPK were 18, 12, and 2 respectively. In addition, NE.MO, NE.FA, and NE.NPK were 12, 10, and 0 (control 0.532 Kg/m<sup>2</sup>) respectively as represented in Table 1 and Figure 1.

**Table 1.** Marjoram; fresh leaves yield, Kg/m<sup>2</sup>, essential oil % and essential yield oil, Kg/m<sup>2</sup>, in response to elicitation with gamma irradiation (GI), chitosan (CH) and yeast (YS) under the use of chemical fertilizer (NPK) and organic fertilizer; Moringa (MO) and fulvic acid (FA) over 2 subsequent seasons (2019 and 2020).

| Application Treatment | Fresh Leaves Yield, Kg/m <sup>2</sup> |       |           | Essential Oil % |       |           | Essential Oil Yield, Kg/m <sup>2</sup> |       |           |
|-----------------------|---------------------------------------|-------|-----------|-----------------|-------|-----------|----------------------------------------|-------|-----------|
|                       | 2019                                  | 2020  | PM        | 2019            | 2020  | PM        | 2019                                   | 2020  | PM        |
| NE.NPK                | 5.920                                 | 6.200 | 6.060(0)  | 0.522           | 0.524 | 0.532(0)  | 3.090                                  | 3.294 | 3.192(0)  |
| NE.MO                 | 6.630                                 | 6.820 | 6.725(11) | 0.600           | 0.592 | 0.596(12) | 3.979                                  | 4.038 | 4.009(26) |
| NE.FA                 | 6.453                                 | 6.696 | 6.574(8)  | 0.590           | 0.582 | 0.586(10) | 3.807                                  | 3.897 | 3.852(21) |
| GI.NPK                | 6.690                                 | 6.882 | 6.786(11) | 0.548           | 0.540 | 0.544(2)  | 3.666                                  | 3.716 | 3.691(16) |
| GI.MO                 | 7.163                                 | 7.440 | 7.301(20) | 0.632           | 0.629 | 0.630(18) | 4.527                                  | 4.680 | 4.604(44) |
| GI.FA                 | 7.045                                 | 7.254 | 7.149(17) | 0.616           | 0.603 | 0.609(12) | 4.340                                  | 4.374 | 4.357(36) |
| CH.NPK                | 6.926                                 | 7.228 | 7.228(19) | 0.580           | 0.571 | 0.575(8)  | 4.017                                  | 4.071 | 4.044(27) |
| CH.MO                 | 7.637                                 | 7.750 | 7.693(27) | 0.705           | 0.692 | 0.699(31) | 5.385                                  | 5.363 | 5.374(68) |
| CH.FA                 | 7.282                                 | 7.502 | 7.392(22) | 0.653           | 0.645 | 0.649(22) | 4.744                                  | 4.839 | 4.792(50) |
| YS.NPK                | 6.808                                 | 7.316 | 7.062(17) | 0.564           | 0.556 | 0.560(5)  | 3.840                                  | 4.068 | 3.954(24) |
| YS.MO                 | 7.518                                 | 7.564 | 7.541(24) | 0.679           | 0.676 | 0.678(28) | 5.105                                  | 5.113 | 5.109(60) |
| YS.FA                 | 7.400                                 | 7.378 | 7.389(21) | 0.642           | 0.624 | 0.633(19) | 4.751                                  | 4.604 | 4.678(46) |
| LSD1%                 | 0.035                                 | 0.031 | 0.027     | 0.003           | 0.005 | 0.004     | 0.022                                  | 0.025 | 0.026     |

Values between parentheses were % over control. PM: pooled mean for two seasons (2019–2020).

#### 4.3. Essential Oils Yield (EOY, Kg/m<sup>2</sup>)

EOY, 3.192 Kg/m<sup>2</sup> (control) increased significantly as % of control as the following: CH.MO, CH.FA, CH.NPK, 68, 50, 27, respectively, and YS.MO, YS.FA, and YS.NPK, 60, 46 and 24, respectively.

Furthermore, GI.MO, GI.FA and GI.NPK were 4436, and 16, respectively. In addition, NE.MO, NE.FA, and NE.NPK were 26, 21, and 0 (control 3.192 Kg/m<sup>2</sup>), respectively as represented in Table 1 and Figure 1. Biomass, FLY, Kg/m<sup>2</sup>, EO%, EOC and Kg/m<sup>2</sup> were significantly increased in response to elicitor, CH > YS > GI integrated with MO > FA > NPK, despite the fact that no pest infestation and microbial disease incidences in the field experiment were detected in either season without using any agrochemical pesticides and/or micro-biocides. The disappearance of any pests and microbial diseases was in agreement with [31,32]. In addition, many researchers supported our results and declared a positive, significant impact on biomass yield production [33,34].

#### 4.4. Quali–Quantitative Bioactive Secondary Metabolites (BSMs)

##### 4.4.1. Essential Oil Contents (EOC)

EOC, 11 terpenoids; &-terpene, cineol,  $\gamma$ -Terpinene, p-cymene, Terpineolene, D-linalol, Terpineol-4ol, Bcaryphellene, &-Terpineol, Tymol, carvacol (Table 2) were measured. The total percentages of these 11 terpenoids were increased significantly as the following:

Values of CH.MO, CH.FA, and CH.NPK were 79.81, 76.48, and 69.66, respectively. Furthermore, YS.MO, YS.FA, and YS.NPK were 70.94, 73.80, and 71.32 respectively, and GI.MO, GI.FA, and GI.NPK were 71.60, 71.04, and 69.58 respectively. In addition, NE.MO, NE.FA, and NE.NPK were 69.03, 68.75, and 67.43 (control).

**Table 2.** Marjoram essential oil contents; in response elicitation with gamma irradiation (GI), chitosan (CH) and yeast (YS) under the use of chemical fertilizer (NPK) and bioorganic fertilizer; Moringa (MO) and fulvic acid (FA) in 2 subsequent seasons (2019 and 2020).

| Application Treatment | Essential Oil Content from Terpenoids |        |              |           |               |             |                |                  |              |       |          |        |
|-----------------------|---------------------------------------|--------|--------------|-----------|---------------|-------------|----------------|------------------|--------------|-------|----------|--------|
|                       | ∞-Ter-Pinene                          | Cineol | Y-Ter Pinene | P-Cy-Mene | Terp-Ineolene | D-Lin-Alool | Terpin-Eol 4ol | Bcar-Yophe Llene | ∞-Ter-Pineol | Tymol | Carvacol | Total% |
| NE.NPK                | 7.15                                  | 1.44   | 12.51        | 2.62      | 2.24          | 1.23        | 23.41          | 1.92             | 3.64         | 9.95  | 9.32     | 67.43  |
| NE.MO                 | 7.75                                  | 1.62   | 12.81        | 2.75      | 2.62          | 1.71        | 23.99          | 1.97             | 3.92         | 9.89  | 1.52     | 69.03  |
| NE.FA                 | 7.53                                  | 1.48   | 12.60        | 2.68      | 2.42          | 1.53        | 23.66          | 1.95             | 3.71         | 9.75  | 1.44     | 68.75  |
| GI.NPK                | 7.75                                  | 1.10   | 12.79        | 2.72      | 2.64          | 1.52        | 23.89          | 1.85             | 3.75         | 9.87  | 1.70     | 69.58  |
| GLMO                  | 7.92                                  | 1.18   | 12.91        | 2.82      | 2.86          | 1.76        | 23.93          | 1.92             | 3.89         | 9.91  | 1.87     | 71.60  |
| GLFA                  | 7.89                                  | 1.77   | 12.99        | 2.83      | 2.71          | 1.60        | 23.95          | 1.90             | 3.81         | 9.97  | 1.62     | 71.04  |
| CH.NPK                | 7.69                                  | 1.52   | 12.75        | 2.66      | 2.63          | 1.05        | 23.76          | 1.78             | 3.72         | 9.75  | 1.75     | 69.66  |
| CH.MO                 | 8.77                                  | 2.72   | 13.80        | 3.51      | 3.45          | 2.32        | 24.81          | 2.75             | 3.63         | 10.80 | 2.25     | 79.81  |
| CH.FA                 | 8.42                                  | 2.35   | 13.31        | 3.25      | 3.31          | 2.25        | 24.35          | 2.27             | 4.35         | 10.42 | 2.20     | 76.48  |
| YS.NPK                | 7.80                                  | 1.72   | 12.82        | 2.71      | 2.60          | 2.55        | 23.85          | 1.88             | 3.81         | 9.86  | 1.72     | 71.32  |
| YS.MO                 | 8.35                                  | 2.18   | 13.32        | 3.15      | 3.21          | 3.32        | 24.35          | 2.27             | 4.19         | 10.25 | 2.35     | 70.94  |
| YS.FA                 | 8.25                                  | 2.11   | 13.25        | 3.12      | 3.18          | 3.27        | 24.11          | 2.15             | 4.12         | 10.17 | 2.23     | 75.86  |
| LSD1%                 |                                       |        |              |           |               |             |                |                  |              |       |          | 0.25   |

#### 4.4.2. Total Phenolic (TPC)

TPC, 7.83 mg GAE/g. DLW. (the control was increased significantly as % of control (Table 3 and Figure 2) as the following:

CH.MO, CH.FA, and CH.NPK were 171, 159, and 97, respectively, and YS.MO, YS.FA, and YS.NPK were 156, 135, and 85, respectively. In addition, GI.MO, GI.FA, GI, and NPK were 122, 109, and 44, respectively. Furthermore, NE.MO, NE.FA, and NE NPK were 63, 51, and 0 (control = 7.83 mg GAE/g DLW).

#### 4.4.3. Total Flavonoids Content (TFC)

TFC, 0.15 mg QE/g DLW (control) was increased significantly, as % of control (Table 3 and Figure 2) as the following:

**Table 3.** Marjoram total phenolic (TPC), flavonoid (TFC), flavonols (TFL), tannin (TAN) in response elicitation with gamma irradiation (GI), chitosan (CH) and yeast (YS) under chemical fertilizer (NPK) and organic fertilizer; Moringa (MO) and fulvic acid (FA) at 2 subsequent seasons (2019 and 2020).

| Application Treatment | TPC, mg GAE, g/DW |       |            | TFC, mg QE/DW |      |           | TFL, mg QE/gDW |      |           | TAN, mg TAE/gDW |      |          |
|-----------------------|-------------------|-------|------------|---------------|------|-----------|----------------|------|-----------|-----------------|------|----------|
|                       | 2019              | 2020  | PM         | 2019          | 2020 | PM        | 2019           | 2020 | PM        | 2019            | 2020 | PM       |
| NE.NPK                | 7.85              | 7.81  | 7.83(0)    | 0.16          | 0.14 | 0.15(0)   | 2.58           | 2.53 | 2.55(0)   | 1.26            | 1.23 | 1.25(0)  |
| NE.MO                 | 12.64             | 12.89 | 12.77(63)  | 0.29          | 0.24 | 0.26(73)  | 3.90           | 3.97 | 3.93(54)  | 1.70            | 1.69 | 1.70(36) |
| NE.FA                 | 11.78             | 11.87 | 11.83(51)  | 0.22          | 0.20 | 0.21(41)  | 3.61           | 3.59 | 3.60(41)  | 1.59            | 1.58 | 1.58(26) |
| GI.NPK                | 11.15             | 11.32 | 11.24(44)  | 0.24          | 0.22 | 0.23(53)  | 4.26           | 4.28 | 4.27(67)  | 1.74            | 1.75 | 1.75(40) |
| GLMO                  | 17.27             | 17.57 | 17.42(122) | 0.33          | 0.29 | 0.31(106) | 4.82           | 4.83 | 4.82(89)  | 2.03            | 2.03 | 2.03(62) |
| GLFA                  | 16.25             | 16.48 | 16.37(109) | 0.28          | 0.25 | 0.26(73)  | 4.59           | 4.60 | 4.59(80)  | 1.85            | 1.86 | 1.86(49) |
| CH.NPK                | 15.31             | 15.46 | 15.39(97)  | 0.34          | 0.30 | 0.32(113) | 4.67           | 4.73 | 4.70(84)  | 2.03            | 2.07 | 2.05(64) |
| CH.MO                 | 21.20             | 21.24 | 21.22(71)  | 0.43          | 0.38 | 0.41(173) | 5.94           | 6.55 | 6.25(144) | 2.33            | 2.32 | 2.33(86) |
| CH.FA                 | 20.18             | 20.38 | 20.28(59)  | 0.38          | 0.33 | 0.35(133) | 5.03           | 5.01 | 5.02(97)  | 2.16            | 2.09 | 2.12(69) |
| YS.NPK                | 14.37             | 14.60 | 14.49(85)  | 0.29          | 0.26 | 0.28(87)  | 4.44           | 4.43 | 4.44(74)  | 1.92            | 1.89 | 1.91(53) |
| YS.MO                 | 19.70             | 20.15 | 19.93(125) | 0.35          | 0.32 | 0.34(127) | 5.39           | 5.87 | 5.63(121) | 2.17            | 2.14 | 2.16(73) |
| YS.FA                 | 18.13             | 18.67 | 18.40(135) | 0.32          | 0.29 | 0.30(100) | 4.82           | 4.78 | 4.80(88)  | 2.03            | 1.99 | 2.01(61) |
| LSD1%                 | 0.07              | 0.08  | -          | 0.04          | 0.03 | -         | 0.05           | 0.06 | -         | 0.06            | 0.07 | -        |

PM: pooled mean for two Seasons (2019–2020) parentheses were % of control (NE > NPK) Values between parentheses are % of control.

Values of CH.MO, CH.FA, CH.NPK were 173, 133, and 113, respectively, and YS.MO, YS.FA, and YS.NPK were 127, 100, and 87 respectively. In addition, values of GI.MO, GI.FA, GI, NPK were 106, 73, and 53 respectively, and NE.MO, NE.FA, NE NPK were 73, 41, and 0 (control = 0.15 mg QE/g DLW).

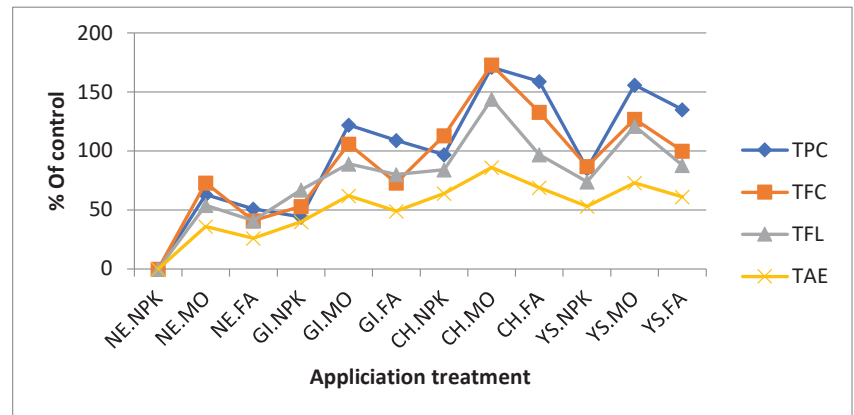


Figure 2. TPC, TFC, TFL, TAE, respectively.

#### 4.4.4. Total Flavonols (TFL)

TFL, 2.55 mg QE/g DLW, increased significantly, as % of control (Table 3 and Figure 2) as the following: values of CH.MO, CH.FA, and CH.NPK, 144, 97, and 84, respectively. Furthermore, YS.MO, YS.FA, YS. and NPK, 121, 88, and 74, respectively. In addition, values of GI.MO, GI.FA, GI, and NPK were 89, 80, and 67, respectively, and NE.MO, NE.FA, and NE NPK were 54, 41, and 0 (control = 2.55 mg QE/g DLW).

#### 4.4.5. Tannin (TAN):

TAN; 1.25 mgTAE/g DLW, was increased significantly, as % of control, Table 3 and Figure 2 summarize the result, and show the following: CH.MO, CH.FA, and CH.NPK were 86, 69, and 64, respectively. In addition, values of YS.MO, YS.FA, and YS.NPK were 73, 61, and 53, respectively.

In addition, values of GI.MO, GI.FA, GI.NPK were 62, 49, and 40, respectively, and NE.MO, NE.FA, and NE.NPK were 36, 26, and 0 (control = 1.55 mg TAE/g DLW)

Elicitor application resulted in significant positive impacts for marjoram BSM production and quality (EO, TPC, TFC, TFL and TAN) as CH > YS > GI integrated with MO > FA > NPK.

Several researchers have supported our results [17,33] under agrochemical agriculture which impacts the environment preventing sustainable development [23].

Furthermore, under bio-fertilizer bio or organic fertilizers, organic, BSMs were increased [35,36].

The overall results manifested strong evidence that CH > YS > GI integrated with MO > FA > NPK could be considered as a reliable technological strategy to improve biomass and BSM (EO, TPC, TFC, TFL, TAN) production and quality of marjoram plants. The disappearance of any microbial diseases or pest infestation from the plant without using any pesticides such as micro-biocides is attributed to the following: (1) enhancing tolerance of plants to biotic and abiotic stresses [37] and leading to strong resistance to pests, microbial agents and nematodes [34]; (2) induced systemic resistance (ISR) prior to infection by regulating systemic resistance (ISR) prior to infection by regulating the expression genes involved in the production and accumulation of bioactive secondary metabolites (phytoalexins) which specific toxins characterized a broad spectrum of biomachrobicide and biopesticides, making them less susceptible against microbial diseases and pest

infecting [38]. Furthermore, (3) chitosan (CH); exhibited strong antifungal and antibacterial [39] nematocidal, virucidal [40,41] and biopesticide attributes [42]. Moringa exhibited anti-fungal traits [43], and improved resistance to pests and microbial diseases [44,45].

## 5. Conclusions

The overall results show strong evidence for the potent of biotic elicitors chitosan > yeast > abiotic, gamma irradiation coupled with organic fertilizers moringa > fulvic acid > traditional agrochemical fertilizer NPK, as reliable CO-friendly solutions, significantly improving marjoram biomass, secondary metabolites production and quality without using agrochemical pesticides and/or microbicides. In addition, chitosan > yeast > gamma irradiation coupled with organic fertilizers exceeded their integration with chemical NPK fertilizer. This highlights the sustainable and reclusive development for marjoram under organic agriculture and could be an alternative to conventional agrochemical agriculture. This section is not mandatory but can be added to the manuscript if the discussion is unusually long or complex.

**Author Contributions:** All authors have equal contributions. All authors have read and agreed to the published version of the manuscript.

**Funding:** This research received no external funding.

**Institutional Review Board Statement:** Not applicable.

**Informed Consent Statement:** Not applicable.

**Data Availability Statement:** Not applicable.

**Conflicts of Interest:** The authors declare no conflict of interest.

## References

1. Saleh, H.M.; Mahmoud, H.H.; Abdou, M.I.; Eskander, S.B. Health Risk Assessment Based on Metal Analysis of Soil and Crops in Al-Dakhla Oasis. *Arab. J. Geosci.* **2021**, *14*, 260. [[CrossRef](#)]
2. Saleh, H.M.; Eskander, S.B.; Mahmoud, H.H.; Abdou, M.I. Groundwater Quality and Health Assessments Based on Heavy Metals and Trace Elements content in Dakhla Oasis, New Valley Governorate, Egypt. *Water Sci.* **2022**, *36*, 1–12. [[CrossRef](#)]
3. Saleh, H.M.; Mahmoud, H.H.; Aglan, R.F.; Bayoumi, T.A. Biological Treatment of Wastewater Contaminated with Cu(II), Fe(II) and Mn(II) Using *Ludwigia Stolonifera* Aquatic Plant. *Environ. Eng. Manag. J.* **2019**, *18*, 1327–1336. [[CrossRef](#)]
4. Saleh, H.M.; Moussa, H.R.; El-Saied, F.A.; Dawoud, M.; Nouh, E.S.A.; Abdel Wahed, R.S. Adsorption of Cesium and Cobalt onto Dried *Myriophyllum Spicatum* L. from Radio-Contaminated Water: Experimental and Theoretical Study. *Prog. Nucl. Energy* **2020**, *125*, 103393. [[CrossRef](#)]
5. Saleh, H.M.; Aglan, R.F.; Mahmoud, H.H. Qualification of Corroborated Real Phytoremediated Radioactive Wastes under Leaching and Other Weathering Parameters. *Prog. Nucl. Energy* **2020**, *119*, 103178. [[CrossRef](#)]
6. Saleh, H.M.; Moussa, H.R.; El-Saied, F.A.; Dawod, M.; Bayoumi, T.A.; Abdel Wahed, R.S. Mechanical and Physicochemical Evaluation of Solidified Dried Submerged Plants Subjected to Extreme Climatic Conditions to Achieve an Optimum Waste Containment. *Prog. Nucl. Energy* **2020**, *122*, 103285. [[CrossRef](#)]
7. Jagetia, G.C. Radioprotective Potential of Plants and Herbs against the Effects of Ionizing Radiation. *J. Clin. Biochem. Nutr.* **2007**, *40*, 74–81. [[CrossRef](#)]
8. Khosravian, P.; Heidari-Soureshjani, S.; Yang, Q. Effects of Medicinal Plants on Radiolabeling and Biodistribution of Diagnostic Radiopharmaceuticals: A Systematic Review. *Plant Sci. Today* **2019**, *6*, 123–131. [[CrossRef](#)]
9. Shala, A.Y. Effect of Different Doses of Gamma Irradiation on Vegetative Growth and Oil Yield of *Ocimum basilicum* L. *J. Plant Prod.* **2019**, *10*, 1–6. [[CrossRef](#)]
10. Uritu, C.M.; Mihai, C.T.; Stanciu, G.-D.; Dodi, G.; Alexa-Stratulat, T.; Luca, A.; Leon-Constantin, M.-M.; Stefanescu, R.; Bild, V.; Melnic, S. Medicinal Plants of the Family Lamiaceae in Pain Therapy: A Review. *Pain Res. Manag.* **2018**, *2018*, 7801543. [[CrossRef](#)]
11. Shylaja, M.R.; Peter, K.V. The Functional Role of Herbal Spices. *Handb. Herbs Spices* **2004**, *2*, 26–45.
12. Peter, K.V.; Shylaja, M.R. Introduction to Herbs and Spices: Definitions, Trade and Applications. In *Handbook of Herbs and Spices*; Elsevier: Amsterdam, The Netherlands, 2012; pp. 1–24.
13. Khan, I.A.; Abourashed, E.A. *Leung's Encyclopedia of Common Natural Ingredients: Used in Food, Drugs and Cosmetics*; John Wiley & Sons: Hoboken, NJ, USA, 2011; ISBN 1118213068.
14. Hossain, M.B.; Brunton, N.P.; Barry-Ryan, C.; Martin-Diana, A.B.; Wilkinson, M. Antioxidant Activity of Spice Extracts and Phenolics in Comparison to Synthetic Antioxidants. *Rasayan J. Chem.* **2008**, *1*, 751–756.



15. Namlı, S.; Işıksalan, Ç.; Akbaş, F.; Toker, Z.; Tilkat, E.A. Effects of UV-B Radiation on Total Phenolic, Flavonoid and Hypericin Contents in *Hypericum Retusum* Aucher Grown under in Vitro Conditions. *Nat. Prod. Res.* **2014**, *28*, 2286–2292. [[CrossRef](#)] [[PubMed](#)]
16. Mohammadparast, B.; Rasouli, M.; Rustaiee, A.R.; Zardari, S.; Agrawal, V. Quantification of Asiatic Acid from Plant Parts of *Centella Asiatica* L. and Enhancement of Its Synthesis through Organic Elicitors in in Vitro. *Hortic. Environ. Biotechnol.* **2014**, *55*, 578–582. [[CrossRef](#)]
17. Mejdoub-Trabelsi, B.; Touihri, S.; Ammar, N.; Riahi, A.; Daami-Remadi, M. Effect of Chitosan for the Control of Potato Diseases Caused by *Fusarium* Species. *J. Phytopathol.* **2020**, *168*, 18–27. [[CrossRef](#)]
18. Andrys, D.; Adaszyńska-Skwirzyńska, M.; Kulpa, D. Jasmonic Acid Changes the Composition of Essential Oil Isolated from Narrow-Leaved Lavender Propagated in in Vitro Cultures. *Nat. Prod. Res.* **2018**, *32*, 834–839. [[CrossRef](#)]
19. Ahamed, T.E.S.; Ahamed, E.S.S. Synergy Prospect Low Gamma Irradiation Doses Incorporating Elicitation with Iron Nanoparticles to Hyper Production Biomass Yield and Bioactive Secondary Metabolites for Cress, Medicinal Plant. *J. Plant Sci.* **2018**, *6*, 157–163.
20. Ahamed, T.E.S. Bioprospecting Elicitation with Gamma Irradiation Combine with Chitosan to Enhance, Yield Production, Bioactive Secondary Metabolites and Antioxidant Activity for Saffron. *J. Plant Sci.* **2019**, *7*, 137–143.
21. Sheshbahreh, M.J.; Dehnavi, M.M.; Salehi, A.; Bahreininejad, B. Effect of Irrigation Regimes and Nitrogen Sources on Biomass Production, Water and Nitrogen Use Efficiency and Nutrients Uptake in Coneflower (*Echinacea purpurea* L.). *Agric. Water Manag.* **2019**, *213*, 358–367. [[CrossRef](#)]
22. Yadav, K.K.; Sarkar, S. Biofertilizers, Impact on Soil Fertility and Crop Productivity under Sustainable Agriculture. *Environ. Ecol.* **2019**, *37*, 89–93.
23. Bombardi, L.M. *Geografia Do Uso de Agrotóxicos No Brasil e Conexões Com a União Europeia*; FFLCH- USP: São Paulo, Brazil, 2017; ISBN 8575063103.
24. Pignati, W.A.; de Souza e Lima, F.A.N.; de Lara, S.S.; Correa, M.L.M.; Barbosa, J.R.; da Costa Leão, L.H.; Pignatti, M.G. Distribuição Espacial Do Uso de Agrotóxicos No Brasil: Uma Ferramenta Para a Vigilância Em Saúde. *Cienc. Saúde Colet.* **2017**, *22*, 3281–3293. [[CrossRef](#)] [[PubMed](#)]
25. de Abreu, P.H.B.; Alonzo, H.G.A. Rural Work and Health Risks: A Review into de “Safe Use” of Pesticides in Brazil. *Cienc. Saúde Colet.* **2014**, *19*, 4197.
26. Pereira, M.M.A.; Morais, L.C.; Marques, E.A.; Martins, A.D.; Cavalcanti, V.P.; Rodrigues, F.A.; Gonçalves, W.M.; Blank, A.F.; Pasqual, M.; Dória, J. Humic Substances and Efficient Microorganisms: Elicitation of Medicinal Plants—A Review. *J. Agric. Sci.* **2019**, *11*, 268–280. [[CrossRef](#)]
27. Arabshahi-Delouee, S.; Urooj, A. Antioxidant Properties of Various Solvent Extracts of Mulberry (*Morus indica* L.) Leaves. *Food Chem.* **2007**, *102*, 1233–1240. [[CrossRef](#)]
28. Ordóñez, A.A.L.; Gomez, J.D.; Vattuone, M.A. Antioxidant Activities of *Sechium Edule* (Jacq.) Swartz Extracts. *Food Chem.* **2006**, *97*, 452–458. [[CrossRef](#)]
29. Adedapo, A.A.; Jimoh, F.O.; Koduru, S.; Afolayan, A.J.; Masika, P.J. Antibacterial and Antioxidant Properties of the Methanol Extracts of the Leaves and Stems of *Calpurnia Aurea*. *BMC Complement. Altern. Med.* **2008**, *8*, 53. [[CrossRef](#)] [[PubMed](#)]
30. Hagerman, A.E.; Butler, L.G. Protein Precipitation Method for the Quantitative Determination of Tannins. *J. Agric. Food Chem.* **1978**, *26*, 809–812. [[CrossRef](#)]
31. Towler, M.J.; Weathers, P.J. Variations in Key Artemisinic and Other Metabolites throughout Plant Development in *Artemisia Annua* L. for Potential Therapeutic Use. *Ind. Crops Prod.* **2015**, *67*, 185–191. [[CrossRef](#)]
32. Boghazian, A.; Amjad, L.; Shahanipour, K. Chemical Constituents and Identification of the Essential Oil of *Artemisia Aucheri* Boiss. in Iran. *Adv. Environ. Biol.* **2014**, *8*, 2339–2344.
33. Adekiya, A.O.; Agbede, T.M.; Aboyeji, C.M.; Dunsin, O.; Ugbe, J.O. Green Manures and NPK Fertilizer Effects on Soil Properties, Growth, Yield, Mineral and Vitamin C Composition of Okra (*Abelmoschus esculentus* (L.) Moench). *J. Saudi Soc. Agric. Sci.* **2019**, *18*, 218–223. [[CrossRef](#)]
34. Kaleri, A.A.; Baloch, A.W.; Baloch, M.; Wahocho, N.A.; Abro, T.F.; Jogi, Q.; Soomro, A.A.; Marri, A.; Bhutto, L.A. 30. Heritability and Correlation Analysis in Bt and Non-Bt Cotton (*Gossypium hirsutum* L.) Genotypes. *Pure Appl. Biol.* **2021**, *5*, 906–912.
35. El-Mohamedy, R.S.R.; Mohamed, S.K. Effect of Moringa Oleifera Seed Oil, Root and Leave Extracts on Growth of Major Pathogenic Fungi of Tomato, Green Bean and Potato in Vitro. *Int. J. Agric. Technol.* **2018**, *14*, 505–520.
36. Tarek Elsayed, S.A.; El Sayed, S.A. The Potentiality Biotic-Elicitation with Chitosan or Vitamin C to Achieve Integrated and Sustainable Development for Sage *Salvia Officinalis* Under Sustainable Agriculture Systems. *J. Plant Sci.* **2021**, *9*, 151–162.
37. Valletta, A.; De Angelis, G.; Badiali, C.; Brasili, E.; Miccheli, A.; Di Cocco, M.E.; Pasqua, G. Acetic Acid Acts as an Elicitor Exerting a Chitosan-like Effect on Xanthone Biosynthesis in *Hypericum perforatum* L. Root Cultures. *Plant Cell Rep.* **2016**, *35*, 1009–1020. [[CrossRef](#)]
38. Gabaston, J.; El Khawand, T.; Waffo-Tegu, P.; Decendit, A.; Richard, T.; Mérillon, J.-M.; Pavela, R. Stilbenes from Grapevine Root: A Promising Natural Insecticide against *Leptinotarsa Decemlineata*. *J. Pest Sci.* **2018**, *91*, 897–906. [[CrossRef](#)]
39. Sathiyabama, M.; Akila, G.; Charles, R.E. Chitosan-Induced Defence Responses in Tomato Plants against Early Blight Disease Caused by *Alternaria Solani* (Ellis and Martin) Sauer. *Arch. Phytopathol. Plant Prot.* **2014**, *47*, 1963–1973. [[CrossRef](#)]
40. Bondok, A.M. Response of Tomato Plants to Salicylic Acid and Chitosan under Infection with Tomato Mosaic Virus. *Am. J. Agric. Environ. Sci.* **2015**, *15*, 1520–1529. [[CrossRef](#)]

41. Firmansyah, D.; Widodo; Hidayat, S.H. Chitosan and Plant Growth Promoting Rhizobacteria Application to Control Squash Mosaic Virus on Cucumber Plants. *Asian J. Plant Pathol.* **2017**, *11*, 148–155. [[CrossRef](#)]
42. Li, Y.; Qin, Y.; Liu, S.; Xing, R.; Yu, H.; Li, K.; Li, P. Preparation, Characterization, and Insecticidal Activity of Avermectin-Grafted-Carboxymethyl Chitosan. *BioMed Res. Int.* **2016**, *2016*, 9805675. [[CrossRef](#)]
43. Zaker, M. Natural Plant Products as Eco-Friendly Fungicides for Plant Diseases Control—A Review. *Agriculturists* **2016**, *14*, 134–141. [[CrossRef](#)]
44. Phiri, C. Influence of Moringa Oleifera Leaf Extracts on Germination and Early Seedling Development of Major Cereals. *Agric. Biol. J. N. Am.* **2010**, *1*, 774–777. [[CrossRef](#)]
45. Ho, T.-T.; Lee, J.-D.; Jeong, C.-S.; Paek, K.-Y.; Park, S.-Y. Improvement of Biosynthesis and Accumulation of Bioactive Compounds by Elicitation in Adventitious Root Cultures of Polygonum Multiflorum. *Appl. Microbiol. Biotechnol.* **2018**, *102*, 199–209. [[CrossRef](#)] [[PubMed](#)]

## Article

# Rhyolite as a Naturally Sustainable Thermoluminescence Material for Dose Assessment Applications

Elsayed Salama <sup>1,\*</sup>, Dalal A. Aloraini <sup>2</sup>, Sara A. El-Khateeb <sup>3</sup> and Mohamed Moustafa <sup>4</sup>

<sup>1</sup> Basic Science Department, Faculty of Engineering, The British University in Egypt (BUE), El-Shorouk City 11837, Egypt

<sup>2</sup> Physics Department, College of Science, Princess Nourah bint Abdulrahman University (PNU), Riyadh 11671, Saudi Arabia; daalorainy@pnu.edu.sa

<sup>3</sup> Nuclear Medicine Technology Department, Inaya Medical Colleges, Riyadh 11352, Saudi Arabia; smohamed@inaya.edu.sa

<sup>4</sup> Department of Physics, School of Science and Engineering, The American University in Cairo (AUC), New Cairo 11835, Egypt; mohamed.orabi@aucegypt.edu

\* Correspondence: elsayed.salama@bue.edu.eg

**Abstract:** Thermoluminescence characteristics of natural rhyolite have been studied. Dose response at a wide dose range of 0.5–2000 Gy has been determined. Minimum detectable dose and thermal fading rate are evaluated. Glow curve deconvolution is conducted after determining the best read-out conditions. The repeated initial rise (RIR) method is used to detect the overlapping peaks, and a glow curve deconvolution procedure is used to extract the thermoluminescence parameters of rhyolite. According to the findings, rhyolite glow curves show five interfering peaks corresponding to five electron trap levels at 142, 176, 221, 298, and 355 °C, respectively, at a heating rate of 3 °C/s. The obtained kinetic order for the deconvoluted peaks showed mixed-order kinetic. The reported results might be useful to introduce rhyolite as a natural sustainable material for radiation dosimetry applications.

**Keywords:** rhyolite; sustainable natural material; thermoluminescence; kinetic parameters

**Citation:** Salama, E.; Aloraini, D.A.; El-Khateeb, S.A.; Moustafa, M.

Rhyolite as a Naturally Sustainable Thermoluminescence Material for Dose Assessment Applications.

*Sustainability* **2022**, *14*, 6918.

<https://doi.org/10.3390/su14116918>

Academic Editors: Hosam M. Saleh and Mohammad Mahmoud Dawoud

Received: 6 May 2022

Accepted: 2 June 2022

Published: 6 June 2022

**Publisher's Note:** MDPI stays neutral with regard to jurisdictional claims in published maps and institutional affiliations.



**Copyright:** © 2022 by the authors. Licensee MDPI, Basel, Switzerland. This article is an open access article distributed under the terms and conditions of the Creative Commons Attribution (CC BY) license (<https://creativecommons.org/licenses/by/4.0/>).

## 1. Introduction

Thermoluminescence dosimetry (TLD) is a proper method for assessing ionizing radiation dosage. TLD materials come in a broad range of physical shapes, allowing for evaluating various radiation characteristics at dosage levels ranging from micro to kilo Gray. The tiny physical size of TL dosimeters and the point that no cables or additional equipment are required during dose measurement are significant benefits. As a result, they are well-suited to many dosimetric applications [1–3].

Sustainable materials are those that can be obtained in enough amounts without exhausting the non-renewable resources or altering the environment natural resources.

These materials can range from bio-based polymers derived from polysaccharides to highly recyclable materials, such as glass, which can be reused indefinitely without the need for additional mineral resources. Recyclable materials, such as waste composites, are used in many industrial applications, such as in stabilization and solidification of radioactive waste [4]. Reuse of cement kiln dust and polystyrene waste could contribute to environmental protection [5]. Cement can be used as a shielding material with modification by using various additives, such as cellulosic waste [6,7], bitumen [8,9], glass [10], polymers [4,11,12], nanomaterials [13,14], and cement wastes [5,15].

Natural minerals are used for a large variety of purposes in modern science and technology, which enhances human life. Quartz is a typical natural mineral with several benefits in a variety of TL dosimetry applications, such as for determining a substance's radiological history [16,17], monitoring of nuclear accident [18], and food irradiation control [19]. Thermoluminescence characteristics of gamma irradiated sandstone showed

that its linear dose-response covers the range of 1–50 Gy followed by sub-linearity at a high dose level [20]. Based on radiation induced free radicals, Egyptian limestone was used as an effective and low-cost electron paramagnetic resonance (EPR) gamma dosimeter [21]. Thermoluminescence characteristics of sedimentary natural calcite in Gebel El Galala, Egypt, revealed an average TL sensitivity of  $322.356 \text{ Gy}^{-1} \text{ mg}^{-1}$  with minimum detectable dosage of  $976.221 \mu\text{Gy}$  and a wide range of linearity, from 1.1 to 330 Gy in response to beta particle irradiation [22]. For the sake of retrospective dosimetry, thermoluminescence properties of natural tuff were investigated in the dose range 0.5–5 Gy, where linear dose-response is obtained [23].

Rhyolite is an igneous rock that extrudes and has a high silica content. It is generally pink or grey in appearance, with tiny grains that are difficult to notice without a hand lens. Rhyolite is made up of quartz, plagioclase, and sanidine, with some hornblende and biotite thrown in [24]. Thermoluminescence emission of rhyolite was recently studied without in-depth investigation of its full dosimetric properties and kinetic parameters involved [25].

A thorough understanding of the kinetic parameters is required for reliable research of thermoluminescent materials for usage in diverse nuclear applications.

The kinetic parameters, on the other hand, are a crucial aspect in describing the physical characteristics of TL materials. This may be done by looking at the thermoluminescence curve of the TL materials after they have been exposed to ionizing radiation. When electrons are liberated from the traps during heating, they recombine with trapped holes, causing light to be emitted. A collection of glow peaks is formed based on the amount of trapping bands in the material, which serves as a fingerprint for each substance. The kind of incident radiation and its energy, as well as the geological origin of minerals, chemical forms, kinds of impurities, and flaws, all influence the glow peaks [26].

The current study aims to investigate the capability of using rhyolite as a natural thermoluminescent dosimeter material. Thermoluminescence characterization, as well as its structural and compositional analysis, will also be investigated.

## 2. Material and Methods

Rhyolite rock was obtained from the Makkah area, Kingdom of Saudi Arabia, around 190 km southeast of Taif, in the mountainous region, at  $20.64^\circ \text{ N}$  longitude and  $42.12^\circ \text{ E}$  latitude. This rock sample was crushed into  $100 \mu\text{m}$  granules and then washed with distilled water to remove organic contaminants. Magnetic separation was used to remove magnetic particles from the sample after it was dried. The powder was annealed at  $400^\circ \text{ C}$  in a muffle furnace for 2 h to eliminate any past radiation exposure, then quickly cooled to room temperature.

At room temperature, a Bruker S8 TIGER XRF spectrometer was used to identify the elemental composition of rhyolite samples while a Rigaku Ultima 4 XRD was used for crystallographic phase identification. An Optica FT-IR Spectrometer was used to measure Fourier transformation infra-red (FTIR) absorption spectra of prepared samples in the spectral range  $400\text{--}4000 \text{ cm}^{-1}$ . According to a qualitative XRF examination of the natural rhyolite sample, silicon was the predominant ingredient (53%), with lesser amounts of aluminum (15.8%), potassium (15.2%), calcium (2.5%), and a variety of other elements as impurities.

For the sake of shaping and forming small rigid disks, 25 mg average weight suitable for the TLD reader samples are compressed at 3 tons using a hydraulic press. The obtained small rhyolite disks of 2 mm diameter and 1 mm thickness are shown in Figure 1.

A Harshaw TL-reader model 3500 (Harshaw, WI, USA) was used for the thermoluminescence measurements. The temperature range for the recorded TL glow curves was  $50\text{--}400^\circ \text{ C}$ , with the heating rate of  $3\text{--}25^\circ \text{ C/s}$ .

The  $^{60}\text{Co}$  irradiation source (GC220), factory-made by the Canadian Atomic Energy Authority, was utilized to gamma irradiate the samples at  $0.3 \text{ Gy/s}$ . The source is provided by the Egyptian National Center for Radiation Research and Technology.



Figure 1. Rhyolite compressed disks at 3 tons.

### 3. Results and Discussions

#### 3.1. Structural Analysis (XRD and FTIR)

The X-ray diffraction pattern (XRD) for natural rhyolite is shown in Figure 2. Crystallographic phase identification and line profile analysis were performed using the Maud computer program by Luca Lutterotti [27]. Sodium aluminum silicate ( $42.193 \pm 0$  wt. %), potassium aluminum silicate ( $32.826 \pm 1.079$  wt. %) and silicon oxide ( $24.982 \pm 0.671$  wt. %) are three identified phases corresponding to three minerals: albite—low, microcline—intermediate, and quartz—low, respectively. The obtained peaks are matched to the assigned peaks regarding the forementioned three phases, which were obtained from the crystal structure database of the *American Mineralogist* [28–30].

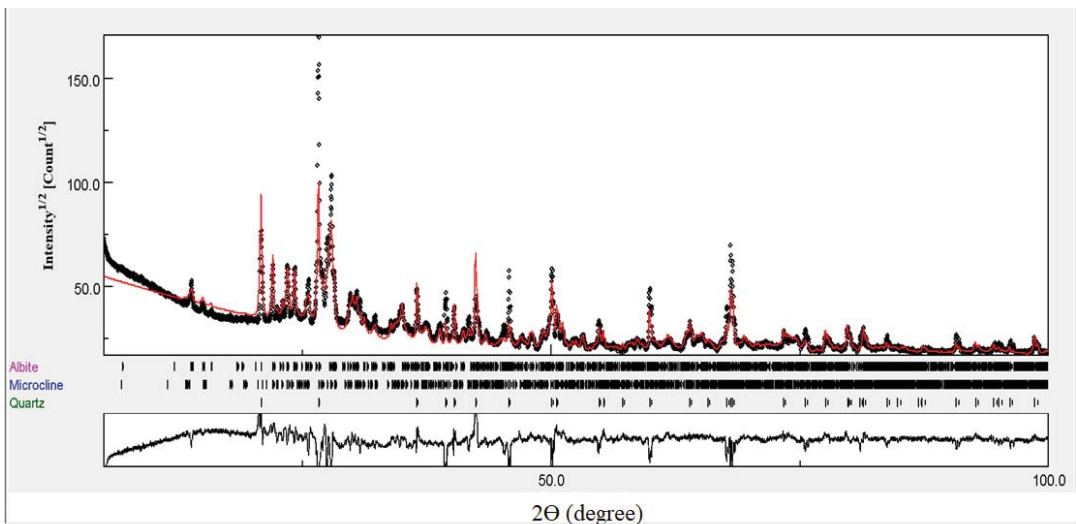


Figure 2. The x-ray diffraction pattern (XRD) for natural rhyolite.

The line profile fitting estimates that the sodium aluminum silicate phase has triclinic structure with crystallite size of 73 nm and the lattice parameters,  $a$ ,  $b$ ,  $c$ ,  $\alpha$ ,  $\beta$ , and  $\gamma$  of 8.14, 12.79, 7.16 Å, 94.26, 116.62, and 87.80°, respectively. The potassium aluminum silicate phase also has triclinic structure with crystallite size of 73 nm and the lattice parameters,

a, b, c,  $\alpha$ ,  $\beta$ , and  $\gamma$  to be 8.60, 13.00, 7.20 Å, 89.98, 115.93, and 89.43°, respectively. Silicon oxide phase has trigonal structure with crystallite size of 73 nm and the lattice parameters, a and b of 4.92 and 5.41 Å, respectively.

Figure 3 shows the FTIR transmission spectrum of the natural rhyolite under investigation. The observed absorption peak at  $3435.91\text{ cm}^{-1}$  can be attributed to the OH group's stretching and bending vibrations [31,32], while the those observed at  $1093\text{ cm}^{-1}$  and  $661\text{ cm}^{-1}$  are attributed to the stretching and bending vibrations of the Si-O in quartz, respectively. The most intense bands recorded at around  $1100\text{ cm}^{-1}$  and  $460\text{ cm}^{-1}$ , are associated with the asymmetric stretching vibrations Si-O(Si) and bending vibrations O-Si-O present in silicate tetrahedra, respectively. The doublet  $800\text{--}780\text{ cm}^{-1}$  is related to the symmetric stretching vibrations of Si-O-Si bridges [33]. This doublet is found in low-temperature quartz and is utilized as the analytical band for determining the phase's quantitative properties [34]. The Al-O-Si vibration in aluminum silicate is shown by the absorption band at  $1384.16\text{ cm}^{-1}$  [35].

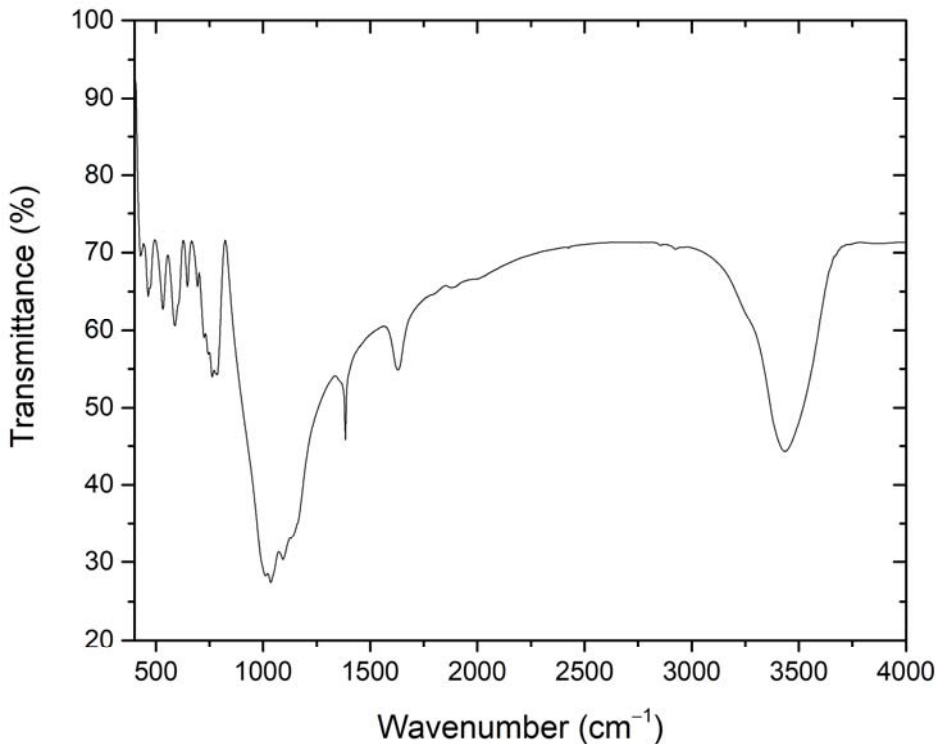
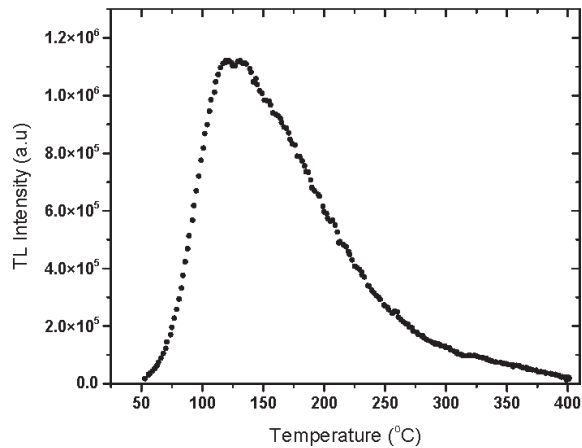


Figure 3. The FTIR transmission spectrum of the investigated natural rhyolite.

Metal cation vibrations, such as  $\text{Na}^+$  and  $\text{Al}^+$ , are responsible for the bands detected at  $588.41$ ,  $532.27$ ,  $463.94$ , and  $428.08\text{ cm}^{-1}$  [36–38]. These findings are matched with those obtained with XRD study.

### 3.2. Glow Curves

The recorded glow curves of 50 Gy gamma irradiated natural rhyolite disks at  $3\text{ °C/s}$  heating rate display one intensified TL peak around  $135\text{ °C}$ , as shown in Figure 4.

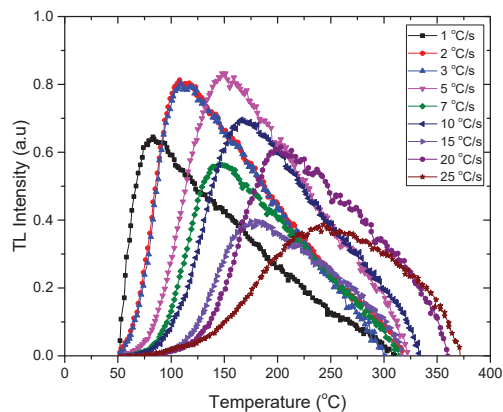


**Figure 4.** Thermoluminescence glow curve of 50 Gy gamma irradiated natural rhyolite disk heated at 3 °C/s heating rate.

The dosimetric properties, such as the effect of heating rate, dose-response, minimum detectable dose, reproducibility of the obtained response, and thermal fading, will be studied as follows.

### 3.3. The Effect of Heating Rate

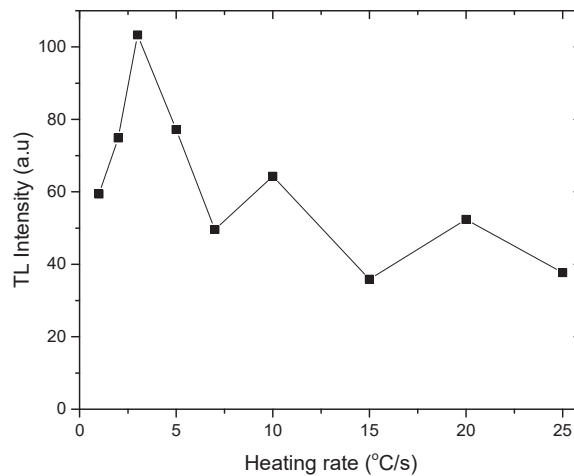
The impact of various heating rates on natural rhyolite disks irradiated with 50 Gy gamma radiation is shown in Figure 5. The acquired findings verified that as the heating rate was increased, the dosimetric peak was pushed to a higher temperature.



**Figure 5.** The effect of heating rate on the thermoluminescence glow curve of 50 Gy gamma irradiated natural rhyolite.

Due to increased interfering of sub-peaks at higher heating rates, the width of all dosimetric peaks at its half maximum increases [39]. This is due to a temperature discrepancy between the TL reading tray (planchet) and the sample's real recorded temperature at high heating rates. As a result, the peak seems to be at a greater temperature than it actually is. Slow heating rates, on the other hand, do not cause this because heat is more homogeneously distributed in the sample, as a result of which there is no change in the peak temperature [40]. Figure 6 shows the results of TL response at various heating rates from 1 to 25 °C/s, where the maximum value was recorded at the 3 °C/s heating rate.





**Figure 6.** Gamma dose response of natural rhyolite at various heating rates.

### 3.4. Dose Response

As shown in Figure 7, the variation of the induced TL with gamma dose over the range 1–20 Gy displays a linear fitting ( $R^2 = 0.999$ ) described by the formula  $I = (1.011 \pm 0.026) D$ ; followed by a supralinearity behavior up to 2000 Gy described by the formula  $I = (202.35 \pm 20.98) D^{1.28 \pm 0.02}$ , where  $I$  refers to the intensity of the TL signal and  $D$  is the irradiation dose. The strong value of  $R^2$  suggested that the studied material possesses a homogeneous delivery of deep electron traps, providing a linear dose-response across the irradiation dosage range studied. The following formula can be used to compute the linearity index  $f(D)$  at a given dosage  $D$  [41]:

$$f(D) = \frac{[S(D) - S_0]/D}{[S(D_1) - S_0]/D_1} \quad (1)$$

where  $S_0$ ,  $S(D)$ ,  $D_1$ , and  $S(D_1)$  denote the TL response at zero dose,  $S(D)$ , dosage in the linear area; and  $S(D_1)$  denotes the TL response corresponding to dose  $D_1$ ; respectively. The value of  $f(D)$  equals one for linear behavior, higher than 1 for supralinearity, and lower than 1 for sublinearity.

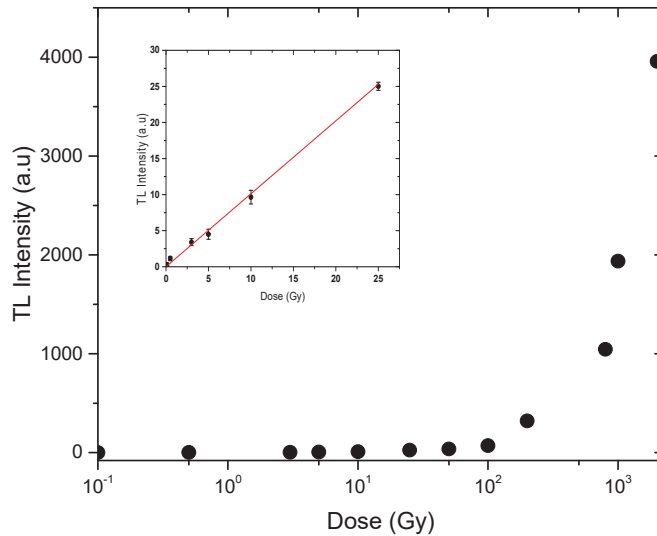
The calculated  $f(D)$  versus irradiation dose from 0.5 to 2000 Gy confirmed the linear-supralinearity criteria within this range because  $f(D)$  equals approximately one for the range of 0.5–25 Gy, while supralinearity behavior for the residual dose range up to 2 kGy where the values of  $f(D)$  are greater than unity are shown in Figure 8.

The unified interaction model has been used extensively to model the behavior of  $f(D)$ . Many experimental measurements have also shown that as the glow peak temperature rises, the supralinearity of the various glow peaks rises. This can be explained based on the increased charge carrier migration distances during the recombination (heating) stage resulting in increased effects of track interaction and, in turn, increased luminescence recombination efficiency [42,43].

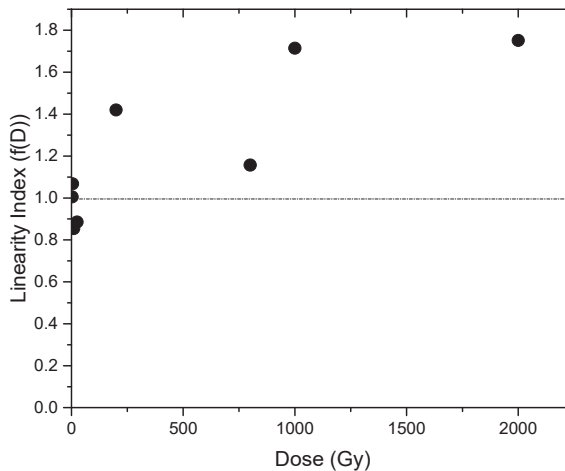
### 3.5. Thermal Fading

The TL-response of Dosimeters is affected by a variety of environmental conditions. The temperature of the surrounding medium is maybe the most critical. After irradiation, heat can liberate electrons from its traps, a process known as thermal fading. The trapping parameters affecting this process are the frequency factor ( $s$ ) and activation energy ( $E$ ) [44]. Figure 9 shows the thermal fading behavior of 50 Gy gamma irradiated rhyolite disks

during a 28-day period. These samples were annealed before the irradiation process and stored at room temperature (20–25 °C) with a humidity of 40–50%.



**Figure 7.** Dose response of natural rhyolite disks in the range of 0.5–2000 Gy.



**Figure 8.** Linearity index of rhyolite at dose range 0.5–2000 Gy.

After 24 h, 52 h, one week, and two weeks, the results showed a 32 percent decrease, 52 percent reduction, and 57 percent reduction. During the remaining research time of two weeks, no additional thermal fading was noticed. In the case where the TL readout is delayed, these data will aid in estimating the precise absorbed dosages.

### 3.6. Reproducibility

Another key criterion in determining reusability of the recommended TL material is its reproducibility for dosimetry applications. The average TL intensity of a collection of annealed rhyolite disks was measured after numerous cycles of 50 Gy gamma irradiation. Based on a standard deviation of six measurements, the obtained data in Figure 10 show that

the rhyolite dosimeter has acceptable reusability, with roughly 4% variance in successive measurements.

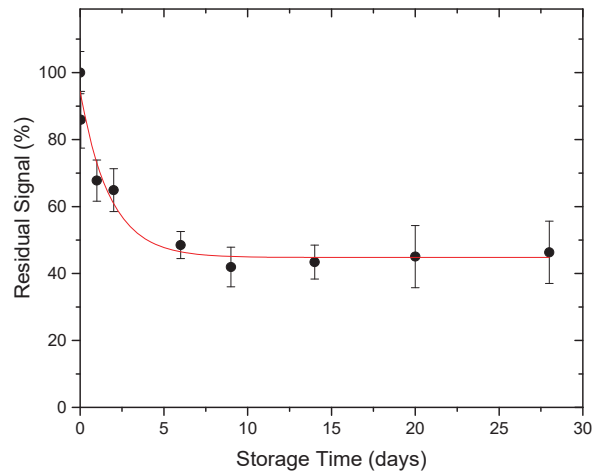


Figure 9. Thermal fading of 50 Gy gamma irradiated natural rhyolite.

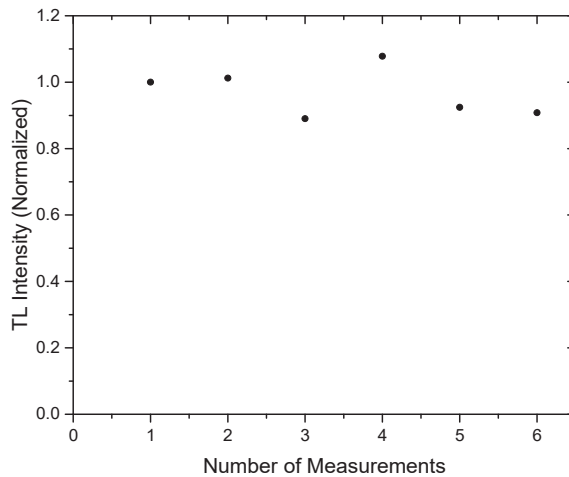


Figure 10. Reproducibility use of natural rhyolite for dosimetry applications.

### 3.7. Minimum Detectable Dose (MDD)

By using the dose calibration factor ( $F$ ), the average background reading ( $B^*$ ), and its standard deviation ( $\sigma_B$ ), the following formula provided by Furetta et al. can be used to compute the rhyolite disks' minimal detectable dose (MDD) (2000) [45].

$$MDD = (B^* + 2\sigma_B)F \quad (2)$$

Rhyolite has dose calibration factor  $F = 0.98$  ( $0.75$ )  $\text{Gy g nC}^{-1}$ , the average background signal  $B^* = 0.40$   $\text{nC g}^{-1}$ , and its standard deviation  $\sigma_B = 0.06$   $\text{nC g}^{-1}$ . The calculated values of the MDD based on the above equation are about  $0.5$  Gy. Thus, natural rhyolite can measure low gamma doses up to  $0.5$  Gy.

### 3.8. Kinetic Parameters Determination

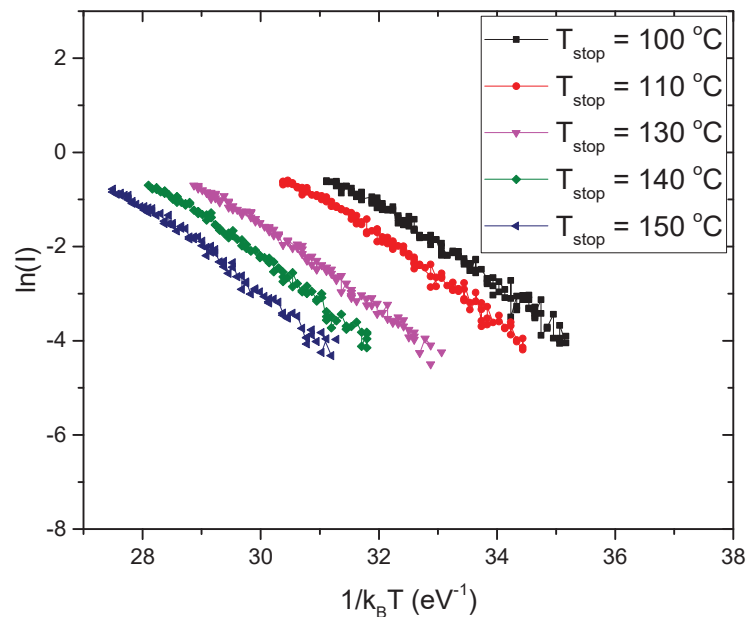
#### 3.8.1. Repeated Initial Rise (RIR) Method

This method was developed by Garlick and Gibson in 1948 and is widely used for determining the activation energy ( $E$ ) [46]. The RIR method is based on the fact that at low temperatures, where TL intensities are less than 10–15% of the maximum intensity corresponding to a specific cut-off temperature, the change in charge carrier concentration in the traps is minimal and independent of the kinetic parameters [47]. The TL-intensity  $I(T)$  can be formulated as:

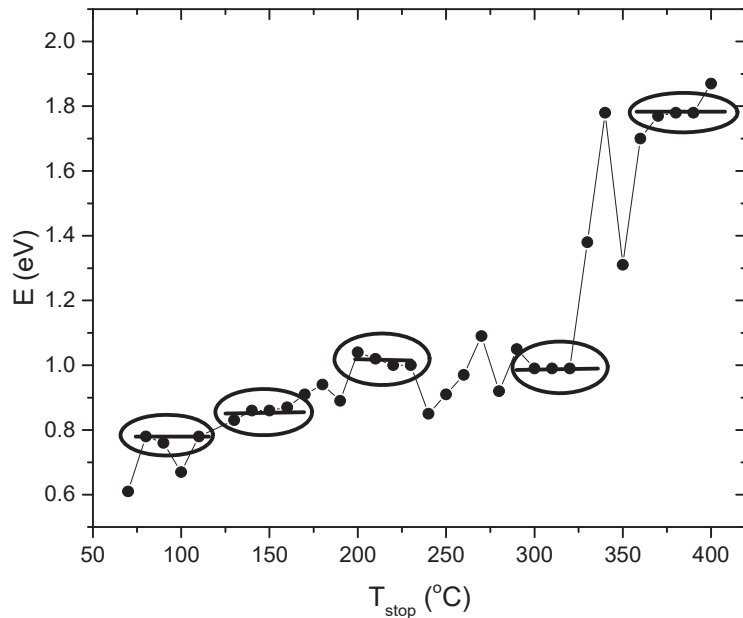
$$I(T) = \text{const.} \cdot e^{-E/kT} \quad (3)$$

The plot of  $\ln(I)$  against  $1/kT$  where  $k$  is the Boltzmann constant, gives a straight line where the activation energy ( $E$ ) can be determined from the slope. This approach may recur with various stopping temperatures  $T_{\text{stop}}$  to acquire a large number of activation energies, and then the number of peaks in the glow curve can be determined if there are many peaks. The irradiation sample was heated at a continuous pace until it reached a certain cut-off temperature  $T_{\text{stop}}$ , at which point a thermoluminescence decay was recorded. Several heating and cooling cycles have produced a set of data  $I(T)$  spanning the temperature range of 333–673 K.

For a section of the data acquired at stopping temperatures of 100, 110, 130, 140, and 150 °C, Figure 11 depicts the relationship between  $\ln(I)$  vs.  $1/kT$ . The activation energy value is anticipated by the slope for each stopping temperature. The graph of the acquired values of the activation energy  $E$  vs.  $T_{\text{stop}}$  is shown in Figure 12. The obtained results displayed that the activation energies are nearly similar in five places (plateau region), indicating that the glow curve has five overlapping peaks with average activation energies of  $0.77 \pm 0.01$ ,  $0.86 \pm 0.01$ ,  $1.01 \pm 0.01$ ,  $0.99 \pm 0.00$ , and  $1.78 \pm 0.01$  eV, respectively.



**Figure 11.** Initial raise plots of natural rhyolite sample at some values of  $T_{\text{stop}}$ .



**Figure 12.** The activation energies ( $E$ ) of natural rhyolite given by the RIR method.

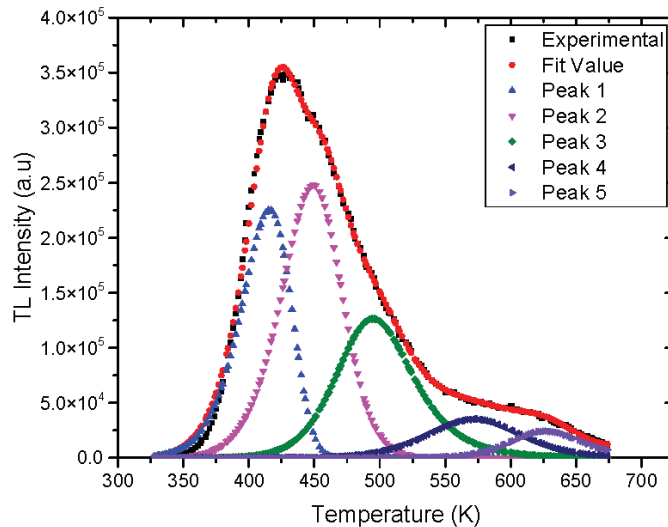
### 3.8.2. Computerized Glow Curve Deconvolution (CGCD) Method

The glow curves of natural rhyolite have been deconvoluted into five interfering peaks using the general order kinetics equation given by Kitis et al. [48].

$$I(T) = n_0 s \exp\left(-\frac{E}{kT}\right) \left[ \frac{(b-1)skT^2}{\beta E} \times \exp\left(-\frac{E}{kT}\right) (1-\Delta) + 1 \right]^{-\frac{b}{b-1}} \quad (4)$$

where  $I$  is the glow-peak intensity,  $s$  ( $s^{-1}$ ) is the frequency factor,  $E$  (eV) is the activation energy,  $n_0$  is the initial concentration of trapped carriers,  $T$  (K) is the absolute temperature,  $k$  ( $eV K^{-1}$ ) is the Boltzmann constant,  $\Delta = 2 kT/E$ , and  $\beta$  is the heating rate. The deconvolution process was carried out using the Korean atomic energy institute's TL-ANAL tool [49]. As initial approximations, the number of peaks (five) and the corresponding values of their activation energies (obtained by the RIR method) were entered into the algorithm. The calculated value of the figure of merit (FOM) for all TL glow peaks determines the accuracy of the study [50]. The fit is satisfactory if the FOM values are between 0.0 and 2.5 percent, 2.5 and 3.5 percent is minor fit, and  $>3.5\%$  is bad fit.

Figure 13 shows the glow curve deconvolution of a natural rhyolite sample irradiated with 50 Gy and recorded at a  $3^\circ C/s$  heating rate. The glow curve deconvolution findings are summarized in Table 1. The computed standard deviation of the mean owing to many measurements or fitting peaks during the deconvolution process is incorporated in the considered activation energy data, which is the uncertainty type A. The acquired findings indicated that the glow curve of rhyolite material has five overlapping peaks created at 142, 176, 221, 298, and  $355^\circ C$ , respectively, at a heating rate of  $3^\circ C/s$ , and that the activation energies are compatible with the RIR method's results. The obtained kinetic order for the deconvoluted peaks showed mixed-order kinetic.



**Figure 13.** Glow curve deconvolution of natural rhyolite at 3 °C/s heating rate and irradiated by 50 Gy.

**Table 1.** The kinetic parameters for natural rhyolite.

| Peak Number | Peak Temperature<br>(°C) | RIR Method<br>E (eV) | CGCD Method |                         |      |
|-------------|--------------------------|----------------------|-------------|-------------------------|------|
|             |                          |                      | E (eV)      | s (s <sup>-1</sup> )    | b    |
| 1           | 142                      | 0.77 ± 0.01          | 0.78 ± 0.02 | 4.60 × 10 <sup>8</sup>  | 1.07 |
| 2           | 176                      | 0.86 ± 0.01          | 0.87 ± 0.02 | 8.29 × 10 <sup>8</sup>  | 1.41 |
| 3           | 221                      | 1.01 ± 0.01          | 1.02 ± 0.05 | 3.02 × 10 <sup>9</sup>  | 2.04 |
| 4           | 298                      | 0.99 ± 0.00          | 0.98 ± 0.01 | 4.46 × 10 <sup>7</sup>  | 1.66 |
| 5           | 355                      | 1.78 ± 0.01          | 1.76 ± 0.02 | 2.00 × 10 <sup>13</sup> | 2.02 |

#### 4. Conclusions

In this paper, natural rhyolite material is shaped into small disks to be used as a thermoluminescence dosimeter. Chemical composition and crystal structure of its composite phases showed that sodium aluminum silicate (42.193 ± 0 wt. %), potassium aluminum silicate (32.826 ± 1.079 wt. %), and silicon oxide (24.982 ± 0.671 wt. %) are the three identified phases of rhyolite composition. Linear dose response up to 25 Gy followed by supralinearity up to 2000 Gy are obtained. The obtained TL characteristics of rhyolite showed that this material has linear dose response up to 25 Gy, followed by supralinearity up to 2000 Gy, as well as relatively high fading rate of 57% after two weeks with no more thermal fading noted. Low detection limit of roughly 0.5 Gy and reasonable repeatability of about 4% variation in successive measurements are noted. These characteristics may qualify rhyolite as the sustainable natural material used in this study for a variety of applications involved radiation dose assessment.

**Author Contributions:** E.S.: methodology, validation, data curation, writing—original draft, writing—review and editing. D.A.A.: conceptualization, methodology, resources. S.A.E.-K.: methodology, writing—original draft. M.M.: methodology. All authors have read and agreed to the published version of the manuscript.

**Funding:** This research was funded by Princess Nourah bint Abdulrahman University, Riyadh, Saudi Arabia, Researchers Supporting Project number [PNURSP2022R57].

**Institutional Review Board Statement:** Not applicable.

**Informed Consent Statement:** Not applicable.

**Data Availability Statement:** Not applicable.

**Acknowledgments:** The authors express their gratitude to Princess Nourah bint Abdulrahman University Researchers Supporting Project number (PNURSP2022R57), Princess Nourah bint Abdulrahman University, Riyadh, Saudi Arabia.

**Conflicts of Interest:** The authors declare no conflict of interest.

## References

- Kron, T. Thermoluminescence dosimetry and its applications in medicine-Part 1: Physics, materials and equipment. *Australas. Phys. Eng. Sci. Med.* **1994**, *17*, 175–199. [[PubMed](#)]
- Moscovitch, M.; John, T.J.; Cassata, J.R.; Blake, P.K.; Rotunda, J.E.; Ramlo, M.; Velbeck, K.J.; Luo, L.Z. The application of LiF:Mg,Cu,P to large scale personnel dosimetry: Current status and future directions. *Radiat. Prot. Dosim.* **2006**, *119*, 248–254. [[CrossRef](#)]
- Chand, S.; Mehra, R.; Chopra, V. Recent developments in phosphate materials for their thermoluminescence dosimeter (TLD) applications. *Luminescence* **2021**, *36*, 1808–1817. [[CrossRef](#)]
- Saleh, H.M.; Salman, A.A.; Faheim, A.A.; El-Sayed, A.M. Polymer and polymer waste composites in nuclear and industrial applications. *J. Nucl. Energy Sci. Power Gener. Technol.* **2020**, *9*, 1000199.
- Saleh, H.M.; Salman, A.A.; Faheim, A.A.; El-Sayed, A.M. Sustainable composite of improved lightweight concrete from cement kiln dust with grated poly (styrene). *J. Clean. Prod.* **2020**, *277*, 123491. [[CrossRef](#)]
- Dawoud, M.M.A.; Hegazi, M.M.; Saleh, H.M.; El Helew, W.K. Removal of stable and radio isotopes from wastewater by using modified microcrystalline cellulose based on Taguchi L16. *Int. J. Environ. Sci. Technol.* **2022**, 1–12. [[CrossRef](#)]
- Dawoud, M.M.A.; Hegazy, M.M.; Helew, W.K.; Saleh, H.M. Overview of Environmental Pollution and Clean Management of Heavy Metals and Radionuclides by using Microcrystalline Cellulose. *J. Nucl. Eng. Sci. Power Gener. Technol.* **2021**, *3*, 2.
- Saleh, H.M.; Bondouk, I.I.; Salama, E.; Esawii, H.A. Consistency and shielding efficiency of cement-bitumen composite for use as gamma-radiation shielding material. *Prog. Nucl. Energy* **2021**, *137*, 103764. [[CrossRef](#)]
- Reda, S.M.; Saleh, H.M. Calculation of the gamma radiation shielding efficiency of cement-bitumen portable container using MCNPX code. *Prog. Nucl. Energy* **2021**, *142*, 104012. [[CrossRef](#)]
- Eid, M.S.; Bondouk, I.I.; Saleh, H.M.; Omar, K.M.; Sayyed, M.I.; El-Khatib, A.M.; Elsafi, M. Implementation of waste silicate glass into composition of ordinary cement for radiation shielding applications. *Nucl. Eng. Technol.* **2021**, *54*, 1456–1463. [[CrossRef](#)]
- Eskander, S.B.; Saleh, H.M.; Tawfik, M.E.; Bayoumi, T.A. Towards potential applications of cement-polymer composites based on recycled polystyrene foam wastes on construction fields: Impact of exposure to water ecologies. *Case Stud. Constr. Mater.* **2021**, *15*, e00664. [[CrossRef](#)]
- Saleh, H.M.; Eskander, S.B. Impact of water flooding on hard cement-recycled polystyrene composite immobilizing radioactive sulfate waste simulate. *Constr. Build. Mater.* **2019**, *222*, 522–530. [[CrossRef](#)]
- Saleh, H.M.; El-Saied, F.A.; Salaheldin, T.A.; Hezo, A.A. Influence of severe climatic variability on the structural, mechanical and chemical stability of cement kiln dust-slag-nanosilica composite used for radwaste solidification. *Constr. Build. Mater.* **2019**, *218*, 556–567. [[CrossRef](#)]
- Saleh, H.M.; El-Sheikh, S.M.; Elshereafy, E.E.; Essa, A.K. Performance of cement-slag-titanate nanofibers composite immobilized radioactive waste solution through frost and flooding events. *Constr. Build. Mater.* **2019**, *223*, 221–232. [[CrossRef](#)]
- Saleh, H.M.; Salman, A.A.; Faheim, A.A.; El-Sayed, A.M. Influence of aggressive environmental impacts on clean, lightweight bricks made from cement kiln dust and grated polystyrene. *Case Stud. Constr. Mater.* **2021**, *15*, e00759. [[CrossRef](#)]
- Preusser, F.; Chithambo, M.L.; Götte, T.; Martini, M.; Ramseyer, K.; Sendezera, E.J.; Susino, G.J.; Wintle, A.G. Quartz as a natural luminescence dosimeter. *Earth Sci. Rev.* **2009**, *97*, 184–214. [[CrossRef](#)]
- Thamóné Bozsó, E.; Fűri, J.; Kovács István, J.; Biró, T.; Király, E.; Nagy, A.; Törökné Sinka, M.; Kónya, P.; Mészárosné Turi, J.; Vigh, C. Characteristics of quartz separates of different formations in Hungary from the aspect of osl dating. *Földt. Kozlony* **2020**, *150*, 61. [[CrossRef](#)]
- Bailiff, I.K.; Stepanenko, V.F.; Göksu, H.Y.; Bøtter-Jensen, L.; Brodski, L.; Chumak, V.; Correcher, V.; Delgado, A.; Golikov, V.; Jungner, H.; et al. Comparison of retrospective luminescence dosimetry with computational modeling in two highly contaminated settlements downwind of the chernobyl NPP. *Health Phys.* **2004**, *86*, 25–41. [[CrossRef](#)]
- Beneitez, P.; Correcher, V.; Millán, A.; Calderón, T. Thermoluminescence analysis for testing the irradiation of spices. *J. Radioanal. Nucl. Chem. Artic.* **1994**, *185*, 401–410. [[CrossRef](#)]
- Soliman, C.; Salama, E. Investigation on the suitability of natural sandstone as a gamma dosimeter. *Nucl. Instrum. Methods Phys. Res. Sect. B Beam Interact. Mater. At.* **2009**, *267*, 3323–3327. [[CrossRef](#)]
- Salama, E. Egyptian limestone for gamma dosimetry: An electron paramagnetic resonance study. *Radiat. Eff. Defects Solids* **2014**, *169*, 325–333. [[CrossRef](#)]
- El-Faramawy, N.; Alazab, H.A.; Gad, A.; Sabry, M. Study of the thermoluminescence kinetic parameters of a  $\beta$ -irradiated natural calcite. *Radiat. Phys. Chem.* **2022**, *190*, 109793. [[CrossRef](#)]



23. Almuqrin, A.; Soliman, C.; ELShokrof, K.; Aloraini, D. Tuff rock as a new thermoluminescent material for gamma dosimetry. *Asian J. Sci. Res.* **2018**, *11*, 126–133. [[CrossRef](#)]
24. DeMouthe, J.F. Natural materials: Sources, properties, and uses. *Rocks Miner.* **2006**, *81*, 3972006.
25. Aloraini, D.A. Sensitization of natural rhyolite rock using high gamma doses for thermoluminescence dosimetry. *Luminescence* **2020**, *35*, 1043–1047. [[CrossRef](#)]
26. Azorín, J.; Furetta, C.; Scacco, A. Preparation and properties of thermoluminescent materials. *Phys. Stat. Solidi* **1993**, *138*, 9–46. [[CrossRef](#)]
27. Lutterotti, L. Total pattern fitting for the combined size-strain-stress-texture determination in thin film diffraction. *Nucl. Instrum. Methods Phys. Res. Sect. B Beam Interact. Mater. At.* **2010**, *268*, 334–340. [[CrossRef](#)]
28. Harlow, G.E. The anorthoclase structures: The effects of temperature and composition. *Am. Mineral.* **1982**, *67*, 975–996.
29. Bailey, S.W. Refinement of an intermediate microcline structure. *Am. Mineral.* **1969**, *54*, 1540–1545.
30. Levien, L.; Prewitt, C.T.; Weidner, D.J.; Prewir, C.T.; Weidner, D.J. Structure and Elastic Properties of Quartz at Pressure. *Am. Mineral.* **1980**, *65*, 920–930.
31. El Makhloufy, S.; Tridane, M.; Majdi, E.M.; Marouani, H.; Zerraf, S.; Belhabra, M.; Cherqaoui, A.; Belaouad, S. Chemical preparation, thermal behavior and infrared studies of the new cyclotriphosphate tetrahydrate of manganese and distrontium,  $\text{MnSr}_2(\text{P}_3\text{O}_9)_2 \cdot 4\text{H}_2\text{O}$ . *Mediterr. J. Chem.* **2019**, *9*, 280–289. [[CrossRef](#)]
32. Liang, Y.; Ouyang, J.; Wang, H.; Wang, W.; Chui, P.; Sun, K. Synthesis and characterization of core-shell structured  $\text{SiO}_2@ \text{YVO}_4 : \text{Yb}^{3+}, \text{Er}^{3+}$  microspheres. *Appl. Surf. Sci.* **2012**, *58*, 3689–3694. [[CrossRef](#)]
33. Mozgawa, W.; Król, M.; Dyczek, J.; Deja, J. Investigation of the coal fly ashes using IR spectroscopy. *Spectrochim. Acta Part A Mol. Biomol. Spectrosc.* **2014**, *132*, 889–894. [[CrossRef](#)]
34. Moenke, H.H.W. Silica, the Three-dimensional Silicates, Borosilicates and Beryllium Silicates. In *The Infrared Spectra of Minerals*; Mineralogical Society of Great Britain and Ireland: Oxford, UK, 2015.
35. Treto-Suárez, M.A.; Prieto-García, J.O.; Mollineda-Trujillo, Á.; Lamazares, E.; Hidalgo-Rosa, Y.; Mena-Ulecia, K. Kinetic study of removal heavy metal from aqueous solution using the synthetic aluminum silicate. *Sci. Rep.* **2020**, *10*, 10836. [[CrossRef](#)]
36. Mandal, A.K.; Agrawal, D.; Sen, R. Preparation of homogeneous barium borosilicate glass using microwave energy. *J. Non. Cryst. Solids* **2013**, *371*, 41–46. [[CrossRef](#)]
37. Study, S.; Consumption, L.E.; Part, D.U.; Utilization, D.; Yoshizawa, N.; Harimoto, K.; Ichihara, M.; Miki, Y.; Takase, K.; Inoue, T. Synthesis, Characterization and Bioactive Study of Borosilicate Sol-Gel Glass Khairy. *Nat. Sci.* **2015**, *13*, 475–476.
38. Rada, S.; Dehelean, A.; Culea, E. FTIR and UV-VIS spectroscopy investigations on the structure of the europium-lead-tellurate glasses. *J. Non. Cryst. Solids* **2011**, *357*, 3070–3073. [[CrossRef](#)]
39. Bos, A.J.J.; Vijverberg, R.N.M.; Pijters, T.M.; McKeever, S.W.S. Effects of Cooling and Heating Rate on Trapping Parameters in LiF: Mg, Ti Crystals. *J. Phys. D Appl. Phys.* **1992**, *25*, 1249–1257. [[CrossRef](#)]
40. Amer, H.A.; Elashmawy, M.M.; Alazab, H.A.; Ezz El-Din, M.R. Suitability of pure nano crystalline LiF as a TLD dosimeter for high dose gamma radiation. *Nucl. Technol. Radiat. Prot.* **2018**, *33*, 93–99. [[CrossRef](#)]
41. Chen, R.; McKeever, S.W.S. Characterization of nonlinearities in the dose dependence of thermoluminescence. *Radiat. Meas.* **1994**, *23*, 667–673. [[CrossRef](#)]
42. Horowitz, Y.S.; Oster, L.; Datz, H. The thermoluminescence dose-response and other characteristics of the high-temperature TL in LiF:Mg,Ti (TLD-100). *Radiat. Prot. Dosim.* **2007**, *124*, 191–205. [[CrossRef](#)]
43. Attix, F.H. Further consideration of the track-interaction model for thermoluminescence in LiF(TLD-100). *J. Appl. Phys.* **1975**, *46*, 81–88. [[CrossRef](#)]
44. Chen, R.; Pagonis, V.; Lawless, J.L. Evaluated thermoluminescence trapping parameters-What do they really mean? *Radiat. Meas.* **2016**, *91*, 21–27. [[CrossRef](#)]
45. Furetta, C.; Prokic, M.; Salamon, R.; Prokic, V.; Kitis, G. Dosimetric characteristics of tissue equivalent thermoluminescent solid TL detectors based on lithium borate. *Nucl. Instrum. Methods Phys. Res. Sect. A Accel. Spectrometers Detect. Assoc. Equip.* **2001**, *456*, 411–417. [[CrossRef](#)]
46. Jose, M.T.; Anishia, S.R.; Annalakshmi, O.; Ramasamy, V. Determination of thermoluminescence kinetic parameters of thulium doped lithium calcium borate. *Radiat. Meas.* **2011**, *46*, 1026–1032. [[CrossRef](#)]
47. Garlick, G.F.J.; Gibson, A.F. The electron trap mechanism of luminescence in sulphide and silicate phosphors. *Proc. Phys. Soc.* **1948**, *60*, 574–590. [[CrossRef](#)]
48. Kitis, G.; Gomez-Ros, J.M.; Tuyn, J.W.N. Thermoluminescence glow-curve deconvolution functions for first, second and general orders of kinetics. *J. Phys. D. Appl. Phys.* **1998**, *31*, 2636–2641. [[CrossRef](#)]
49. Chung, K.S.; Choe, H.S.; Lee, J.I.; Kim, J.L.; Chang, S.Y. A computer program for the deconvolution of thermoluminescence glow curves. *Radiat. Prot. Dosim.* **2005**, *115*, 345–349. [[CrossRef](#)]
50. Balian, H.G.; Eddy, N.W. Figure-of-merit (FOM), an improved criterion over the normalized chi-squared test for assessing goodness-of-fit of gamma-ray spectral peaks. *Nucl. Instrum. Methods* **1977**, *145*, 389–395. [[CrossRef](#)]



## Article

# Fluorine-18 Fluorodeoxyglucose Isolation Using Graphene Oxide for Alternative Radiopharmaceutical Spillage Decontamination in PET Scan

Mohammad Khairul Azhar Abdul Razab <sup>1,\*</sup>, Norazlina Mat Nawi <sup>2,\*</sup>, Fara Hana Mohd Hadzuan <sup>1</sup>, Nor Hakim Abdullah <sup>3</sup>, Maimanah Muhamad <sup>4</sup>, Rosidah Sunaiwi <sup>1</sup>, Fathirah Ibrahim <sup>1</sup>, Farah Amanina Mohd Zin <sup>3</sup> and An'amt Mohamed Noor <sup>3</sup>

- <sup>1</sup> Medical Radiation Programme, School of Health Sciences, Universiti Sains Malaysia, Health Campus, Kubang Kerian 16150, Kelantan, Malaysia; farahadzuan@student.usm.my (F.H.M.H.); rosidah98@student.usm.my (R.S.); fathirah\_ibrahim94@yahoo.com (F.I.)
  - <sup>2</sup> Department of Nuclear Medicine, Radiotherapy & Oncology, School of Medical Sciences, Universiti Sains Malaysia, Health Campus, Kubang Kerian 16150, Kelantan, Malaysia
  - <sup>3</sup> Advanced Materials Research Cluster, Faculty of Bioengineering and Technology, Universiti Malaysia Kelantan, Jeli Campus, Jeli 17600, Kelantan, Malaysia; norhakimin@umk.edu.my (N.H.A.); farahamanina2751@gmail.com (F.A.M.Z.); anamt@umk.edu.my (A.M.N.)
  - <sup>4</sup> Nuclear Medicine & Molecular Imaging Department, Chancellor Tuanku Muhriz Hospital, Cheras 56000, Kuala Lumpur, Malaysia; maimanah@ppukm.ukm.edu.my
- \* Correspondence: khairul.azhar@usm.my (M.K.A.A.R.); norazlina@usm.my (N.M.N.)

**Citation:** Razab, M.K.A.A.; Nawi, N.M.; Hadzuan, F.H.M.; Abdullah, N.H.; Muhamad, M.; Sunaiwi, R.; Ibrahim, F.; Zin, F.A.M.; Noor, A.M. Fluorine-18 Fluorodeoxyglucose Isolation Using Graphene Oxide for Alternative Radiopharmaceutical Spillage Decontamination in PET Scan. *Sustainability* **2022**, *14*, 4492. <https://doi.org/10.3390/su14084492>

Academic Editors: Hosam M. Saleh and Mohammad Mahmoud Dawoud

Received: 16 March 2022

Accepted: 7 April 2022

Published: 9 April 2022

**Publisher's Note:** MDPI stays neutral with regard to jurisdictional claims in published maps and institutional affiliations.



**Copyright:** © 2022 by the authors. Licensee MDPI, Basel, Switzerland. This article is an open access article distributed under the terms and conditions of the Creative Commons Attribution (CC BY) license (<https://creativecommons.org/licenses/by/4.0/>).

**Abstract:** Radiopharmaceuticals (RPC) used for diagnostic and therapeutic purposes in nuclear medicine may contaminate surface areas due to spillage during its preparation or accident during RPC transfer from laboratory to the treatment room. Fluorine-18 Fluorodeoxyglucose (<sup>18</sup>F-FDG) is the most common RPC for positron emission tomography (PET) scan in nuclear medicine due to its ideal annihilation converted energy at 511 keV and short half-life at 109.8 min. Ineffective medical waste management of <sup>18</sup>F-FDG may pose a risk to the environment or cause unnecessary radiation doses to the personnel and public. Depending on the incident rate of these events, simple decontamination methods such as the use of chemicals and swabs might not be cost-effective and sustainable in the environment. This study aims to propose an alternative method to decontaminate <sup>18</sup>F-FDG by using graphene oxide (GO). GO was synthesised using the Hummers method while the physical morphology was analysed using a field emission scanning electron microscope (FESEM). <sup>18</sup>F-FDG adsorption efficiency rate using GO nanolayers was analysed based on the kinetic study of the GO:<sup>18</sup>F-FDG mixtures. The chemical adsorbability of the material was analysed via UV-vis spectrophotometer to interlink the microstructures of GO with the sorption affinity interaction. Resultantly, the adsorption rate was effective at a slow decay rate and the optical adsorption of GO with <sup>18</sup>F-FDG was dominated by the  $\pi \rightarrow \pi^*$  plasmon peak, which was near 230 nm. By elucidating the underlining GO special features, an alternative technique to isolate <sup>18</sup>F-FDG for the decontamination process was successfully proven.

**Keywords:** radiopharmaceutical; radioactive spillage; decontamination; radioactivity; adsorption; nuclear medicine

## 1. Introduction

Radiopharmaceutical (RPC) resources are essential for nuclear imaging and therapeutic purposes in nuclear medicine. Fluorine-18 Fluorodeoxyglucose (<sup>18</sup>F-FDG) is the most ideal RPC for positron emission tomography (PET) scans due to its ideal half-life and versatile molecular structure [1,2]. Fluorine is considered a favourable atom in drug development due to its physical properties, including a small van der Waals radius (1.47 Å),

high electronegativity, and ability to form a strong bond with carbon (C-F energy bond of 112 kcal/mol) [3]. In comparison with a carbon-hydrogen bond (C-H energy bond of 98 kcal/mol),  $^{18}\text{F}$ -FDG is more thermally stable and oxidation resistant [3]. Unexpected radioactive contamination might occur in a nuclear medicine department either from source handling, such as breakage of a radionuclide vial, or may originate from the patient either by sneezing, vomiting, or urinating [4]. The hazard associated with radioactive contamination and waste depends on the concentration and nature of the activity of the radionuclide [5].  $^{18}\text{F}$ -FDG, an unstable radioisotope, will decay in the human metabolic process and produce positrons, thereby leading to an annihilation process with electrons and producing pairs of 511 keV gamma-ray photons in 180° directions [6]. This energy is quite high and exposes the personnel, patient, and public to unnecessary radiation doses.

The high demand for PET scans requires mass production of  $^{18}\text{F}$ -FDG using cyclotron, which indirectly leads to an increase in the incident rate of radionuclide spillage contaminations. Meanwhile, the usage of a large volume of simple decontamination chemical agents might not be sustainable in the environment [7], and is not cost-effective as its periodic purchase is met with limited production. Thus, alternative decontamination agents must be considered by ensuring the application of a competent material for radionuclide decontamination, which is more efficient, environmentally friendly, and economical in terms of long-term usage of the resources [8].

Graphene oxide (GO) is a nanolayer material that has a carbon compound and is rich in oxygenated functional groups, which makes it a fitting adsorbent for various molecules either in aqueous or dispersed in a polymeric solution [9]. GO also has several desirable properties, such as high surface area, high mechanical strength, electrical conductivity, large pore volume structure, and high solubility due to abundant oxygen-based functional groups [9]. GO is a two-dimensional (2D), carbon-based material that has a single-atom-thin full  $\text{sp}^2$  hybridised carbon structure with minimal defects, which makes it a well-known adsorbent [10]. Due to its uniquely tuneable physicochemical characteristics [11] and biocompatibility [12], GO has been used in many applications such as the removal of metal ions [13], biomedical [14], electrochemical energy [15], catalysis [16], sensing [17], polymers composite [18], removal of heavy metals [19], wastewater treatment [20] and antibacterial agents [21].

The availability of various functional groups such as carboxyl, hydroxyl, epoxy and keto groups on its nano surface [22] give advantages to GO as a super adsorbent carbon material to efficiently interact with any hazardous and toxic liquid, gas or solid contaminants [23]. Practically, radioactive waste has been decontaminated using special chemical agents which might chemically produce other chemical by-products [24] due to chemical interactions with unstable energetic radionuclide.

Application of GO nanosheets in trapping radionuclides has been conducted on  $^{238}\text{U}$  [25],  $^{137}\text{Cs}$  [26],  $^{131}\text{I}$  [27],  $^{232}\text{Th}$ ,  $^{95}\text{Am}$ ,  $^{94}\text{Pu}$ ,  $^{63}\text{Eu}$ ,  $^{38}\text{Sr}$  and  $^{99\text{m}}\text{Tc}$  [28]. However, adsorption and chemical adsorption characterization of short-live radionuclides such as the  $^{18}\text{F}$  radionuclide by using GO has not been comprehensively reported. Herewith, we conduct experiments to prove the efficiency of  $^{18}\text{F}$ -FDG decontamination by using GO, which is a stable carbon-based material with minimal production of chemical by-products. The interactions between these compound mixtures with different concentration of GO and activities for energy variations were characterized by using UV-vis spectrometer for complex adsorption capabilities.

## 2. Materials and Methods

Graphite powder, a naturally occurring form of crystalline carbon along with inorganic compound potassium permanganate ( $\text{KMnO}_4$ ) and corrosive substances, sulphuric acid ( $\text{H}_2\text{SO}_4$ ) and phosphoric acid ( $\text{H}_3\text{PO}_4$ ), were used to make up the GO mixture. Hydrogen peroxide ( $\text{H}_2\text{O}_2$ , 30%) and ice cubes were used to initiate and phase out the oxidation process. Consequently, hydrochloric acid (HCl) and distilled water were used for the centrifugation process.  $^{18}\text{F}$ -FDG was obtained at the Nuclear Medicine & Molecular Imaging

Department, Chancellor Tuanku Muhriz Hospital, Universiti Kebangsaan Malaysia. A dose calibrator (Capintec CRC-25R, Capintec Inc., Florham Park, NJ, USA) was used to monitor and record the activity of the radionuclides. The characterisation of the synthesised GO was performed using FESEM (FEI Quanta™ 450 FEG, FEI Company, Hillsboro, OR, USA) at SEM Laboratory, School of Health Sciences, Universiti Sains Malaysia. Furthermore, a morphological analysis of the nanolayers and their porosity was conducted. Meanwhile, the chemical adsorbability affinity of the GO-<sup>18</sup>F-FDG was analysed using a UV-vis spectrometer (CARY 100 Bio, Agilent Technologies Inc., Santa Clara, CA, USA) at the Analytical Laboratory, School of Health Sciences, Universiti Sains Malaysia.

### 2.1. Synthesis of Graphene Oxide

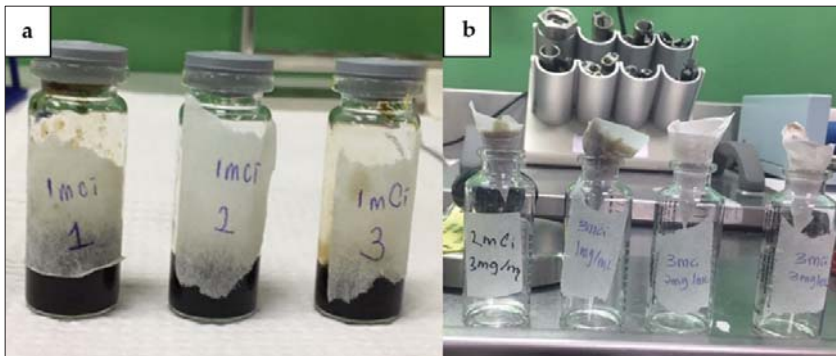
The Graphene oxide was synthesised by the widely used Hummer's method [29–31]. About 3 g of graphite and 18 g of KMnO<sub>4</sub> were added to the 320 mL of H<sub>2</sub>SO<sub>4</sub> and 80 mL of H<sub>3</sub>PO<sub>4</sub> in a ratio of 4:1, respectively. The mouth of the beaker was closed with an aluminium foil and stirred for three days continuously before transferring the reagent into a 500 mL ice cube along with 27 mL of H<sub>2</sub>O<sub>2</sub> (30%) to stop the oxidation and cooling process. The dark brown mixture formed was known as graphite oxide, which was then washed with HCl to separate the GO from the chemical by-products and unexfoliated graphite. About 15 mL of the mixture and 15 mL of HCL were mixed and centrifuged at 5000 g/rpm for 10 min. This washing process was repeated thrice before washing with distilled water several times and centrifuged with the same setting until a pH of 5 was achieved.

### 2.2. Isolation of <sup>18</sup>F-FDG

The GO concentrations were varied into 1 mg/mL, 2 mg/mL, and 3 mg/mL, which were obtained by applying Equation (1), where  $M_1$  is the initial concentration of the solution,  $V_1$  is the volume of the solution,  $M_2$  is the concentration of the diluted solution after adding more solvent, and  $V_2$  is the volume of the diluted solution.

$$M_1 V_1 = M_2 V_2 \quad (1)$$

The FDG dispenser (NUCLEMED 317R3, NUCLEMED BV, Roeselare, Belgium) was used to accurately prepare the 37 MBq, 74 MBq, and 111 MBq of <sup>18</sup>F-FDG, and three different concentrations of GO were added into each glass serum vial as shown in Figure 1a. The mixture of GO-<sup>18</sup>F-FDG was then poured on a filter paper, and the sediment was obtained as depicted in Figure 1b. The radioactivity of the sediment along with the filter paper and the filtrate (if available) were obtained using the dose calibrator ionisation chamber over the function of time ( $A_0$  = initial activity,  $A_0/4$  = 54.9 min,  $A_0/2$  = 109.8 min,  $A_0/3/4$  = 164.7 min, and  $A_0/16$  = 219.6 min). The radioactivity of each activity with different concentrations was compared to the natural decay of <sup>18</sup>F-FDG by plotting the decay graph. A Geiger–Muller survey meter (Model Fluke 451B, Fluke Corporation, Everett, WA, USA) was used during the experiment to measure the radiation exposure, ensuring there was no leakage or spillage of the radionuclide source on any surfaces in the laboratory.

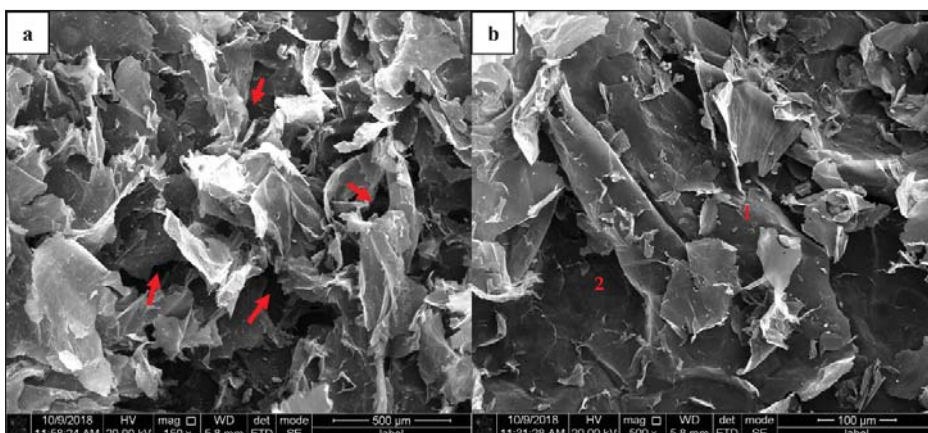


**Figure 1.** (a) GO solution with 1 mg/mL, 2 mg/mL and 3 mg/mL mixed with  $^{18}\text{F}$ -FDG of 1mCi (~37 MBq) in glass serum vials. (b) GO: $^{18}\text{F}$ -FDG mixture poured into filter papers.

### 3. Results and Discussions

#### 3.1. Characterisation of GO Nanolayers

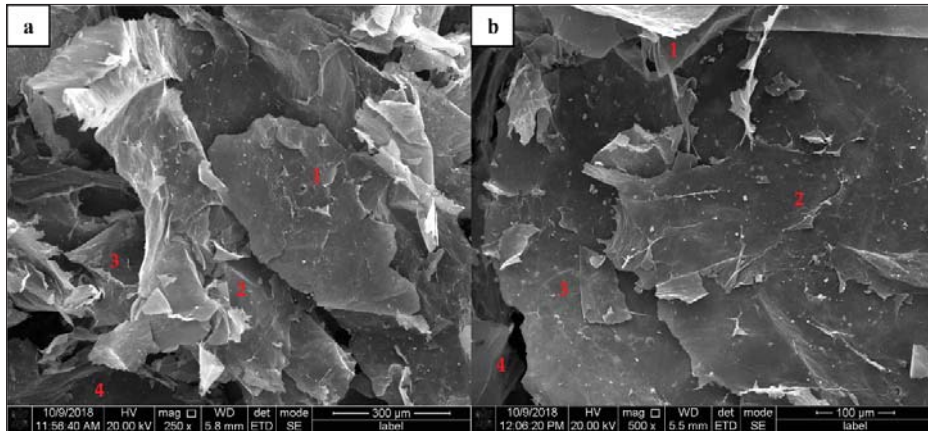
Graphene oxide (GO) images obtained from the FESEM were well defined and interlinked two-dimensional (2D) graphene sheets. Figure 2a,b show random sophisticated 2D structures with different magnifications. The surface appears as a wrinkly ‘wax tissue layer’ with hollow structures (red arrows in Figure 2a) and a continuous vast layer-by-layer surface area with random size of GO flakes (numbering layers in Figure 2b). This feature is advantageous to the GO in terms of ‘wrapping’ or entrapping other materials with various chemical bonds by the numerous carbon functional groups existing at the molecular structure level [32]. It also shows that the ‘wax tissue layer’ [33,34], which resembles the GO sheet, reflects that the deformation of the graphene layers was due to the oxidation process in the synthesised GO. Hence, the carbon lattice became distorted following the addition of oxygen lattice into the structures [35]. The generated hollow pores as shown in Figure 2a could be formed via the hydrothermal method by crumpling graphene sheets together, which results in the formation of voids between the sheets [32]. These features in the GO appear to be advantageous in terms of the hydrophilicity and dispersion into various media, including aqueous and organic solvents.



**Figure 2.** GO flake 2D structures with random ‘wax-tissue’ layers and complex hollow structures. (a) Complex hollow structures with wrinkles and exfoliated tissue layers, (b) wrinkles and exfoliated stacked structures with random small flakes.

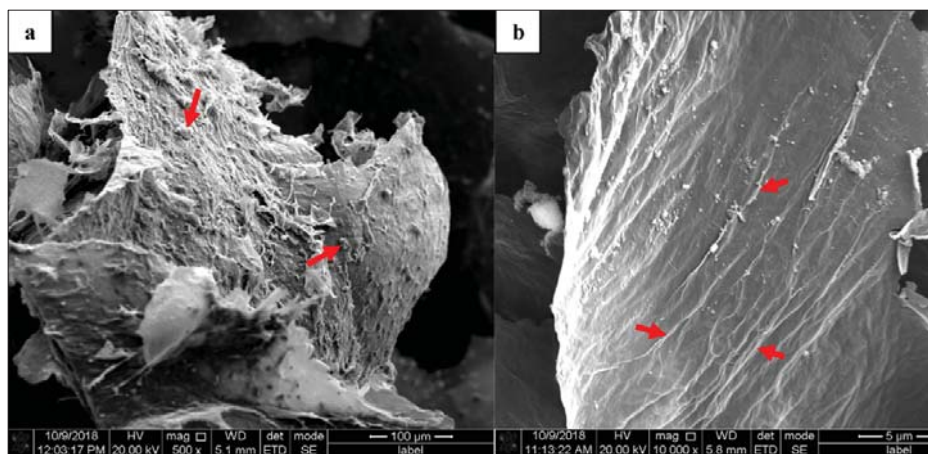


Stacked GO structures can be clearly seen in Figure 3a,b for 250 $\times$ , and 500 $\times$  magnification. The stacking structures enhance the continuous interaction probabilities with other compounds, where the large substrate surface area will participate in the molecular interactions [33]. The interactions probabilities are continuously increased with stacking layers by layers of GO and might be trapped within the compound with increasing depth via complex interactions.



**Figure 3.** GO substrate surface stacked nanostructures. (a) Random stacks of small-flake GO nano-layers, (b) flat surface of large-flake GO nano-layers.

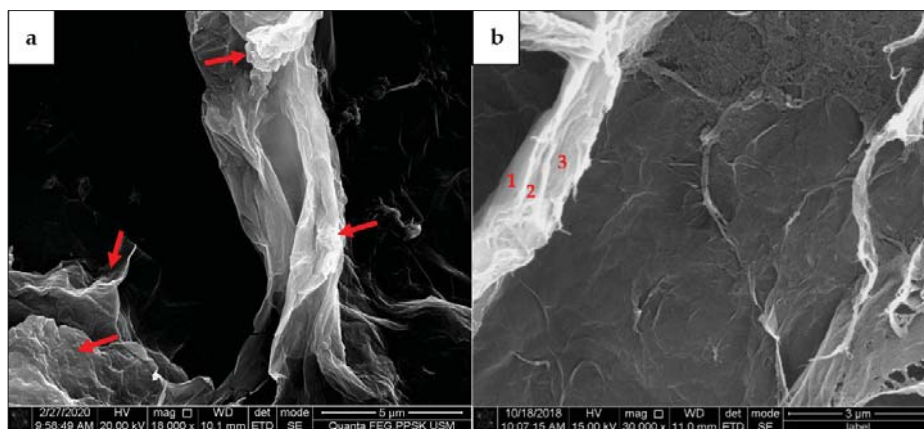
Meanwhile, a single substrate of GO nanolayers can be seen in a close-up micrograph in Figure 4a,b. The micrograph enhances the size of the nano substrate surface for molecular interactions to trap the  $^{18}\text{F}$ -FDG and other compounds. Some contaminants on the GO surface can be seen in Figure 4a, which might be due to the incomplete washing of some foreign particles (red arrows). However, Figure 4b shows a significant structure of single wax tissue layers of GO with wrinkles and exfoliated networking lines on the surface (arrows), ready for the adsorption process via the molecular interaction of many available functional groups.



**Figure 4.** Close-up of single substrate GO nanolayers. (a) Contaminants existed on the GO nanolayers, (b) continuous wrinkle and exfoliated networking lines ready for adsorption interactions.



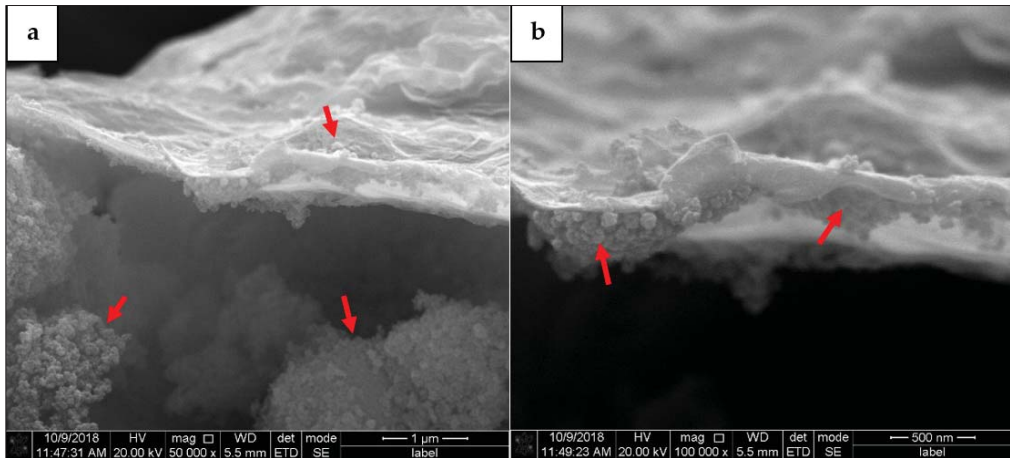
In additions, the complex structures of GO nanolayers have been focused within smaller scales as those shown in Figure 5a,b. The agglomerated ‘wax tissue’ nanolayers with non-uniform structures are shown in Figure 5a. The complex wrinkles and exfoliated structures can be seen via the red arrows, whereas the agglomerated long strand ‘wax-tissue’ nanolayers can be seen on another site. On the other hand, Figure 5b shows the multiple stacking layers that can still be identified from the agglomerated wax tissue layers. These structures demonstrate that the continuous multiplex nanolayers randomly existed for fine focused micrograph and widely spread on the GO substrates.



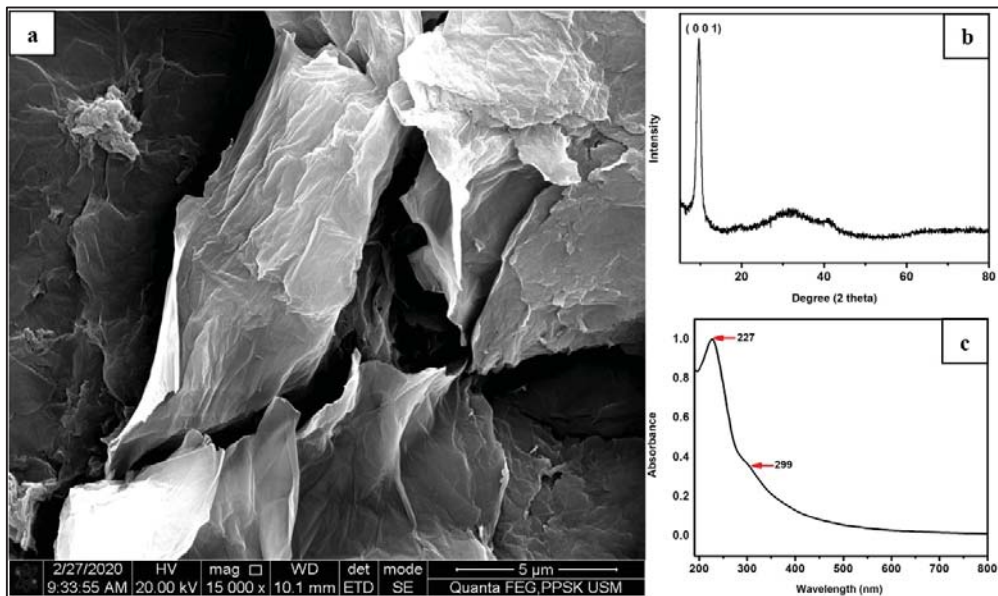
**Figure 5.** Agglomerated ‘wax-tissues’ GO with stacking layers. (a) Random and long strand agglomerated ‘wax-tissue’ nanolayers, (b) identification of stacking layers on agglomerated GO structures.

Moreover, agglomerated wrinkle and exfoliated structures have been further characterized with smaller scales to show a close up image of the 2D single nanolayers of the ‘wax-tissue’ GO structures as shown in Figure 6a,b. It can be seen that the small spherical agglomerated GO nanostructures are randomly attached on the upper site as shown in Figure 6a and the lower site as shown in Figure 6b of the single nanolayers. This phenomenon proves the complex random structures of agglomerated GO nanolayers existed along the stacking surfaces and promote high interactions with any materials via molecular interactions [36]. However, agglomerated unattached spherical nano structures are also randomly seen in Figure 6a, which leads to random complex interactions efficiency during the adsorption process [37].

In Figure 7a, a stacking wrinkles and exfoliated GO nanolayers has been selected for characterization by using X-ray diffraction technique (XRD) (Bruker D2, Bruker Corporation, Billerica, MA, USA) and UV–vis spectrometer. XRD spectrum of the GO is similar to the GO reported in other previous published works. It can be seen in Figure 7b that the characteristic peak of GO centred at  $10.0^\circ$ , which was assigned to the (0,0,1) reflection of GO. The UV–visible adsorption spectra of GO are shown in the Figure 7c. As revealed by the spectrum, two characteristic peaks of GO were observed at 227 and 229 nm, which were  $\pi \rightarrow \pi^*$  transition of aromatic C–C bond and the  $n \rightarrow \pi^*$  of C=O group, respectively. This is in agreement with the results published elsewhere [38].



**Figure 6.** (a) Attached and free spherical agglomerated GO structures and (b) small spherical agglomerated GO nano structures have been randomly attached on the stacked wrinkles and exfoliated single GO nanolayer.



**Figure 7.** (a) Stacking wrinkles and exfoliated GO nanolayers [34], (b) XRD characterization of GO centred at  $10.0^\circ$ , and (c) UV–vis spectrum characteristic peaks of GO observed at 227 and 299 nm.

### 3.2. Kinetic Study

The kinetic study of the isolation of GO- $^{18}\text{F}$ -FDG mixtures for different concentrations of GO concentrations and RPC activities was extrapolated using the radioactive decay equation as shown in Equation (2), where  $A$  is the radionuclide activity,  $A_0$  is the initial radionuclide activity,  $\lambda$  is the decay constant, and  $t$  is the decay time. Each of the activities (37 MBq, 74 MBq and 111 MBq) that were mixed with different GO concentrations (1, 2, 3 mg/mL) and trapped by using a filter paper were measured using a dose calibrator within specific periods (54.9 min,

109.8 min, 164.7 min, and 219.6 min). The activities were differentiated in order to investigate the influence of the positrons and gamma-ray photons' production rate on the molecular adsorption process. Three graphs to study the kinetics of the  $^{18}\text{F}$ -FDG isolated by GO based on activity over time were plotted for different values of  $A_0$  as shown in Figures 8–10.

$$\ln(A/A_0) = -\lambda t \quad (2)$$

Figures 8–10 depict the exponentially plotted graph of GO: $^{18}\text{F}$ -FDG activities versus time for three different concentrations (1, 2, and 3 mg/ mL). From these graphs, the activity of GO: $^{18}\text{F}$ -FDG was exponentially decreased to half from their approximate initial activities within 109.8 min, which is the natural half-life of  $^{18}\text{F}$  [39]. From the graph, the first term half-life for three different activities (37 MBq, 74 MBq and 111 MBq) are sharply reduced due to their active decay processes with respect to its initial activities (high activity), becoming stagnant for the second term of its half-life and approximately close to zero for total decay (219.6 min). The decay process depends on the activities of the radionuclide, where higher activities promote active interactions with random decay processes in the nucleus. In this study, the existence of different concentrations of GO with RPC influenced the nuclear decay process within the unstable  $^{18}\text{F}$  nucleus, where there are different activities has been measured for different concentrations in a specific natural half-life. This phenomenon might be due to the adsorption of GO at the molecular level which is mostly via van der Waals and ionic interactions [40], causing some inter-molecular changes of weak nuclear and electromagnetic forces in  $^{18}\text{F}$  during its decay process. Influence of the weak nuclear forces that control the nuclear activities for any radioisotope decay [41], might cause some changes in the decay rate of the materials during complex molecular interactions.

Generally, 1 mg/mL concentration of GO can trap the  $^{18}\text{F}$ -FDG effectively, where the activity is always higher in each measured time as shown in Figures 8–10. This might be due to random nuclear interaction activities in the  $^{18}\text{F}$  nucleus, where vast numbers of electrons for higher concentrations might fluctuate or slow the molecular interactions. Fluctuation at the initial activity due to a high decay rate may be attributed to the reactivity of the orbital electrons of fluorine, which actively tend to be stabilised via complex interaction [42].

The adsorption interactions might also be influenced by the physical volume of the RPC that coagulate with certain GO concentrations, where the insoluble process might occur due to saturated solutions. It also shows that a higher concentration of GO could reduce the activity of  $^{18}\text{F}$ -FDG due to the interactions occurring at molecular levels. High activities of  $^{18}\text{F}$ -FDG (111 MBq and 74 Mbq) actively produce positron, which originates from the nucleus and leads to an annihilation process rather than adsorption interaction with the GO. Figures 9 and 10 show the undifferentiation for low and high concentrations of GO and their influence on the activity decay of  $^{18}\text{F}$ -FDG, where the line is almost redundant with each other. However, the slower decay process provides a likelihood for adsorption interactions, where the line is seen to be identical at 50 min onwards in Figure 6, as well as the whole measurable activity in Figure 8. This might be due to the availability of free electron clouds in  $^{18}\text{F}$ -FDG, which have more chance to be interacted with and form functional groups in the GO chemical structures at low activity.

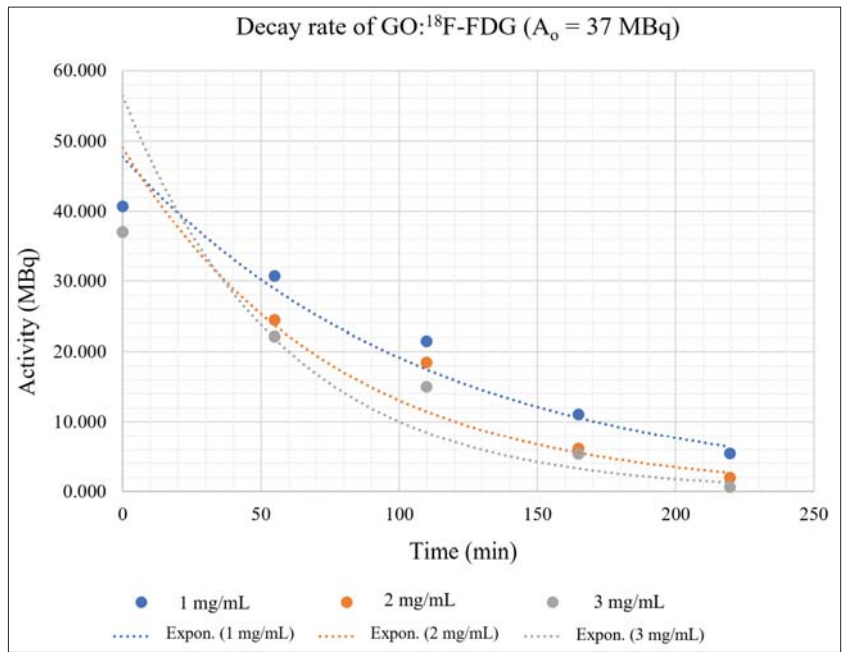


Figure 8. GO:<sup>18</sup>F-FDG mixtures with an initial activity of 37 MBq and different concentrations of GO.

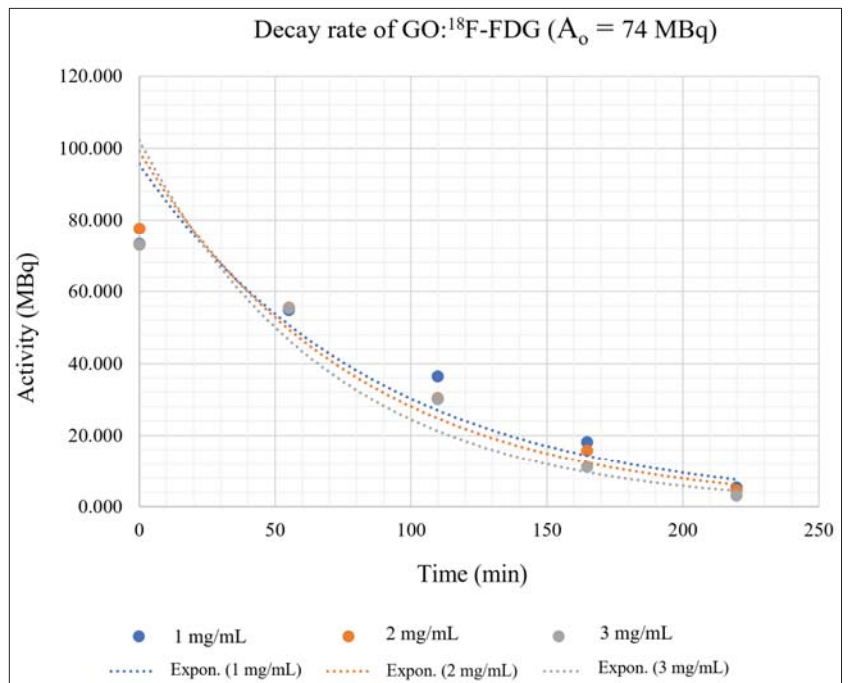
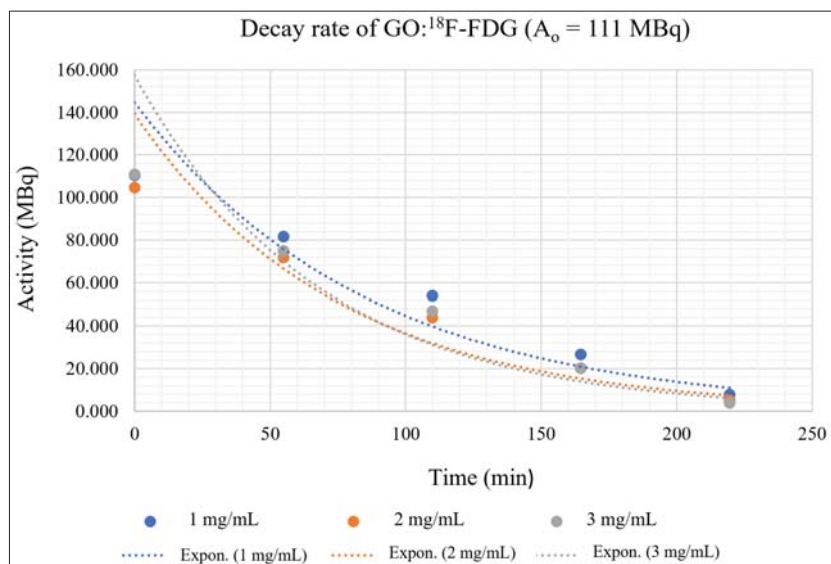


Figure 9. GO:<sup>18</sup>F-FDG mixtures with an initial activity of 74 MBq and different concentrations of GO.



**Figure 10.** GO:<sup>18</sup>F-FDG mixtures with an initial activity of 111 MBq and different concentrations of GO.

### 3.3. UV-Vis Spectrometry and Chemical Analysis

The study of absorbability of the graphene oxide and the radionuclide using the UV-vis spectrophotometer provided detailed information about the peak of the wavelength based on the Beer-Lambert law [43]. The GO and <sup>18</sup>F-FDG UV-visible adsorption spectra were obtained as shown in Figure 11. A single band GO adsorption peak can be observed, which was centred at 220 nm as depicted by the dashed red line. This band value indicates the  $\pi \rightarrow \pi^*$ , the transition of aromatic C-C bonds, which have numerous  $sp^2$  bonds into the molecular mixtures [44]. The molecule absorbs the UV-vis light starting at the wavelength of 200 nm and begins to decline before attaining the peak at 220 nm. Thereafter, the molecule continues to decline to show that the functional group of GO has partially decreased as it passes a higher value of wavelength. The optical adsorption of GO is dominated by the  $\pi \rightarrow \pi^*$  plasmon peak, which is near 230 nm [45]. This occurrence depends on two conjugative effects: clusters of nanometer-scale  $sp^2$  and the chromophore unit, such as C=C, C=O and C-O bonds [45].

The chemical structure of <sup>18</sup>F is  $1s^2 2s^2 2p^5$  and has a single free orbital electron. It is able to produce high energetic photons with 511 keV which activate the orbital electrons of the functional groups and delocalize on to the GO nano sheets via continuous  $\pi \rightarrow \pi^*$  stacking interactions due to the stacked nanolayers of GO structures. The 511 keV photons energy might eject the orbital electrons at available functional groups to provide free molecular vacancy to be filled in by unstable <sup>18</sup>F atoms. The electrons might interact with epoxy bridges, hydroxyl groups, and pairwise carboxyl groups in GO nanolayers [45] and might be influenced by excess energies received during the internal nuclear decay, leading to the annihilation process as shown in Figure 12.

The peak obtained at 220 nm was probably due to the aggregation of chromophore effects that were affected by the mixture of GO:<sup>18</sup>F-FDG for different GO concentrations [46]. The 1 mg/mL showed the highest peak and the highest adsorbability compared to 2 mg/mL and 3 mg/mL of GO concentrations. This result is in line with the kinetic study illustrated in Figure 8, where a slow decay rate of low <sup>18</sup>F-FDG activity provided the chances for the molecular adsorption rate to occur. Higher concentrations might yield a complex saturated phase between the molecular mixtures to interact within a short time, whereas higher activities will generate excess energy to the particles for the annihilation process or eject the electrons from orbitals without interactions. The mixture probably modified the

oxygen-containing functional groups, thereby causing the mixture to absorb a slightly lower range of UV-vis wavelength. The wavelength of adsorption also depends on the energy difference between the bonding or antibonding and non-bonding orbital concerned [47].

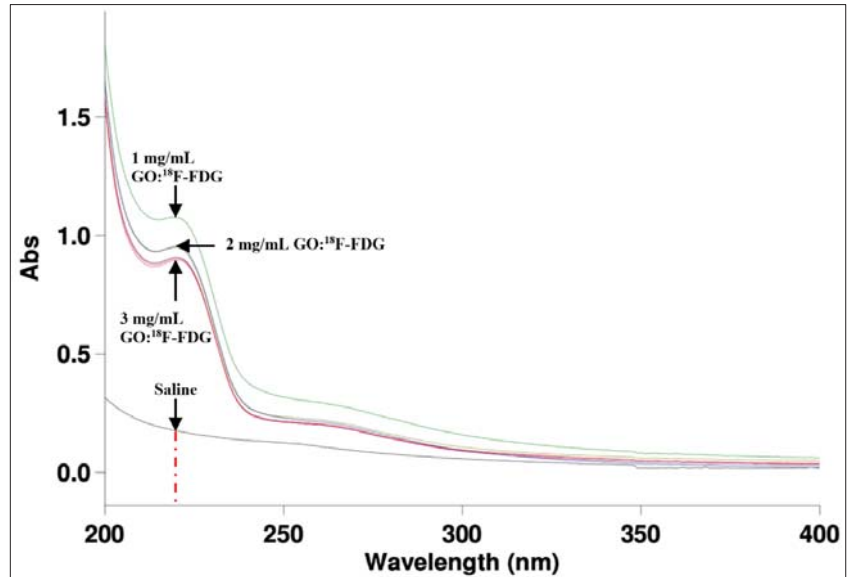


Figure 11. The UV-vis adsorption of  $\text{GO}^{18}\text{F-FDG}$  with different concentrations has been seen on at the peak of 220 nm.

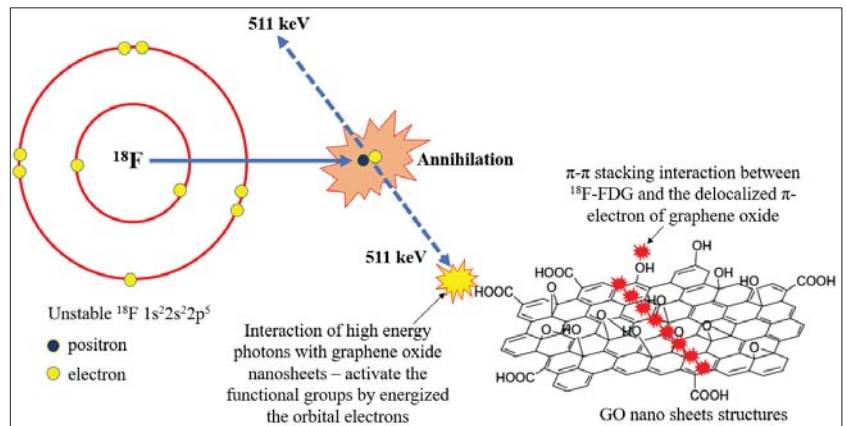


Figure 12. Illustration of energetic gamma rays produced by unstable  $^{18}\text{F}$  when activating the adsorption process with functional groups and GO nanosheet structures.

#### 4. Conclusions

Conclusively, GO has demonstrated high sorption affinity towards the radionuclide of a pure radiopharmaceutical. The high sorption capacity and the ability to coagulate with any reactive elements at molecular structures, such as  $^{18}\text{F-FDG}$ , makes it a prime option for alternative radionuclides decontamination. The 'wax tissue' nanolayers and vast surface area have been shown to help GO wrap and adsorb radionuclides effectively. The adsorption rate was effective at a slow decay rate of  $^{18}\text{F-FDG}$ , where more available free



electrons are ready for the adsorption interaction with GO functional groups. Fluctuation of electron interactions and the active annihilation process occurred at high activity, thereby reducing the coagulation process within a short time due to the energetic nuclear process. The optical adsorption of GO with  $^{18}\text{F}$ -FDG is dominated by the  $\pi \rightarrow \pi^*$  plasmon peak, which is near 230 nm.

**Author Contributions:** Conceptualization, M.K.A.A.R. and A.M.N.; methodology, M.K.A.A.R., A.M.N. and N.H.A.; software, N.H.A. and F.A.M.Z.; validation, M.K.A.A.R., A.M.N. and N.H.A.; formal analysis, M.K.A.A.R., F.H.M.H., A.M.N. and F.A.M.Z.; investigation, M.K.A.A.R., N.M.N.; resources, M.K.A.A.R., N.M.N., A.M.N., M.M. and F.A.M.Z.; data curation, F.H.M.H., R.S. and F.I.; writing—original draft preparation, M.K.A.A.R. and F.H.M.H.; writing—review and editing, M.K.A.A.R., N.M.N., A.M.N.; visualization, M.K.A.A.R., A.M.N.; supervision, M.K.A.A.R., N.M.N., N.H.A. and M.M.; project administration, F.H.M.H., R.S. and F.I., M.M.; funding acquisition, M.K.A.A.R. and N.M.N. All authors have read and agreed to the published version of the manuscript.

**Funding:** This work was supported by a Short-Term Research Grant from Universiti Sains Malaysia [304/PPSK/6315499]. The APC was funded by Universiti Sains Malaysia.

**Institutional Review Board Statement:** Not applicable.

**Informed Consent Statement:** Not applicable.

**Data Availability Statement:** Not applicable.

**Acknowledgments:** We express our appreciation to Nik Fakurudin Nik Ali and Wan Norhasikin Wan Marizam of the School of Health Sciences, Universiti Sains Malaysia, for their help in obtaining the FESEM micrographs. Our appreciation goes to the Department of Nuclear Medicine, Radiotherapy & Oncology, Hospital Universiti Sains Malaysia and Nuclear Medicine & Molecular Imaging Department, Chancellor Tuanku Muhriz Hospital, Universiti Kebangsaan Malaysia for the use of their facilities when conducting the research project.

**Conflicts of Interest:** The authors declare no conflict of interest.

## References

1. Payolla, B.; Massabni, A.F.; Orvig, C. Radiopharmaceuticals for Diagnosis in Nuclear Medicine: A short review. *Eclat. Quim.* **2019**, *44*, 11–19. [[CrossRef](#)]
2. Jacobson, O.; Kiesewetter, D.; Chen, X. Fluorine-18 Radiochemistry, Labeling Strategies and Synthetic Routes. *Bioconjugate Chem.* **2014**, *26*, 1–18. [[CrossRef](#)] [[PubMed](#)]
3. Park, B.; Kitteringham, N. Effects of Fluorine Substitution on Drug Metabolism: Pharmacological and Toxicological Implications. *Drug Metab. Rev.* **1994**, *26*, 605–643. [[CrossRef](#)] [[PubMed](#)]
4. Nawi, N.M.; Ahmad, N.S.; Abdullah, R.; Zainon, W.M.N.W.; Razab, M.K.A.A. Correlation of external dose rate with whole body clearance estimation in radioiodine therapy for rhTSH and THW patients. *J. Radiat. Res. Appl. Sci.* **2020**, *13*, 240–245. [[CrossRef](#)]
5. Ramesha, G.; Vijaya Kumara, A.; Muralidhara, H.; Sampath, S. Graphene and graphene oxide as effective adsorbents toward anionic and cationic dyes. *J. Colloid Interface Sci.* **2011**, *361*, 270–277. [[CrossRef](#)]
6. Jiang, W.; Chalich, Y.; Deen, M.J. Sensors for Positron Emission Tomography Applications. *Sensors* **2019**, *19*, 5019. [[CrossRef](#)]
7. Shivanand, B.; Akchata, S.; Lavanya, K. Influence of decontaminating agents and swipe materials on laboratory simulated working surfaces wet spilled with sodium perchlorate. *Indian J. Nucl. Med.* **2017**, *32*, 173–176. [[CrossRef](#)]
8. Lee, W.; Ojovan, M.; Jantzen, C. *Radioactive Waste Management and Contaminated Site Clean-Up*; Woodhead Publishing: Cambridge, UK, 2013; pp. 301–326.
9. Fu, S.; Sun, Z.; Huang, P.; Li, Y.; Hu, N. Some Basic Aspects of Polymer Nanocomposites: A critical review. *Nano Mater. Sci.* **2019**, *1*, 2–30. [[CrossRef](#)]
10. Smith, A.; LaChance, A.; Zeng, S.; Liu, B.; Sun, L. Synthesis, properties, and applications of graphene oxide/reduced graphene oxide and their nanocomposites. *Nano Mater. Sci.* **2019**, *1*, 31–47. [[CrossRef](#)]
11. Sajjad, S.; Leghari, S.A.K.; Iqbal, A. Study of Graphene Oxide Structural Features for Catalytic, Antibacterial, Gas Sensing and Metals Decontamination Environmental Applications. *ACS Appl. Mater. Interfaces* **2017**, *9*, 43393–43414. [[CrossRef](#)]
12. Zhao, Y.; Zhang, Z.; Pan, Z.; Liu, Y. Advanced Bioactive Nanomaterials for Biomedical Applications. *Exploration* **2021**, *1*, 20210089. [[CrossRef](#)]
13. Novacek, M.; Jankovsky, O.; Luxa, J.; Sedmidubsky, D.; Pumera, M.; Fila, V.; Lhotka, M.; Klimova, K.; Matejkova, S.; Sofer, Z. Tuning of Graphene Oxide Composition by Multiple Oxidations for Carbon Dioxide Storage and Capture of Toxic Metals. *J. Mater. Chem. A* **2017**, *5*, 2739–2748. [[CrossRef](#)]



14. Prasadh, S.; Suresh, S.; Wong, R. Osteogenic Potential of Graphene in Bone Tissue Engineering Scaffolds. *Materials* **2018**, *11*, 1430. [[CrossRef](#)]
15. Raccichini, R.; Varzi, A.; Passerini, S.; Scrosati, B. The Role of Graphene for Electrochemical Energy Storage. *Nat. Mater.* **2015**, *14*, 271–279. [[CrossRef](#)] [[PubMed](#)]
16. Ng, Y.H.; Ikeda, S.; Matsumura, M.; Amal, R. A Perspective on Fabricating Carbon-based Nanomaterials by Photocatalysis and their Applications. *Energy Environ. Sci.* **2012**, *5*, 9307–9318. [[CrossRef](#)]
17. Wen, J.; Xu, Y.; Li, H.; Lu, A.; Sun, S. Recent Applications of Carbon Nanomaterials in Fluorescence Biosensing and Bioimaging. *Chem. Commun.* **2015**, *51*, 11346–11358. [[CrossRef](#)]
18. Shtein, M.; Nadiv, R.; Buzaglo, M.; Kahil, K.; Regev, O. Thermally Conductive Graphene Polymer Composites: Size, Percolation and Synergy Effects. *Chem. Mater.* **2015**, *27*, 2100–2106. [[CrossRef](#)]
19. Zunita, M.; Irawanti, R.; Koesmawati, T.A.; Lugitua, G.; Wenten, I.G. Graphene Oxide (GO) Membrane in Removing Heavy Metals from Wastewater: A Review. *Chem. Eng. Trans.* **2020**, *82*, 415–420.
20. Ng, L.Y.; Chua, H.Y.; Ng, C.Y. Incorporation of Graphene Oxide-based Nanocomposite in the Polymeric Membrane for Water and Wastewater Treatment: A review on Recent Development. *J. Environ. Chem. Eng.* **2021**, *9*, 105994. [[CrossRef](#)]
21. Aunkor, M.T.H.; Raihan, T.; Prodhon, S.H.; Metselaar, H.S.C.; Malik, S.U.F.; Azad, A.K. Antibacterial Activity of Graphene Oxide Nanosheet Against Multidrug Resistant Superbugs Isolated from Infected Patients. *R. Soc. Open Sci.* **2020**, *7*, 200640. [[CrossRef](#)]
22. Eigler, S.; Hirsch, A. Chemistry with Graphene and Graphene Oxide—Challenges for Synthetic Chemists. *Angew. Chem. Int. Ed.* **2014**, *53*, 7720–7738. [[CrossRef](#)] [[PubMed](#)]
23. Sabzehmeidani, M.M.; Mahnaee, S.; Ghaedi, M.; Heidari, H.; Roy, V.A.L. Carbon Based Materials: A review of Adsorbents for Inorganic and Organic Compounds. *Mater. Adv.* **2021**, *2*, 598–627. [[CrossRef](#)]
24. Felcorn, E. *Technology Reference Guide for Radiologically Contaminated Surfaces*; U.S. Environmental Protection Agency: Washington, DC, USA, 2006; pp. 11–18.
25. Zhao, G.; Wen, T.; Yang, X.; Yang, S.; Liao, L.; Hu, J.; Shao, D.; Wang, X. Preconcentration of U(VI) Ions on Few-layered Graphene Oxide Nanosheets from Aqueous Solutions. *Dalton Trans.* **2012**, *41*, 6182–6188. [[CrossRef](#)]
26. Rauwel, P.; Rauwel, E. Towards the Extraction of Radioactive Cesium-137 from Water via Graphene/CNT and Nanostructured Prussian Blue Hybrid Nanocomposites: A Review. *Nanomaterials* **2019**, *9*, 682. [[CrossRef](#)] [[PubMed](#)]
27. Suksompong, T.; Thongmee, S.; Sudprasert, W. Efficacy of a Graphene Oxide/Chitosan Sponge for Removal of Radioactive Iodine-131 from Aqueous Solutions. *Life* **2021**, *11*, 721. [[CrossRef](#)] [[PubMed](#)]
28. Romanchuk, A.Y.; Slesarev, A.S.; Kalmykov, S.N.; Kosynkin, D.V.; Tour, T.M. Graphene Oxide for Effective Radionuclide Removal. *Phys. Chem. Chem. Phys.* **2013**, *15*, 2321–2327. [[CrossRef](#)]
29. Noor, A.M.; Yusoff, N.F.A.; Huang, N.M.; Kari, Z.A.; Razab, M.K.A.A.; Bakar, M.H.A.; Lee, S.W.; Abdullah, N.H. Facile Preparation of Graphene Oxide Silver Aerogel for Antibacterial. *J. Trop. Resour. Sustain. Sci.* **2018**, *6*, 41–44.
30. Zin FA, M.; Noor, A.M.; Razab, M.K.A.A.; Abdullah, N.H.; Lee, S.W. Synthesis of Silver Graphene Oxide Nanocomposite Reinforced with Kenaf Cellulose Nanofibril Aerogel. *AIP Conf. Proc.* **2019**, *2068*, 020045-1–020045-6.
31. Noor, A.M.; Zin, F.M.; Wei, L.S.; Huang, N.M.; Bakar, M.H.A.; Sajab, M.S.; Razab, M.K.A.A.; Abdullah, N.H.; Kari, Z.A. Laser Scribe Silver-reduced Graphene Oxide as Novel Bactericidal Filter. *AIP Conf. Proc.* **2019**, *2068*, 020026-1–020026-6.
32. Zobir, S.A.M.; Rashid, S.A.; Tan, T. Recent Development on the Synthesis Techniques and Properties of Graphene Derivatives. In *Synthesis, Technology and Applications of Carbon Nanomaterials*; Rashid, S.A., Othman, R.N.I.R., Hussein, M.Z., Eds.; Matthew Deans: Oxford, UK, 2019; pp. 77–107.
33. Razab, M.K.A.A.; Mansor, M.S.; Noor, A.M.; Latif, N.F.F.A.; Rozi, S.M.; Jaafar, K.N.; Jamaludin, F. Characterization of GO:I-131 for Radioactive Clinical Waste Water Management in Nuclear Medicine. *Mater. Sci. Forum.* **2020**, *1010*, 561–566. [[CrossRef](#)]
34. Razab, M.K.A.A.; Mansor, M.S.; Noor, A.M.; Rozi, S.M.; Latif, N.F.F.A.; Jaafar, K.N.; Jamaludin, F. Preliminary Study of the Potential Graphene Oxide as Radioactive Clinical Wastewater Adsorbability in Nuclear Medicine. *IOP Conf. Ser. Earth Environ. Sci.* **2020**, *96*, 012037. [[CrossRef](#)]
35. Diez-Pascual, A.; Sainz-Urruela, C.; Vallés, C.; Vera-López, S.; San Andrés, M. Tailorable Synthesis of Highly Oxidized Graphene Oxides via an Environmentally-Friendly Electrochemical Process. *Nanomaterials* **2020**, *10*, 239. [[CrossRef](#)] [[PubMed](#)]
36. Yang, N.; Yang, D.; Zhang, G.; Chen, L.; Liu, D.; Cai, M.; Fan, X. The Effects of Graphene Stacking on the Performance of Methane Sensor: A First-Principles Study on the Adsorption, Band Gap and Doping of Graphene. *Sensors* **2018**, *18*, 422. [[CrossRef](#)] [[PubMed](#)]
37. Kamali, N.; Ghasemi, J.B.; Ziarani, G.M.; Moradian, S.; Badiei, A. Design, Synthesis, and Nanoengineered Modification of Spherical Graphene Surface by LDH for Removal of As(III) from Aqueous Solutions. *Chin. J. Chem. Eng.* **2022**, in press. [[CrossRef](#)]
38. Aliyev Efiliz, V.; Khan, M.M.; Lee, Y.J.; Abetz, C.; Abetz, V. Structural Characterization of Graphene Oxide: Surface Functional Groups and Fractionated Oxidative Debris. *Nanomaterials* **2019**, *9*, 1180. [[CrossRef](#)]
39. Smajlagic, I.; Rowshanpour, R.; Milkin, L.; Dudding, T. Organofluorine Compounds in Fluorine-18 Positron Emission Tomography Imaging. *Res. Rev. Health Care Open Acc. J.* **2020**, *5*, 488–491.
40. Kuilla, T.; Bhadra, S.; Yao, D.; Kim, N.H.; Bose, S.; Lee, J.H. Recent Advances in Graphene Based Polymer Composites. *Prog. Polym. Sci.* **2010**, *35*, 1350–1375. [[CrossRef](#)]
41. Jenkins, D. Nuclear Structure and Radioactive Decay. In *Radiation Detection for Nuclear Physics*; IOP Publishing: Bristol, UK, 2020; pp. 1–32.

42. Alauddin, M.M. Positron Emission Tomography (PET) Imaging with  $^{18}\text{F}$ -based Radiotracers. *Am. J. Nucl. Med. Mol. Imaging* **2012**, *2*, 55–76.
43. Yang, S.; Chen, Q.; Shi, M.; Zhang, Q.; Lan, S.; Maimaiti, T.; Li, Q.; Ouyang, P.; Tang, K.; Yang, S.T. Fast Identification and Quantification of Graphene Oxide in Aqueous Environment by Raman Spectroscopy. *Nanomaterials* **2020**, *10*, 770. [[CrossRef](#)]
44. Zin, F.A.M.; Noor, A.M.; Lee, S.W.; Sajab, M.S.; Razab, M.K.A.A.; Abdullah, N.H.; Ishak, W.M.F.W.; Wong, K.N.S.S.; Zaudin, N.A.C. Graphene Oxide Silver Cellulose Alginate for Antibacterial. *Mater. Sci. Forum.* **2020**, *1010*, 590–595.
45. Maslekar, N.; Zetterlund, P.B.; Kumar, P.V.; Agarwal, V. Mechanistic Aspects of the Functionalization of Graphene Oxide with Ethylene Diamine: Implications for Energy Storage Applications. *ACS Appl. Nano Mater.* **2021**, *4*, 3232–3240. [[CrossRef](#)]
46. Lai, Q.; Zhu, S.; Luo, X.; Zou, M.; Huang, S. Ultraviolet-visible Spectroscopy of Graphene Oxides. *AIP Adv.* **2012**, *2*, 032146-1–032146-5. [[CrossRef](#)]
47. Yu, L.; Yan, Q.; Ruzsinszky, A. Key Role of Antibonding Electron Transfer in Bonding on Solid Surfaces. *Phys. Rev. Mater.* **2019**, *3*, 092801. [[CrossRef](#)]

## Article

# Asphaltene or Polyvinylchloride Waste Blended with Cement to Produce a Sustainable Material Used in Nuclear Safety

Hosam M. Saleh <sup>1,\*</sup>, Ibrahim I. Bondouk <sup>2</sup>, Elsayed Salama <sup>3</sup>, Hazem H. Mahmoud <sup>1</sup>, Khalid Omar <sup>2</sup> and Heba A. Esawii <sup>3,4</sup>

<sup>1</sup> Radioisotope Department, Nuclear Research Center, Egyptian Atomic Energy Authority (EAEA), Cairo 11787, Egypt; hazem\_h\_mansour@yahoo.com

<sup>2</sup> Physics Department, Faculty of Science, University of Tanta, Tanta 31111, Egypt; ibrahim.bondok@science.tanta.edu.eg (I.I.B.); khalid.omar@science.tanta.edu.eg (K.O.)

<sup>3</sup> Basic Science Department, Faculty of Engineering, The British University in Egypt (BUE), El Shorouk City 11837, Egypt; elsayed.salama@bue.edu.eg (E.S.); hyba.esawii@bue.edu.eg or heba.esawii@aucegypt.edu (H.A.E.)

<sup>4</sup> School of Science and Engineering, The American University in Cairo (AUC), Cairo 11835, Egypt

\* Correspondence: hosam.saleh@eaea.org.eg

**Abstract:** The current research uses sustainable methods to preserve the environment, such as exploiting municipal or industrial waste that may harm the environment. The wreckage of polyvinyl chloride (PVC) pipes and asphaltene are used as additives to cement to improve its mechanical properties, while stabilizing the radioactive waste resulting from the peaceful uses of nuclear materials, or enhancing its radiation shielding efficiency. New composites of Portland cement with ground PVC or asphaltene up to 50% are investigated. Fast neutron removal cross-section ( $\Sigma_R$ ) and gamma shielding parameters, such as mass attenuation coefficient (MAC), half-value layer (HVL), effective atomic number ( $Z_{eff}$ ), and exposure build-up factor (EBF) at wide energy range and thickness, are determined. The compressive strength and apparent porosity of the examined composites are examined to test the durability of the prepared composites as stabilizers for radioactive waste. The obtained results show that the bulk density of hardened cementitious composites was slightly increased by increasing the additive amount of PVC or asphaltene. The compressive strength of cement composites reached more than 4.5 MPa at 50 wt.% PVC and 8.8 MPa at 50 wt.% asphaltene. These values are significantly higher than those recommended by the US Nuclear Regulatory Commission (3.4 MPa). Additionally, the obtained results demonstrate that although the gamma MAC is slightly decreased by adding asphaltene or PVC, the neutron removal cross-section was highly increased, reaching 171% in the case of 50 wt.% asphaltene and 304% in the case of 50 wt.% PVC. We can conclude that cement composites with PVC or asphaltene have optimized radiation shielding properties and can stabilize radioactive waste.

**Keywords:** asphaltene; cement; polyvinylchloride; radiation shielding; waste immobilization

**Citation:** Saleh, H.M.; Bondouk, I.I.; Salama, E.; Mahmoud, H.H.; Omar, K.; Esawii, H.A. Asphaltene or Polyvinylchloride Waste Blended with Cement to Produce a Sustainable Material Used in Nuclear Safety. *Sustainability* **2022**, *14*, 3525. <https://doi.org/10.3390/su14063525>

Academic Editor: Castorina Silva Vieira

Received: 28 February 2022

Accepted: 15 March 2022

Published: 17 March 2022

**Publisher's Note:** MDPI stays neutral with regard to jurisdictional claims in published maps and institutional affiliations.



**Copyright:** © 2022 by the authors. Licensee MDPI, Basel, Switzerland. This article is an open access article distributed under the terms and conditions of the Creative Commons Attribution (CC BY) license (<https://creativecommons.org/licenses/by/4.0/>).

## 1. Introduction

Radiation shielding and radioactive waste stabilization are two critical requirements for safe peaceful nuclear applications. The various applications of radioactive materials have adhere to general radiation protection principles, such as justification, optimization, and dose and risk limits [1]. The reduction in personnel dose is a fundamental principle of radiation protection. To reduce the occupational radiation hazard, the level of radiation must be assessed, and three parameters are typically emphasized in controlling the radiation hazard: time, distance, and shielding [1].

The stabilization of radioactive waste reduces the possibility of radioactive contamination, migration, or the dispersing of radionuclides. Stabilization is defined as the transformation of waste into another form through solidification, embedding, or encapsulation

for safe handling, transportation, storage, and disposal in designated landfills. Radioactive waste is encapsulated by physically surrounding it in materials such as bitumen or cement, which isolates it and retains radionuclides. Packaging or immobilization protects the radioactive substances, and prevents them from being accessed by the environment or escaping into the environment [2]. Furthermore, radioactive materials constantly irradiate through the immobilizing medium, sometimes at high levels of radiation. Radionuclides with long half-lives have extended irradiation periods and make the immobilization process a problem with no simple solution, necessitating the use of another material with high radiation shielding properties.

In the solidification/stabilization process, radioactive waste is converted into a stable solid form that is insoluble by cementation or vitrification, so as to prevent the radio contamination of the surrounding environment [3].

The excellent compressive strength and cost-effectiveness of cement allow it to be widely used as a stabilizer for hazardous and radioactive waste produced initially or as a by-product from treatment operations [4,5]. Cementation technology is used for the immobilization of radioactive waste. The practice of encapsulating radioactive waste in Portland cement began during the early years of the nuclear industry due to its low cost, availability, and compatibility with aqueous waste. The properties of cement vary depending on the type of cement used and the additives used, as well as the desired characteristics that the slurry design should have in order to maintain the durability of the cement. To achieve this goal, several studies and experiments have been carried out with the target of increasing the cement's stability, lifetime, and quality, while decreasing the cement's deterioration. Portland cement can be modified using a range of additives. These may include cellulose waste [6,7], bitumen [8,9], glass [10], polymers [11–14], nanomaterials [15,16] and cement wastes [17,18].

With the growing problem of the high levels of problematic plastic waste produced today, polyvinylchloride (PVC) is the third most-produced synthetic polymer on a global scale. Annually, approximately 39.3 million tons are consumed worldwide, with a 3.2% increase in demand per year [19]. The recycling of PVC waste, including mechanical, chemical, re-extrusion, and burning, has been a leading cause of the presence of dioxin in incinerators when they are burned, and poses a harmful waste problem [20]. PVC wastes require recycling to overcome the many troubles of waste disposal and attain a sustainable solution for various industries, including nuclear applications. PVC wastes can be mixed with cement as a sustainable additive to produce cementitious products suitable for the immobilization of radioactive waste or as a shielding construction material. This technique is an environmentally friendly and economic method for developing economies such as Egypt, due to the great need to dispose of PVC and radioactive waste at the same time.

Another type of problematic material is asphaltene, since it can form dense flocculation and deposits in reservoirs, wellbores, and transportation pipelines, and thus can cause severe operational and production problems. Fortunately, asphaltene is a low-cost hydrocarbon byproduct produced during deep oil refining, with no significant uses in the pavement industry. Recently, asphaltenes were chemically modified for use as a novel thermal conductivity enhancer for liquid paraffin [21], and have been used with cement as additives to asphalt emulsion-stabilized layers [22]. Presently, asphaltene is characterized by its proper ability to mix with cement and produce a new composite of reasonable radiation shielding properties.

This research offers a comparative study to evaluate the mechanical properties, gamma attenuation and fast neutron removal cross-section of two cement composites, namely, a cement–PVC composite and a cement–asphaltene composite. This research reports on a systematic study demonstrating the effects of the incorporation of various ratios of grated PVC waste or asphaltene emulsion into Portland cement to improve the durability and mechanical properties of the produced composite, which will be used as a solidifying agent for radioactive waste, to enhance the attenuation coefficient required to achieve radiation safety in a shielding construction material, or to achieve the two purposes at the same

time. This study aimed to investigate the suitability of some cement additives of definite compositions for producing proper composites with good performances and high densities, using different types of aggregates (asphaltene or PVC) that could enhance the shielding efficiency or achieve the safe stabilization of radioactive waste. The most significant issue in the present study is the elimination of two problematic wastes (asphaltene and PVC), and the production of an innovative product with reasonable efficiency that can be used in the immobilization of radioactive waste or radiation shielding construction, with eco-sustainability, low energy demands, and cost minimization.

## 2. Methodology of Research

### 2.1. Materials

#### 2.1.1. Portland Cement

A commercially available Portland cement supplied by El Sewedy cement company, CEM1(42.5 N), was used in this study as the binding material, developed according to Egyptian Standard Specifications, ES 4756-1/2005 [23], and the British Standard Institution (BSI), EN 197-1/2011 [24].

#### 2.1.2. Polyvinylchloride (PVC)

Scraps of polyvinylchloride pipes were collected as municipal solid waste and cleaned with tap water. The large pieces were crushed and sieved to obtain fine particles of polyvinyl waste appropriate for the subsequent blending with cement [25].

#### 2.1.3. Asphaltene

The asphaltene used in this study was of commercial grade. Asphaltene is a fraction of a hydrocarbon fuel, consisting of condensed polynuclear aromatic ring systems at the center bearing alkyl side chains with hetero elements, the FT-IR spectrum has been presented previously in the literature [26].

### 2.2. Preparation of Cementitious Samples

Portland cement, the major component used in this study, was hydrated with 35% tap water without any additives to prepare the blank samples, or was blended with various additives, such as asphaltene or PVC, to prepare the different composites at various additive ratios.

Each group of compositions contained more than six specimens, three of which were subjected to compressive strength tests, three to porosity and water absorption measurements, and the remaining were subjected to attenuation testing. The pastes of various groups were poured into cylindrical bottles that were internally coated with Vaseline, manually compacted, tightly closed, and safely stored in the laboratory at room temperature (25.5 °C in wet conditions) for 28 days to allow complete reaction and proper solidification. After curing, the solidified samples were demolded and subjected to mechanical integrity tests, permeability spectroscopic analysis, and attenuation measurements.

### 2.3. Assessment of Mechanical Properties

The mechanical integrity is here expressed as compressive strength in MPa for cementitious samples—either cement mixed with asphaltene or PVC, or cement hydrated without any additives. In the Italian testing machine, Ma test E 159 SP, cylindrical samples were loaded axially between the loading plates to determine the maximum load before sample cracking, determined via the ASTM C109 standard test method [27]. Furthermore, the boiling water technique was used to measure porosity, bulk density, and water absorption following ASTM C 20-00 [28]. Using the water displacement method, which is based on Archimedes' saturation technique, the masses of porous specimens, both dry and in water, were recorded. The following two equations can be used to calculate apparent porosity.

$$P = [(W - D)/V] \times 100 \quad (1)$$

$$V = W - S \quad (2)$$

P—apparent porosity (%), W—saturated mass of the specimen (g), D—dry mass of the specimen (g), S—suspended weight of the specimen (g), V—exterior volume of the specimen (cm<sup>3</sup>).

Then, the bulk density (r) can be calculated from the volume and saturated mass of the sample, as:

$$r = D/V \quad (3)$$

#### 2.4. Determination of Gamma-Ray Shielding by Theoretical Aspects

The attenuation of  $\gamma$ -rays by a medium can be described by the well-known Lambert-Beer formula [29]:

$$I = B \times I_0 \times e^{-\mu_m x \rho} \quad (4)$$

where  $I$  and  $I_0$  are, respectively, the transmitted and initial intensities of photons;  $B(X, E)$  is the build-up factor, depending on the penetration depth  $x$  of the material and energy  $E$  of the incident photon;  $\mu_m$  is the mass attenuation coefficient (cm<sup>2</sup>/g) and  $\rho$  is the mass density (g/cm<sup>3</sup>). The mass attenuation coefficients (MAC) of the prepared samples at an energy range of 0.015–15 MeV were calculated using Phy-X/PSD, a user-friendly online software. This program, published by the National Institute of Standards and Technology, includes the coefficients of attenuation of all elements in the periodic table at various energies (NIS) [30].

The radiation protection efficiency (RPE), which is provided by the following equation, may be used to study the shielding efficiency of an absorber sample.

$$I = \left(1 - \frac{I}{I_0}\right) \times 100 \quad (5)$$

The effective atomic number ( $Z_{eff}$ ) of a sample containing a mixture of elements is the ratio of its effective atomic cross-section ( $\sigma_a$ ) to its electronic cross-section ( $\sigma_e$ ), and can be calculated using the following formula [31]:

$$Z_{eff} = \frac{\sigma_a}{\sigma_e} = \frac{\sum_i f_i A_i (\mu_m)_i}{\sum_i f_i \frac{A_i}{Z_i^2} (\mu_m)_i} \quad (6)$$

where  $A_i$  and  $Z_i$  are the atomic weight and the atomic number, respectively, of the  $i$ -element inside the sample. The term  $f_i$  refers to the fractional abundance. The Auto- $Z_{eff}$  program is a user-friendly software presented recently by Taylor that can be used for the quick computation of  $Z_{eff}$  [32].

The equivalent atomic number ( $Z_{eq}$ ) of the prepared sample at a specific energy may be calculated using the fractional mass attenuation coefficient owing to Compton scattering  $R = (\mu_m)_{comp}/(\mu_m)_{total}$ . This may be accomplished by matching  $R_1$  and  $R_2$  for two pure elements with two consecutive atomic numbers  $Z_1$  and  $Z_2$  at the same energy, resulting in  $R$  being positioned between  $R_1$  and  $R_2$  (near to  $R$ ). The logarithmic interpolation formula of  $Z_{eq}$  is as follows [33]:

$$Z_{eq} = \frac{Z_1(\log R_2 - \log R) + Z_2(\log R - \log R_1)}{\log R_2 - \log R_1} \quad (7)$$

Harima et al. created the Geometric Progression (G-P) approximation, which is used to calculate the exposure build-up factors (EBF) of the prepared samples (1993). Using the interpolation formulas below, one can calculate the G-P fitting parameters and the related EBF [34,35].

$$B(E, X) = 1 + \frac{b-1}{K-1} (K^X - 1) \text{ for } K \neq 1 \quad (8)$$

$$B(E, X) = 1 + (b-1)X \text{ for } K = 1 \quad (9)$$

where  $X$  is the penetration depth ( $X \leq 40$  mfp),  $b$  is the EBF value at 1 mfp,  $K(E, X)$  is the multiplicative dose factor, and  $b, c, a, X_K$  and  $d$  are the computed G-P fitting parameters, which depend on the attenuating medium and the source energy. The G-P fitting parameters ( $b, c, a, X_K$ , and  $d$ ) of the prepared samples throughout the 0.015–15 MeV gamma-ray energy range up to 40 mfp may be interpolated using a comparable logarithmic formula, such as Formula (5) [36,37]. The G-P fit requirements for the elements were derived from a research study conducted by the American Nuclear Society [38].

The fast neutron removal cross-section ( $\Sigma_R$ ) of this material is the proportion of fast neutrons removed from a beam of neutrons during its penetration and after the first contact with the target material. For neutron energies of 2–12 MeV, the effective removal cross-section is nearly constant [36]. In the case of a combination of components, the removal cross-section may be calculated using the following formula:

$$\Sigma_R = \sum_i w_i (\Sigma_R)_i \quad (10)$$

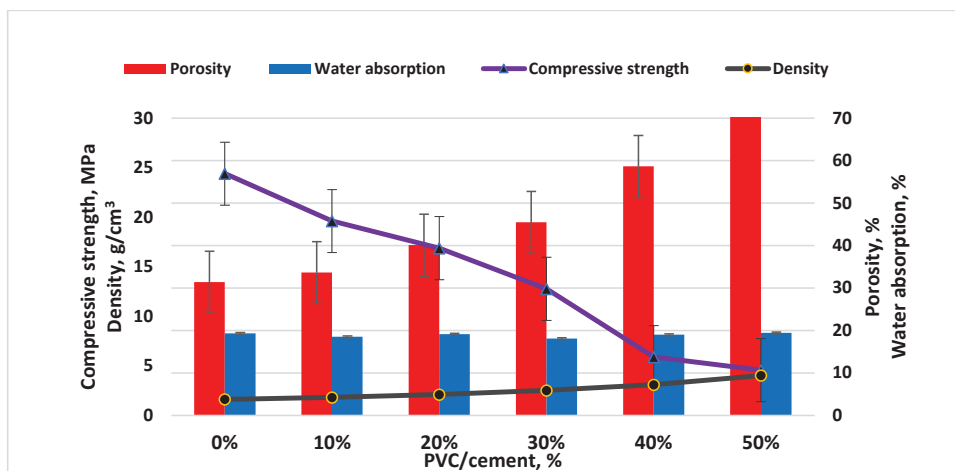
where  $w_i$  and  $(\Sigma_R)_i$  are the elemental weight fraction and removal cross-section, respectively. Dividing by the mass density ( $\rho$ ), the fast neutron mass removal cross-section  $\Sigma_R/\rho$  ( $\text{cm}^2 \text{g}^{-1}$ ) can be calculated.

### 3. Results and Discussion

#### 3.1. Investigation of Mechanical Integrity and Porosity

##### 3.1.1. Cement-Based PVC

The mechanical stability, reflected in the compressive strength of the reference sample of cement without any additives, had the highest value of 24.4 MPa; this is compared with the steady decrease in compressive strength, to 4.5 MPa, with an increasing PVC ratio from 10 to 50 wt.%, as shown in Figure 1. This fall in compressive strength is attributed to the heterogeneity between the two components, and their pores. On the other hand, the porosity showed the opposite trend; a gradual increase in porosity was correlated with an increasing PVC content in cement. The behavior of porosity explains the decreasing compressive strength.



**Figure 1.** Compressive strength, density, water absorption, and porosity of cement blended with extended ratios of PVC.

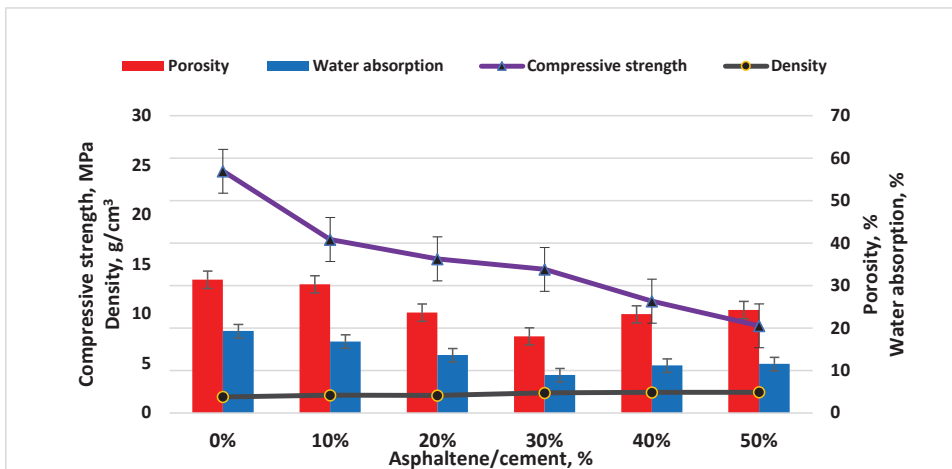
However, the bulk density of the hardened cementitious composites was slightly increased by increasing the additive amount of PVC granules, due to their relatively



high density, while the water absorption showed a constant value while increasing the addition of recycled PVC. According to previous research and in agreement with the current experiment, absorption affinity indirectly reflects the porosity due to permeable pore volume and connectivity [39]. As per the US Nuclear Regulatory Commission, the standard value relative to the compressive strength of solidified radioactive waste has to be more than 3.4 MPa [40], and the compressive strength of cement mixed with 50 wt.% PVC has reached more than 4.5 MPa; this value is significantly higher than recommended, and displays the standard parameters required for the immobilization of low and intermediate levels of radioactive waste.

### 3.1.2. Cement-Based Asphaltene

To examine the effect of increasing the addition of asphaltene into cement paste on the mechanical properties of the produced composite, the compressive strength, bulk density, porosity and water absorption are reported in Figure 2. In this condition, asphaltene will produce a homogeneous mixture with cement compared with PVC. A significant improvement in porosity to 24.24 can be observed with the gradual decrease in water absorption by increasing the amount of asphaltene, due to the potential filling of voids and pores inside the cementitious paste with asphaltene granules. A reasonable decrease in compressive strength was achieved with higher additions of the asphaltene, to reach 8.8 MPa at 50 wt.% asphaltene. It can be concluded from the results presented in Figures 1 and 2 that the heterogeneity and low density of the PVC with cement are higher than in the case of using asphaltene with cement, thus the porosity and water absorption increase while the compressive strength decreases [41,42].



**Figure 2.** Compressive strength, density, water absorption, and porosity of cement blended with extended ratios of asphaltene.

A slight increase in the bulk density of the cementitious samples including asphaltene was detected when increasing the ratio of mixed asphaltene. Despite the presence of asphaltene not causing improvements in the mechanical integrity, the compressive strength of cement-based asphaltene at 50 wt.% has a value more than twice that required of materials used in radioactive waste stabilization, according to the standard specifications previously mentioned (3.4 MPa) [40], and this value is higher than in the case of PVC with cement (4.5 MPa). It is possible to conclude that asphaltene is more advantageous than PVC when mixed with cement up to 50 wt.%, and that it could be considered as a good additive to Portland cement for use in the solidification/stabilization of radioactive

waste. Table 1 shows a descriptive comparison between the results here obtained and those reported previously in the recent literature.

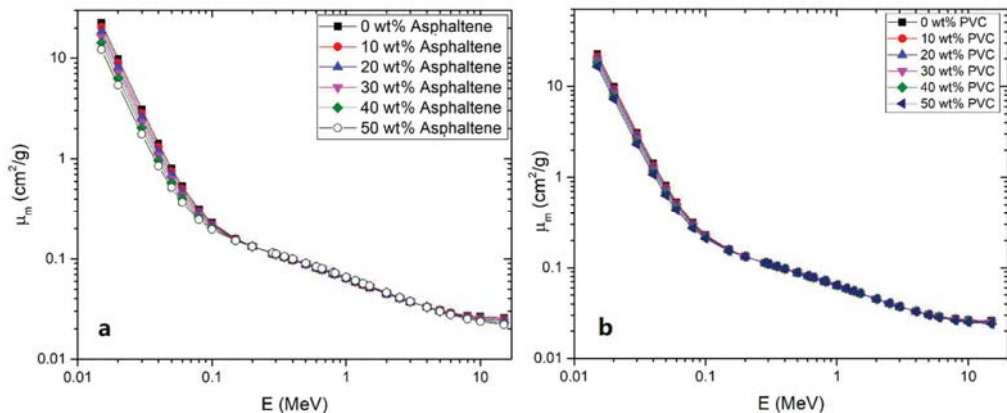
**Table 1.** Comparing the mechanical properties of the present materials and others previously studied.

| System                                 | Compressive Strength, MPa | Porosity, % | Reference     |
|----------------------------------------|---------------------------|-------------|---------------|
| Standard value                         | 3.4                       | -           | [40]          |
| Cement without additives               | 32.0–36.5                 | 27.5–30.0   | [43,44]       |
| Cement mixed with bitumen (30 wt.%)    | 7.62                      | 60.14       | [8]           |
| Cement mixed with PVC (50 wt.%)        | 4.5                       | 78.3        | Present study |
| Cement mixed with asphaltene (50 wt.%) | 8.8                       | 24.24       | Present study |

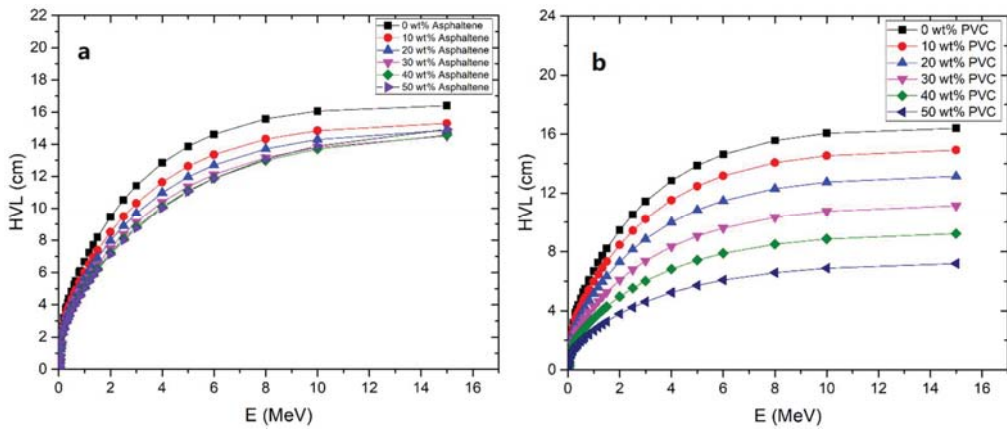
### 3.2. Radiation Shielding Performance

#### 3.2.1. Gamma-Rays Shielding Properties

The obtained results of the mass attenuation coefficients (MAC) of the prepared samples are shown in Figure 3. A regular trend in the MAC for all the prepared samples is observed. The MAC values are dramatically reduced at low photon energies of less than 0.1 MeV, where photoelectric interactions are prominent. The controlling of the photoelectric effect in such a region is perceived as a dramatic drop in the MAC. Compton scattering eventually became the dominant interaction as the energy range increased from 0.1 to 1 MeV, and the likelihood of interaction was inversely related to the energy. Therefore, the values of the MAC for all samples were also gradually decreasing. The MAC values for all samples increased somewhat in the energy range 1.02–15 MeV, where the pair formation interaction became the most prominent and was directly proportional to the energy. The obtained results indicate that adding asphaltene or PVC to cement samples slightly decreases the mass attenuation coefficient, and in turn increases the half-value layer of the cement, as shown in Figures 3 and 4. This was expected due to the low  $Z_{eff}$  of asphaltene and PVC compared with cement.



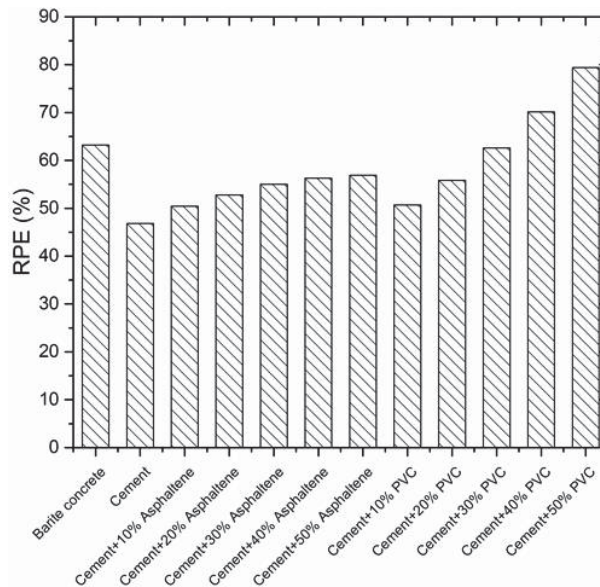
**Figure 3.** Mass attenuation coefficients of cement samples containing different concentrations of (a) asphaltene and (b) PVC.



**Figure 4.** Half value layer (HVL) results of the cement samples containing different concentrations of (a) asphaltene and (b) PVC.

3.2.2. Radiation Protection Efficiency (RPE)

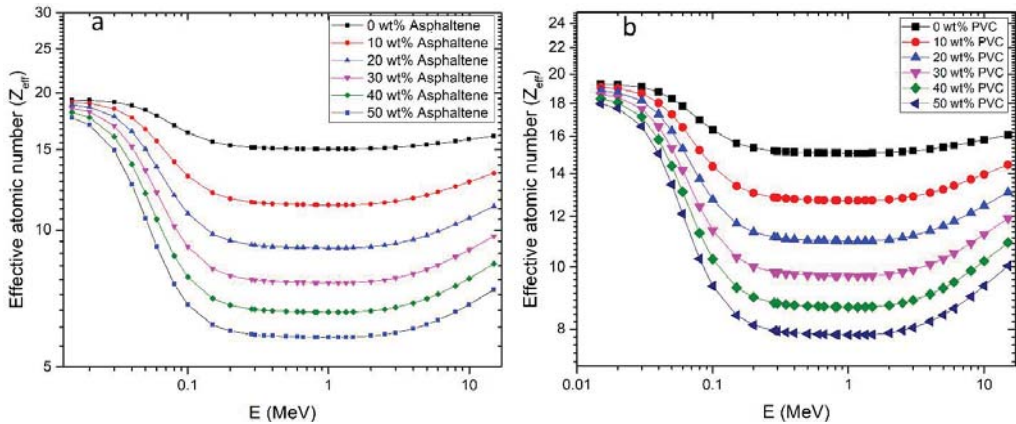
The prepared samples' radiation protection efficiencies compared with those of known materials, such as barite concrete at 0.662 MeV and 2 cm thickness, are shown in Figure 5. The obtained results show that cement with asphaltene and cement with PVC have larger RPEs than pure cement. Additionally, cement with 50% PVC has the largest RPE (79.4%) compared with pure cement (46.8%) and barite concrete (63.2%). The enhanced RPE of cement with the addition of asphaltene or PVC indicates these composites for use in radioactive waste stabilization. Moreover, the highest RPE of cement with 50% PVC recommends its use for gamma radiation shielding applications, more strenuously than concrete.



**Figure 5.** Radiation protection efficiency (RPE) results of the cement samples containing different concentrations of asphaltene and PVC.

### 3.2.3. Effective Atomic Number ( $Z_{eff}$ )

Figure 6 shows the predicted effective atomic number  $Z_{eff}$  findings for the samples including asphaltene or PVC at energy ranges of 0.015–15 MeV. The  $Z_{eff}$  varies depending on the dominant interaction in each energy range, since the attenuation cross-section is proportional to  $Z^{4-5}$  for photoelectric attenuation, to  $Z$  for a Compton interaction, and to  $Z^2$  for pair creation [45].



**Figure 6.** Effective atomic numbers of the cement samples containing different concentrations of (a) asphaltene and (b) PVC.

### 3.2.4. Exposure Build-Up Factors (EBF)

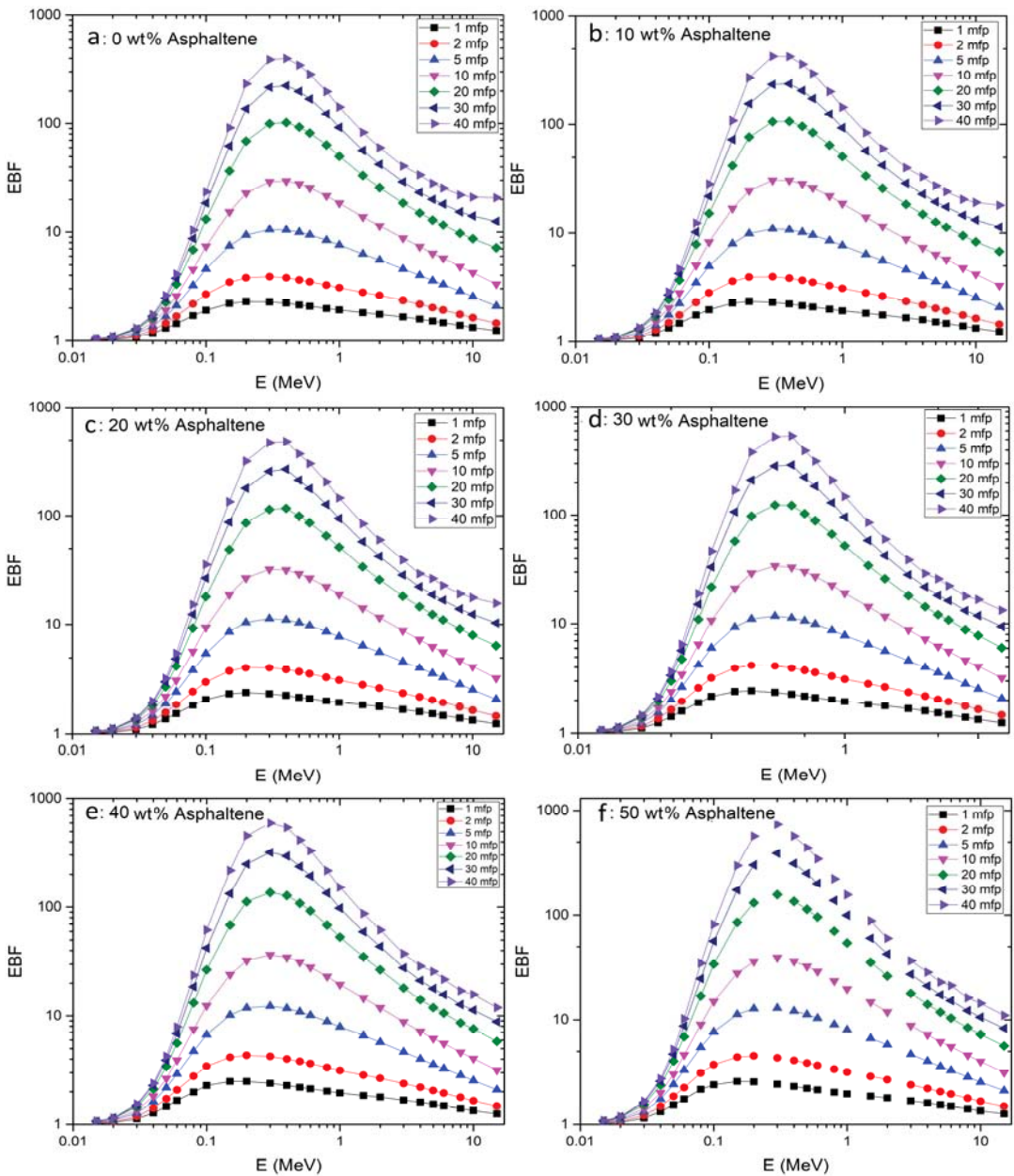
The computed gamma-ray energy exposure buildup factors (EBF), as a function of the incoming energy at 1, 2, 5, 10, 20, 30 and 40 MFP, are presented in Figures 7 and 8 for the cement samples with asphaltene and PVC, respectively, based on the acquired G-P fitting parameters ( $b$ ,  $c$ ,  $a$ ,  $X_k$ , and  $d$ ) for each sample.

Using the photon energy, additive concentrations (PVC or asphaltene), and penetration depth dependencies of the EBF, the data may be understood. The lowest EBF values were found in low- and high-energy areas, whereas values in the intermediate energy zone were greater for all asphaltene and PVC concentrations, as shown in Figures 7a–f and 8a–f, respectively. In the low- and high-energy areas, total absorption was most likely caused by the photoelectric effect and pair creation. Multiple Compton scattering, and hence larger EBF values, were seen in the intermediate area [45].

### 3.2.5. Fast Neutron Removal Cross-Section

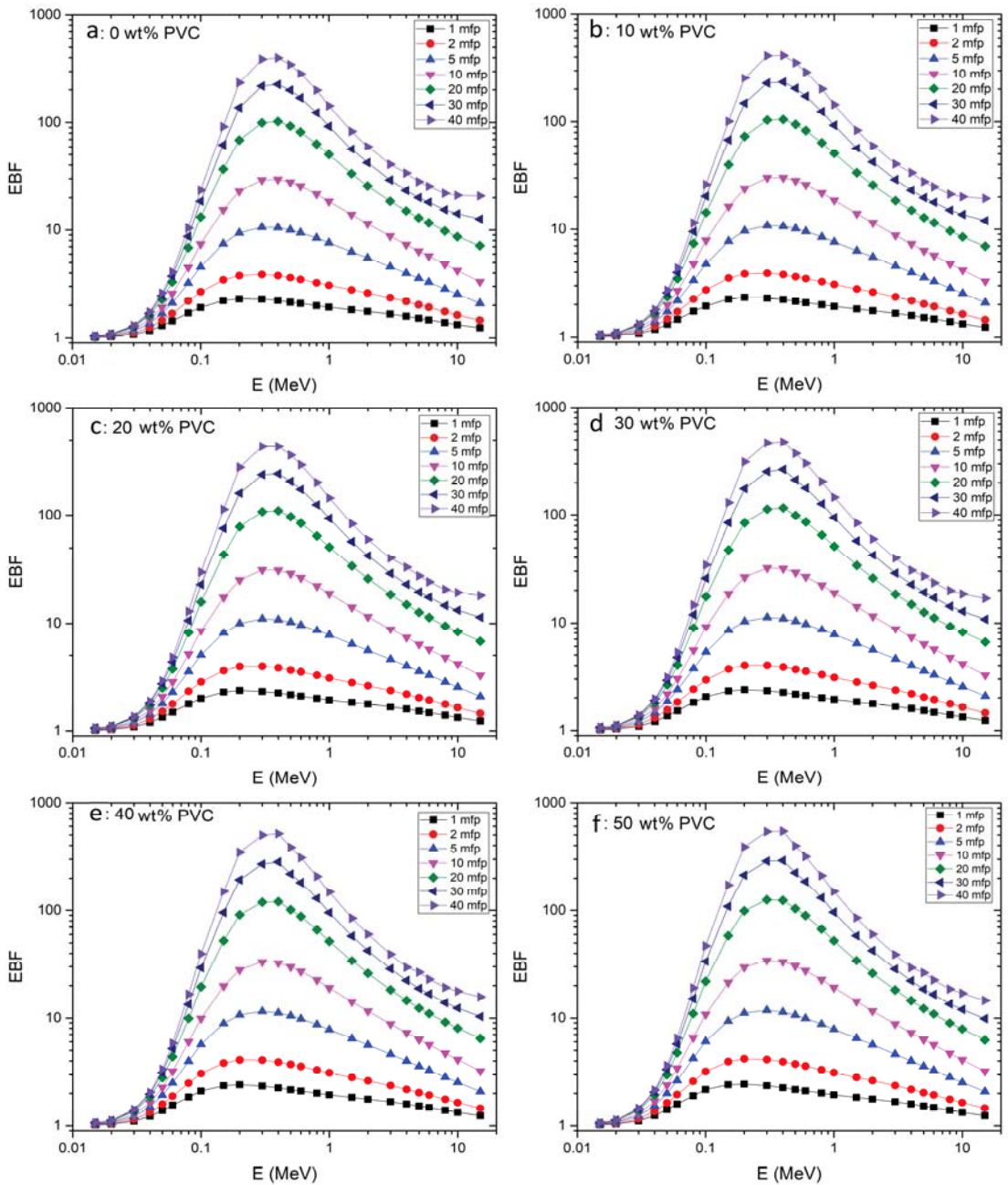
Furthermore, the calculated fast neutron removal cross-sections  $\Sigma_R$  of the examined samples are shown in Figure 9a,b. Although the gamma MAC is slightly decreased with the adding of asphaltene or PVC, the neutron removal cross-section was highly increased, reaching 171% in the case of 50 wt.% asphaltene and 304% in the case of 50 wt.% PVC.

This can be attributed to the higher fast neutron removal cross-sections of the constituent elements of both PVC and asphaltene. The effective fast neutrons mass removal cross-sections  $\Sigma_R/\rho$  ( $\text{cm}^2 \text{g}^{-1}$ ) of cement and PVC are 0.03069 and  $0.06252 \text{ cm}^2 \text{g}^{-1}$ , respectively [46], while for asphaltene this value is about  $0.08820 \text{ cm}^2 \text{g}^{-1}$ . Finally, based on the obtained radiation shielding results, we have found that adding PVC or asphaltene does not significantly change the gamma shielding qualities, but it does improve the neutron removal cross-section and the mechanical properties of the cement.

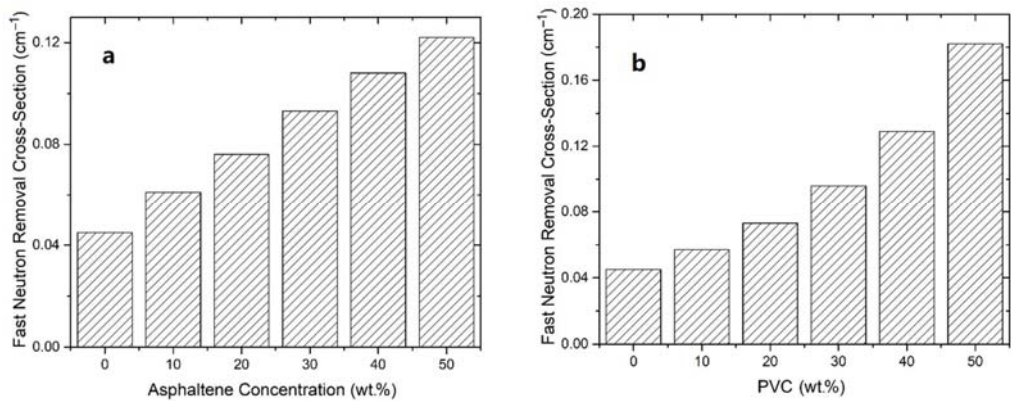


**Figure 7.** Exposure build-up factors of the cement samples containing different concentrations of asphaltene at photon energies of 0.015–15 MeV up to 40 mfp for (a) 0 wt.% asphaltene, (b) 10 wt.% asphaltene, (c) 20 wt.% asphaltene, (d) 30 wt.% asphaltene, (e) 40 wt.% asphaltene and (f) 50 wt.% asphaltene.





**Figure 8.** Exposure build-up factors of the cement samples containing different concentrations of PVC at photon energies of 0.015–15 MeV up to 40 mfp for (a) 0 wt.% PVC, (b) 10 wt.% PVC, (c) 20 wt.% PVC, (d) 30 wt.% PVC, (e) 40 wt.% PVC and (f) 50 wt.% PVC.



**Figure 9.** Fast neutron removal cross-sections of the cement samples containing different concentrations of (a) asphaltene and (b) PVC.

Comparisons between the results obtained here for the prepared composites and those for the well-known ones such as Barite concrete and Portland cement are shown in Table 2. The tabulated results indicate that cement mixed with bitumen has a higher mass attenuation coefficient than the other composites, while the fast neutron removal cross section of cement mixed with PVC or asphaltene showed the highest values.

**Table 2.** Comparison between similar shielding materials.

| System                                    | Range of $\mu_m$ (cm <sup>2</sup> /g) $\times 10^{-2}$ (at 0.662 MeV) | Fast Neutron Mass Removal Cross-Sections, $\Sigma_R/\rho$ (cm <sup>2</sup> g <sup>-1</sup> ) | Reference     |
|-------------------------------------------|-----------------------------------------------------------------------|----------------------------------------------------------------------------------------------|---------------|
| Barite concrete                           | 6.7–7.8                                                               | 0.041–0.027                                                                                  | [47,48]       |
| Portland cement                           | 7.76                                                                  | 0.031                                                                                        | [30]          |
| Cement mixed with bitumen (10–50 wt.%)    | 9.94–14.11                                                            | -                                                                                            | [8]           |
| Cement mixed with PVC (10–50 wt.%)        | 7.78–7.84                                                             | 0.045–0.182                                                                                  | Present study |
| Cement mixed with asphaltene (10–50 wt.%) | 7.80–8.01                                                             | 0.045–0.122                                                                                  | Present study |

#### 4. Conclusions

In this study, the elimination of two problematic waste products (asphaltene and PVC), in order to produce an innovative product with a reasonable efficiency that can be used in the immobilization of radioactive waste or radiation shielding construction, has been conducted, while the achieving of environmental sustainability, low energy demand, and cost minimization have been considered in parallel.

Asphaltene or PVC were mixed with Portland cement in different proportions up to 50%. The performances of the resulting compounds were evaluated using several parameters, such as compressive strength, porosity, bulk density, water absorption, and attenuation coefficient. The physical and mechanical stabilities of the modified cement composites gradually decreased with the increases in the amounts of both additives, while the attenuation and isolation performance, as well as  $\gamma$ -radiation shielding, were slightly affected. The effective cross-sections for removing neutron mass from cement with PVC or asphaltene were significantly increased. The results of this study show that the new compound prepared by mixing cement with asphaltene or PVC can be used to safely



encapsulate hazardous toxic and radioactive wastes, while providing adequate radiation shielding from gamma-rays for the environment at the same time.

**Author Contributions:** H.M.S.: methodology, validation, data curation, writing—original draft, writing—review and editing. I.I.B.: conceptualization, methodology, resources. E.S.: methodology, writing—original draft. H.H.M.: methodology. K.O.: visualization, H.A.E.: methodology. All authors have read and agreed to the published version of the manuscript.

**Funding:** This research received no external funding.

**Institutional Review Board Statement:** Not applicable.

**Informed Consent Statement:** Not applicable.

**Data Availability Statement:** Not applicable.

**Conflicts of Interest:** The authors declare that they have no known competing financial interests or personal relationships that could have appeared to influence the work reported in this paper.

## References

- Do, K.-H. General Principles of Radiation Protection in Fields of Diagnostic Medical Exposure. *J. Korean Med. Sci.* **2016**, *31*, S6–S9. [[CrossRef](#)] [[PubMed](#)]
- Bayoumi, T.A.; Reda, S.M.; Saleh, H.M. Assessment Study for Multi-Barrier System Used in Radioactive Borate Waste Isolation Based on Monte Carlo Simulations. *Appl. Radiat. Isot.* **2012**, *70*, 99–102. [[CrossRef](#)] [[PubMed](#)]
- Saleh, H.M.; Eskander, S.B. Long-Term Effect on the Solidified Degraded Cellulose-Based Waste Slurry in Cement Matrix. *Acta Montan. Slovaca* **2009**, *14*, 291–297.
- Saleh, H.M.; Mahmoud, H.H.; Aglan, R.F.; Bayoumi, T.A. Biological Treatment of Wastewater Contaminated with Cu(Ii), Fe(Ii) and Mn(Ii) Using Ludwigia Stolonifera Aquatic Plant. *Environ. Eng. Manag. J.* **2019**, *18*, 1327–1336. [[CrossRef](#)]
- Saleh, H.M.; Moussa, H.R.; El-Saied, F.A.; Dawoud, M.; Noun, E.S.A.; Abdel Wahed, R.S. Adsorption of Cesium and Cobalt onto Dried *Myriophyllum spicatum* L. from Radio-Contaminated Water: Experimental and Theoretical Study. *Prog. Nucl. Energy* **2020**, *125*, 103393. [[CrossRef](#)]
- Saleh, H.M.; Eskander, S.B.; Fahmy, H.M. Mortar Composite Based on Wet Oxidative Degraded Cellulosic Spinney Waste Fibers. *Int. J. Environ. Sci. Technol.* **2014**, *11*, 1297–1304. [[CrossRef](#)]
- Dawoud, M.M.A.; Hegazy, M.M.; Helew, W.K.; Saleh, H.M. Overview of Environmental Pollution and Clean Management of Heavy Metals and Radionuclides by Using Microcrystalline Cellulose. *J. Nucl. Energy Sci. Power Gener. Technol.* **2021**, *10*, 100201.
- Saleh, H.M.; Bondouk, I.I.; Salama, E.; Esawii, H.A. Consistency and Shielding Efficiency of Cement-Bitumen Composite for Use as Gamma-Radiation Shielding Material. *Prog. Nucl. Energy* **2021**, *137*, 103764. [[CrossRef](#)]
- Reda, S.M.; Saleh, H.M. Calculation of the Gamma Radiation Shielding Efficiency of Cement-Bitumen Portable Container Using MCNPX Code. *Prog. Nucl. Energy* **2021**, *142*, 104012. [[CrossRef](#)]
- Eid, M.S.; Bondouk, I.I.; Saleh, H.M.; Omar, K.M.; Sayyed, M.I.; El-Khatib, A.M.; Elsafi, M. Implementation of Waste Silicate Glass into Composition of Ordinary Cement for Radiation Shielding Applications. *Nucl. Eng. Technol.* **2021**. [[CrossRef](#)]
- Eskander, S.B.; Saleh, H.M.; Tawfik, M.E.; Bayoumi, T.A. Towards Potential Applications of Cement-Polymer Composites Based on Recycled Polystyrene Foam Wastes on Construction Fields: Impact of Exposure to Water Ecologies. *Case Stud. Constr. Mater.* **2021**, *15*, e00664. [[CrossRef](#)]
- Saleh, H.; Salman, A.; Faheim, A.; El-Sayed, A. Polymer and Polymer Waste Composites in Nuclear and Industrial Applications. *J. Nucl. Energy Sci. Power Gener. Technol.* **2020**, *9*, 1000199.
- Saleh, H.M.; Eskander, S.B. Impact of Water Flooding on Hard Cement-Recycled Polystyrene Composite Immobilizing Radioactive Sulfate Waste Simulate. *Constr. Build. Mater.* **2019**, *222*, 522–530. [[CrossRef](#)]
- Smirnova, O.M.; Menéndez Pidal de Navascués, I.; Mikhailevskii, V.R.; Kolosov, O.I.; Skolota, N.S. Sound-Absorbing Composites with Rubber Crumb from Used Tires. *Appl. Sci.* **2021**, *11*, 7347. [[CrossRef](#)]
- Saleh, H.M.; El-Saied, F.A.; Salaheldin, T.A.; Hezo, A.A. Influence of Severe Climatic Variability on the Structural, Mechanical and Chemical Stability of Cement Kiln Dust-Slag-Nanosilica Composite Used for Radwaste Solidification. *Constr. Build. Mater.* **2019**, *218*, 556–567. [[CrossRef](#)]
- Saleh, H.M.; El-Sheikh, S.M.; Elshereafy, E.E.; Essa, A.K. Performance of Cement-Slag-Titanate Nanofibers Composite Immobilized Radioactive Waste Solution through Frost and Flooding Events. *Constr. Build. Mater.* **2019**, *223*, 221–232. [[CrossRef](#)]
- Saleh, H.M.; Salman, A.A.; Faheim, A.A.; El-Sayed, A.M. Sustainable Composite of Improved Lightweight Concrete from Cement Kiln Dust with Grated Poly (Styrene). *J. Clean. Prod.* **2020**, *277*, 123491. [[CrossRef](#)]
- Saleh, H.M.; Salman, A.A.; Faheim, A.A.; El-Sayed, A.M. Influence of Aggressive Environmental Impacts on Clean, Lightweight Bricks Made from Cement Kiln Dust and Grated Polystyrene. *Case Stud. Constr. Mater.* **2021**, *15*, e00759. [[CrossRef](#)]
- Ragab, A.A.; Mohammedy, M.M.; El-Shafie, M. Using Waste Flexible Polyvinyl Chloride Treated with DOP/Calcium Hydroxide for Enriching the Performance of Oxidizing Bitumen. *J. Therm. Anal. Calorim.* **2019**, *136*, 1079–1091. [[CrossRef](#)]

20. Kou, S.C.; Lee, G.; Poon, C.S.; Lai, W.L. Properties of Lightweight Aggregate Concrete Prepared with PVC Granules Derived from Scraped PVC Pipes. *Waste Manag.* **2009**, *29*, 621–628. [[CrossRef](#)] [[PubMed](#)]
21. Glova, A.D.; Nazarychev, V.M.; Larin, S.V.; Lyulin, A.V.; Lyulin, S.V.; Gurtovenko, A.A. Asphaltenes as Novel Thermal Conductivity Enhancers for Liquid Paraffin: Insight from in Silico Modeling. *J. Mol. Liq.* **2021**, *346*, 117112. [[CrossRef](#)]
22. Uddin, M.M.; Kamran, F.; Hashemian, L. Performance Comparison of Asphalt Emulsion Stabilized Granular Base Modified with Cement or Asphaltenes. *Can. J. Civ. Eng.* **2021**. [[CrossRef](#)]
23. *ESS-4756-1/2005*; Ordinary Portland Cement (OPC) CEM1 (42.5 N). Egyptian Standard Specifications: Cairo, Egypt, 2005.
24. *BSI-197-1/2011*; Cement, Composition, Specifications and Conformity Criteria for Common Cements. British Standards Institution: London, UK, 2011; Volume 1.
25. Wang, J.; Wang, H.; Yue, D. Separation of Waste Polymethyl Methacrylate and Polyvinyl Chloride Mixtures by Flotation after Fenton Oxidation. *J. Clean. Prod.* **2019**, *228*, 1218–1228. [[CrossRef](#)]
26. Speight, J.G.; Moschopedis, S.E. On the Molecular Nature of Petroleum Asphaltenes. In *Chemistry of Asphaltenes*; ACS Publications: Washington, DC, USA, 1981.
27. *ASTM C109/C109M-16a*; ASTM Standard Test Method for Compressive Strength of Hydraulic Cement Mortars (Using 2-in. or [50-Mm] Cube Specimens). ASTM International: West Conshohocken, PA, USA, 2016.
28. *ASTM C20-00*; ASTM Standard Test Methods for Apparent Porosity, Water Absorption, Apparent Specific Gravity, and Bulk Density of Burned Refractory Brick and Shapes by Boiling Water. ASTM International: West Conshohocken, PA, USA, 2015.
29. Singh, V.P.; Badiger, N.M.; Kaewkhao, J. Radiation Shielding Competence of Silicate and Borate Heavy Metal Oxide Glasses: Comparative Study. *J. Non-Cryst. Solids* **2014**, *404*, 167–173. [[CrossRef](#)]
30. Berger, M.J. Photon Cross-Sections Database. NIST Standard Reference Database 8 (XGAM). 1998. Available online: <http://physics.nist.gov/PhysRefData/Xcom/Text/XCOM.html> (accessed on 1 February 2022).
31. Tijani, S.A.; Kamal, S.M.; Al-Hadeethi, Y.; Arib, M.; Hussein, M.A.; Wageh, S.; Dim, L.A. Radiation Shielding Properties of Transparent Erbium Zinc Tellurite Glass System Determined at Medical Diagnostic Energies. *J. Alloys Compd.* **2018**, *741*, 293–299. [[CrossRef](#)]
32. Taylor, M.L.; Smith, R.L.; Dossing, F.; Franich, R.D. Robust Calculation of Effective Atomic Numbers: The Auto-Zeff Software. *Med. Phys.* **2012**, *39*, 1769–1778. [[CrossRef](#)]
33. Sathiyaraj, P.; Samuel, E.J.J.; Valeriano, C.C.S.; Kurudirek, M. Effective Atomic Number and Buildup Factor Calculations for Metal Nano Particle Doped Polymer Gel. *Vacuum* **2017**, *143*, 138–149. [[CrossRef](#)]
34. Harima, Y. An Historical Review and Current Status of Buildup Factor Calculations and Applications. *Radiat. Phys. Chem.* **1993**, *41*, 631–672. [[CrossRef](#)]
35. Kavaz, E.; Yorgun, N.Y. Gamma Ray Buildup Factors of Lithium Borate Glasses Doped with Minerals. *J. Alloys Compd.* **2018**, *752*, 61–67. [[CrossRef](#)]
36. Kaplan, M.F. *Concrete Radiation Shielding: Nuclear Physics, Concrete Properties, Design and Construction*; Longman Scientific & Technical: Harlow, UK, 1989; ISBN 0470213388.
37. Singh, V.P.; Badiger, N.M. Gamma Ray and Neutron Shielding Properties of Some Alloy Materials. *Ann. Nucl. Energy* **2014**, *64*, 301–310. [[CrossRef](#)]
38. *ANSI/ANS-6.4.3*; Gamma-Ray Attenuation Coefficients and Buildup Factors for Engineering Materials. American Nuclear Society: La Grange Park, IL, USA, 1991.
39. Babu, K.G.; Babu, D.S. Behaviour of Lightweight Expanded Polystyrene Concrete Containing Silica Fume. *Cem. Concr. Res.* **2003**, *33*, 755–762. [[CrossRef](#)]
40. NRC. *Waste Form Technical Position, Revision 1*; US Nuclear Regulatory Commission: Washington, DC, USA, 1991.
41. Zingg, L.; Briffaut, M.; Baroth, J.; Malecot, Y. Influence of Cement Matrix Porosity on the Triaxial Behaviour of Concrete. *Cem. Concr. Res.* **2016**, *80*, 52–59. [[CrossRef](#)]
42. Prêt, D.; Sardini, P.; Beaufort, D.; Zellagui, R.; Sammartino, S. Porosity Distribution in a Clay Gouge by Image Processing of <sup>14</sup>C-PolyMethylMethAcrylate (<sup>14</sup>C-PMMA) Autoradiographs: Case Study of the Fault of St. Julien (Basin of Lodève, France). *Appl. Clay Sci.* **2004**, *27*, 107–118. [[CrossRef](#)]
43. Saleh, H.M.; Aglan, R.F.; Mahmoud, H.H. Qualification of Corroborated Real Phytoremediated Radioactive Wastes under Leaching and Other Weathering Parameters. *Prog. Nucl. Energy* **2020**, *119*, 103178. [[CrossRef](#)]
44. Saleh, H.M.; Moussa, H.R.; El-Saied, F.A.; Dawod, M.; Bayoumi, T.A.; Abdel Wahed, R.S. Mechanical and Physicochemical Evaluation of Solidified Dried Submerged Plants Subjected to Extreme Climatic Conditions to Achieve an Optimum Waste Containment. *Prog. Nucl. Energy* **2020**, *122*, 103285. [[CrossRef](#)]
45. Salama, E.; Maher, A.; Youssef, G.M. Gamma Radiation and Neutron Shielding Properties of Transparent Alkali Borosilicate Glass Containing Lead. *J. Phys. Chem. Solids* **2019**, *131*, 139–147. [[CrossRef](#)]
46. El-Khayatt, A.M. Calculation of Fast Neutron Removal Cross-Sections for Some Compounds and Materials. *Ann. Nucl. Energy* **2010**, *37*, 218–222. [[CrossRef](#)]
47. Picha, R.; Channuie, J.; Khaweerat, S.; Liamsuwan, T.; Promping, J.; Ratanatongchai, W.; Silva, K.; Wonglee, S. Gamma and Neutron Attenuation Properties of Barite-Cement Mixture. *J. Phys. Conf. Ser.* **2015**, *611*, 012002. [[CrossRef](#)]
48. Akkurt, I.; Akyildirim, H.; Karipcin, F.; Mavi, B. Chemical Corrosion on Gamma-Ray Attenuation Properties of Barite Concrete. *J. Saudi Chem. Soc.* **2012**, *16*, 199–202. [[CrossRef](#)]

Review

# Chelating Agents in Assisting Phytoremediation of Uranium-Contaminated Soils: A Review

Yue You <sup>1</sup>, Junfeng Dou <sup>1</sup>, Yu Xue <sup>2</sup>, Naifu Jin <sup>1</sup> and Kai Yang <sup>1,\*</sup>

- <sup>1</sup> College of Water Sciences, Beijing Normal University, Beijing 100875, China; 202021470042@mail.bnu.edu.cn (Y.Y.); doujf@bnu.edu.cn (J.D.); n.jin@bnu.edu.cn (N.J.)  
<sup>2</sup> School of Chemical and Environmental Engineering, China University of Mining and Technology, Beijing 100083, China; 1810380315@student.cumb.edu.cn  
\* Correspondence: yangk@bnu.edu.cn; Tel.: +86-138-1175-3081

**Abstract:** Massive stockpiles of uranium (U) mine tailings have resulted in soil contamination with U. Plants for soil remediation have low extraction efficiency of U. Chelating agents can mobilize U in soils and, hence, enhance phytoextraction of U from the soil. However, the rapid mobilization rate of soil U by chelating agents in a short period than plant uptake rate could increase the risk of groundwater contamination with soluble U leaching down the soil profile. This review summarizes recent progresses in synthesis and application of chelating agents for assisting phytoremediation of U-contaminated soils. In detail, the interactions between chelating agents and U ions are initially elucidated. Subsequently, the mechanisms of phytoextraction and effectiveness of different chelating agents for phytoremediation of U-contaminated soils are given. Moreover, the potential risks associated with chelating agents are discussed. Finally, the synthesis and application of slow-release chelating agents for slowing down metal mobilization in soils are presented. The application of slow-release chelating agents for enhancing phytoextraction of soil U is still scarce. Hence, we propose the preparation of slow-release biodegradable chelating agents, which can control the release speed of chelating agent into the soil in order to match the mobilization rate of soil U with plant uptake rate, while diminishing the risk of residual chelating agent leaching to groundwater.

**Keywords:** chelator; soil uranium; mobilization; phytoextraction; slow release

**Citation:** You, Y.; Dou, J.; Xue, Y.; Jin, N.; Yang, K. Chelating Agents in Assisting Phytoremediation of Uranium-Contaminated Soils: A Review. *Sustainability* **2022**, *14*, 6379. <https://doi.org/10.3390/su14106379>

Academic Editors: Hosam M. Saleh and Mohammad Mahmoud Dawoud

Received: 13 April 2022

Accepted: 18 May 2022

Published: 23 May 2022

**Publisher's Note:** MDPI stays neutral with regard to jurisdictional claims in published maps and institutional affiliations.



**Copyright:** © 2022 by the authors. Licensee MDPI, Basel, Switzerland. This article is an open access article distributed under the terms and conditions of the Creative Commons Attribution (CC BY) license (<https://creativecommons.org/licenses/by/4.0/>).

## 1. Introduction

Nuclear energy is a major source of low-carbon electricity and plays an important role in the achievement of carbon neutrality. According to the World Nuclear Performance Report 2021, there are 443 operational reactors with a total capacity of  $3.94 \times 10^5$  MWe, and 57 reactors with a total capacity of  $5.88 \times 10^4$  MWe under construction worldwide [1]. The global nuclear power generation reached  $2.55 \times 10^3$  TWh in 2020, meanwhile the annual global demand for uranium (U), a primary element used in nuclear energy, has increased to  $6.25 \times 10^4$  t [1,2]. At the same time, soil contamination with U has become a serious environmental issue.

There are two main sources of U in soils, i.e., natural source and anthropogenic source. U naturally occurs in soil parent materials. Due to different accumulation levels of U in different soil parent materials, the concentration of U in soils can vary greatly. For example, the average background concentration of soil U in the United States (US) is 3.5 mg/kg, and that in China is 3.13 mg/kg, whereas Portugal reaches 25.1 mg/kg [3]. The background concentration of U in the environment is usually low. However, anthropogenic activities (e.g., industrial and agricultural production and military activities) have emitted a large amount of U into the environment, resulting in distinct accumulation of U in soils [4–9]. U tailings are the main source of U in contaminated soils. For example, U contamination in the soil and groundwater within the catchment of a U mill tailings pond can be caused by the hydrological cycle around the tailings pond [10].

Although U has a long half-life and relatively weak radioactivity, it may induce chemical and radiological toxicity in organisms after long-term exposure to U-contaminated soils or U accumulation in the organism through the food chain [11–17]. On the one hand, U can induce ionic toxicity similar to that of cadmium (Cd), copper (Cu), zinc (Zn), and other heavy metals. The ionic toxicity of U increases with U concentration in the contaminated environmental substrate. On the other hand, the radiation from the decay of U can cause oral necrosis, anemia or chronic diseases of lung and kidney in mild cases, and central nervous system damage or death in severe cases [17,18]. In addition, chronic U exposure can cause chromosome aberrations and increase cancer risk [19,20]. Therefore, it is of great importance to clean up U-contaminated soils.

Among common remediation technologies for soil contamination with heavy metals and radionuclides, phytoextraction is a popular in situ technology for large-scale soil remediation due to its low cost and environmental friendliness. Although several plants (e.g., broad bean (*Vicia faba* L.), willow (*Salix smithiana* Willd.), radish (*Raphanus sativus* L.), Indian mustard (*Brassica juncea* L.), and sunflower (*Helianthus annuus* L.)) have the ability to absorb U from soils [21–25], hyperaccumulator plant species of U have not yet been discovered. In addition, plants for remediation of U-contaminated soils usually have low extraction efficiency of U, which results in a long-term remediation period and consequently hinders large-scale phytoremediation of U-contaminated soils. Apart from searching for U hyperaccumulators, numerous studies have showed that chelating agents can mobilize heavy metals and radionuclides in soils and therefore enhance plant uptake of these contaminants [26–28]. Due to the lack of U hyperaccumulators, chelating agent-assisted phytoremediation can be an effective approach for U-contaminated soil remediation.

It should be noted several previous studies found that the mobilization rate of soil U by chelating agents exceeded the plant U uptake rate, consequently causing groundwater contamination with soluble U through leaching processes as well as transient phytotoxicity [26,28]. In fact, U contamination in groundwater is also a global environmental issue. It is reported that the groundwater in India, South Korea, the US, and Zambia has been contaminated with U to a varying extent [29]. In Nambe, New Mexico, US, the maximum groundwater U concentration reached 1200 ng/mL, which is conspicuously greater than the drinking water standard (20 ng/mL) recommended by the US Environmental Protection Agency (US EPA) [30]. U in contaminated groundwater can enter into the human body via groundwater drinking pathway and consequently pose a risk to human health. Epidemiological studies found that U mainly accumulates in kidney. Long-term consumption of U-contaminated groundwater can induce kidney tubular cell death, resulting in kidney diseases [30,31]. In addition, chronic drinking of U-contaminated groundwater can cause other detrimental health effects, such as hindering bone growth [32], disrupting metabolic processes in liver [33], affecting germ cell growth [34,35], and triggering inflammatory responses in nervous system [36]. Therefore, it is necessary to tackle the secondary pollution issue due to the short-term rapid mobilization of soil U so as to achieve effective phytoremediation and ensure groundwater safety.

This review elucidates the interactions between chelating agents and U ions, and then explains the phytoextraction mechanisms and summarizes recent progresses in synthesis and application of chelating agents in assisting phytoremediation of U-contaminated soils. The major factors influencing phytoextraction efficiency are given. The environmental risks of existing chelating agents are also discussed. Finally, recent advances in slow-release technology are reviewed, with synthesis and application of slow-release chelating agents for slowing down metal mobilization in soils in order to match plant uptake rate presented. This review aims at shedding light on the promise of slow-release biodegradable chelating agents for enhancing phytoextraction of soil U. This novel approach is considered as a green and sustainable remediation technology for U-contaminated soils.

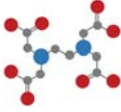


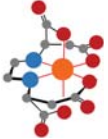
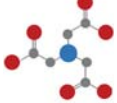
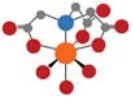

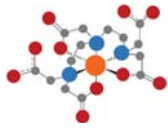
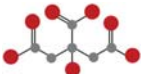
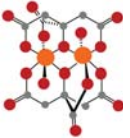
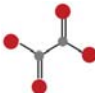
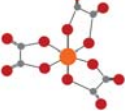
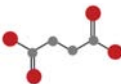

## 2. Interactions between Chelating Agents and U Ions


### 2.1. Mechanisms of Chelation

The atomic number of U is 92. There are 92 protons and 146 neutrons in the nucleus, forming four electron-filled layers (K, L, M, N) and three under-filled electron layers (O, P, Q). The six electrons ( $5f^3 6d^1 7s^2$ ) on the three underfilled electron sublayers are valence electrons, which determine the chemical properties of U [11]. After losing six valence electrons, the outermost energy level of U is filled ( $S^2 P^6$ ), forming noble gas structure, which has a strong affinity with oxygen. Therefore, U usually exists in the forms of oxides and oxyalts in the crust and soil. Specifically, U is mainly present in the form of uranyl ion ( $UO_2^{2+}$ ) in soils, which has a strong complexing ability to form stable complexes with phosphate ( $PO_4^{3-}$ ), carbonate ( $CO_3^{2-}$ ), hydroxyl ( $OH^-$ ), sulfate ( $SO_4^{2-}$ ), etc., and consequently reduces the mobility and bioavailability of U in soils [37,38].

Chelating agent refers to ligand which can form a cyclic structure complex with central ions (usually metal ions). Once in the soil, it can chelate with heavy metals and radionuclides to form water-soluble and exchangeable metal-chelating agent complexes, which can increase their mobility and bioavailability, and consequently promote plant uptake of these contaminants [39]. Chelating agents can be divided into two main categories including aminopolycarboxylate chelating agents (APCAs) (e.g., aminotriacetic acid (NTA), ethylenediaminetetraacetic acid (EDTA), ethylenediaminedisuccinic acid (EDDS), and N, N-Bis(carboxymethyl)-glutamic acid (GLDA)) [40,41] and low molecular weight organic acids (LMWOAs) (e.g., citric acid (CA), oxalic acid (OA), and succinic acid (SA)) [42,43]. In addition, APCAs can be classified as biodegradable and non-biodegradable [44], whereas LMWOAs are biodegradable [26,45]. The chemical structures and biodegradability of commonly used chelating agents are shown in Table 1.

**Table 1.** Structures and biodegradability of commonly used chelating agents, and structures and stability of chelates formed by  $UO_2^{2+}$  with these chelating agents.

| Category                                      | Chelator                                  | Chelator Structure                                                                  | Biodegradability                                                                                 | U Chelate Structure                                                                  | $\log K_U^*$                                                          |
|-----------------------------------------------|-------------------------------------------|-------------------------------------------------------------------------------------|--------------------------------------------------------------------------------------------------|--------------------------------------------------------------------------------------|-----------------------------------------------------------------------|
| Aminopolycarboxylate chelating agents (APCAs) | Ethylenediaminetetraacetic acid (EDTA)    |    | Half-life > 40 d [46]                                                                            |    | 7.4<br>( $UO_2^{2+}$ :EDTA = 1:1) 17.87<br>( $UO_2^{2+}$ :EDTA = 2:1) |
|                                               | Ethylenediaminedisuccinic acid (EDDS)     |    | Completely degraded after 54 d [47]                                                              |    | 10.7                                                                  |
|                                               | Nitrilotriacetic acid (NTA)               |    | 75% degraded after 21 d [48]                                                                     |    | 9.5                                                                   |
|                                               | Diethylenetriaminepentaacetic acid (DTPA) |    | Similar to EDTA [49]                                                                             |    | 11                                                                    |
| Low molecular weight organic acids (LMWOAs)   | Citric acid (CA)                          |   | 69% degraded after 20 d [50]                                                                     |   | 8.96                                                                  |
|                                               | Oxalic acid (OA)                          |  | Hard to degrade in nature due to the formation of Ca-oxalate [21]                                |  | 6.36                                                                  |
|                                               | Succinic acid (SA)                        |  | Half-life < 2 min and 200 h in soil solution and for microbial mineralization, respectively [51] |  | 3.87                                                                  |

Notes: ; \* Data was sourced from [26,52,53].

Cyclic chelate formed by metal ion with ligand through coordination bonds has strong stability. Table 1 shows the structures of chelates formed by  $UO_2^{2+}$  with commonly used chelating agents. The stability constant ( $K$ ) is used to indicate the stability of metal chelate, which increases with  $K$  value.  $K$  value is calculated using the following equation [54–57]:

$$K_{ML}^T = \frac{C_{ML}}{C_M C_L}$$

where  $C_{ML}$ ,  $C_M$ , and  $C_L$  are concentrations of metal chelate, metal ion, and ligand, respectively;  $K_{ML}^T$  is the stability constant.

It is worth noting that EDTA has the highest  $K$  values for various heavy metal chelates compared to other chelating agents (Table 1) and therefore has been widely used in mobi-



lization of metal contaminants in soils and soil washing over past decades [58]. However, the tertiary amine in EDTA molecule makes it difficult to be biodegraded. As a result, long-term retention of non-degradable EDTA in the environment has posed a critical risk to the ecology and human health [59–63]. As shown in Table 1, biodegradable EDDS has a high  $K$  value for U chelate. Moreover, its chemical structure is similar to that of EDTA. Thus, EDDS has become an ideal substitute for EDTA [64–67]. The  $K$  value of NTA for U chelate is slightly lower than that of EDDS. However, the use of NTA should be restricted due to its carcinogenic effect [44,68]. For example, iron (Fe)-NTA can induce renal cell carcinoma, which is widely used to perform oxidative tissue damage and carcinogenesis experiments [69–71]. CA, which is a natural LMWOA, also has a high  $K$  value for U chelate. Previous studies showed that CA increased the bioavailability of U in soils more effectively compared to other chelating agents (i.e., OA, EDDS, and NTA) [26,72].

## 2.2. Mobilization of Soil U by Chelating Agents

Soil texture, pH, and redox potential (Eh) are dominant factors influencing the effect of chelating agents on mobilizing U in soils [26,73–75]. Table 2 presents the mobilization efficiency of soil U by different chelating agents. The dosages of chelating agents ranged from 0.5 to 50 mmol/kg. The experimental soil pH values ranged from 5.6 to 7.3. The soil U concentration reached nearly 1000 mg/kg. Among the chelating agents listed in Table 2, the effect of CA on mobilizing U in soils, in particular, in sandy soil, was the most significant, with the exception of  $\text{NH}_4$ -citrate > CA in the loamy sand and heavy clay in the study by Duquène, et al. [26]. A possible explanation for the different effects of CA on mobilizing U in soils with contrasting textures is that the soil containing higher silt and clay contents has a larger specific surface area, which can result in stronger adsorption of contaminants and consequently reduce the mobilization efficiency of soil U by chelating agents [76,77]. In addition, there are a large number of functional groups (e.g., amino and carboxyl groups) in soils with high organic matter (OM) content, which has a strong adsorption capacity for U ions [78–80]. This can also affect the effectiveness of chelating agents in mobilization of soil U. A similar trend was observed in Jiang, et al., which showed that the mobilization efficiency of chromium (Cr) in contaminated soils by CA was in the following decreasing order: sandy soil > loam > clay soil [81]. The mobilization efficiency of soil heavy metals by chelating agents tends to increase with increasing soil acidity [82]. For example, Yang, et al., found that the mobilization efficiency of heavy metals in the soil solution with low pH by EDDS was significantly higher than that with high pH [83]. Likewise, Wang, et al., showed that the mobilization efficiency of heavy metals by chelating agents (i.e., GLDA and NTA) in the strongly acidic soil was 4-times higher than that in the alkaline soil, and the chelating agents were more effective in mobilizing heavy metals in the sandy soil compared to the clay soil at a wide soil pH range of 4 to 10 [82]. The leaching experiment of Kantar and Honeyman showed that the lower pH of eluent facilitated the mobilization of soil U by CA [84]. In addition, Eh can significantly influence the chemical forms of U present in soils and therefore control the solubility of U in the soil [73]. Specifically, at low Eh, U is present in solid phases, whereas at high Eh, U carbonates are transformed into soluble phases, which tend to migrate with water. To sum up, chelating agents can transform soil U from solid phase to soluble phase by forming high  $K$  value complex compounds with  $\text{UO}_2^{2+}$ . In particular, sandy soil with low pH, high Eh, and low OM content is favorable for the mobilization of U by chelating agents.



**Table 2.** Effects of different chelating agents on mobilizing U in soils with different textures.

| Item                                                                       | Reference                         |                                    |                                         |                                                 |                                   |                                  |                                                                    |
|----------------------------------------------------------------------------|-----------------------------------|------------------------------------|-----------------------------------------|-------------------------------------------------|-----------------------------------|----------------------------------|--------------------------------------------------------------------|
|                                                                            | [85]                              | [72]                               | [86]                                    |                                                 | [26]                              |                                  | [27]                                                               |
| Soil characteristics                                                       |                                   |                                    |                                         |                                                 |                                   |                                  |                                                                    |
| Texture                                                                    | Silty loam                        | Loam                               | Sandy loam                              | Sand                                            | Loamy sand                        | Heavy clay                       | Medium clay                                                        |
| OM (%)                                                                     | 3.4                               | 4.2                                | 3.47                                    | 4.9                                             | 7.8                               | 9.2                              | 12.1                                                               |
| pH                                                                         | 6.8                               | 7.3                                | 5.58                                    | 6.9                                             | 7.2                               | 6.7                              | 6.67                                                               |
| Total U (mg/kg)                                                            | 909                               | 280                                | 272                                     | 14                                              | 13                                | 41                               | 18                                                                 |
| Source of U contamination                                                  | Industrial                        | Industrial                         | U mine site                             | Industrial                                      | Industrial                        | Uraniferous shale                | UO <sub>2</sub> (NO <sub>3</sub> ) <sub>3</sub> ·6H <sub>2</sub> O |
| Experimental design                                                        |                                   |                                    |                                         |                                                 |                                   |                                  |                                                                    |
| Chelator                                                                   | CA and OA                         | CA, EDTA, and MA                   | CA, EDTA, and EDDS                      | CA, EDDS, OA, NTA, and NH <sub>4</sub> -citrate |                                   |                                  | CA and EDDS                                                        |
| Chelator dosage (mmol/kg)                                                  | 2, 10, and 20                     | 0.5, 1, 5, 10, and 20              | 0.5, 2, 2.5, 5, 10, 15, 25, and 50      | 5                                               |                                   |                                  | 5, 5 + 5, 10, and 10 + 10                                          |
| Test conditions                                                            | Soil incubation                   | Soil incubation and pot experiment | Column leaching test                    | Soil incubation                                 | Soil incubation                   | Soil incubation                  | Soil incubation and pot experiment                                 |
| Result of most effective mobilization of soil U                            |                                   |                                    |                                         |                                                 |                                   |                                  |                                                                    |
| Chelator and dosage (mmol/kg)                                              | CA<br>20                          | CA<br>20                           | CA<br>50                                | CA<br>5                                         | NH <sub>4</sub> -citrate<br>5     | NH <sub>4</sub> -citrate<br>5    | CA<br>10 + 10                                                      |
| Days taken to reach the maximum U concentration in soil solution           | 1                                 | 1                                  | 6                                       | 1                                               | 1                                 | 1                                | 8                                                                  |
| Maximum U concentration in soil solution and increment compared to control | 775 mg/kg, increased by 140 times | 240 mg/L, increased by 200 times   | 2000–2400 Bq/kg, increased by 356 times | 5019 µg/L, increased by 479 times               | 1106 µg/L, increased by 368 times | 733 µg/L, increased by 366 times | 1463.6 µg/L, increased by 215 times                                |

### 3. Chelating Agent-Assisted Phytoremediation of U-Contaminated Soils

#### 3.1. Mechanisms of Phytoextraction of U from Soils

Phytoextraction is a common technology for phytoremediation of U-contaminated soils, which transfers U from the soil to plant roots, stems, and leaves, and therefore cleans up the soil. Specifically, plant uptakes U<sup>4+</sup> or U<sup>6+</sup> ions through epidermal cells [3,87]. U cations (e.g., UO<sub>2</sub><sup>2+</sup>) can be absorbed by roots through the same carrier or ion channel as calcium (Ca<sup>2+</sup>), Fe<sup>3+</sup>, magnesium (Mg<sup>2+</sup>), and other necessary elements. U anions (e.g., UO<sub>2</sub>(CO<sub>3</sub>)<sub>2</sub><sup>2-</sup>) can pass through plant cell membranes in a way similar to CO<sub>3</sub><sup>2-</sup> [88]. For most plants, the majority of U is enriched in roots [89,90], with a small proportion of plants, such as *Sesbania rostrata* and water lily (*Nymphaea tetragona* Georgi) can further transfer the absorbed U upward to stems, leaves, and fruits [3].

The dominant factors affecting root uptake of soil U include chemical forms of U, soil environmental conditions (e.g., pH and Eh), and plant species [3,72,89–92]. U is mainly present in the form of UO<sub>2</sub><sup>2+</sup> in soils. PO<sub>4</sub><sup>3-</sup> and CO<sub>3</sub><sup>2-</sup> are common ligands for U ions and can form uranyl phosphate, uranyl carbonate or triple uranyl-calcium carbonate complexes. The formation of uranyl phosphate and uranyl carbonate in soils usually depends on the contents of PO<sub>4</sub><sup>3-</sup> and CO<sub>3</sub><sup>2-</sup> in the soil [90]. Moreover, soil pH can influence U solubility and sorption or desorption in soils, and consequently affect the bioavailability of soil U. Soil OM is rich in functional groups (e.g., carboxyl, hydroxyl, and aromatic groups) containing lone pairs of electrons, which can cause the formation of different U compounds by altering soil Eh [93]. Moreover, when U is taken up by root cells, it is translocated to the mid-column before being released into the xylem [3]. The transpiration and expression of transporter protein genes can influence the translocation of U to the aboveground parts. For example, three genes including IRT1, FRO2, and FIT1 were found to affect U translocation in *Arabidopsis thaliana* L. [94,95].

#### 3.2. Mechanisms of Assisted Phytoextraction of U from Soils

The principle of chelating agent-assisted phytoremediation of U-contaminated soils is to use chelating agents to desorb U ions from soil particle surface into soil solution, and

therefore increase the solubility of soil U. The chelating agent-mobilized U can be readily available for plant uptake and facilitate phytoextraction of U from the soil. Table 3 lists the effects of commonly used chelating agents on phytoextraction of U from soils. It can be seen that although CA has a relatively lower *K* value for U chelate than EDDS (Table 1), CA was the most effective in enhancing the phytoextraction of soil U in all phytoremediation trials presented in Table 3. This can be related to the following three reasons: (1) CA can reduce soil pH value, which may be favorable for the mobilization of soil U [72,96]. Lozano, et al., found that CA had the most significant effect on the dissolution of U with acidic pH, whereas the maximum dissolution of U with the addition of EDDS, EDTA or no chelating agent was under alkaline conditions [86]. (2) CA can form U-CA complexes, which increase the solubility and bioavailability of U in soils [91]. (3) CA can improve plant tolerance to the bioavailable U in soils [97]. Rong, et al., found that 5 mmol/kg CA addition could alleviate cell damage and improve the tolerance of perennial ryegrass (*Lolium perenne* L.) to soil U [98]. They claimed that the optimal dosage of CA can avoid adverse effects (e.g., etiolation, withering, and even death) of CA in excess amounts on plant growth as well as improve the buffer capacity of cytosol, enhance the photosynthesis of perennial ryegrass, and decrease the electrical conductivity (EC) and malondialdehyde (MDA) content while increasing the contents of soluble proteins and enhancing the activities of antioxidant enzymes in the shoots and roots. Likewise, a significant increase in antioxidant enzyme activities in the leaves of *Macleaya cordata* grown in the CA-treated soils has been noted, thereby mitigating the oxidative stress induced by U and chelating agent and facilitating the phytoextraction of soil U [27]. As shown in Table 3, the application rates of chelating agents in assisting phytoremediation of U-contaminated soils ranged from 0.5 to 25 mmol/kg. At a high application rate, the toxic effect of EDDS on plant growth was more pronounced than that of CA and OA [99]. In addition, compared to the single application at a high rate, multiple consecutive applications of chelating agents at a relatively low rate can alleviate the toxicity of mobilized U to plants and increase phytoextraction efficiency of soil U. It is well known that hyperaccumulator plant species play an important role in phytoremediation. At present, the Global Hyperaccumulator Database records 759 hyperaccumulators. However, there is still a lack of U-related hyperaccumulator plant species [100]. Therefore, the enhancement of phytoextraction of soil U as assisted by chelating agents can be a possible approach for filling the current gap of U hyperaccumulator plant species.

**Table 3.** Effects of different chelating agents on assisting phytoextraction of U from soils.

| Chelator                                                        | Plant                                                                                    | Total U (mg/kg) | Source of U Contamination                                                     | Incubation Period                                                              | Dosage (mmol/kg) | Application Frequency | Result of Most Effective Mobilization of Soil U                                                                                                                                                                                                                                                    | Ref. |
|-----------------------------------------------------------------|------------------------------------------------------------------------------------------|-----------------|-------------------------------------------------------------------------------|--------------------------------------------------------------------------------|------------------|-----------------------|----------------------------------------------------------------------------------------------------------------------------------------------------------------------------------------------------------------------------------------------------------------------------------------------------|------|
| AA <sup>1</sup> , CA, and MA                                    | 10 species <sup>6</sup>                                                                  | 280 and 750     | Industrial                                                                    | 28 d of growth prior to chelator addition and harvested 7 d after addition     | 20               | Single                | CA was the most effective in enhancing U accumulation in plants. After 20 mmol/kg CA addition, shoot U concentrations in four plant species ( <i>B. juncea</i> , <i>B. chinensis</i> , <i>B. narinosa</i> , and amaranth) increased by more than 1000 times compared to control within a few days. | [72] |
| CA, CDTA <sup>2</sup> , DTPA, EDTA, HEDTA <sup>3</sup> , and OA | Sunflower ( <i>Helianthus annuus</i> L.) and Indian mustard ( <i>Brassica juncea</i> L.) | 300             | Additional UO <sub>2</sub> (NO <sub>3</sub> ) <sub>3</sub> ·6H <sub>2</sub> O | 28 d of growth prior to chelator addition and harvested 42–56 d after addition | 1–25             | Single                | CA was the most effective in desorption of U ions and enhancing plant accumulation of U. 20 mmol/kg CA addition to loamy acid soil resulted in the highest U concentration in sunflower shoots, being 150 times greater than control.                                                              | [89] |

Table 3. Cont.

| Chelator                                                            | Plant                                                                                                                       | Total U (mg/kg) | Source of U Contamination                                                                     | Incubation Period                                                                          | Dosage (mmol/kg)                                                         | Application Frequency                                                                                                       | Result of Most Effective Mobilization of Soil U                                                                                                                                                                                                                                                                                                                                          | Ref.  |
|---------------------------------------------------------------------|-----------------------------------------------------------------------------------------------------------------------------|-----------------|-----------------------------------------------------------------------------------------------|--------------------------------------------------------------------------------------------|--------------------------------------------------------------------------|-----------------------------------------------------------------------------------------------------------------------------|------------------------------------------------------------------------------------------------------------------------------------------------------------------------------------------------------------------------------------------------------------------------------------------------------------------------------------------------------------------------------------------|-------|
| AC <sup>4</sup> , CA, EDDS, NTA, and OA                             | Indian mustard ( <i>Brassica juncea</i> cv. Vitasso) and ryegrass ( <i>Lolium perenne</i> cv. Melvina)                      | 14              | Industrial U-contaminated soil (sand, labelled as BK1)                                        | 28 d of growth prior to chelator addition and harvested 4–14 d after addition              | 5                                                                        | Single                                                                                                                      | The Indian mustard shoot U concentration was in the following decreasing order: EDDS > AC > CA > OA > NTA in BK1; and CA > AC > EDDS > OA = NTA in BI. The ryegrass shoot U concentration was in the following decreasing order: CA > AC > OA > EDDS > NTA in BK1; and CA = AC > OA = EDDS > NTA in BI.                                                                                  | [21]  |
|                                                                     |                                                                                                                             | 41              | Natural U-enriched soil (heavy clay, labelled as BI)                                          |                                                                                            |                                                                          |                                                                                                                             |                                                                                                                                                                                                                                                                                                                                                                                          |       |
| AC and CA                                                           | Kochia ( <i>Kochia scoparia</i> L. Schrad.), sunflower ( <i>Helianthus annuus</i> L.), and sweet corn ( <i>Zea mays</i> L.) | 78.7            | Depleted U-contaminated soil                                                                  | 45 d of growth prior to chelator addition and harvested 6 d after addition                 | 20                                                                       | Single                                                                                                                      | AC was as effective in enhancing plant uptake of U as CA. The kochia leaves U concentration was in the following decreasing order: CA > AC, whereas that in the stems: AC > CA. The sunflower leaves U concentration was in the following decreasing order: AC > CA, whereas that in the stems: AC = CA. Corn had the lowest U uptake capacity and was considered as a negative control. | [101] |
| CA and MA                                                           | Indian mustard ( <i>Brassica juncea</i> L.)                                                                                 | 100             | Additional UO <sub>2</sub> (NO <sub>3</sub> ) <sub>2</sub> ·6H <sub>2</sub> O                 | 66 d of growth prior to chelator addition and harvested 7 d after addition                 | 5, 10, and 20                                                            | Single                                                                                                                      | A total of two restorations were carried out. In the first round, the maximum plant accumulation of U was noted in 10 mmol/kg CA treatment after 45 d and in 20 mmol/kg CA treatment after 55 d. In the second round, the maximum plant accumulation of U was noted in 20 mmol/kg MA treatment after both 55 and 65 d.                                                                   | [102] |
| CA and mixture of CA, MA, OA, and LA <sup>5</sup> (labelled as Mix) | Mustard ( <i>Brassica juncea</i> var. <i>tumida</i> )                                                                       | 47.75           | Additional UO <sub>2</sub> (NO <sub>3</sub> ) <sub>2</sub> ·6H <sub>2</sub> O                 | 60 d of growth prior to chelator addition and harvested 7 d after addition                 | 5 for CA and molar ratio of CA: MA: OA: LA in Mix = 2.5:2.31:1.1:5:0.044 | Single                                                                                                                      | Mix was more effective in enhancing U accumulation in mustard.                                                                                                                                                                                                                                                                                                                           | [103] |
| CA, EDDS, and OA                                                    | Red watter grass ( <i>Zebrina pendula</i> Schnizl)                                                                          | 150             | Additional UO <sub>2</sub> (CH <sub>3</sub> CO <sub>2</sub> ) <sub>2</sub> ·2H <sub>2</sub> O | 90 d of growth prior to chelator addition and harvested 7 d after the last addition        | 2.5, 5, and 7.5                                                          | Three consecutive applications every three days                                                                             | CA was the most effective in enhancing U accumulation in <i>Zebrina pendula</i> Schnizl. Addition of 5 mmol/kg CA resulted in the highest U concentration in the plant, being 5.7 times greater than control.                                                                                                                                                                            | [99]  |
| CA, EDDS, and OA                                                    | <i>Macleaya cordata</i>                                                                                                     | 18              | Additional UO <sub>2</sub> (NO <sub>3</sub> ) <sub>2</sub> ·6H <sub>2</sub> O                 | Chelator addition at the beginning of flowering and harvested 14 d after the last addition | 5 and 10                                                                 | Except for 10 mmol/kg EDDS, all other chelators were applied both in a single application and two consecutive applications. | The enhanced U uptake was in the following decreasing order: CA > EDDS > OA. Two consecutive applications of 10 mmol/kg CA resulted in the most significantly promoted solubilization of soil U, being 215 times greater than control.                                                                                                                                                   | [27]  |
| CA, EDDS, and OA                                                    | Sunflower ( <i>Helianthus annuus</i> L.)                                                                                    | 15              | Additional UO <sub>2</sub> (CH <sub>3</sub> CO <sub>2</sub> ) <sub>2</sub> ·2H <sub>2</sub> O | 60 d of growth prior to chelator addition and harvested 7 d after the last addition        | 2.5, 5, and 7.5                                                          | Three consecutive applications every three days                                                                             | 5 mmol/kg CA addition resulted in the highest U phytoextraction efficiency, being 1.78 times greater than control.                                                                                                                                                                                                                                                                       | [28]  |

Notes: <sup>1</sup> AA: Acetic acid; <sup>2</sup> CDTA: Trans-1,2-diaminocyclohexane-N,N,N',N'-tetraacetic acid; <sup>3</sup> HEDTA: N-hydroxyethylenediaminetriacetic acid; <sup>4</sup> AC: Ammonium citrate; <sup>5</sup> LA: Lactic acid; <sup>6</sup> 10 species: Amaranth (*Amaranth cruentus* L.), Indian mustard (*Brassica juncea* L.), bush bean (*Phaseolus vulgaris* L.), Chinese cabbage (*Brassica chinensis* L.), Chinese mustard (*Brassica narinosa* L.), corn (*Zea mays*), cow pea (*Pisum sativum* L.), field pea (*Pisum sativum* L.), sunflower (*Helianthus annuus* L.), and winter wheat (*Triticum aestivum* L.).

### 3.3. Environmental Risks

Chelating agents can rapidly increase the mobility of soil heavy metals and radionuclides through chelation once applied to the soil. However, during the short period of rapid mobilization of soil heavy metals and radionuclides, plants may only be able to absorb a small proportion of the mobilized metal ions in the soil, whereas the remaining large amount of mobilized metal ions exists in the soil and may cause contamination to

subsurface soil and groundwater through leaching [60,62,63,104]. In addition, a sudden short-term release of bioavailable and substantial heavy metals and radionuclides in the soil may cause transient phytotoxicity and consequently inhibit plant growth [97,105–108]. For example, Chen, et al., compared the growth of sunflowers in soils treated with EDDS, CA, and OA at high (7.5 mmol/kg), medium (5 mmol/kg), and low (2.5 mmol/kg) application rates [28]. They found that all chelating agents reduced sunflower biomass, and a greater reduction was noted in soils treated with higher dosage of chelating agents. Whereas Römken, et al., found that although EDTA increased the concentrations of bioavailable heavy metals in the soil, the plant uptake of heavy metals did not exhibit an increasing trend after EDTA application [109]. This could be attributed to the limitations in plant uptake capacity for and tolerance to U, beyond which plant growth and uptake of soil bioavailable U will be affected. Similar results were obtained by Hou, et al., which showed that the germination of tomato, cabbage, and radish seeds was significantly inhibited at a soil U concentration greater than 320 mg/kg [24]. Therefore, plants have a limited uptake capacity for soil U, and excess amounts of mobilized U in soils in a short period can be toxic to plants.

In addition, chelating agents can influence the soil ecosystem by affecting soil microbial metabolism. For example, additional chelating agents (e.g., EDTA and EDDS) can affect the activity of soil microorganisms, especially dehydrogenase activity and basal respiration [110]. Lee and Sung found that EDTA inhibited the microbial activity in heavy metal-contaminated soils [111]. Soil microorganisms depend directly or indirectly on soil solutions to absorb food and water, and increased concentrations of bioavailable metals in soils may poison microorganisms [109]. Nevertheless, Cao, et al., found that biodegradable chelating agents (e.g., EDDS and methylglycinediacetic acid (MGDA)) could alleviate soil heavy metal stress and therefore benefit the bacterial community in the soil [112]. Thus, varying chelating agents may bring different effects on the soil ecosystem.

Barona, et al., found that EDTA increased the leachability of heavy metals in the soil and led to a weak adsorption of metal ions by soil compounds, which contributed to phytoextraction [113]. The study of Udovic and Lestan showed that the mobility of residual lead (Pb) in the EDTA-washed soil increased during the soil aging process [114]. The column leaching experiment of Wu, et al., also demonstrated that Cu, Zn, and Pb migrated into the leachate with rainwater after EDTA application to the soil, and the heavy metal concentrations in the leachate increased linearly with increasing rainfall [60]. This indicated that the migration of soil heavy metals increased by EDTA, which was conducive to phytoextraction. However, if the mobilized heavy metals in soils were not absorbed by plants in time, they may migrate to groundwater with rainwater, and consequently cause more serious environmental problems. Huang, et al., found that DTPA contributed more significantly to the leakage of soil Pb than acid rain under planting conditions, posing a great risk of groundwater pollution [115]. Nowack, et al., elucidated the unavailability of chelated metal leaching by preferential flow processes during the chelating agent-enhanced phytoextraction [104]. They pointed out that the application of chelating agents to soils should be limited to areas where the connection to groundwater has been broken, or where groundwater contamination is not an issue. Chang, et al., found that CA enhanced the accumulation of U in crop plants (i.e., edible rape, Indian mustard, canola, and sunflower), whereas additional CA could lead to groundwater pollution with downward U migration [97]. Additionally, CA promoted the phytoextraction of U from the soil in the short term, whereas the additional U-CA complexes could be converted into less available forms (e.g., U trioxide) after dissociation in the long term, which could consequently reduce the phytoextraction efficiency after the first few croppings [97]. Thayalakumaran, et al., found that Cu leaching was much greater than herbaceous uptake after EDTA application [116]. Therefore, when using chelating agents to assist phyto remediation of U-contaminated soils, it is necessary to consider the reasonable application rate and precipitation during the application.

## 4. Slow-Release Chelating Agents

### 4.1. Slow-Release Technology

Slow-release technology, which aims at extending the release time of a substance, was first used in the pharmaceutical industry and has since been applied to synthesize a wide range of slow-release materials such as slow-release fertilizers, slow-release pesticides, and food packaging [117–119]. Controlled-release technology is also a way to extend the release time, which allows the core material to be released at a specific rate or concentration level [120,121]. There is a slight difference between the two technologies, but essentially both extend the release time of core material, so this paper does not make a detailed distinction between the two. Slow-release fertilizers are designed to control and slow down the release speed of nutrients so as to reduce fertilization as well as nutrient loss and increase crop yield [119]. In the food packaging industry, the quality of food products for long-term storage is maintained or improved by slow release of substances such as antimicrobials, antioxidants, enzymes, and spices [122–124]. Although used in different industries, slow-release materials usually consist of three parts, i.e., core material which is the active substance to be released, wall/carrier material which can regulate the release speed of core material, and binding agent which forms the core material and wall/carrier material into a cohesive whole.

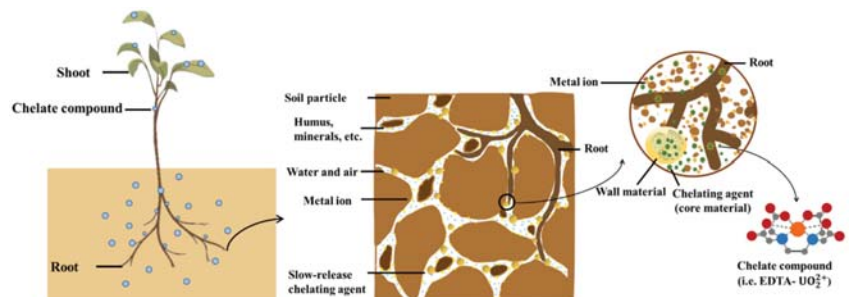
There are four common approaches which can be used to achieve slow-release effect, including blending, multilayer composite-controlled release, multi-hole adsorption carrier, and microencapsulation [125,126]. To be specific, the blending approach uses the principle of chaotic convection in fluid mechanics to prepare different forms of polymers and films [127]. The multi-layer composite controlled-release approach originated from the layer-by-layer coating (LBL) approach in the pharmaceutical field. Han and Floros first proposed the concept of multi-layer composite controlled-release approach, which is mainly composed of internal controlled-release layer, intermediate active film layer, and external barrier layer [128]. The inner layer is used to control the diffusion rate of active substance to food surface, the intermediate matrix layer contains the active substance, and the outer layer serves to prevent the extravasation loss of active substance. Multi-hole adsorption carrier controls the drug release speed by modulating and modifying the porous material to allow selective adsorption of target molecules. Microencapsulation uses coating material to encapsulate the core material to form particles less than 1000  $\mu\text{m}$  in diameter [129,130]. Microencapsulation is popular due to its simple operation and inexpensive equipment. The common methods for preparing slow-release microcapsules include emulsion solvent evaporation [131], spray drying [105], emulsion dispersion [132], chemical crosslinking, ion exchange, and complex coalescence [133].

Slow-release technology has recently received growing attention in environmental pollution treatment. In *in situ* chemical remediation, slow-release technology can control the release of active compounds, reduce the non-selective consumption of oxidants, and maintain the treatment effect for a longer period [134]. For example, Christenson, et al., prepared a slow-release oxidant by heating the mixed paraffin and potassium permanganate and cooling them in the mold [135]. Their five-year field-scale test showed that the slow-release oxidant gradually reduced trichloroethene (TCE) in a low permeable aquifer by 89% and was only refurbished yearly. Tang, et al., used chitosan and urea as carriers to prepare sodium persulfate slow-release material, which can prolong the generation time of free radicals and improve the degradation of OM [136]. In bioremediation, slow-release technology can continuously provide substrate, improve the removal efficiency of pollutants, and maintain a longer period of anaerobic dechlorination [134]. For example, Tsai, et al., reported that the slow-release material prepared by vegetable oil, cane molasses, and surfactants, provided nutrients for microorganisms and changed the subsurface environment to anaerobic conditions, which were conducive to reductive dechlorination. The removal efficiency of TCE in the contaminated groundwater reached 99% after 50 d [137]. In the study of Yeum, et al., slow-release precipitating tablets and slow-release floating tablets,

both prepared from hydroxypropyl methylcellulose, were applied to in situ biological denitrification systems to provide a continuous carbon source for microorganisms [138].

#### 4.2. Slow-Release Chelating Agent-Assisted Phytoremediation

To address the current bottleneck problem that the rapid mobilization rate of soil heavy metals and radionuclides by chelating agents does not match the plant uptake rate of bioavailable metal ions in the soil [28,105], slow-release chelating agents have been developed to control the release speed of chelating agent so as to avoid a sudden increase in soil bioavailable heavy metals and radionuclides which exceed plant tolerance and consequently cause phytotoxicity. The mechanisms of slow-release chelating agent-assisted phytoremediation of heavy metal- or radionuclide-contaminated soils are illustrated in Figure 1. As shown in Figure 1, the chelating agent as core material is wrapped by degradable wall material. After being applied to the soil, the wall material will gradually degrade meanwhile the internal chelating agent can be released to form chelates with metal ions in the soil, which can increase their solubility and therefore facilitate plant uptake of the contaminants.



**Figure 1.** Mechanisms of slow-release chelating agent-assisted phytoremediation of heavy metal- and radionuclide-contaminated soils.

Slow-release chelating agents and slow-release fertilizers have conspicuous similarities in their slow-releasing behaviors. Based on the comparatively mature preparation methods for slow-release fertilizers, slow-release chelating agents can also be prepared in two main ways, i.e., one method is to synthesize slow-release carrier and then use diffusion mechanism to import chelating agent into the carrier in liquid form (e.g., [139–141]). The other method is to use granular solid chelating agent as core material, and polymer organic or inorganic materials is selected as wall material to encapsulate chelating agent particles inside the slow-release chelating agent (e.g., [105,131,142,143]).

Until now, most studies have used synthetic organic polymers (e.g., polyethylene, polycaprolactone, and ethylene-vinyl acetate copolymer) as wall/carrier material to prepare slow-release chelating agents. However, these synthetic materials can be harmful to the environment. In contrast, biodegradable natural organic polymers (e.g., starch, cellulose, and chitosan) and organic-inorganic hybrid materials (e.g., acrylamide + montmorillonite and cellulose + zeolite) are ideal wall/carrier materials, which have been used to synthesize slow-release fertilizers. Current research on slow-release chelating agents with biodegradable materials as wall/carrier material is relatively limited. Very recently, Wang, et al., prepared a slow-release chelating agent with chitosan and cyclodextrin as carrier materials and CA as core material [141]. In addition, considering the similarity between slow-release chelating agents and slow-release fertilizers, some wall/carrier materials applied to slow-release fertilizers (e.g., starch, cellulose, and chitosan) may also be ideal for the synthesis of slow-release chelating agents. Furthermore, slow-release materials can cause a burst-release effect after application in the water and soil environment [144,145]. The burst-release effect can be induced when a large amount of core material is released after the shell of slow-release material with a shell-core structure degrades or the shell



breaks down due to the increased internal pressure. To mitigate the above disadvantage, polymers, such as polyvinyl alcohol (PVA) and gelatine, can be added to increase the toughness of outer wall and enable it to withstand a certain amount of internal pressure. Zhang, et al., prepared a biodegradable carboxymethylcellulose and PVA blended film. They found that the water permeability of the film could be adjusted by changing the ratios of PVA and formaldehyde [146]. If this film was applied to slow-release chelating agents, the slow-release period could be prolonged. Han, et al., prepared a blended film from starch and PVA that is biodegradable and has good compatibility [147], which may also be used as a slow-release carrier for slow-release chelating agents.

It is worth noting that the aforementioned organic polymers and inorganic materials have been used in preparation of adsorbents [148–152], suggesting that these materials may promote the adsorption of some metal ions onto the wall/carrier material, leading to a temporary passivation effect. Kos, et al., used EDDS and EDTA in conjunction with acrylamide hydrogel to assist the phytoextraction of soil Pb [153]. They found that 10 mmol/kg EDDS addition significantly increased the leachable Pb, whereas 5 mmol/kg EDDS addition not only increased the phytoextraction efficiency of soil Pb, but also effectively controlled the leaching of soil Pb. Hydrogel can be a promising carrier for the synthesis of slow-release chelating agents as the chelating agent can be released into the soil through water loss from the hydrogel. Moreover, hydrogel can maintain the soil nutrient balance by retaining water in the soil. Hydrogel-based slow-release fertilizers have also been reported by other researchers [154–158]. If the functions of nutrient supply, water retention, and controlled release of chelating agent were incorporated into hydrogel-based slow-release chelating agents, chelating agent-assisted phytoextraction technology could be significantly advanced.

Until now, only a few studies have examined the effectiveness of slow-release chelating agents in assisting phytoremediation of heavy metal-contaminated soils, whereas its application in phytoremediation of U-contaminated soils has been scarce. Table 4 lists slow-release chelating agents which have been used to remediate heavy metal- and radionuclide-contaminated soils in recent years. As shown in Table 4, the particle sizes of slow-release chelating agents ranged from 5–20  $\mu\text{m}$  to 3–5 mm. EDTA is the most commonly used chelating agent in these studies. The slow-release period of these chelating agents ranged from several days to months, which is mainly related to the particle size of chelating agent and properties of wall/carrier material. Among the chelating agents listed in Table 4, those with higher molecular weight organic compounds as the wall/carrier material possessed a longer slow-release period. Recently, the first biodegradable slow-release chelating agent with CA as core material has been prepared by Wang, et al., who used carboxymethyl- $\beta$ -cyclodextrin (CMCD) and hydroxypropyl chitosan as carriers [141]. They found that the novel slow-release chelating agent had a noticeable slow-release effect on CA, which could reduce the impact of soil bioavailable U on Indian mustard (*Brassica juncea* L.) growth and promote the absorption and accumulation of U in the plant. However, compared with the slow-release chelating agent (i.e., microencapsulated EDTA) in Xie, et al., the release rate of the aforementioned slow-release CA in water is faster [131]. In addition, due to the lack of long-term soil incubation experiment, the dynamic interactions between the slow-release CA and U as well as other metals in the soil remain unclear. Therefore, the slow-release period of slow-release CA prepared by Wang, et al., in soils is hard to be estimated [141].



**Table 4.** Components, synthesis methods, particle size, and slow-release performance of slow-release chelating agents applied in remediation of heavy metal- and radionuclide-contaminated soils.

| Wall/Carrier Material                                                                                                                                                     | Core Material        | Synthesis Method           | Particle Size      | Slow-Release Period                                                                                                                                                      | Contaminant    | Dosage (mmol/kg) | Test Conditions | Ref.  |
|---------------------------------------------------------------------------------------------------------------------------------------------------------------------------|----------------------|----------------------------|--------------------|--------------------------------------------------------------------------------------------------------------------------------------------------------------------------|----------------|------------------|-----------------|-------|
| Silicate                                                                                                                                                                  | EDTA-Na <sub>2</sub> | Spray drying               | 3–5 mm             | Release of EDTA from slow-release EDTA was still significantly lower than from uncoated solid EDTA in soil after 18 d.                                                   | Pb and Zn      | 13               | Pot experiment  | [105] |
| Talc, polyethylene, ethylene-vinyl acetate copolymer, ethylene-octene-1 copolymer, and polyoxyethylene monomethyl ether Diethylenetriamine and hexamethylene diisocyanate | EDTA-Na <sub>2</sub> | Coating                    | -                  | Release of 75% EDTA ranged from 3 to 210 d in water                                                                                                                      | Pb             | 4                | Pot experiment  | [142] |
| Polycaprolactone                                                                                                                                                          | EDTA-Na <sub>4</sub> | Interfacial polymerization | 5.78 µm in average | Release of 85% EDTA in water after 5 d                                                                                                                                   | -              | -                | Pot experiment  | [143] |
| Polycaprolactone                                                                                                                                                          | EDTA                 | Solvent evaporation        | 65 ± 15 µm         | Release of 93% EDTA in water after 30 d<br>Release of EDTA from slow-release EDTA was still significantly lower than from non-microencapsulated EDTA in water after 3 d. | Cu and Pb      | 3 and 6          | Pot experiment  | [131] |
| Chitosan and its derivatives                                                                                                                                              | EDTA-Na <sub>2</sub> | Spray drying               | 5–20 µm            | Release of EDTA from slow-release EDTA was still significantly lower than from non-microencapsulated EDTA in water after 3 d.                                            | Cd, Cu, and Pb | 4 and 8          | Pot experiment  | [159] |
| Hydroxypropyl chitosan-graft-carboxymethyl-β-cyclodextrin                                                                                                                 | CA                   | Spray drying               | -                  | Cumulative release of 80% CA in water after 2 d                                                                                                                          | U              | 5                | Pot experiment  | [141] |

Application rate of slow-release chelating agents is one of the most important factors influencing mobilization of soil U. As summarized from Table 3, the application rates of chelating agents alone in assisting phytoremediation of U-contaminated soils ranged from 0.5 to 25 mmol/kg. In addition, previous studies reported that chelating agents (e.g., EDDS, EDTA, and DIPA) reduced plant biomass and even caused plant mortality at application rates greater than 5–7.5 mmol/kg [27,28,160,161]. The impact of chelating agents on plant growth is also related to the types of chelating agent and plant. For example, Chen, et al., found that 7.5 mmol/kg EDDS addition significantly inhibited the growth of *Zebrina pendula* Schnizl and sunflower (*Helianthus annuus* L.) [28,160]. Hu, et al., also noted some toxic symptoms such as chlorosis and necrotic spots occurred during *Macleaya cordata* growth after the addition of 5 and 10 mmol/kg EDDS [27]. In contrast, under the same experimental conditions, the aforementioned plants exhibited much higher tolerance to CA treatments. As shown in Table 4, the application rates of slow-release chelating agents in assisting phytoremediation of heavy metal and radionuclide-contaminated soils ranged from 3 to 13 mmol/kg, which is close to the above application rate range of chelating agents alone. Moreover, when comparing the effectiveness of chelating agents and slow-release chelating agents in enhancing phytoextraction of soil contaminants, the amount of core material in the slow-release chelating agent should be equal to that of chelating agent alone. At present, research on the use of slow-release chelating agents in assisting phytoremediation of U-contaminated soils is still at juvenile stage. The evaluation of their effectiveness in enhancing phytoextraction of soil heavy metals and radionuclides reported in scientific literature are exclusively obtained from laboratory pot experiments with no field applications (Table 4). Hence, it is recommended that pilot-scale tests should be conducted to investigate the effect of slow-release chelating agents on enhancing phytoextraction of soil U under field conditions. This effort can provide a better evaluation of slow-release performance. In

addition, bench-scale accelerated aging tests (e.g., wet–dry cycling and freeze–thaw cycling) can be carried out to investigate the effect of slow-release chelating agents on controlling the release speed of core material under simulated natural aging conditions, which can make a contribution to elucidation of long-term slow-release mechanisms.

#### 4.3. Evaluation of Slow-Release Performance

The slow-release performance of slow-release chelating agents can be indicated by the increasing rate of core material (i.e., chelating agent) content in the soil with time after application. The common methods for evaluating slow-release performance of slow-release materials include hydrostatic dissolution, soil incubation, and soil column leaching [162–166]. In the hydrostatic dissolution method, slow-release material is added to deionized water. The mixture is then maintained at a constant temperature. The amount of core material released into the water is measured regularly to calculate its release speed with time. The method is simple, fast, and well reproducible. However, it ignores the effect of soil environmental conditions on the slow-release performance. The soil incubation method simulates the release of core material in the soil and is closer to natural environmental conditions compared to the hydrostatic dissolution test. In the soil column leaching method, slow-release material is subjected to leaching test, and the concentration of core material in the leachate collected with time is measured. Among the above methods for evaluating slow-release performance, hydrostatic dissolution method has been widely used (e.g., [141,167–169]) due to its simple operating procedure, controllable environmental conditions, and convenient comparison between different slow-release materials. Considering the complexity of actual contaminated site environment, it is necessary to evaluate the slow-release performance of slow-release chelating agents in soils. Li, et al., first synthesized a slow-release chelating agent with EDTA as core material and silicate as coating material [105]. They demonstrated that the change of DOC concentration in the leachate could reflect the slow-release performance of coated EDTA. In contrast to the inorganic wall material in Li, et al., Xie, et al., used polyethylene as the wall material of microcapsule, and the concentration of EDTA in aqueous solution released from the microcapsule was determined by an ion chromatography (IC) [143]. Likewise, Shibata, et al., prepared polymer-coated EDTA and also characterized the slow-release property based on the variation of EDTA concentration in distilled water using a high-performance liquid chromatography (HPLC) [142]. The EDTA concentration in the solution can be determined by HPLC after pretreatment with an extractant containing Cu or Fe ions [170], and Shibata, et al., used a  $\text{CuSO}_4$  solution as extractant. However, due to the lack of details about the operating procedures of the above methods, it is difficult to compare the slow-release results obtained from different studies. The longest release period of slow-release chelating agent recorded in literature is a polymer-coated EDTA synthesized by Shibata, et al., who reported that 75% of the EDTA in the slow-release chelating agent was released into the water after 210 d [142]. The pot experiment showed that among the five slow-release chelating agents with different wall materials, the EDTA coated with 40% talc, 45% polyethylene, 10% ethylene-octene-1 copolymer, and 5% polyoxoethylene monomethyl ether (0.72 mmol/g) were the most effective in reducing Pb and EDTA concentrations in the soil solution and increasing Pb enrichment in *Sorghum bicolor* L. seedlings with a release period of 80 d [142].

## 5. Conclusions and Future Perspectives

With the rapid development of nuclear energy and on-going U mining, cleaning up of U-contaminated soils has become a major global challenge. At present, no U hyperaccumulator plant species have been found, whereas plants for soil remediation have low extraction efficiency and long-term remediation period for U-contaminated soils. Both APCAs (e.g., EDTA and EDDS) and LMWOAs (e.g., CA and OA) can enhance phytoextraction of soil U by increasing bioavailable U in the soil via forming soluble chelate compounds. CA, which can be generated by organisms and is biodegradable, has a pronounced effect on mobilizing U in soils, and therefore assists phytoextraction of U from the soil. It should be noted that

after chelating agents are applied to the soil, the mobility and bioavailability of soil U can increase rapidly in a short period, resulting in the problem that the increasing rate of soil bioavailable U does not match the plant uptake rate of and tolerance to U. The majority of mobilized U may not be absorbed by roots and remained in the soil, posing a non-negligible contamination risk to groundwater through leaching processes. Slow-release chelating agents synthesized by slow-release technology can control the release speed of chelating agent so that the mobilization rate of soil U matches plant uptake rate of U.

Currently, research on synthesis and application of slow-release chelating agents in assisting phytoremediation of U-contaminated soils is still in its infancy. The slow-release CA synthesized by Wang, et al., is the only slow-release chelating agent which was used to enhance phytoextraction of soil U [141]. Meanwhile most of the existing slow-release chelating agents designed for phytoremediation of heavy metal-contaminated soils contain non-biodegradable EDTA as core material, which would cause secondary pollution. In addition, the effective performance of the aforementioned slow-release CA was noted in laboratory pot experiments, whereas its effectiveness in assisting phytoremediation of U-contaminated soils in the field remains unclear. Future work can mainly include: (1) selecting and developing environmentally friendly wall/carrier materials and cost-effective preparation methods. Natural materials (e.g., starch, cellulose, and chitosan) and simple preparation methods with low cost (e.g., interfacial polymerization and spray drying) should be screened for synthesis of slow-release chelating agents prior to large-scale application. (2) Some existing wall/carrier materials (e.g., chitosan and its derivatives) of slow-release chelating agents have high adsorption capacity for heavy metals and radionuclides. They can have a passivation effect on these contaminants in soils. Therefore, it is necessary to eliminate the above negative impact of wall/carrier materials of slow-release chelating agents on mobilizing soil U. This can be achieved by optimizing the ratio of wall/carrier material to core material and modifying the surface porous structure of slow-release chelating agent. (3) Existing slow-release chelating agents have been mainly added to soils in the form of solutions. Synthesis of hydrogel-based slow-release chelating agent can be a promising research direction because hydrogel as a carrier for chelating agents has the potential to combine controlled release of chelating agent into the soil with soil and water conservation, thus improving the soil environment. (4) The present systematic review showed that CA is the most effective in enhancing phytoextraction of U from contaminated soils compared to other commonly used chelating agents. However, CA is easily decomposed in soils. Thus, it is encouraged to evaluate the long-term effect of CA on mobilization of soil U as well as explore methods for maintaining the effectiveness of CA during natural aging processes. (5) Soil microorganisms play an important role in the formation of soil fertility, transformation of contaminants as well as nutrient elements [171]. Therefore, it is also necessary to investigate the effect of microbial metabolic activities in rhizosphere soils on the slow-release performance of slow-release chelating agents and explore the transport mechanisms of complex compound formed by chelating agents with U ions at the plant-soil interface. This endeavor can contribute to the combination of chelating agent- and microorganisms-assisted phytoremediation of U-contaminated soils. (6) The studies of Saleh, et al., demonstrated that aquatic plants including *Eichhornia crassipes*, *Ludwigia stolonifera*, and *Myriophyllum spicatum* have an enormous accumulation capacity of heavy metals (e.g., Cd, Cr, Cu, and Pb) and radionuclides (e.g., cesium (Cs) and cobalt (Co)) [172–177]. Therefore, apart from the above on-going research relevant to slow-release chelating agents, the effect of chelating agents on enhancing the accumulation of U and other radionuclides in these aquatic plants in contaminated paddy soils and riparian zones can be investigated.

**Author Contributions:** Conceptualization, K.Y. and Y.Y.; Literature Search and Data Analysis, Y.Y., K.Y. and Y.X.; Writing—Original Draft Preparation, Y.Y. and K.Y.; Writing—Review and Editing, K.Y., J.D. and N.J.; Funding Acquisition, K.Y.; Supervision, K.Y. and J.D. All authors have read and agreed to the published version of the manuscript.

**Funding:** This research was funded by the National Key Research and Development Program of China, grant number 2020YFC1806603, the National Natural Science Foundation of China, grant number 41907095, and the Fundamental Research Funds for the Central Universities, grant number 2020NTST24. The APC was funded by the National Key Research and Development Program of China, grant number 2020YFC1806603.

**Institutional Review Board Statement:** Not applicable.

**Informed Consent Statement:** Not applicable.

**Data Availability Statement:** Data is contained within the article.

**Conflicts of Interest:** The authors declare no conflict of interest.

## References

- World Nuclear Association. *World Nuclear Performance Report 2021—COP26 Edition*; World Nuclear Performance Report; World Nuclear Association: London, UK, 2021; pp. 3–13.
- World Nuclear Association. *The Nuclear Fuel Report: Global Scenarios for Demand and Supply Availability 2021–2040*; World Nuclear Association: London, UK, 2021.
- Chen, L.; Liu, J.; Zhang, W.; Zhou, J.; Luo, D.; Li, Z. Uranium (U) Source, Speciation, Uptake, Toxicity and Bioremediation Strategies in Soil-Plant System: A Review. *J. Hazard. Mater.* **2021**, *413*, 125319. [[CrossRef](#)] [[PubMed](#)]
- Winde, F. Uranium Pollution of the Wonderfonteinspruit, 1997–2008 Part 1: Uranium Toxicity, Regional Background and Mining-Related Sources of Uranium Pollution. *Water SA* **2010**, *36*, 239–256.
- Yan, X.; Luo, X. Radionuclides Distribution, Properties, and Microbial Diversity of Soils in Uranium Mill Tailings from Southeastern China. *J. Environ. Radioact.* **2015**, *139*, 85–90. [[CrossRef](#)] [[PubMed](#)]
- Lu, Z.; Liu, Z. Pollution Characteristics and Risk Assessment of Uranium and Heavy Metals of Agricultural Soil around the Uranium Tailing Reservoir in Southern China. *J. Radioanal. Nucl. Chem.* **2018**, *318*, 923–933. [[CrossRef](#)]
- Sabol, J. Uranium in the Beginning of the Nuclear Age: Reflections on the Historical Role of Jáchymov and an Overview of Early and Present Epidemiological Studies. In *Uranium in Plants and the Environment*; Gupta, D.K., Walther, C., Eds.; Springer International Publishing: Cham, Switzerland, 2020; ISBN 978-3-030-14961-1.
- Chen, L.; Wang, J.; Beiyuan, J.; Guo, X.; Wu, H.; Fang, L. Environmental and Health Risk Assessment of Potentially Toxic Trace Elements in Soils near Uranium (U) Mines: A Global Meta-Analysis. *Sci. Total Environ.* **2021**, *816*, 151556. [[CrossRef](#)]
- Gongalsky, K.B. Impact of Pollution Caused by Uranium Production on Soil Macrofauna. *Environ. Monit. Assess.* **2003**, *89*, 197–219. [[CrossRef](#)]
- Ma, W.; Gao, B.; Guo, Y.; Sun, Z.; Zhang, Y.; Chen, G.; Zhu, X.; Zhang, C. Occurrence and Distribution of Uranium in a Hydrological Cycle around a Uranium Mill Tailings Pond, Southern China. *Int. J. Environ. Res. Public Health* **2020**, *17*, 773. [[CrossRef](#)]
- Bourdon, B.; Turner, S.; Henderson, G.M.; Lundstrom, C.C. Introduction to U-Series Geochemistry. *Rev. Mineral. Geochem.* **2003**, *52*, 1–21. [[CrossRef](#)]
- Brugge, D.; de Lemos, J.L.; Oldmixon, B. Exposure Pathways and Health Effects Associated with Chemical and Radiological Toxicity of Natural Uranium: A Review. *Rev. Environ. Health* **2005**, *20*, 177–194. [[CrossRef](#)]
- Zhu, G.; Xiang, X.; Chen, X.; Wang, L.; Hu, H.; Weng, S. Renal Dysfunction Induced by Long-Term Exposure to Depleted Uranium in Rats. *Arch. Toxicol.* **2009**, *83*, 37–46. [[CrossRef](#)]
- Brugge, D.; Buchner, V. Health Effects of Uranium: New Research Findings. *Doug Brugge Va Buchner* **2011**, *26*, 231–249. [[CrossRef](#)] [[PubMed](#)]
- Cheng, H.; Lawrence Edwards, R.; Shen, C.-C.; Polyak, V.J.; Asmerom, Y.; Woodhead, J.; Hellstrom, J.; Wang, Y.; Kong, X.; Spötl, C.; et al. Improvements in  $^{230}\text{Th}$  Dating,  $^{230}\text{Th}$  and  $^{234}\text{U}$  Half-Life Values, and U–Th Isotopic Measurements by Multi-Collector Inductively Coupled Plasma Mass Spectrometry. *Earth Planet. Sci. Lett.* **2013**, *371*–372, 82–91. [[CrossRef](#)]
- Dewar, D. Uranium Mining: Environmental and Human Health Effects. In *Nuclear Non-Proliferation in International Law—Volume IV: Human Perspectives on the Development and Use of Nuclear Energy*; Black-Branch, J.L., Fleck, D., Eds.; T.M.C. Asser Press: Hague, The Netherlands, 2019; ISBN 978-94-6265-267-5.
- Ma, M.; Wang, R.; Xu, L.; Xu, M.; Liu, S. Emerging Health Risks and Underlying Toxicological Mechanisms of Uranium Contamination: Lessons from the Past Two Decades. *Environ. Int.* **2020**, *145*, 106107. [[CrossRef](#)] [[PubMed](#)]
- Meinrath, A.; Schneider, P.; Meinrath, G. Uranium Ores and Depleted Uranium in the Environment, with a Reference to Uranium in the Biosphere from the Erzgebirge/Sachsen, Germany. *J. Environ. Radioact.* **2003**, *64*, 175–193. [[CrossRef](#)]
- Mészáros, G.; Bognár, G.; Kőteles, G.J. Long-Term Persistence of Chromosome Aberrations in Uranium Miners. *J. Occup. Health* **2004**, *46*, 310–315. [[CrossRef](#)]
- Wolf, G.; Arndt, D.; Kotschy-Lang, N.; Obe, G. Chromosomal Aberrations in Uranium and Coal Miners. *Int. J. Radiat. Biol.* **2009**, *80*, 147–153. [[CrossRef](#)]

21. Duquène, L.; Vandenhove, H.; Tack, F.; Meers, E.; Baeten, J.; Wannijn, J. Enhanced Phytoextraction of Uranium and Selected Heavy Metals by Indian Mustard and Ryegrass Using Biodegradable Soil Amendments. *Sci. Total Environ.* **2009**, *407*, 1496–1505. [[CrossRef](#)]
22. Mihalik, J.; Tlustoš, P.; Szaková, J. Comparison of Willow and Sunflower for Uranium Phytoextraction Induced by Citric Acid. *J. Radioanal. Nucl. Chem.* **2010**, *285*, 279–285. [[CrossRef](#)]
23. Stojanović, M.D.; Stevanović, D.R.; Milojković, J.V.; Grubišić, M.S.; Iliš, D.A. Phytotoxic Effect of the Uranium on the Growing Up and Development of the Plant of Corn. *Water Air Soil Pollut.* **2010**, *209*, 401–410. [[CrossRef](#)]
24. Hou, J.; Wang, C.; Zhou, Y.; Li, S.; Hayat, T.; Alsaedi, A.; Wang, X. Effects of Uranium Stress on Physiological and Biochemical Characteristics in Seedlings of Six Common Edible Vegetables. *J. Radioanal. Nucl. Chem.* **2018**, *316*, 1001–1010. [[CrossRef](#)]
25. Lai, J.; Liu, Z.; Luo, X. A Metabolomic, Transcriptomic Profiling, and Mineral Nutrient Metabolism Study of the Phytotoxicity Mechanism of Uranium. *J. Hazard. Mater.* **2020**, *386*, 121437. [[CrossRef](#)] [[PubMed](#)]
26. Duquène, L.; Tack, F.; Meers, E.; Baeten, J.; Wannijn, J.; Vandenhove, H. Effect of Biodegradable Amendments on Uranium Solubility in Contaminated Soils. *Sci. Total Environ.* **2008**, *391*, 26–33. [[CrossRef](#)] [[PubMed](#)]
27. Hu, N.; Lang, T.; Ding, D.; Hu, J.; Li, C.; Zhang, H.; Li, G. Enhancement of Repeated Applications of Chelates on Phytoremediation of Uranium Contaminated Soil by *Maclaya cordata*. *J. Environ. Radioact.* **2019**, *199–200*, 58–65. [[CrossRef](#)] [[PubMed](#)]
28. Chen, L.; Yang, J.; Wang, D. Phytoremediation of Uranium and Cadmium Contaminated Soils by Sunflower (*Helianthus Annuus* L.) Enhanced with Biodegradable Chelating Agents. *J. Clean Prod.* **2020**, *263*, 121491. [[CrossRef](#)]
29. Balaram, V.; Rani, A.; Rathore, D.P.S. Uranium in Groundwater in Parts of India and World: A Comprehensive Review of Sources, Impact to the Environment and Human Health, Analytical Techniques, and Mitigation Technologies. *Geosyst. Geoenviron.* **2022**, *1*, 100043. [[CrossRef](#)]
30. Kurttio, P.; Harmoinen, A.; Saha, H.; Salonen, L.; Karpas, Z.; Komulainen, H.; Auvinen, A. Kidney Toxicity of Ingested Uranium From Drinking Water. *Am. J. Kidney Dis.* **2006**, *47*, 972–982. [[CrossRef](#)]
31. Bjørklund, G.; Semenova, Y.; Pivina, L.; Dadar, M.; Rahman, M.M.; Aaseth, J.; Chirumbolo, S. Uranium in Drinking Water: A Public Health Threat. *Arch. Toxicol.* **2020**, *94*, 1551–1560. [[CrossRef](#)]
32. Arzuaga, X.; Gehlhaus, M.; Strong, J. Modes of Action Associated with Uranium Induced Adverse Effects in Bone Function and Development. *Toxicol. Lett.* **2015**, *236*, 123–130. [[CrossRef](#)]
33. Guéguen, Y.; Souidi, M.; Baudelin, C.; Dudoignon, N.; Grison, S.; Dublineau, I.; Marquette, C.; Voisin, P.; Gourmelon, P.; Aigueperse, J. Short-Term Hepatic Effects of Depleted Uranium on Xenobiotic and Bile Acid Metabolizing Cytochrome P450 Enzymes in the Rat. *Arch. Toxicol.* **2006**, *80*, 187–195. [[CrossRef](#)]
34. Wang, S.; Ran, Y.; Lu, B.; Li, J.; Kuang, H.; Gong, L.; Hao, Y. A Review of Uranium-Induced Reproductive Toxicity. *Biol. Trace Elem. Res.* **2020**, *196*, 204–213. [[CrossRef](#)]
35. Angenard, G.; Muczynski, V.; Coffigny, H.; Duquenne, C.; Frydman, R.; Habert, R.; Livera, G.; Rouiller-Fabre, V. In Vitro Effects of Uranium on Human Fetal Germ Cells. *Reprod. Toxicol.* **2011**, *31*, 470–476. [[CrossRef](#)]
36. Saint-Marc, B.; Elie, C.; Manens, L.; Tack, K.; Benderitter, M.; Gueguen, Y.; Ibanez, C. Chronic Uranium Contamination Alters Spinal Motor Neuron Integrity via Modulation of SMN1 Expression and Microglia Recruitment. *Toxicol. Lett.* **2016**, *254*, 37–44. [[CrossRef](#)] [[PubMed](#)]
37. Aide, M.T. Chemical Thermodynamics of Uranium in the Soil Environment. In *Uranium—Safety, Resources, Separation and Thermodynamic Calculation*; IntechOpen: London, UK, 2017; ISBN 978-1-78923-119-9.
38. Wang, X.; Shi, Z.; Kinniburgh, D.G.; Zhao, L.; Ni, S.; Wang, R.; Hou, Y.; Cheng, K.; Zhu, B. Effect of Thermodynamic Database Selection on the Estimated Aqueous Uranium Speciation. *J. Geochem. Explor.* **2019**, *204*, 33–42. [[CrossRef](#)]
39. Sarkar, D.; Andra, S.S.; Saminathan, S.K.M.; Datta, R. Chelant-Aided Enhancement of Lead Mobilization in Residential Soils. *Environ. Pollut.* **2008**, *156*, 1139–1148. [[CrossRef](#)] [[PubMed](#)]
40. Bucheli-Witschel, M.; Egli, T. Environmental Fate and Microbial Degradation of Aminopolycarboxylic Acids. *Fems Microbiol. Rev.* **2001**, *25*, 69–106. [[CrossRef](#)]
41. Egli, T. Biodegradation of Metal-Complexing Aminopolycarboxylic Acids. *J. Biosci. Bioeng.* **2001**, *92*, 89–97. [[CrossRef](#)]
42. Hu, Y.-H.; Wei, S.-H.; Zhou, Q.-X.; Zhan, J.; Ma, L.-H.; Niu, R.-C.; Li, Y.-M.; Wang, S.-S. Application of Chelator in Phytoremediation of Heavy Metals Contaminated Soils: A Review. *J. Agro-Environ. Sci.* **2010**, *29*, 2055–2063.
43. Bian, X.; Cui, J.; Tang, B.; Yang, L. Chelant-Induced Phytoextraction of Heavy Metals from Contaminated Soils: A Review. *Pol. J. Environ. Stud.* **2018**, *27*, 2417–2424. [[CrossRef](#)]
44. Pinto, I.S.S.; Neto, I.F.F.; Soares, H.M.V.M. Biodegradable Chelating Agents for Industrial, Domestic, and Agricultural Applications—A Review. *Environ. Sci. Pollut. Res.* **2014**, *21*, 11893–11906. [[CrossRef](#)]
45. Huang, G.; You, J.; Zhou, X.; Ren, C.; Islam, M.S.; Hu, H. Effects of Low Molecular Weight Organic Acids on Cu Accumulation by Castor Bean and Soil Enzyme Activities. *Ecotox. Environ. Safe* **2020**, *203*, 110983. [[CrossRef](#)]
46. Lai, H.-Y. Negative Effects of Chelants on Soil Qualities of Five Soil Series. *Int. J. Phytoremediat.* **2014**, *17*, 228–234. [[CrossRef](#)] [[PubMed](#)]
47. Meers, E.; Tack, F.M.G.; Verloo, M.G. Degradability of Ethylenediaminedisuccinic Acid (EDDS) in Metal Contaminated Soils: Implications for Its Use Soil Remediation. *Chemosphere* **2008**, *70*, 358–363. [[CrossRef](#)] [[PubMed](#)]
48. Baek, N.H.; Clesceri, N.L. NTA Biodegradation and Removal in Subsurface Sandy Soil. *Water Res.* **1986**, *20*, 345–349. [[CrossRef](#)]



49. Means, J.L.; Kucak, T.; Crerar, D.A. Relative Degradation Rates of NTA, EDTA and DTPA and Environmental Implications. *Environ. Pollut.* **1980**, *1*, 45–60. [[CrossRef](#)]
50. Wen, J.; Stacey, S.P.; McLaughlin, M.J.; Kirby, J.K. Biodegradation of Rhamnolipid, EDTA and Citric Acid in Cadmium and Zinc Contaminated Soils. *Soil Biol. Biochem.* **2009**, *41*, 2214–2221. [[CrossRef](#)]
51. Gunina, A.; Smith, A.R.; Kuzyakov, Y.; Jones, D.L. Microbial Uptake and Utilization of Low Molecular Weight Organic Substrates in Soil Depend on Carbon Oxidation State. *Biogeochemistry* **2017**, *133*, 89–100. [[CrossRef](#)]
52. Smith, R.M.; Martell, A.E. *Critical Stability Constants Volume 6: Second Supplement*; Springer: New York, NY, USA, 1989; Volume 6, ISBN 978-1-4615-6766-0.
53. Leydier, A.; Lin, Y.; Arrachart, G.; Turgis, R.; Lecerclé, D.; Favre-Reguillon, A.; Taran, F.; Lemaire, M.; Pellet-Rostaing, S. EDTA and DTPA Modified Ligands as Sequestering Agents for Uranyl Decorporation. *Tetrahedron* **2012**, *68*, 1163–1170. [[CrossRef](#)]
54. Smith, R.M.; Martell, A.E. Critical Stability Constants, Enthalpies and Entropies for the Formation of Metal Complexes of Aminopolycarboxylic Acids and Carboxylic Acids. *Sci. Total Environ.* **1987**, *64*, 125–147. [[CrossRef](#)]
55. Chen, C.-Y.; Chen, C.-Y. Stability Constants of Polymer-Bound Iminodiacetate-Type Chelating Agents with Some Transition-Metal Ions. *J. Appl. Polym. Sci.* **2002**, *86*, 1986–1994. [[CrossRef](#)]
56. Vukovic, S.; Hay, B.P.; Bryantsev, V.S. Predicting Stability Constants for Uranyl Complexes Using Density Functional Theory. *Inorg. Chem.* **2015**, *54*, 3995–4001. [[CrossRef](#)]
57. Singh, J.; Srivastav, A.N.; Singh, N.; Singh, A. Stability Constants of Metal Complexes in Solution. In *Stability and Applications of Coordination Compounds*; IntechOpen: London, UK, 2019; ISBN 978-1-83880-058-1.
58. Tandy, S.; Bossart, K.; Mueller, R.; Ritschel, J.; Hauser, L.; Schulin, R.; Nowack, B. Extraction of Heavy Metals from Soils Using Biodegradable Chelating Agents. *Environ. Sci. Technol.* **2004**, *38*, 937–944. [[CrossRef](#)] [[PubMed](#)]
59. Jiang, X.J.; Luo, Y.M.; Zhao, Q.G.; Baker, A.J.M.; Christie, P.; Wong, M.H. Soil Cd Availability to Indian Mustard and Environmental Risk Following EDTA Addition to Cd-Contaminated Soil. *Chemosphere* **2003**, *50*, 813–818. [[CrossRef](#)]
60. Wu, L.H.; Luo, Y.M.; Xing, X.R.; Christie, P. EDTA-Enhanced Phytoremediation of Heavy Metal Contaminated Soil with Indian Mustard and Associated Potential Leaching Risk. *Agric. Ecosyst. Environ.* **2004**, *102*, 307–318. [[CrossRef](#)]
61. Liphadzi, M.S.; Kirkham, M.B. Availability and Plant Uptake of Heavy Metals in EDTA-Assisted Phytoremediation of Soil and Composted Biosolids. *S. Afr. J. Bot.* **2006**, *72*, 391–397. [[CrossRef](#)]
62. Na, Z.; Yanshan, C.; Yu, F. Leaching of Cd and Pb from a Contaminated Soil with EDTA and EDDS: Effectiveness and Health Risk Assessment. *Environ. Chem.* **2011**, *30*, 958–963.
63. Udovic, M.; Lestan, D. EDTA and HCl Leaching of Calcareous and Acidic Soils Polluted with Potentially Toxic Metals: Remediation Efficiency and Soil Impact. *Chemosphere* **2012**, *88*, 718–724. [[CrossRef](#)]
64. Luo, C.; Shen, Z.; Li, X. Enhanced Phytoextraction of Cu, Pb, Zn and Cd with EDTA and EDDS. *Chemosphere* **2005**, *59*, 1–11. [[CrossRef](#)]
65. Beiyan, J.; Tsang, D.C.W.; Valix, M.; Baek, K.; Ok, Y.S.; Zhang, W.; Bolan, N.S.; Rinklebe, J.; Li, X.-D. Combined Application of EDDS and EDTA for Removal of Potentially Toxic Elements under Multiple Soil Washing Schemes. *Chemosphere* **2018**, *205*, 178–187. [[CrossRef](#)]
66. Tao, Y.; Brigante, M.; Zhang, H.; Mailhot, G. Phenanthrene Degradation Using Fe(III)-EDDS Photoactivation under Simulated Solar Light: A Model for Soil Washing Effluent Treatment. *Chemosphere* **2019**, *236*, 124366. [[CrossRef](#)]
67. Zhao, Y.; Li, H.; Li, B.; Lai, Y.; Zang, L.; Tang, X. Process Design and Validation of a New Mixed Eluent for Leaching Cd, Cr, Pb, Cu, Ni, and Zn from Heavy Metal-Polluted Soil. *Anal. Methods* **2021**, *13*, 1269–1277. [[CrossRef](#)]
68. Leibold, E.; Deckardt, K.; Mellert, W.; Potthoff-Karl, B.; Grundler, O.; Jäckh, R. NTA and Fe(III)NTA: Differential Patterns of Renal Toxicity in Subchronic Studies. *Hum. Exp. Toxicol.* **2002**, *21*, 445–452. [[CrossRef](#)] [[PubMed](#)]
69. Toyokuni, S. Reactive Oxygen Species-Induced Molecular Damage and Its Application in Pathology. *Pathol. Int.* **1999**, *49*, 91–102. [[CrossRef](#)] [[PubMed](#)]
70. Iqbal, M.; Okazaki, Y.; Okada, S. Curcumin Attenuates Oxidative Damage in Animals Treated with a Renal Carcinogen, Ferric Nitrilotriacetate (Fe-NTA): Implications for Cancer Prevention. *Mol. Cell. Biochem.* **2009**, *324*, 157–164. [[CrossRef](#)] [[PubMed](#)]
71. Hirayama, T. Development of Chemical Tools for Imaging of Fe(II) Ions in Living Cells: A Review. *Acta Histochem. Cytochem.* **2018**, *51*, 137–143. [[CrossRef](#)]
72. Huang, J.W.; Blaylock, M.J.; Kapulnik, Y.; Ensley, B.D. Phytoremediation of Uranium-Contaminated Soils: Role of Organic Acids in Triggering Uranium Hyperaccumulation in Plants. *Environ. Sci. Technol.* **1998**, *32*, 2004–2008. [[CrossRef](#)]
73. Gavrilescu, M.; Pavel, L.V.; Cretescu, I. Characterization and Remediation of Soils Contaminated with Uranium. *J. Hazard. Mater.* **2009**, *163*, 475–510. [[CrossRef](#)]
74. Prieto, C.; Lozano, J.C.; Rodríguez, P.B.; Tomé, F.V. Enhancing Radium Solubilization in Soils by Citrate, EDTA, and EDDS Chelating Amendments. *J. Hazard. Mater.* **2013**, *250–251*, 439–446. [[CrossRef](#)]
75. Orr, R.; Hocking, R.K.; Pattison, A.; Nelson, P.N. Extraction of Metals from Mildly Acidic Tropical Soils: Interactions between Chelating Ligand, pH and Soil Type. *Chemosphere* **2020**, *248*, 126060. [[CrossRef](#)]
76. Pepper, I.L.; Brusseau, M.L. Chapter 2—Physical-Chemical Characteristics of Soils and the Subsurface. In *Environmental and Pollution Science*, 3rd ed.; Brusseau, M.L., Pepper, I.L., Gerba, C.P., Eds.; Academic Press: Cambridge, MA, USA, 2019; ISBN 978-0-12-814719-1.

77. Rakhsh, F.; Golchin, A.; Beheshti Al Agha, A.; Nelson, P.N. Mineralization of Organic Carbon and Formation of Microbial Biomass in Soil: Effects of Clay Content and Composition and the Mechanisms Involved. *Soil Biol. Biochem.* **2020**, *151*, 108036. [[CrossRef](#)]
78. Crançon, P.; van der Lee, J. Speciation and Mobility of Uranium(VI) in Humic-Containing Soils. *Radiochim. Acta* **2003**, *91*, 673–679. [[CrossRef](#)]
79. Kantar, C. Heterogeneous Processes Affecting Metal Ion Transport in the Presence of Organic Ligands: Reactive Transport Modeling. *Earth-Sci. Rev.* **2007**, *81*, 175–198. [[CrossRef](#)]
80. Ratnikov, A.N.; Sviridenko, D.G.; Popova, G.I.; Sanzharova, N.I.; Mikailova, R.A. The Behaviour of Uranium in Soils and the Mechanisms of Its Accumulation by Agricultural Plants. In *Uranium in Plants and the Environment*; Gupta, D.K., Walther, C., Eds.; Springer International Publishing: Cham, Switzerland, 2020; ISBN 978-3-030-14961-1.
81. Jiang, X.; Li, X.; Zhang, J.; Lv, J.; Chang, J.; Cui, D. Study of Citric Acid on Extraction and Washing from Different Soil Polluted by Cr. *Chin. Agric. Sci. Bull.* **2012**, *28*, 278–281.
82. Wang, K.; Liu, Y.; Song, Z.; Khan, Z.H.; Qiu, W. Effects of Biodegradable Chelator Combination on Potentially Toxic Metals Leaching Efficiency in Agricultural Soils. *Ecotox. Environ. Safe* **2019**, *182*, 109399. [[CrossRef](#)] [[PubMed](#)]
83. Yang, R.; Luo, C.; Zhang, G.; Li, X.; Shen, Z. Extraction of Heavy Metals from E-Waste Contaminated Soils Using EDDS. *J. Environ. Sci.* **2012**, *24*, 1985–1994. [[CrossRef](#)]
84. Kantar, C.; Honeyman, B.D. Citric Acid Enhanced Remediation of Soils Contaminated with Uranium by Soil Flushing and Soil Washing. *J. Environ. Eng.* **2006**, *132*, 247–255. [[CrossRef](#)]
85. Ebbs, S.D.; Norvell, W.A.; Kochian, L.V. The Effect of Acidification and Chelating Agents on the Solubilization of Uranium from Contaminated Soil. *J. Environ. Qual.* **1998**, *27*, 1486–1494. [[CrossRef](#)]
86. Lozano, J.C.; Blanco Rodríguez, P.; Vera Tomé, F.; Calvo, C.P. Enhancing Uranium Solubilization in Soils by Citrate, EDTA, and EDDS Chelating Amendments. *J. Hazard. Mater.* **2011**, *198*, 224–231. [[CrossRef](#)]
87. Sarthou, M.C.M.; Devime, F.; Baggio, C.; Figuet, S.; Alban, C.; Bourguignon, J.; Ravel, S. Calcium-Permeable Cation Channels Are Involved in Uranium Uptake in *Arabidopsis thaliana*. *J. Hazard. Mater.* **2022**, *424*, 127436. [[CrossRef](#)]
88. Croteau, M.-N.; Fuller, C.C.; Cain, D.J.; Campbell, K.M.; Aiken, G. Biogeochemical Controls of Uranium Bioavailability from the Dissolved Phase in Natural Freshwaters. Available online: <https://pubs.acs.org/doi/pdf/10.1021/acs.est.6b02406> (accessed on 1 April 2022).
89. Shahandeh, H.; Hossner, L.R. Enhancement of Uranium Phytoaccumulation from Contaminated Soils. *Soil Sci.* **2002**, *167*, 269–280. [[CrossRef](#)]
90. Shahandeh, H.; Hossner, L. Role of Soil Properties in Phytoaccumulation of Uranium. *Water Air Soil Pollut.* **2002**, *141*, 165–180. [[CrossRef](#)]
91. Laurette, J.; Larue, C.; Llorens, I.; Jaillard, D.; Jouneau, P.-H.; Bourguignon, J.; Carrière, M. Speciation of Uranium in Plants upon Root Accumulation and Root-to-Shoot Translocation: A XAS and TEM Study. *Environ. Exp. Bot.* **2012**, *77*, 87–95. [[CrossRef](#)]
92. Shahid, M.; Austruy, A.; Echevarria, G.; Arshad, M.; Sanaullah, M.; Aslam, M.; Nadeem, M.; Nasim, W.; Dumat, C. EDTA-Enhanced Phytoremediation of Heavy Metals: A Review. *Soil. Sediment. Contam.* **2013**, *23*, 389–416. [[CrossRef](#)]
93. Zhou, P.; Gu, B. Extraction of Oxidized and Reduced Forms of Uranium from Contaminated Soils: Effects of Carbonate Concentration and pH. *Environ. Sci. Technol.* **2005**, *39*, 4435–4440. [[CrossRef](#)] [[PubMed](#)]
94. Doustaly, F.; Combes, F.; Fiévet, J.B.; Berthet, S.; Hugouvieux, V.; Bastien, O.; Aranjuelo, I.; Leonhardt, N.; Rivasseau, C.; Carrière, M.; et al. Uranium Perturbs Signaling and Iron Uptake Response in *Arabidopsis thaliana* Roots. *Metallomics* **2014**, *6*, 809–821. [[CrossRef](#)] [[PubMed](#)]
95. Berthet, S.; Villiers, F.; Alban, C.; Serre, N.B.C.; Martin-Laffon, J.; Figuet, S.; Boisson, A.-M.; Bligny, R.; Kuntz, M.; Finazzi, G.; et al. *Arabidopsis thaliana* Plants Challenged with Uranium Reveal New Insights into Iron and Phosphate Homeostasis. *New Phytol.* **2018**, *217*, 657–670. [[CrossRef](#)] [[PubMed](#)]
96. Malaviya, P.; Singh, A. Phytoremediation Strategies for Remediation of Uranium-Contaminated Environments: A Review. *Crit. Rev. Environ. Sci. Technol.* **2012**, *42*, 2575–2647. [[CrossRef](#)]
97. Chang, P.; Kim, K.-W.; Yoshida, S.; Kim, S.-Y. Uranium Accumulation of Crop Plants Enhanced by Citric Acid. *Environ. Geochem. Health* **2005**, *27*, 529–538. [[CrossRef](#)]
98. Rong, L.; Zhang, S.; Wang, J.; Li, S.; Xie, S.; Wang, G. Phytoremediation of Uranium-Contaminated Soil by Perennial Ryegrass (*Lolium perenne* L.) Enhanced with Citric Acid Application. *Environ. Sci. Pollut. Res.* **2022**, *29*, 33002–33012. [[CrossRef](#)]
99. Li, C.; Dan, W.; Chan, L.; Cui, Z. Effect of Three Kinds of Chelating Agents on Phytoremediation in U and Cd Contaminated Soil by *Zebrina pendula*. *Atomic Energy Sci. Technol.* **2018**, *52*, 1359–1366. [[CrossRef](#)]
100. Manara, A.; Fasani, E.; Furini, A.; DalCorso, G. Evolution of the Metal Hyperaccumulation and Hypertolerance Traits. *Plant Cell Environ.* **2020**, *43*, 2969–2986. [[CrossRef](#)]
101. Sevostianova, E.; Lindemann, W.C.; Ulery, A.L.; Rimmenga, M.D. Plant Uptake of Depleted Uranium from Manure-Amended and Citrate Treated Soil. *Int. J. Phytoremediat.* **2010**, *12*, 550–561. [[CrossRef](#)] [[PubMed](#)]
102. Wan, Q.; Pan, N.; Jin, Y.; Xia, C. Study on remediation for uranium contaminated soils enhanced by chelator using brassica mustard. In *Progress Report on Nuclear Science and Technology in China*; Atomic Energy Press: Beijing, China, 2012; Volume 2, ISBN 978-7-5022-5602-9.



103. Qi, F.; Zha, Z.; Du, L.; Feng, X.; Wang, D.; Zhang, D.; Fang, Z.; Ma, L.; Jin, Y.; Xia, C. Impact of Mixed Low-Molecular-Weight Organic Acids on Uranium Accumulation and Distribution in a Variant of Mustard (*Brassica juncea* VarTumida). *J. Radioanal. Nucl. Chem.* **2014**, *302*, 149–159. [[CrossRef](#)]
104. Nowack, B.; Schulin, R.; Robinson, B.H. Critical Assessment of Chelant-Enhanced Metal Phytoextraction. *Environ. Sci. Technol.* **2006**, *40*, 5225–5232. [[CrossRef](#)] [[PubMed](#)]
105. Li, H.; Wang, Q.; Cui, Y.; Dong, Y.; Christie, P. Slow Release Chelate Enhancement of Lead Phytoextraction by Corn (*Zea mays* L.) from Contaminated Soil—A Preliminary Study. *Sci. Total Environ.* **2005**, *339*, 179–187. [[CrossRef](#)] [[PubMed](#)]
106. Yadav, S.K. Heavy Metals Toxicity in Plants: An Overview on the Role of Glutathione and Phytochelatins in Heavy Metal Stress Tolerance of Plants. *S. Afr. J. Bot.* **2010**, *76*, 167–179. [[CrossRef](#)]
107. Yan, A.; Wang, Y.; Tan, S.N.; Mohd Yusof, M.L.; Ghosh, S.; Chen, Z. Phytoremediation: A Promising Approach for Revegetation of Heavy Metal-Polluted Land. *Front. Plant Sci.* **2020**, *11*, 359. [[CrossRef](#)] [[PubMed](#)]
108. Pietrini, I.; Grifoni, M.; Franchi, E.; Cardaci, A.; Pedron, F.; Barbafieri, M.; Petruzzelli, G.; Vocciante, M. Enhanced Lead Phytoextraction by Endophytes from Indigenous Plants. *Soil Syst.* **2021**, *5*, 55. [[CrossRef](#)]
109. Römkens, P.; Bouwman, L.; Japenga, J.; Draaisma, C. Potentials and Drawbacks of Chelate-Enhanced Phytoremediation of Soils. *Environ. Pollut.* **2002**, *116*, 109–121. [[CrossRef](#)]
110. Epelde, L.; Ma Becerril, J.; Alkorta, I.; Garbisu, C. Heavy Metal Phytoremediation: Microbial Indicators of Soil Health for the Assessment of Remediation Efficiency. In *Advances in Applied Bioremediation*; Singh, A., Kuhad, R.C., Ward, O.P., Eds.; Springer: Berlin/Heidelberg, Germany, 2009; ISBN 978-3-540-89621-0.
111. Lee, J.; Sung, K. Effects of Chelates on Soil Microbial Properties, Plant Growth and Heavy Metal Accumulation in Plants. *Ecol. Eng.* **2014**, *73*, 386–394. [[CrossRef](#)]
112. Cao, A.; Carucci, A.; Lai, T.; La Colla, P.; Tamburini, E. Effect of Biodegradable Chelating Agents on Heavy Metals Phytoextraction with *Mirabilis jalapa* and on Its Associated Bacteria. *Eur. J. Soil Biol.* **2007**, *43*, 200–206. [[CrossRef](#)]
113. Barona, A.; Aranguiz, I.; Elias, A. Metal Associations in Soils before and after EDTA Extractive Decontamination: Implications for the Effectiveness of Further Clean-up Procedures. *Environ. Pollut.* **2001**, *113*, 79–85. [[CrossRef](#)]
114. Udovic, M.; Lestan, D. Pb, Zn and Cd Mobility, Availability and Fractionation in Aged Soil Remediated by EDTA Leaching. *Chemosphere* **2009**, *74*, 1367–1373. [[CrossRef](#)] [[PubMed](#)]
115. Huang, X.; Luo, D.; Chen, X.; Wei, L.; Liu, Y.; Wu, Q.; Xiao, T.; Mai, X.; Liu, G.; Liu, L. Insights into Heavy Metals Leakage in Chelator-Induced Phytoextraction of Pb- and Tl-Contaminated Soil. *Int. J. Environ. Res. Public Health* **2019**, *16*, 1328. [[CrossRef](#)] [[PubMed](#)]
116. Thayalakumaran, T.; Robinson, B.; Vogeler, I.; Scotter, D.; Clothier, B.; Percival, H. Plant Uptake and Leaching of Copper during EDTA-Enhanced Phytoremediation of Repacked and Undisturbed Soil. *Plant Soil* **2003**, *254*, 415–423. [[CrossRef](#)]
117. Mastromatteo, M.; Mastromatteo, M.; Conte, A.; del Nobile, M.A. Advances in Controlled Release Devices for Food Packaging Applications. *Trends Food Sci. Technol.* **2010**, *21*, 591–598. [[CrossRef](#)]
118. Yusoff, S.N.M.; Kamari, A.; Aljafree, N.F.A. A Review of Materials Used as Carrier Agents in Pesticide Formulations. *Int. J. Environ. Sci. Technol.* **2016**, *13*, 2977–2994. [[CrossRef](#)]
119. Al-Rawajfeh, A.E.; Alrbaihat, M.R.; Alshamaileh, E.M. Chapter 4—Characteristics and Types of Slow- and Controlled-Release Fertilizers. In *Controlled Release Fertilizers for Sustainable Agriculture*; Lewu, F.B., Volova, T., Thomas, S., Rakhimov, K.R., Eds.; Academic Press: Cambridge, MA, USA, 2021; ISBN 978-0-12-819555-0.
120. Lubkowski, K.; Grzmil, B. Controlled Release Fertilizers. *Pol. J. Chem. Technol.* **2007**, *9*, 83–84. [[CrossRef](#)]
121. Liu, G.; Zotarelli, L.; Li, Y.; Dinkins, D.; Wang, Q.; Ozores-Hampton, M. Controlled-Release and Slow-Release Fertilizers as Nutrient Management Tools. Available online: <https://edis.ifas.ufl.edu/publication/HS1255> (accessed on 21 September 2021).
122. Almasi, H.; Oskouie, M.J.; Saleh, A. A Review on Techniques Utilized for Design of Controlled Release Food Active Packaging. *Crit. Rev. Food Sci. Nutr.* **2020**, *61*, 2601–2621. [[CrossRef](#)]
123. Kuai, L.; Liu, F.; Chiou, B.-S.; Avena-Bustillos, R.J.; McHugh, T.H.; Zhong, F. Controlled Release of Antioxidants from Active Food Packaging: A Review. *Food Hydrocoll.* **2021**, *120*, 106992. [[CrossRef](#)]
124. Vasile, C.; Baican, M. Progresses in Food Packaging, Food Quality, and Safety—Controlled-Release Antioxidant and/or Antimicrobial Packaging. *Molecules* **2021**, *26*, 1263. [[CrossRef](#)]
125. Heirlings, L.; Siró, I.; Devlieghere, F.; Bavel, E.V.; Cool, P.; Meulenaer, B.D.; Vansant, E.F.; Debevere, J. Influence of Polymer Matrix and Adsorption onto Silica Materials on the Migration of  $\alpha$ -Tocopherol into 95% Ethanol from Active Packaging. *Food Addit. Contam.* **2007**, *21*, 1125–1136. [[CrossRef](#)] [[PubMed](#)]
126. Cerisuelo, J.P.; Bermúdez, J.M.; Aucejo, S.; Catalá, R.; Gavara, R.; Hernández-Muñoz, P. Describing and Modeling the Release of an Antimicrobial Agent from an Active PP/EVOH/PP Package for Salmon. *J. Food Eng.* **2013**, *116*, 352–361. [[CrossRef](#)]
127. LaCoste, A.; Schaich, K.M.; Zumbunnen, D.; Yam, K.L. Advancing Controlled Release Packaging through Smart Blending. *Packag. Technol. Sci.* **2005**, *18*, 77–87. [[CrossRef](#)]
128. Han, J.H.; Floros, J.D. Simulating Diffusion Model and Determining Diffusivity of Potassium Sorbate Through Plastics to Develop Antimicrobial Packaging Films. *J. Food Process Preserv.* **1998**, *22*, 107–122. [[CrossRef](#)]
129. Whelehan, M.; Marison, I.W. Microencapsulation Using Vibrating Technology. *J. Microencapsul.* **2011**, *28*, 669–688. [[CrossRef](#)] [[PubMed](#)]

130. Rathore, S.; Desai, P.M.; Liew, C.V.; Chan, L.W.; Heng, P.W.S. Microencapsulation of Microbial Cells. *J. Food Eng.* **2013**, *116*, 369–381. [[CrossRef](#)]
131. Xie, Z.; Wu, L.; Chen, N.; Liu, C.; Zheng, Y.; Xu, S.; Li, F.; Xu, Y. Phytoextraction of Pb and Cu Contaminated Soil With Maize and Microencapsulated EDTA. *Int. J. Phytoremediat.* **2012**, *14*, 727–740. [[CrossRef](#)]
132. Ding, C.; Li, Y. A Slow-Release Chelating Agent for Heavy Metal Soil Remediation. Patent Registration Number 201910960626, 14 January 2020.
133. Ocak, B. Complex Coacervation of Collagen Hydrolysate Extracted from Leather Solid Wastes and Chitosan for Controlled Release of Lavender Oil. *J. Environ. Manag.* **2012**, *100*, 22–28. [[CrossRef](#)]
134. O'Connor, D.; Hou, D.; Ok, Y.S.; Song, Y.; Sarmah, A.K.; Li, X.; Tack, F.M.G. Sustainable in Situ Remediation of Recalcitrant Organic Pollutants in Groundwater with Controlled Release Materials: A Review. *J. Control Release* **2018**, *283*, 200–213. [[CrossRef](#)]
135. Christenson, M.; Kambhu, A.; Reece, J.; Comfort, S.; Brunner, L. A Five-Year Performance Review of Field-Scale, Slow-Release Permanganate Candles with Recommendations for Second-Generation Improvements. *Chemosphere* **2016**, *150*, 239–247. [[CrossRef](#)]
136. Tang, X.; Yu, C.; Lei, Y.; Wang, Z.; Wang, C.; Wang, J. A Novel Chitosan-Urea Encapsulated Material for Persulfate Slow-Release to Degrade Organic Pollutants. *J. Hazard. Mater.* **2022**, *426*, 128083. [[CrossRef](#)] [[PubMed](#)]
137. Tsai, T.T.; Liu, J.K.; Chang, Y.M.; Chen, K.F.; Kao, C.M. Application of Polycolloid-Releasing Substrate to Remediate Trichloroethylene-Contaminated Groundwater: A Pilot-Scale Study. *J. Hazard. Mater.* **2014**, *268*, 92–101. [[CrossRef](#)] [[PubMed](#)]
138. Yeum, Y.; Han, K.; Kang, J.-H.; Kim, D.-W.; Park, C.-W.; Kwon, S.; Kim, Y. Production, Characterization, and Evaluation of Two Types of Slow-Releasing Carbon Source Tablets for in-Situ Heterotrophic Nitrate Denitrification in Aquifers. *Chemosphere* **2020**, *260*, 127478. [[CrossRef](#)] [[PubMed](#)]
139. Essawy, H.A.; Ghazy, M.B.M.; El-Hai, F.A.; Mohamed, M.F. Superabsorbent Hydrogels via Graft Polymerization of Acrylic Acid from Chitosan-Cellulose Hybrid and Their Potential in Controlled Release of Soil Nutrients. *Int. J. Biol. Macromol.* **2016**, *89*, 144–151. [[CrossRef](#)] [[PubMed](#)]
140. Pang, L.; Gao, Z.; Feng, H.; Wang, S.; Wang, Q. Cellulose Based Materials for Controlled Release Formulations of Agrochemicals: A Review of Modifications and Applications. *J. Control Release* **2019**, *316*, 105–115. [[CrossRef](#)]
141. Wang, G.; Wang, B.; Fan, W.; Deng, N. Enhanced Phytoremediation of Uranium-Contaminated Soils by Indian Mustard (*Brassica juncea* L.) Using Slow Release Citric Acid. *Environ. Sci. Pollut. Res.* **2021**, *28*, 61061–61071. [[CrossRef](#)]
142. Shibata, M.; Konno, T.; Akaike, R.; Xu, Y.; Shen, R.; Ma, J.F. Phytoremediation of Pb Contaminated Soil with Polymer-Coated EDTA. *Plant Soil* **2007**, *290*, 201–208. [[CrossRef](#)]
143. Xie, Z.; Chen, N.; Liu, C.; Zhou, J.; Xu, S.; Zheng, Y.; Li, F.; Xu, Y. Synthesis and Characterization of Ethylenediamine Tetraacetic Acid Tetrasodium Salt Loaded in Microcapsules with Slow Release Properties. *Chin. J. Chem. Eng.* **2010**, *18*, 149–155. [[CrossRef](#)]
144. Yoo, J.; Won, Y.-Y. Phenomenology of the Initial Burst Release of Drugs from PLGA Microparticles. *ACS Biomater. Sci. Eng.* **2020**, *6*, 6053–6062. [[CrossRef](#)]
145. Chen, J.; Lü, S.; Zhang, Z.; Zhao, X.; Li, X.; Ning, P.; Liu, M. Environmentally Friendly Fertilizers: A Review of Materials Used and Their Effects on the Environment. *Sci. Total Environ.* **2018**, *613–614*, 829–839. [[CrossRef](#)]
146. Zhang, L.; Zhang, G.; Lu, J.; Liang, H. Preparation and Characterization of Carboxymethyl Cellulose/Polyvinyl Alcohol Blend Film as a Potential Coating Material. *Polym. Plast. Technol. Eng.* **2013**, *52*, 163–167. [[CrossRef](#)]
147. Han, X.; Chen, S.; Hu, X. Controlled-Release Fertilizer Encapsulated by Starch/Polyvinyl Alcohol Coating. *Desalination* **2009**, *240*, 21–26. [[CrossRef](#)]
148. Anghel, N.; Marius, N.; Spiridon, I. Heavy Metal Adsorption Ability of a New Composite Material Based on Starch Strengthened with Chemically Modified Cellulose. *Polym. Adv. Technol.* **2019**, *30*, 1453–1460. [[CrossRef](#)]
149. Wan, M.-W.; Petrisor, I.G.; Lai, H.-T.; Kim, D.; Yen, T.F. Copper Adsorption through Chitosan Immobilized on Sand to Demonstrate the Feasibility for in Situ Soil Decontamination. *Carbohydr. Polym.* **2004**, *55*, 249–254. [[CrossRef](#)]
150. Zhou, Y.; Gao, B.; Zimmerman, A.R.; Fang, J.; Sun, Y.; Cao, X. Sorption of Heavy Metals on Chitosan-Modified Biochars and Its Biological Effects. *Chem. Eng. J.* **2013**, *231*, 512–518. [[CrossRef](#)]
151. Li, B.; Li, M.; Zhang, P.; Pan, Y.; Huang, Z.; Xiao, H. Remediation of Cd (II) Ions in Aqueous and Soil Phases Using Novel Porous Cellulose/Chitosan Composite Spheres Loaded with Zero-Valent Iron Nanoparticles. *React. Funct. Polym.* **2022**, *173*, 105210. [[CrossRef](#)]
152. O'Connell, D.W.; Birkinshaw, C.; O'Dwyer, T.F. Heavy Metal Adsorbents Prepared from the Modification of Cellulose: A Review. *Bioresour. Technol.* **2008**, *99*, 6709–6724. [[CrossRef](#)]
153. Kos, B.; Le tan, D. Influence of a Biodegradable ([S,S]-EDDS) and Nondegradable (EDTA) Chelate and Hydrogel Modified Soil Water Sorption Capacity on Pb Phytoextraction and Leaching. *Plant Soil* **2003**, *253*, 403–411. [[CrossRef](#)]
154. Noppakundilokrat, S.; Pheathcharat, N.; Kiatkamjornwong, S. Multilayer-Coated NPK Compound Fertilizer Hydrogel with Controlled Nutrient Release and Water Absorbency. *J. Appl. Polym. Sci.* **2015**, *132*, 41249. [[CrossRef](#)]
155. Ramli, R.A. Slow Release Fertilizer Hydrogels: A Review. *Polym. Chem.* **2019**, *10*, 6073–6090. [[CrossRef](#)]
156. Zhang, X.; Liu, Y.; Lu, P.; Zhang, M. Preparation and Properties of Hydrogel Based on Sawdust Cellulose for Environmentally Friendly Slow Release Fertilizers. *Green Process. Synth.* **2020**, *9*, 139–152. [[CrossRef](#)]
157. Kareem, S.A.; Dere, I.; Gungula, D.T.; Andrew, F.P.; Saddiq, A.M.; Adebayo, E.F.; Tame, V.T.; Kefas, H.M.; Joseph, J.; Patrick, D.O. Synthesis and Characterization of Slow-Release Fertilizer Hydrogel Based on Hydroxy Propyl Methyl Cellulose, Polyvinyl Alcohol, Glycerol and Blended Paper. *Gels* **2021**, *7*, 262. [[CrossRef](#)] [[PubMed](#)]

158. Rizwan, M.; Rubina Gilani, S.; Iqbal Durani, A.; Naseem, S. Materials Diversity of Hydrogel: Synthesis, Polymerization Process and Soil Conditioning Properties in Agricultural Field. *J. Adv. Res.* **2021**, *33*, 15–40. [[CrossRef](#)] [[PubMed](#)]
159. Wang, G.; Zhang, S.; Xu, L.; Li, Q. The Slow-Release Chelating Agent and Its Preparation Method for Phytoremediation of Soil. Patent Registration Number 201610567644.8, 7 December 2016.
160. Chen, L.; Wang, D.; Long, C.; Cui, Z. Effect of Biodegradable Chelators on Induced Phytoextraction of Uranium- and Cadmium-Contaminated Soil by *Zebrina Pendul*. *Schnizl. Sci. Rep.* **2019**, *9*, 19817. [[CrossRef](#)]
161. Arshad, M.; Naqvi, N.; Gul, I.; Yaqoob, K.; Bilal, M.; Kallerhoff, J. Lead Phytoextraction by *Pelargonium hortorum*: Comparative Assessment of EDTA and DIPA for Pb Mobility and Toxicity. *Sci. Total Environ.* **2020**, *748*, 141496. [[CrossRef](#)]
162. Broschat, T.K.; Moore, K.K. Release Rates of Ammonium-Nitrogen, Nitrate-Nitrogen, Phosphorus, Potassium, Magnesium, Iron, and Manganese from Seven Controlled-Release Fertilizers. *Commun. Soil Sci. Plant Anal.* **2007**, *38*, 843–850. [[CrossRef](#)]
163. Dai, J.; Fan, X.; Yu, J.; Liu, F.; Zhang, Q. Study on the Rapid Method to Predict Longevity of Controlled Release Fertilizer Coated by Water Soluble Resin. *Agric. Sci. China* **2008**, *7*, 1127–1132. [[CrossRef](#)]
164. Medina, L.C.; Sartain, J.B.; Obreza, T.A.; Hall, W.L.; Thiex, N.J. Evaluation of a Soil Incubation Method to Characterize Nitrogen Release Patterns of Slow- and Controlled-Release Fertilizers. *J. AOAC Int.* **2014**, *97*, 643–660. [[CrossRef](#)]
165. Jia, Y.; Hu, Z.; Mu, J.; Zhang, W.; Xie, Z.; Wang, G. Preparation of Biochar as a Coating Material for Biochar-Coated Urea. *Sci. Total Environ.* **2020**, *731*, 139063. [[CrossRef](#)]
166. Purnomo, C.W.; Saputra, H. Chapter 6—Manufacturing of Slow and Controlled Release Fertilizer. In *Controlled Release Fertilizers for Sustainable Agriculture*; Lewu, F.B., Volova, T., Thomas, S., Rakhimol, K.R., Eds.; Academic Press: Cambridge, MA, USA, 2021; ISBN 978-0-12-819555-0.
167. Kottegoda, N.; Sandaruwan, C.; Priyadarshana, G.; Siriwardhana, A.; Rathnayake, U.A.; Berugoda Arachchige, D.M.; Kumarasinghe, A.R.; Dahanayake, D.; Karunaratne, V.; Amaratunga, G.A.J. Urea-Hydroxyapatite Nanohybrids for Slow Release of Nitrogen. *ACS Nano* **2017**, *11*, 1214–1221. [[CrossRef](#)]
168. Ni, B.; Liu, M.; Lü, S. Multifunctional Slow-Release Urea Fertilizer from Ethylcellulose and Superabsorbent Coated Formulations. *Chem. Eng. J.* **2009**, *155*, 892–898. [[CrossRef](#)]
169. Xie, Z.; Chen, N.; Xu, S.; Xu, Y. A Complexing Agent Microcapsule for Phytoremediation of Soil and Its Preparation Method. Patent Registration Number 200810220712.9, 2 September 2009.
170. Cagnasso, C.E.; López, L.B.; Rodríguez, V.G.; Valencia, M.E. Development and Validation of a Method for the Determination of EDTA in Non-Alcoholic Drinks by HPLC. *J. Food Compos. Anal.* **2007**, *20*, 248–251. [[CrossRef](#)]
171. Khan, M.S.; Zaidi, A.; Wani, P.A.; Oves, M. Role of Plant Growth Promoting Rhizobacteria in the Remediation of Metal Contaminated Soils. *Environ. Chem. Lett.* **2009**, *7*, 1–19. [[CrossRef](#)]
172. Saleh, H.M. Water Hyacinth for Phytoremediation of Radioactive Waste Simulate Contaminated with Cesium and Cobalt Radionuclides. *Nucl. Eng. Des.* **2012**, *242*, 425–432. [[CrossRef](#)]
173. Saleh, H.M.; Bayoumi, T.A.; Mahmoud, H.H.; Aglan, R.F. Uptake of Cesium and Cobalt Radionuclides from Simulated Radioactive Wastewater by *Ludwigia stolonifera* Aquatic Plant. *Nucl. Eng. Des.* **2017**, *315*, 194–199. [[CrossRef](#)]
174. Saleh, H.M.; Aglan, R.F.; Mahmoud, H.H. *Ludwigia stolonifera* for Remediation of Toxic Metals from Simulated Wastewater. *Chem. Ecol.* **2018**, *35*, 164–178. [[CrossRef](#)]
175. Saleh, H.M.; Mahmoud, H.H.; Aglan, R.F.; Bayoumi, T.A. Biological Treatment of Wastewater Contaminated with Cu (II), Fe (II) and Mn (II) Using *Ludwigia stolonifera* Aquatic Plant. *Environ. Eng. Manag. J.* **2019**, *18*, 1327–1336. [[CrossRef](#)]
176. Saleh, H.M.; Moussa, H.R.; El-Saied, F.A.; Dawoud, M.; Nouh, E.S.A.; Abdel Wahed, R.S. Adsorption of Cesium and Cobalt onto Dried *Myriophyllum spicatum* L. from Radio-Contaminated Water: Experimental and Theoretical Study. *Prog. Nucl. Energy* **2020**, *125*, 103393. [[CrossRef](#)]
177. Saleh, H.M.; Moussa, H.R.; Mahmoud, H.H.; El-Saied, F.A.; Dawoud, M.; Abdel Wahed, R.S. Potential of the Submerged Plant *Myriophyllum spicatum* for Treatment of Aquatic Environments Contaminated with Stable or Radioactive Cobalt and Cesium. *Prog. Nucl. Energy* **2020**, *118*, 103147. [[CrossRef](#)]

MDPI  
St. Alban-Anlage 66  
4052 Basel  
Switzerland  
Tel. +41 61 683 77 34  
Fax +41 61 302 89 18  
[www.mdpi.com](http://www.mdpi.com)

*Sustainability* Editorial Office  
E-mail: [sustainability@mdpi.com](mailto:sustainability@mdpi.com)  
[www.mdpi.com/journal/sustainability](http://www.mdpi.com/journal/sustainability)





MDPI  
St. Alban-Anlage 66  
4052 Basel  
Switzerland

Tel: +41 61 683 77 34

[www.mdpi.com](http://www.mdpi.com)



ISBN 978-3-0365-7249-9